Visualizing the influence of the Fermi surface on Superconductivity

A Thesis submitted in partial fulfillment of the requirements for the

degree of Doctor of Philosophy

Edwin Herrera Vasco

Thesis Supervisors:

Hermann Suderow Rodriguez

Isabel Guillamón Gómez

Departamento de Física de la Materia Condensada
Universidad Autónoma de Madrid,
Madrid, Spain

November 2016

This template was downloaded from the website LaTexTemplates (http://www.latextemplates.com).
It has been extensively modified by the author of this thesis.
FIRST PRINTING, NOVEMBER 2016

And high up above or down below
When you're too in love to let it go
But if you never try you'll never know
Just what you're worth.
Fix You.
COLDPLAY

Llegando al final,
se acaba siempre en el comienzo:
A la mamá de los pollitos,
a Tavines
y
a Lile.

Agradecimientos

Un amigo vale más que un Nobel
Juan Gossaín [1]

En el tabaco, en el café, en el vino,
al borde de la noche se levantan
como esas voces que a lo lejos cantan
sin que se sepa qué, por el camino.
Livianamente hermanos del destino,
dióscuros, sombras pálidas, me espantan
las moscas de los hábitos, me aguantan
que siga a flote entre tanto remolino.
Los muertos hablan más pero al oído,
y los vivos son mano tibia y techo,
suma de lo ganado y lo perdido.
Así un día en la barca de la sombra,
de tanta ausencia abrigará mi pecho
esta antigua ternura que los nombra.
Poema a los Amigos.
Julio Cortázar

Quiero inciar agradeciendo al Departamento Administrativo de Ciencia, Tecnología e Innovación de Colombia (COLCIENCIAS) y su convocatoria 568 del 2012, que en nombre del Gobierno de Colombia, financiaron mis estudios y estancia como estudiante de doctorado. Muchas gracias a todos los Colombianos que juciosamente pagan sus impuestos e hicieron de esta tesis una realidad, a todos y cada uno de ellos: MUCHAS GRACIAS.

A la Universidad Autónoma de Madrid, al Departamento de Física de la Materia Condensada y al Segainvex por haber permitido usar los espacios y recursos para el desarrollo de esta Tesis.

A Hermann Suderow por haber confiado en mí sin conocerme, por estar siempre ahí cuando más lo necesité, gracias por tu ejemplo como director y como ser humano. Admiro tu capacidad y habilidad para mezclar inteligencia, física, carácter, alegría y corazón, gracias por ser mi *Doktorvater*.

A Isabel Guillamón, gracias por los secretos microscópicos que me compartiste, por ayudarme a crecer con tus siempre amables explicaciones, gracias por ser paciente cuando no sabia algo y por transmitirme los consejos que se necesitan para saber medir, todavá me faltan muchos más. Siempre serás la Profesora.

Al Señor Profesor Sensebastián Vieira, muchas gracias por sus puntuales visitas, por los consejos que me regaló, por su eficacia y buen olfato para encontrar lo verdadero en las medidas. Gracias por las veces que me motivó a ir más allá y sobre todo por los palabras de aliento cuando las cosas no iban tan bien. Es un orgullo haber trabajado al lado de alguien con tanta experiencia y sabiduría. Muchas gracias por las palmadas en la espada y por el premio Edwin.

A los profesores J. G. Ramírez y E. Patiño, quienes me ayudaron incondicinalmente en el inicio de esta aventura que hoy da sus frutos.

A Andrés Buendía, gracias por tus manos, tu alegría, tu prudencia, tu sabiduría; esa que solo da la calle y los buenos amigos, gracias por salvarme cuando "sufría" y por dejarme jugar con tus herramientas, gracias a eso me enamoré de la Dremell. Espero que algún día alguien me ragale una de navidad o cumpleaños.

A Chema y a Rafa, los nuevos salvadores "manitas", muchas gracias por ayudarme con mis últimos medidas y por no hacer ruido. Por los cafés y las cervecitas.

A Macarena, porque sin su ayuda el laboratorio sería un caos.

A Antón Fente, muchas gracias monito por tu amistad, por haberme presentado a tu familia, por el lindo atardecer en Vigo, junto con Rosalia y Che. Gracias por ser el primero que se preocupó por mí en los iniciales días de acoplamiento, que siempre son los más duros. Gracias por ser mi primer parcero de la Universidad y haber seguido en paralelo esta etapa de nuestras vidas. Gracias, porque sin tí la vida en el laboratorio habría sido muy aburrida. Gracias por las sonrisas, por las tardes que hablabamos entre racs y cables de la vida. Eres un hombre con un corazón sin maldad, sensible, justo, disciplinado y correcto. " Moitas Grazas parce".

A Manu. Muchas gracias por tu incondicional amistad, por tu originalidad en el momento de actuar como Manu, por tantas salseadas y eventos random. Gracias Manu por tus palabras de ánimo y tu compañía fuera del lab. Para tí también "Moitas Grazas parce".

A Laura, Lauri. Gracias por tu sonrisas y las carcajadas de felicidad que transpasan paredes. La alegría se te nota siempre. Que orgulloso me siento de haber compartido pocos pero lindos momentos contigo.

A Aday. Muchas gracias parce por las escapadas en bici y las escaladas. Felicitaciones en la nueva etapa: Doc.

A Antonio. El gran Antonio, fuí con un Coloso del lab a donde ya no hay Coloso en Grecia. Gracias por las historias compartidas en el viaje. Qué maravilla es verte haciendo parkour en tus videos de Youtube. Ya tenemos fotos con George para la eternidad.

A Isidoro, porque JuanPe y los otros me dijeron que era un gato. Las relojerías te podráin pagar muy bien por ser tan puntual. Gracias por las sonrisas y por los almuerzos compartidos.

A Tomás y a la bellita Cris. Los recuerdo mucho en el albúm de fotos que tengo en mi cabeza. Gracias Tomás por las advertencias criogénicas despresurizadas. Ya tengo nuevas historias para hacer reir a Cris.

A JuanP y la linda Ana. Gracias por los consejos para comprar a Nathalia. Gacias por ayudarme con el diseño de la portada de esta tesis y sobre todo por guardarme los secretos de la vida. Mil discúlpas por no haberlos acompañado en la fiesta del compromiso del amor (estaba escribiendo parte de estas hojas). Hacen parte de los referentes como pareja complice, feliz y cariñosa en la que participa un físico que también es músico y dibujante.

A Jon el Vasco, porque siempre será mejor morir cayendo en un globo que por falta de oxígeno en el lab. Gracias por la buena energía, por los goles, eres un crack, salud!!!.

A Oscar Bacca, mi amigo de antes y de siempre, desde el colegio y el servivio militar. La

distancia nunca fué un obstaculo. Muchas gracias mi Baquita querido por acompañarme en esta etapa. Seguiran más, muchas más.

A Nathalia. Chyqui, tu vocecita y tus mensajes siempre me sacaban una sonrisa. Que lindo ha sido verte crecer.

A Pepis, muchas gracias por esa clase de guitarra que nunca practiqué. Gracias por ser tan noble, tan buen amigo y por aterrizarme cuando lo necesitaba. Por los bailecitos de salsa en el lab. Que bonito fué, es y será verte siempre con Ele. Gracias por presentarme y compartirme tus amigos: Guille, Pou, al Javis, George-I y George-II. Simpre te recordaré como el amigo con el que por primera vez fuí a la nieve. También porque te he visto crecer, cuando llegaste al lab eras un bebito Pepe, ahora ya eres un casi Doctor. Ánimo Pepis. El próximo año serás mi profesor de matlab.

A Victor, a Fran, a David es bueno verlos y saber que los nuevos vientos son más fuertes y llevan más lejos a los navegantes. Mucho ánimo y sobre todo mucha paciencia. Que viva la música, la prudencia, la alegía y el frío, por que sin Helio no hay tesis.

A Thomas, que siempre esta sonriendo. Felicidades por tu matrimonio.

A Mario, mi Marito del alma, mi Marito querido, orejitas de Vinil. No sé como coincidimos, son tantas cosas, tantos eventos en paralelo, tanta vida y tanta alegría que ya somos el olvido que seremos. Muchas gracias por dejarme ser del primer círculo. Gracias por las aventuras, por haberme acompañado en mis viajes dentro de dos modelos de un "medio de trasnporte novedoso". Por la música, por las llamadas de 1 hora. Por la cultura, por las letras, por lo que no se puede escribir. Por Candela, por el Anónimo, por ThunderCat, por Abbott y Costello, por la Mili, por el Mario Kart. Y porque no le volveremos a dar diamantes a los cerdos: somos seres de luz.

A Cesar, mi chicharrito de oro, un Maratonista original. Buen padre, buen hijo, buen amigo. Las lágrimas del Q las evaporó su tesis y ahora ésta las convierte en plasma. Dedico estas palabras a todo eso que sucedió en los tiempos que prometimos no volver a nombrar y sobre todo al triunfo de la amistad. Gracias por enseñarme a nadar, a correr, a montar bici, a alimentarme bien, a ver las cosas desde un espectro más amplio. Gracias por haber venido a visitarme y por aguantarme en mi vida firulí. Gracias por que "en la vida mijo lo único que nos queda grande es la talla XXL". Felicitaciones a mí por tener un amigo como usted. Muacks.

A Nico, el Nicks. Gracias parcerito por la buena energá siempre, por su ejemplo como ser humano para con el planeta y todo lo que significa vida. Gracias por las noches que me acompañó macerando polvitos con paciencia y amor para que las medidas salieran bien. Muchas gracias por la fortaleza que siempre muestra, por su ejemplo de ser padre, ser amigo y ser buen hijo. Me da mucha envídia cuando lo veo bailar mejor que yo. Aún así, lo quiero mucho. Besos a Dyoni y al Javi.

A Angelita, la Bri. Muchas gracias Morena de mi corazón por la musicalidad de la vida y porque simpre me haces saber que cuento contigo. La próxima "fiestiada" será en tu apartamento, contigo de DJ, una botella de JackMiel en ese balconcito en que hablamos tantas veces y desde donde se vé un pedacito de cielo.

A Juliana, ahora mamá Juli. Cuando te conocí pensé que eras una gomela mimada. Luego la vida se encargó de mostrarme ese corazón tan bello que esconde una mujer tan original como tú. Gracias Juli porque desde cualquier país siempre me hiciste saber que era importante para ti. Espero haber retribuido un poco tanto aprecio y amistad. Te voy a acompañar en esta nueva etapa con Archi y Gabriel. Los quiero mucho.

Checito, porque al final seremos dos fechas y entre ellas se nos fué la vida. Gracias totales dijo tu compatriota, que al igual que tu pone tanto amor al acto de estar vivo. Infinitas gracias por todos los paseos de madrugada, de mañana, de tarde, de domingo, de sábados después de esas fiestas tan... H... Che!!! Gracias por ayudarme con el disfráz de Sherk-Yoda-Grichn, aprendimos

que las vacas también pueden ser dlamatas...ajajaja. Gracias por las cenas de hamburgato looser en Alcobronx, por las salidas a meda noche del lab, por los almuerzos a las hora que nadie almorzaba, por ser tan original y no haberte dejado contaminar de la adultez, gracias por las sonrisas y los chistes malos. Voy por chamartin Che, creo que me pasé y voy por el kilómetro 17.

A Walter White y Jesse Pinkman, por acompañarme en esa semana santa donde no había ni viento por Madrid.

Al Parque Warner por haberme permitido descubrir mi afición a las montañas rusas y las sobredosis de adrenalina, los sueños de niño sí se cumplen.

Quiero agradecer especialmente a Augusto y a Pauli. Si algún día escribo una novela va a ser de su historia de amor. Gracias por acompañarme siempre desde cualquier parte del planeta. Gracias por cuidarme y por aconsejarme cuando hacia las cosas mal. Gracias por los licorcitos por Skype, por las navidades, cumpleaños y año nuevos a través de la pantalla, por los audios de Whastapp llenos de alegría y fuerza. Gracias por los regalos que me dan, siempre me gustan. Que privilegio contar con ustedes en mi vida. Ahora Sofi sabrá que es tener un Tío Ed. Los quiero mucho, siempre.

A la Abuelita Hermestina, sé que nunca podre agradecerte que me llevaras los zapatos lilmpios en una bolsa mientras yo con mi botas caminaba entre el barro, así llegaba al Colegio con los zapaticos limpios y tu te llevabas mis botas sucias para que a la siguiente mañana estuvieran limpias y volvieramos a la misma aventura entre los charcos y los carros que nos chispeaban de barro. Gracias Abuelita por la vida.

A Lile. Hermanita tu mano siempre ha esta do cerca, gracias por tu amor para con el mundo, gracias por ser tan fuerte. Admiro tu capacidad para enfrentar la vida. Envidio tu fortaleza para encontrar la respuesta siempre en el amor y la fé. Que lindo ha sido tenerte a mi lado de por vida. Me siento muy orgulloso de tu esfuerzo y dedicación para cumplir tus sueños. Besitos Lile, te quiero.

A mi mamá y a mi papá, sin su amor, sin su manos, sin sus trasnochadas, sin su ejemplo, sin su esfuerzo, sin las empanadas, sin los sandwich, sin las pizzas, sin la tiendita, sin los helados, sin los refrescos, sin la EDIS, sin la máquina de coser y la guitarra. Sin todo lo que son ustedes, yo no sería nada. Cada una de las letras de este documento estan dedicadas a ustedes. Los días y las noches no serán suficientes para agradecer su sacrificio por Lile y por mí. GRACIAS MAMÁ Y PAPÁ POR TODO EL AMOR.

Contents

Motivation

In the book of Kittel, a well-known citation attributed to Mackintosh states that metals are "a solid with a Fermi surface". When metals become superconducting, BCS theory tells us that a gap opens at the Fermi level, so that all electronic states at the Fermi surface are lost. The shape and the properties of electrons at and close to the Fermi surface remain however fundamental to understand the superconducting behavior.

Many Fermi surfaces consist of different sheets with a topology that can be varied. For example, in the well-known system MgB_2, two-dimensional and three-dimensional sheets are found together in the same material. Electron-phonon coupling in each sheet is different and leads to different values of the superconducting gap. Furthermore, the anisotropy is large and also influences the superconducting density of states.

The electronic properties at and close to the Fermi surface also influence other aspects of superconductors. Here we focus on visualizing these aspects by studying the spatial variation in the density of states that characterizes superconductors. We center the attention on the shape of vortices, the orientation of the vortex lattice, the dynamics of vortices and excitations, Fano and Friedel like, due to electronic correlations.

We address superconductors with very different electronic properties close to the Fermi level. First, we analyze a system with a complex Fermi surface, yet simple single gap superconducting behavior, β-Bi_2Pd. We determine the influence of the complex Fermi surface in the vortex behavior (Chapter 3) and make a detailed visualization of the tilted vortex lattice (Chapter 4). We then analyze vortex dynamics in a crystalline system, $Rh_9In_4S_4$, where disorder is so strong that it has produced peculiar pinning landscapes leading to unstable vortex lattices (Chapter 5). Finally, we study a highly ordered system where electronic correlations lead to profound changes in the electronic structure close to the Fermi level, URu_2Si_2 (Chapter 6). By making detailed atomic size imaging and spectroscopy and viewing Friedel-like oscillations at the surface, we unveil how these electronic correlations influence the superconducting state.

The level of understanding that we now have from the Fermi surface and electronic interactions is very high and this thesis has hopefully contributed to advance such understanding.

However, applications of superconductors and other condensed matter systems need experiments where the parameters controlling the critical temperature or the Fermi surface can be varied and handled at will. This will really bring us closer to superconductors working at room temperature or carrying much more current, or any other interesting application stemming out from electronic correlations (for example topological superconductivity).

Strain, changes in the electronic density by gate voltage or very high magnetic fields are routinely used to shape the macroscopic properties of the systems presented in this thesis. Adding such control parameters to microscopic visualizations of the Fermi surface as obtained by photoemission and STM is probably the next important step.

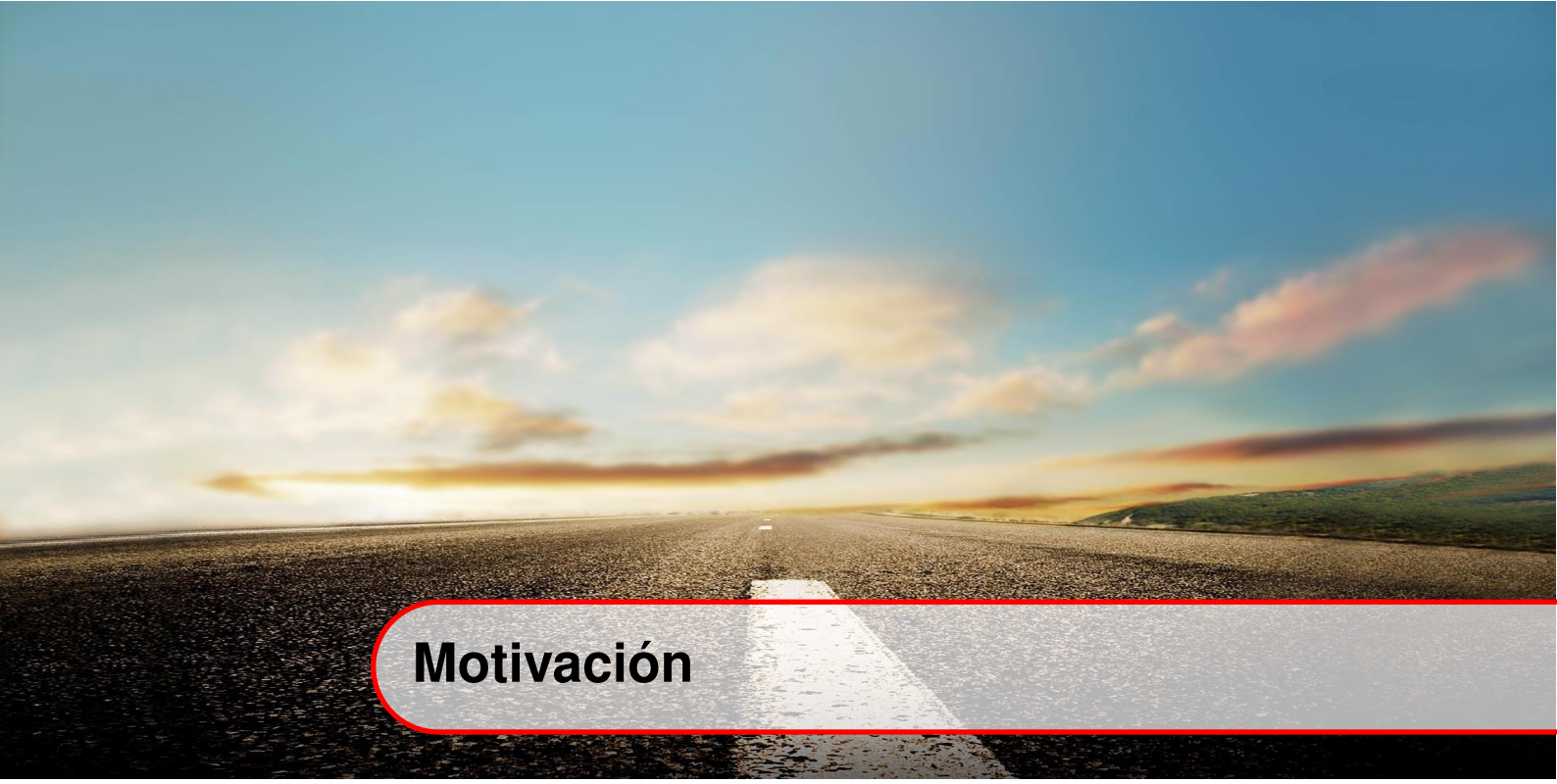

Motivación

En el libro de introducción a la física de estado sólido de Kittel, se incluye una conocida cita de Mackintosh en la que se define a los metales como "sólidos con una superficie de Fermi". Cuando los metales transitan al estado superconductor, la teoría BCS nos dice que un gap de energía se abre en el nivel de Fermi debido a nuevas interacciones que surgen entre los electrones que se encuentran en su proximidad. Por ello, estudiar el comportamiento de los estados electrónicos que se encuentran en la superficie de Fermi y su proximidad es fundamental para entender las propiedades de los superconductores.

Las superficies de Fermi a menudo están formadas por diferentes capas con topología diversa. Por ejemplo, en el caso conocido del superconductor MgB_2, encontramos en el mismo material capas bidimensionales y tridimensionales. El acoplamiento electrón-fonón es muy diferente en cada capa, y conduce a valores distintos del gap superconductor dentro de la misma superficie de Fermi. Asimismo, la fuerte anisotropía de sus propiedades electrónicas tiene una influencia notable en la densidad de estados superconductora. Otras propiedades de los superconductores se ven también afectadas por la estructura electrónica de la superficie de Fermi y sus proximidades. En esta Tesis nos planteamos como objetivo visualizar dichas propiedades mediante el estudio de la variación espacial de la densidad de estados electrónica que caracteriza a los superconductores. En concreto, hemos centrado nuestra atención en la forma de los vórtices superconductores, la orientación y dinámica de la red de vórtices, y la presencia de excitaciones, de tipo Fano y Friedel, que surgen de las correlaciones electrónicas.

En esta Tesis Doctoral hemos estudiado superconductores con propiedades electrónicas cerca del nivel de Fermi muy diferentes. Primero analizamos el material β-Bi_2Pd, que presenta una superficie de Fermi compleja y al mismo tiempo un gap superconductor único y sencillo. Hemos determinado la influencia de la superficie de Fermi en el comportamiento de la red de vórtices (Capítulo 3) y realizado un estudio detallado de la red bajo campos magnéticos inclinados (Capítulo 4). A continuación, hemos investigado la dinámica de vórtices en un nuevo superconductor cristalino descubierto en 2015, $Rh_9In_4S_4$, donde el valor extremo de sus parámetros superconductores y la presencia de fuerte desorden producen redes de vórtices inestables (Capítulo 5). Finalmente, hemos estudiado un sistema muy ordenado, URu_2Si_2, donde las correlaciones electrónicas modifican profundamente la estructura electrónica cerca del nivel

de Fermi (Capítulo 6). Mediante un estudio topográfico y espectroscópico a escala atómica y la visualización de oscilaciones tipo Friedel, hemos determinado la influencia de las correlaciones electrónicas en el estado superconductor.

El nivel de comprensión que ahora tenemos de la superficie de Fermi y las interacciones electrónicas es muy alto, habiendo contribuido esta Tesis a avanzar en dicha comprensión. Sin embargo, el desarrollo de aplicaciones basadas en materiales superconductores, y en otros sistemas de la materia condensada, requiere aún de experimentos en los que se puedan modificar o manejar a voluntad los parámetros que controlan la temperatura crítica o las propiedades de la superficie de Fermi. Esto nos llevará mucho más cerca de los superconductores que mantengan esta propiedad hasta temperatura ambiente o que sean capaces de transportar corrientes eléctricas mayores, o cualquier otra aplicación interesante que surja de las correlaciones electrónicas (por ejemplo superconductividad topológica).

Otros parámetros como la aplicación de tensiones, los cambios en la densidad electrónica por voltajes de puerta o el uso de campos magnéticos elevados se utilizan de manera rutinaria para modificar las propiedades macroscópicas de los superconductores estudiados en esta Tesis. El próximo paso importante será, por tanto, aadir estos parámetros de control a los métodos de visualización microscópica de la superficie de Fermi, como es la microscopía de efecto túnel.

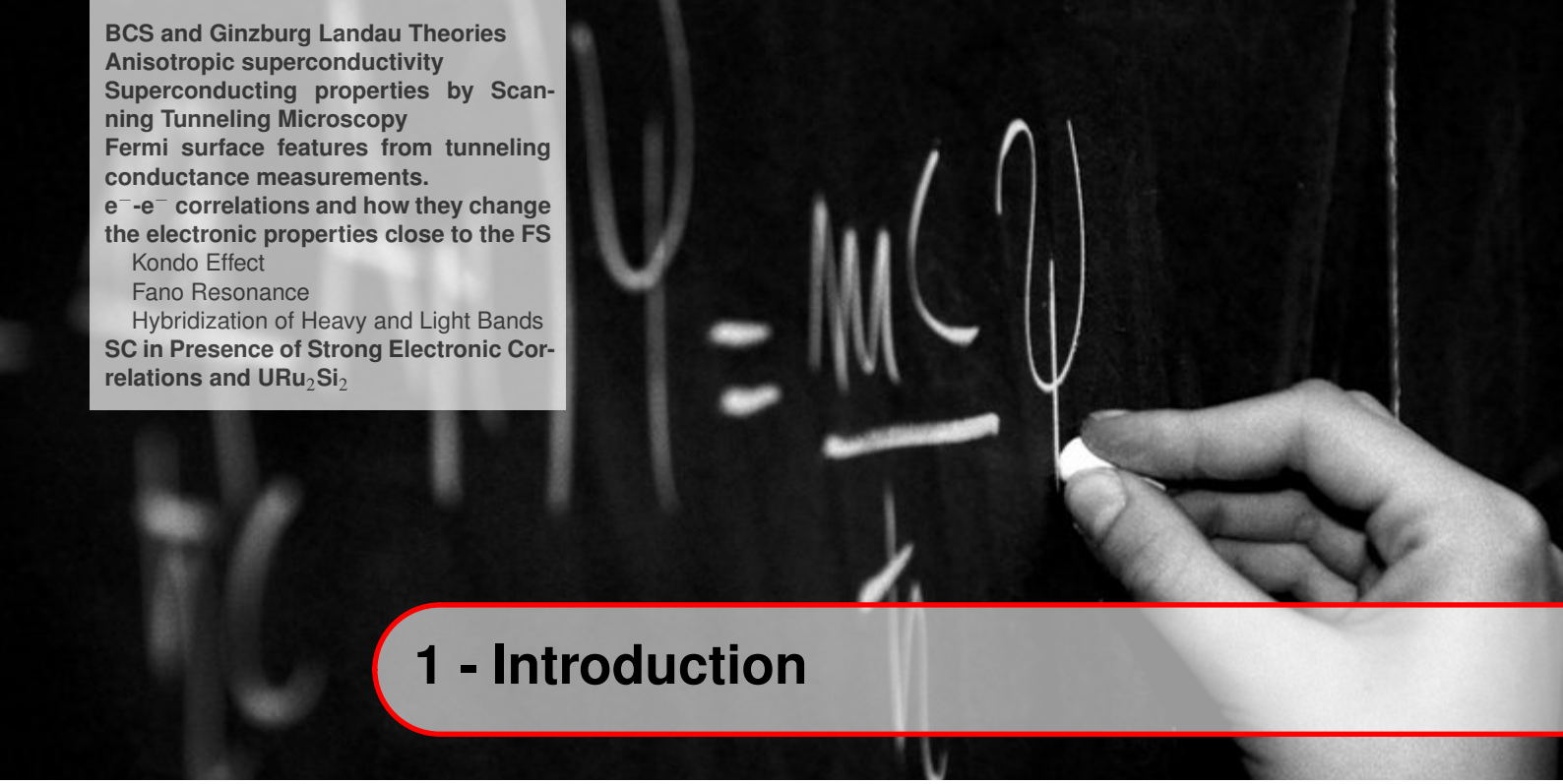

1 - Introduction

"...your eyes can deceive you;
don't trust them."
Obi-Wan "Ben" Kenobi to Luke Skywalker
Star Wars: Episode IV - A New Hope (1977)

George Lucas

2016 marks the 35th anniversary of the invention of the Scanning Tunneling Microscope (STM). With this technique, we can map a material with atomic resolution in real space. It is a true Pandora box with powerful winds emerging from the new insight from measuring at atomic scale.

This chapter gives an overview of the properties of superconducting materials. Its aim is to introduce the essential concepts needed to understand the results presented in this document.

First I will summarize phenomenological theories of superconductivity and briefly mention BCS microscopic theory. Then, I will describe specific properties of anisotropic and d-wave superconductors. In the third part, I will show how vortices have been observed by scanning tunneling microscopy. Then I will present the consequences of a complex Fermi surface in superconductivity, presenting two-gap superconducting properties in the example of MgB2. Finally, I will describe modifications in the Fermi surface from electronic correlations and briefly mention a few compounds that are considered unconventional superconductors.

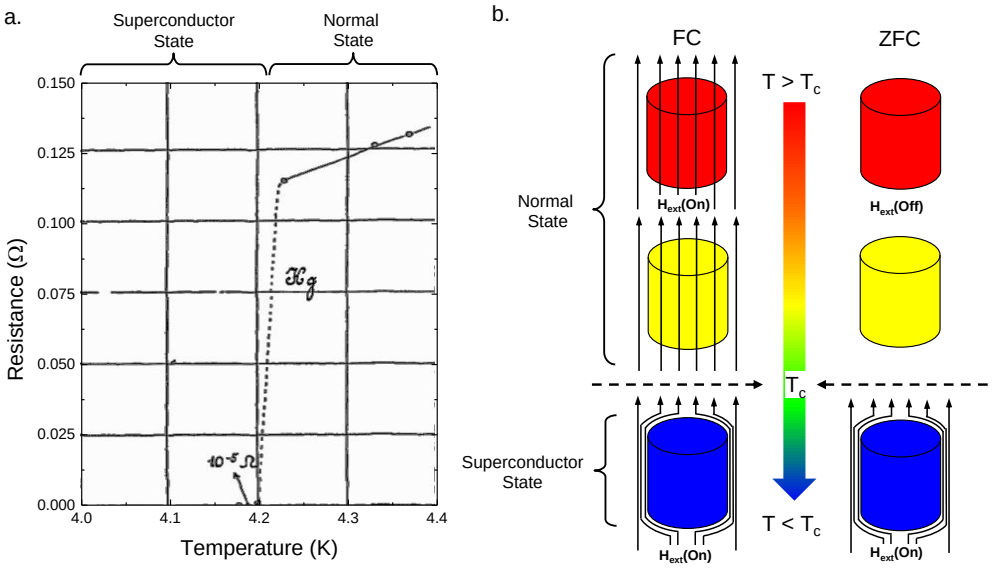

Figure 1.1 (a) Historic plot of the resistance as a function of the temperature in a sample of solid Mercury measured by Kameling Onnes in 1911 [2]. The abrupt drop of the resistance to zero, which Onnes reported in his notebook as *"Kwik nagenoeg nul"* translated as *"Mercury[’s resistance] practically zero"* [3] marked the starting point of the superconducting research field. **(b)** *Meissner Effect* in a superconductor. (Left) Field Cooled (FC): if the superconductor in its normal state is placed in a magnetic field B_{on}, the field will penetrate the material. If this is then cooled below T_c, in the presence of this field, the field will be expelled from the material. (Right) Zero Field Cooled (ZFC): if the superconductor in the normal state is cooled below T_c without any magnetic field present B_{off}, and is then placed in an external magnetic field (B_{on}), the field is screened from the interior of the superconductor [4].

1.1 BCS and Ginzburg Landau Theories

Zero Resistance and Meissner Effect.

Heike Kamerlingh Onnes found that the resistance of a mercury sample dropped to an value near to zero, close to the boiling temperature of liquid helium [6], the superconductivity’s world was born. Figure 1.1 (a) shows the reported measurement. The temperature on which the transition took place is called *critical temperature* T_c. For many years the most significant property of a superconductor was the *zero resistance* until 1933, when Walther Meissner and Robert Ochsenfeld reported that a superconductor ejects a magnetic field from its interior during its transition to the superconducting state [7]. This result established the second distinguishing characteristic of a superconductor: *perfect diamagnetism* or *Meissner effect* and it’s briefly explained in Figure 1.1 (b). Above a certain critical field, called H_c, superconductivity is destroyed. H_c is related to the difference in free energy of normal and superconducting states by: [8].

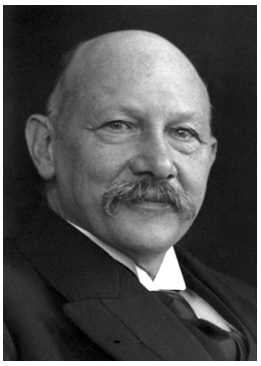

K. Onnes, Nobel Prize in Physics in 1913 *"for his investigations on the properties of matter at low temperatures"* [5].

$$G_n - G_s = \frac{1}{2}\mu_0 H_c^2 \tag{1.1}$$

H_c is called *thermodynamic critical field* and has a temperature dependence that follows approximately a parabolic law.

$$H_c(T) = H_c(0)[1-(T/T_c)^2] \tag{1.2}$$

As I will describe in next sections, another important feature of a superconductor is a discontinuous increase in its specific heat at T_c, below which it drops rapidly.

Phenomenological Theories

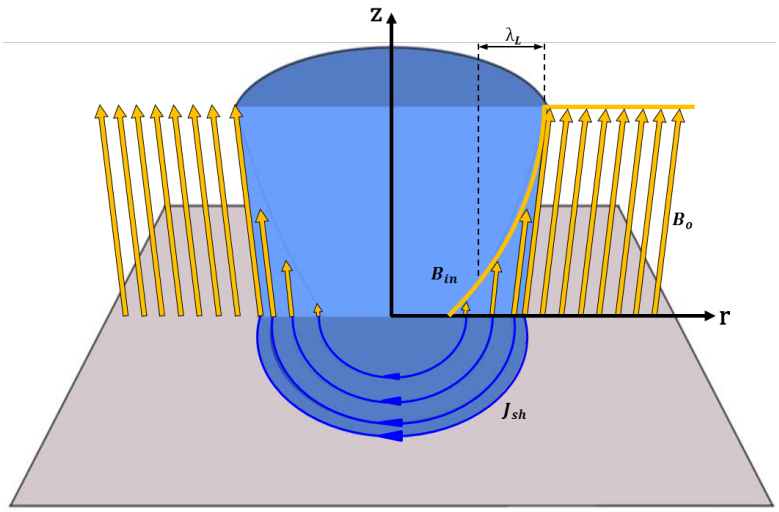

Figure 1.2 Schematic diagram of exclusion of magnetic field from interior of superconductor cylinder of radius R in an axial applied field B_o. There is a layer of thickness λ_L, where the magnetic field has a exponential attenuation according to equation 1.6 (yellow curve line). Shielding currents j_{sh} are also shown.

London Equations

One of the first steps towards understanding the superconductivity was presented in 1935 by Fritz and Heinz London [9]. They assumed that the supercurrent is carried by *superconducting electrons* with mass m_e, charge e and density of the superlectrons n_s. Starting with the Drude-Lorentz equation of motion for electrons in a metal, they proposed the following equations to describe the electric and magnetic fields inside a superconductor:

$$\mathbf{E} = \frac{m_e}{n_s e^2}\frac{\partial \mathbf{J_s}}{\partial t} \tag{1.3}$$

$$\mathbf{B} = -\frac{m_e}{n_s e^2}\nabla \times \mathbf{J_s} \tag{1.4}$$

Equations 1.3 and 1.4 are called *London Equations*. Combining the second London equation with Maxwell equation $\nabla \times \mathbf{B} = \mu_0 \mathbf{J_s}$ we get the following equation for the magnetic field in a superconductor

$$\nabla^2 \mathbf{B} - \frac{1}{\lambda_L^2}\mathbf{B} = 0 \tag{1.5}$$

with the solution

$$\mathbf{B}(r) = \mathbf{B}_0 exp(-r/\lambda_L) \tag{1.6}$$

Here they defined the *London penetration depth*

$$\lambda_L = \sqrt{\frac{m_e}{\mu_0 n_s e^2}} \tag{1.7}$$

Which is related with the distance that an external magnetic field penetrates into the material. $\mathbf{B}(r)$ exhibits an exponential attenuation, therefore a magnetic field is screened from the interior of a superconductor. Shielding currents cancel the interior magnetic field. Figure 1.1 is a schematic representation of a superconductor cylinder placed in a magnetic field B_o. Using Maxwell's equations $\nabla \times \mathbf{B_{in}} = \mu_0 \nabla \times \mathbf{M} = \mu_0 \mathbf{J_{sh}}$ where $\mathbf{J_{sh}}$ is the shielding current density, we obtain $\mathbf{J_{sh}} = -\mathbf{J_0} exp[-(R-r)/\lambda_L]$ (horizontal blue Circles in figure 1.1). This current density shields or screens the magnetic field from the interior of the superconductor.

Ginzburg-Landau Theory

The next remarkable theoretical approach towards understanding the superconductivity came in 1950. Vitaly Ginzburg and Lev Landau postulated a phenomenological model in terms of a order parameter to describe a superconductor in a macroscopic character [12], the result is known as *Ginzburg Landau Theory (GL)*. The *GL* is based on idea exposed by Landau in 1937. Landau, studying phase transitions from a general thermodynamic point of view, proposed a phenomenological expression for the free energy as a Taylor expansion in the *order parameter* [13]. Applying variational method to the Landau's free energy expansion, GL describes the superconductivity in terms of a complex order parameter ϕ, which may be written in the form of a product involving a phase factor θ and a modulus $|\phi(\mathbf{r})|$, given by

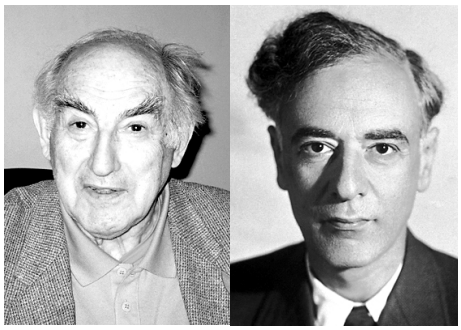

V. L. Ginzburg Nobel Prize in Physics in 2003 and L. D. Landau Nobel Prize in Physics in 1962, *"for his pioneering contributions to the theory of superconductors and superfluids"* [10] and *"for his pioneering theories for condenses matter, especially liquid hellium"* [11] respectively.

$$\phi(\mathbf{r}) = |\phi(\mathbf{r})| e^{i\theta} \tag{1.8}$$

where $|\phi|^2$ represents the density of superconducting electrons n_s^* of mass m^* and charge e^* which are connected with the electron properties (mass m, charge e and density n_S) by $m^* = 2m$, $e^* = 2e$ and $n_s^* = \frac{1}{2} n_s$. The *super-electrons* begin to form at the transition temperature and become more numerous as the temperature falls. Therefore, their density n_s^* is a measurement of the order that exists in the superconductor phase.

Since the order parameter evolves continuously from zero below T_c, it is natural to expand the free energy as a power series in the order parameter. The basic postulate of *GL-Theory* is that, in the superconductor state, close to the transition temperature below T_c, the Gibbs free energy G_S can be expanded in a series

$$G_s(\phi) = G_n + \frac{1}{V} \int d^3\vec{r} \left[\alpha |\phi|^2 + \frac{\beta}{2} |\phi|^4 + \frac{1}{2m^*} |(i\hbar\nabla + e^*\mathbf{A})\phi|^2 + \frac{1}{2\mu_0} B^2 - \mathbf{B}\cdot\mathbf{M} \right] \tag{1.9}$$

where G_n is the free energy of the normal state, $\mathbf{B} = \nabla \times \mathbf{A} = \mu_0 \mathbf{H}$, with $\mathbf{A}$ vector potential,$\mathbf{M}$ is the magnetization, α and β are coefficients which depend of the material. Ginzburg and Landau minimize the free energy (Eq. 1.9) to obtain two coupled differential equations, which involves the order parameter and the vector potential, these equations are known as Ginzburg-Landau equations:

$$\alpha\phi + \beta|\phi|^2\phi + \frac{1}{2m^*} |(i\hbar\nabla + e^*\mathbf{A})\phi|^2 = 0 \tag{1.10}$$

$$\mathbf{J} = i\hbar \frac{e^*}{2m^*} (\phi\nabla\phi^* - \phi^*\nabla\phi) - \frac{e^{*2}}{m^*} \phi^*\phi\mathbf{A} \tag{1.11}$$

In the original paper Ginzburg and Landau [12] solved the equations to determine the properties of the superconducting state and discuss how normal and superconductor phases coexist in

equilibrium in an external magnetic field. They classified superconductors into two classes, depending on the energy of the interface between the normal and superconducting states. As a result, the GL equations predicted two characteristic lengths to classify the superconductors according to their response in a external magnetic field: the *coherence length* ξ and the *penetration depth* λ.

The *coherence length* ξ is the characteristic length over which $\phi(\mathbf{r})$ decays appreciably from its equilibrium value ϕ_0. In figure 1.3 is shown graphically its significance, we see that $\phi(\mathbf{r})$ is close to ϕ_0 far inside the superconductor ($n_s \leq |\phi_0|^2$), has intermediate values in a transition layer near the interface with a width on the order of ξ ($0 < n_s < |\phi_0|^2$) and is zero at the interface with the normal phase ($n_s = 0$).

The *penetration depth* λ is the characteristic length where the magnetic field has a exponential attenuation inside the superconductor (see Fig.1.1).

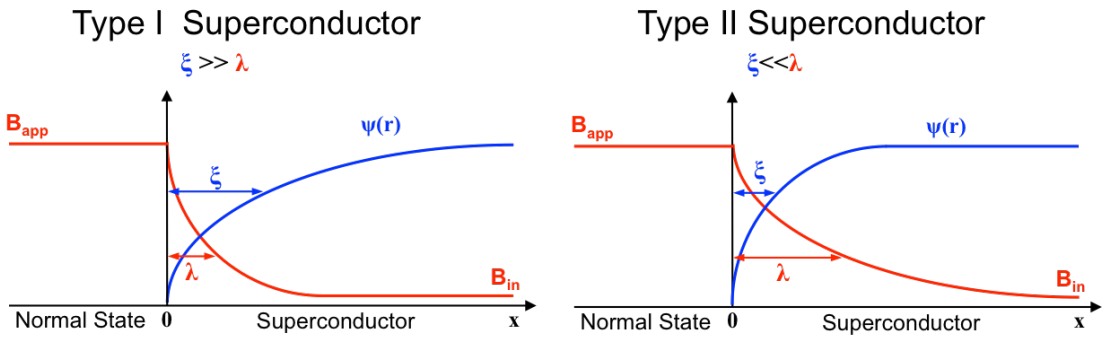

Figure 1.3 Schematic diagram of a one dimensional variations of the coherence length ξ, the penetration depth λ and the order parameter $\psi(x)$. The relationships between coherence length and penetration depth determines the superconductors response in external magnetic field (B_{app}). The case $\xi >> \lambda$ ($\kappa << 1$) refers to a type I, the case $\xi << \lambda$ ($\kappa >> 1$) refers to a type II.

The ratio of the two characteristic lengths is known as the Ginzburg Landau parameter κ,

$$\kappa = \frac{\lambda}{\xi} \tag{1.12}$$

this parameter allows classify the superconductors according to the energy balance between normal and superconductor phases in an external magnetic field. When the coherence length exceeds the penetration depth $\xi > \lambda$ it is not energetically favorable to create boundaries between the normal and superconducting phases, except in a thin external film layer of width λ. When the penetration depth is larger than the coherence length $\lambda > \xi$, it becomes energetically favorable for the superconductor to create domains of normal material surrounded by superconducting material. Inside these regions, as we will see in the next section, the magnetic flux penetrates in quantized units by forming vortices. The exact crossover value for these situations is $\kappa = 1/\sqrt{2}$ and it is the criterion to divide the superconductors in two groups: *Type I* when $\kappa < 1/\sqrt{2}$ and *Type II* when $\kappa > 1/\sqrt{2}$. Figure 1.3 shows a qualitative representation of the parameters to divide the superconductors in Type I and Type II.

Figure 1.4 shows the magnetization curves of type I and type II superconductors. Type I superconductors remain superconducting (perfect diamagnetism or Meissner phase) until the external magnetic field H_{app} exceeds the critical field H_c, at which point it will turn completely normal (Figure 1.4a). Type II superconductors are characterized by two critical fields, H_{c1} and H_{c2}. For fields $0 < H_{app} < H_{c1}$ the superconductor is in the Meissner phase. In the interval $H_{c1} < H_{app} < H_{c2}$ the superconductor enters in the mixed phase (Shubnikov phase) [14]

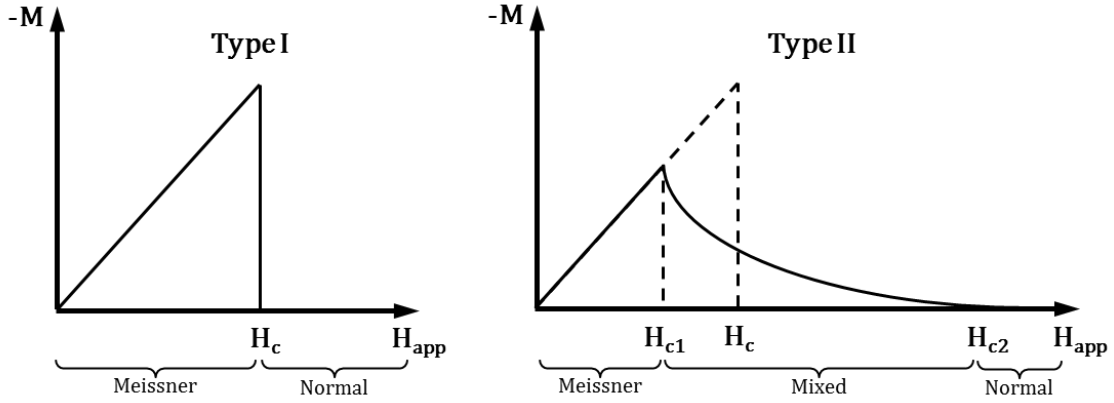

Figure 1.4 (a) Magnetization for Type I superconductor, above the critical field H_c the material becomes normal. **(b)** Magnetization for a Type II superconductor, it has two critical fields, H_{c1}, the field where the flux begins to penetrate, and, H_{c2}, the field where the material becomes normal. (H_c represents the thermodynamic critical field)

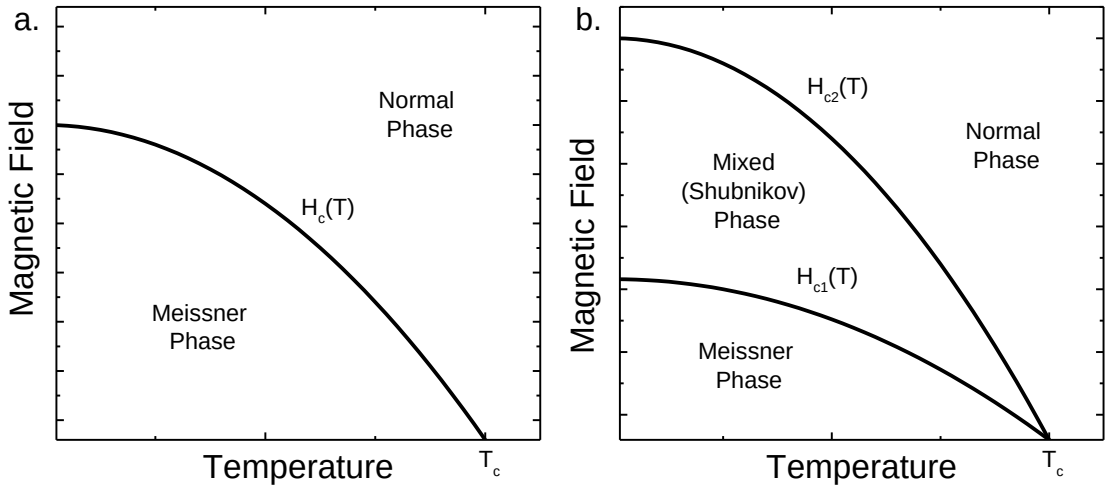

Figure 1.5 Magnetic phase diagrams as a function of the temperature showing the the Normal and Meissner state of a Type-I superconductor **(a)** and the additional mixed state of a Type-II superconductor **(b)**.

developing regions inside the material where part of the magnetic flux penetrates as vortices. Finally when $H_{c2} < H_{app}$ the material is in normal state (see Fig. 1.5).

From the GL- Theory, the lower and the upper critical magnetic fields, H_{c1} and H_{c2}, respectively are given by

$$H_{c1} = \frac{\phi_0}{4\pi\lambda^2} \ln \kappa \tag{1.13}$$

$$H_{c2} = \frac{\phi_0}{2\pi\xi^2} \tag{1.14}$$

When the applied magnetic field is perpendicular to the surface of the superconductor, the upper critical field is truly H_{c2}. When it is parallel to the surface, however, it turns out that the superconducting phase can persist in a thin layer up to the higher value $H_{c3} = 1.69H_{c2}$ [4, 8].

Vortices

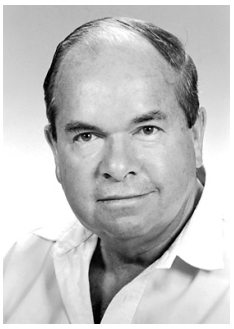

A. A. Abrikosov, Nobel Prize in Physics 2003 for *"pioneering contributions to the theory of superconductors and superfluids"*. [10].

In 1957 (the same year as BCS) A. Abrikosov [15], solves the issue about how the magnetic field can penetrate a Type-II superconductor. He introduces the idea that for magnetic fields ($H_{c1} < H < H_{c2}$) the magnetic flux penetrates in a periodic arrangement of flux tubes. In the ideal case this array is an hexagonal lattice and it is called the *vortex lattice (VL)*. In a first approximation, an isolated vortex can be described as shown in figure 1.6 (a): a cylindrical normal core which has a radius of ξ carrying a magnetic flux quantum given by the expression $\phi_o = h/2e = 2.07 \times 10^{-15}$ T m^2. The core is surrounded by a region of larger radius λ within which the magnetic field $H(r)$ and screening supercurrents J_s flowing around the core are presented together. The current density $J_s(r)$ of these shielding currents decays with the distance from the core in an approximately exponential manner. The modulus of the order parameter $|\phi(\mathbf{r})|$ (i.e. the density of superconducting electrons, n^*), is zero at the center of the vortex and it recovers its equilibrium value at $r = \xi$. As the magnetic field penetrates in the same direction through each vortex, their interaction is repulsive. The force per unit length between two consecutive vortices is given by [4, 8]

$$F_{12} = \frac{\phi_0^2}{8\pi^2\lambda^2} K_0\left(\frac{r_{12}}{\lambda}\right) \tag{1.15}$$

where K_0 is a zeroth-order Hankel function of imaginary argument. As we can see the strength of the repulsion is of the order of the penetration length distance. The energy per unit of length associated to each vortex is proportional to[4, 8]

$$E_{12} = \frac{\phi_0^2}{4\pi\lambda^2} \ln(\kappa) \tag{1.16}$$

Since interaction between vortices is repulsive, the vortices assume the arrangement that will keep them farthest apart. Abrikosov demonstrated that for superconductors in the clean limit, i.e. compounds where the mean free path is larger than the coherence length ($\ell > \xi$) [15], as a result of minimize the free energy of the system, vortices are arranged in a lattice with hexagonal symmetry. This configuration is illustrated in figure 1.6 (b).

However, as a consequence of particular electronic properties in some superconductors the vortex lattice can be ordered with other types of symmetries (square or rhombohedric) [16, 17].

The intervortex distance between nearest neighbors in the hexagonal configuration only depends on the magnitude of the magnetic field and is given by the expression

$$d_\Delta = \left(\frac{4}{3}\right)^{\frac{1}{4}} \left(\frac{\phi_0}{H}\right)^{\frac{1}{4}} \tag{1.17}$$

Since Abrikosov's theoretical prediction of the vortex state, there have been enormous efforts to understand magnetic vortices in type II superconductors. Figure 1.7 shows images of the vortex lattice acquired by different experimental techniques. Two remarkable historical points are: in 1967 (ten years after the Abrikosov prediction) the Abrikosov vortex lattice was observed for the first time in Pb using magnetic decoration [18] (Fig. 1.7 (a)), and, in 1989 (seven years after the STM invention) the first tunneling spectroscopy map of the vortex lattice in 2H-$NbSe_2$ was reported [19] (Fig. 1.7 (b)).

One of the key parameters to analyze the importance of the thermal fluctuations in a vortex system, is the Ginzburg number, or Levanyuk-Ginzburg number [24, 25], given by

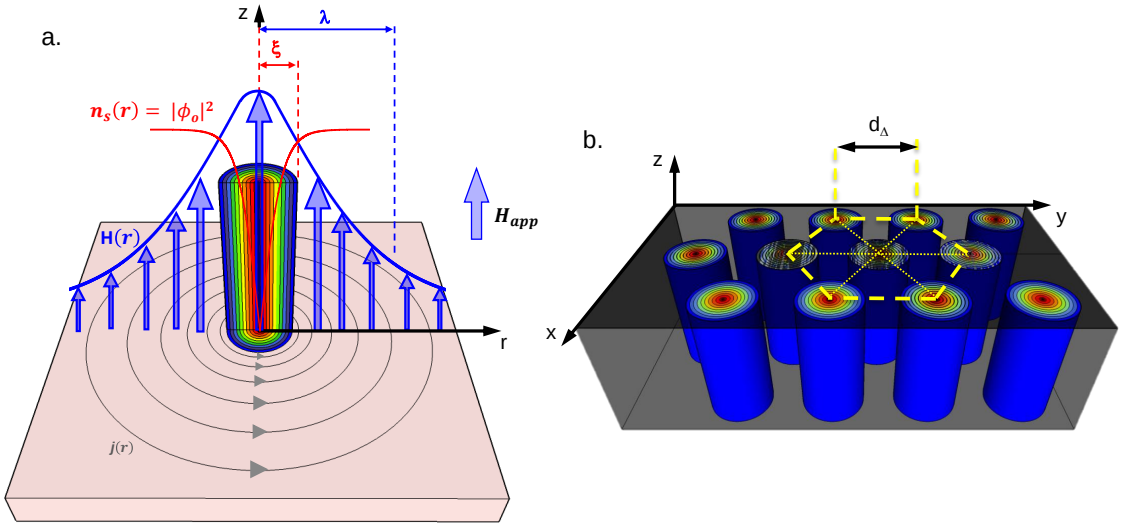

Figure 1.6 (a) Schematic representation of an isolated vortex. It consists of a cylindrical core with circular supercurrents around it (grey color). The pair wavefunction (or the superfluid density N_s)(red line) drops to zero at a scale of the coherence length ξ, which is much smaller than the magnetic penetration depth λ. Thus, the magnetic field profile $B(r)$ decreases radially from the center (blue line). (b) Schematic representation of the hexagonal Abrikosov vortex lattice, the intervortex distance is given by $d_\Delta = (\frac{4}{3})^{\frac{1}{4}}\sqrt{\frac{\phi_0}{H}}$ where ϕ_0 is the flux quantum and H the magnetic field (in Tesla)

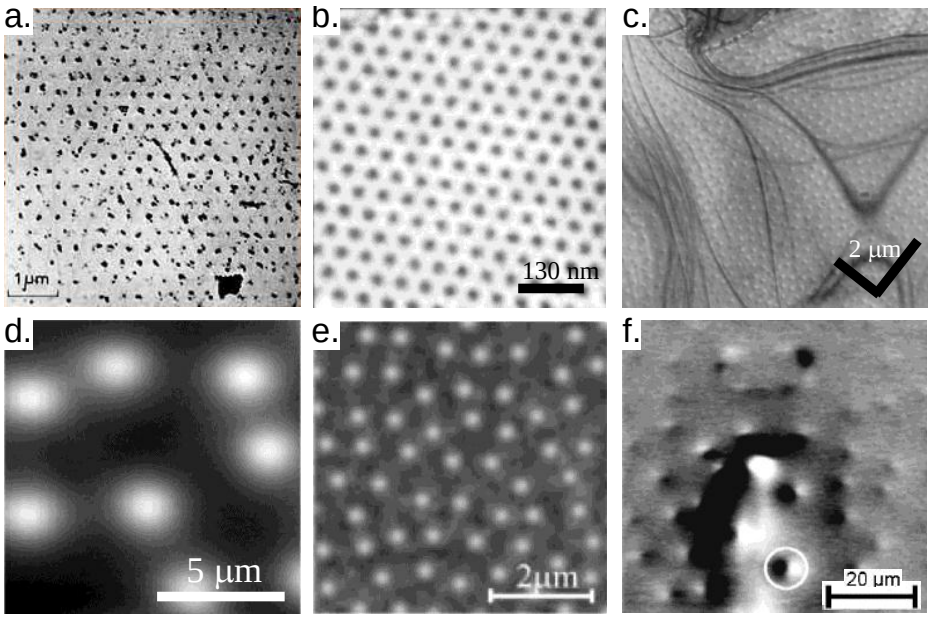

Figure 1.7 Vortex lattice on Type-II superconductors observed by different experimental techniques. **(a)** Fist image of the Abrikosov vortex lattice by Bitter Decoration on Pb at 195G and 1.1 K (1967) [18]. **(b)** First image of vortex lattice reported by scanning tunnel microscopy in 2H-$NbSe_2$ at 1T and 1.8K [19]. **(c)** Image of the vortex lattice by Lorentz Microscopy in Nb film at 100G and 4.5K (1992) [20]. **(d)** Scanning Hall probe images of vortices in YBaCuO film at 0.1 mT and 60 K (1997) [21]. **(e)** Magnetic-force microscopy of vortex lattice in Nb film at 40G and 4.3K (2002)[22]. **(f)** Low-Temperature Scanning Electron Microscopy on YBaCuO film patterned as SQUID at 0.2G and 77K (2001) [23]

$$G_i = \frac{1}{2}\left(\frac{\mu_o k_B T_c}{4\pi H_c^2 \xi_{GL}^3}\right)^2 \approx 10^{-9}\frac{\kappa^4 T_c^2}{H_{c2}(0)} \tag{1.18}$$

where k_B is the Boltzman constant. The Ginzburg number establishes a relation between the thermal energy and the condensation superconducting energy in a volume of ξ^3. A larger G_i implies a higher influence of the thermal fluctuations in the physical properties of the superconducting material. The T_c dependence of the G_i, implies that High-T_c superconductors are the perfect candidates to be influenced by the thermal excitations; fluctuations can also be important for high κ low T_c superconductors. Typical numbers for low T_c superconductors are ($\sim 10^{-14} - 10^{-7}$) [24] and for high Tc superconductors $\sim 10^{-2} - 10^{-3}$ [24, 26].

BCS Theory

In 1957 (same year of Abrikosov vortex lattice prediction) John Bardeen, Leon Neil Cooper and John Robert Schrieffer published *Microscopic Theory of Superconductivity* [28] and, *Theory of Superconductivity* [29] papers that revolutionized the point of view of our understanding of superconductivity. One of the important steps to the successful formulation of the microscopic theory of superconductivity was the calculation for two electrons interacting above a filled Fermi sea, done by Cooper in 1956 [30]. Cooper showed that this two electron system can have a bound state in the presence of an arbitrarily weak attractive interaction. This result is a consequence of the Fermi statistics and of the existence of the Fermi sea background. This pair of bound electrons is called Cooper pair. The energy of this system is obtained by solving the Schrödinger equation for the Cooper pair wavefunction, and is given by:

J. Bardeen, L. N. Cooper and J. R. Schrieffer, Nobel Prize in Physics 1972 *"for their jointly developed theory of superconductivity, usually called the BCS-theory"* [27] respectively.

$$E = 2E_F - 2\hbar\omega_c e^{\frac{-2}{N(0)V}} \tag{1.19}$$

where E_F is the Fermi Energy, ω_c the cyclotron frequency, $N(0)$ the density of states at the Fermi level and V the potential energy. We can note some important properties of equation 1.19; there is a bound state with negative energy with respect to the Fermi energy. A bound state suggests a gap in the energy spectrum, which is consistent with the exponentially falling heat capacity observed experimentally. The bound state is obtained regardless of how small V is. Cooper found that E takes its minimum value when the electrons which form the Cooper pair, have a momentum k with the same magnitude but opposite sign and an antisymmetric spin wave function.

One of the most important results of the BCS theory was the understanding of the origin of the attractive interaction between electrons. The attractive potential between electrons comes when the motion of the ion cores are taken into account. The physical idea is explain in figure 1.8 for the two electron system. The first electron polarizes the medium by attracting positive ions, then these excess positive charge start to attract the second electron, giving an effective attractive interaction between them. When this attractive potential is strong enough to overcome the repulsive Coulomb interaction, the superconductivity state emerges.

Cooper pair has a spatial extension that is defined by the coherence length ξ_0. An energy gap opens in the superconductor and is called the superconducting gap. Using a variational method, Bardeen, Cooper and Schrieffer studied the structure of the wave function of the Cooper pairs

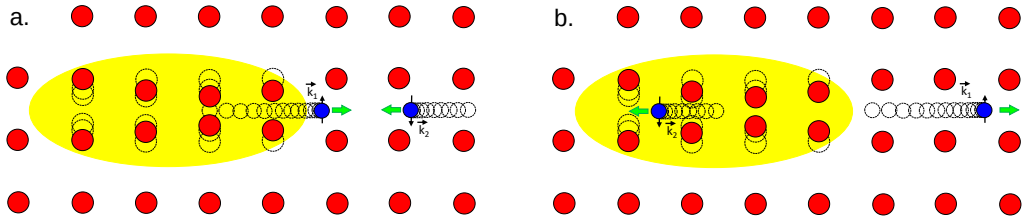

Figure 1.8 Schematic representation of the attractive interaction between two electrons (blue) mediated by charge fluctuation (yellow). In (a) an electron (+k↑) is moving in a solid attracting the positive ions (red) which surround it. In (b) Another electron (-k↓) is attracted to the area with excess of positive charge.

extending it to a system of many electrons. Solving the pairing Hamiltonian of this many body system, they found the possibles energies:

$$E = (\Delta^2 + \xi_k^2)^{\frac{1}{2}} \tag{1.20}$$

where $\xi_k = (\hbar^2 k^2/2m) - E_F$, is the kinetic energy with respect to the Fermi energy and Δ is the superconducting gap, given by:

$$\Delta = \hbar\omega_c \left(sinh\left(\frac{1}{N(0)V}\right)\right)^{-1} \approx 2\hbar\omega_c e^{\frac{-1}{N(0)}V} \tag{1.21}$$

The BCS theory establishes an universal relation between the energy gap and the thermal energy which destroys the superconducting state, $k_B T_c$, it can be written as:

$$\Delta = 1.764 k_B T_c \tag{1.22}$$

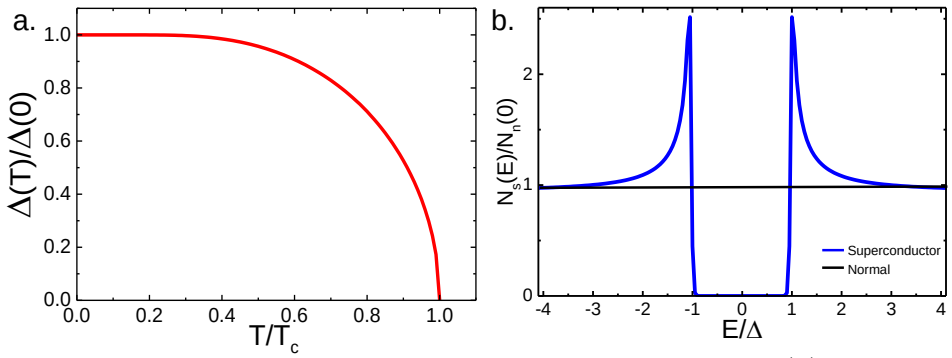

Figure 1.9 (a) Temperature dependence of the energy gap in the BSC theory $\Delta(E)$, normalized to the value at $T = 0$ K, $\Delta(0)$. **(b)** Superconducting density of states $N_s(E)$ as a function of the energy, normalized to the density of states at the normal phase $N_n(E)$. The quasiparticle peaks appears at values of $E = \Delta$.

Figure 1.9 shows the temperature dependence of the superconducting gap and the superconducting density of state as a function of energy according to

$$\frac{N_s(E)}{N_n(\xi)} = \begin{cases} \frac{E}{(E^2-\Delta^2)^{1/2}}, & \text{if } E > \Delta \\ 0, & \text{if } E < \Delta \end{cases} \tag{1.23}$$

where $N_s(E)$ and $N_n(\xi)$ are the density of states in the superconducting and normal state respectively. $N_s(E)$ has not accessible states in a range of 2Δ around the Fermi energy. For energies equal to $\pm\Delta$, $N_s(E)$ diverges, given origin to the so-called quasi-particles peaks. Tunneling spectroscopy is a popular tool for superconducting gap measurements.

1.2 Anisotropic superconductivity

The BCS theory supposes that the superconducting gap, Δ, is constant over the Fermi surface, i.e., it value is the same for any value of momentum, k. However an anisotropy in the electron-phonon interaction with respect to k, can rise an anisotropy in the value of Δ. Thus the spatial part of the superconducting order parameter can be expressed at $\approx \Delta(k)e^{i\Phi(k)}$, where $\Delta(k)$ is the magnitude of the superconducting gap and $\Phi(k)$ is the phase of the order parameter, both of which may have a momentum-dependence in k-space. The anisotropy in the superconducting order parameter can be very strong, and for some cases the value of Δ can be zero at some points in the momentum space. The shape of the gap anisotropy in momentum space, define the type of the order parameter symmetry. An illustration of different symmetries for the superconducting gap is shown in figure 1.10.

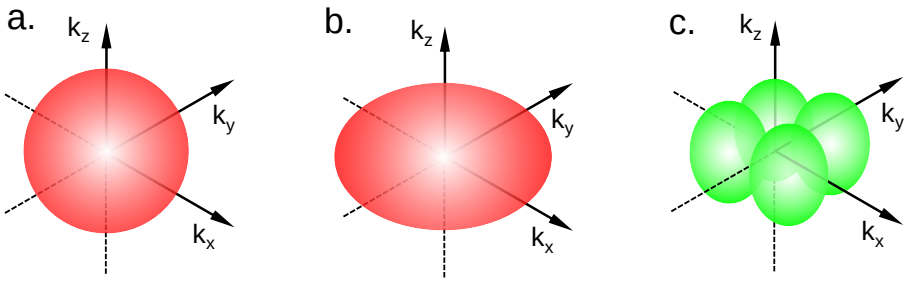

Figure 1.10 Schematic representation in spherical coordinates in the k-space of the superconducting gap symmetries. **(a)** isotropic s-wave, **(b)** anisotropic s-wave, **(c)** $d_{x^2-y^2}$-wave.

As shown in Figure 1.10, in momentum space, an *s*-wave superconducting gap has isotropic magnitude in all directions. *s*-wave gaps can have variations in magnitude around the Fermi surface, which give a anisotropy *s*-wave superconductor. A *d*-wave gap breaks rotational symmetry such that different regions of the Brillouin zone phases differing by 180-degrees. At the boundary between these regions, the magnitude of the superconducting gap will be identically zero, because the phase switches signs. If a Fermi surface intersects this boundary, it will feature special spots called 'nodes' where the superconducting gap is exactly zero.

Many consider, $CeCu_2Si_2$ at the starting point of *d*-wave superconductor. $CeCu_2Si_2$, a type of heavy fermion material, was discovered in 1978 by Frank Steglich [31]. In the early eighties, many more d-wave heavy fermion superconductors were discovered, including UBe_13, UPt_3 and URu2Si_2. In 1986 J. G. Bednorz and K. A. Muller discovered the high-temperature superconductivity in the d-wave compound $LaBaCu_2$[32], giving rise to the birth of the new family of materials called high-temperature superconductors. There are numerous other materials showing some form of complex superconductivity where the phase changes sign in different parts of the Fermi surface. Organic superconductors, several U based ferromagnetic superconductors or ruthenates are just a few examples.

A relevant case of anisotropy superconductivity appears is the so-called multiband superconductors. After the BCS theory was published, Suhl et al. [33] investigated an extension to superconductors with two bands crossing the Fermi surface. The two interacting electron bands lead to the creation of two superconducting gaps.

Diverse experimental results reveal signals of the superconducting gap anisotropies. Among the most usual techniques, to have a first idea about the special superconducting symmetries, we have measurements of the specific heat, the upper critical magnetic field and tunneling spectroscopy.

Specific Heat

BCS theory, predicts that the electronic specific heat follows a standard behavior with two well defined features: An abrupt jump at T_c from the normal state value γT_c to the superconducting state value C_S with ratio of $(C_S - \gamma T_c)/\gamma T_c = 1.43$ [4], and, for $T \ll T_c$, an electronic contribution to the specific heat C_e governed by the exponential function on temperature $C_S \approx Ae^{-\Delta(0)/k_B T}$. Figure 1.A shows details of this jump and the low-T exponential behavior for the Aluminium: a BCS superconductor. Measurements of the specific heat in multiband and/or anisotropic superconductors have exposed remarkable deviations from the BCS standard curve. Those striking features are the jump magnitude at T_c, a fast increase at low-temperature and a small kink (shoulder or peak) in between (see Fig. 3.2).

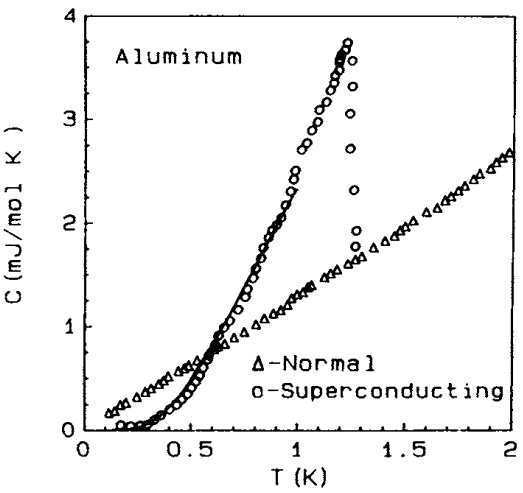

Fig. 1. A Specific heat as a function of the temperature in Al, a BCS superconductor [4].

Upper critical magnetic field

The slope of the upper critical field (H_{c2}) near the transition temperature allows to discern between the BCS conventional limit and the anisotropic properties. In 1966 Werthamer, Helfand and Hohenberg [34] proposed a model which fits H_{c2} in the weak coupling BCS limit. The model is known as the WHH approximation and predicts that the slope of H_{c2} is constant near T_c and becomes gradually less negative upon cooling. Figure 3.C shows the temperature dependence of H_{c2} for samples of $Ti_{0.56}Nb_{0.44}$ and $Ti_{0.356}V_{0.65}$ with theoretical WHH curves which describe the behavior of the experimental data [34]. By contrast, the temperature dependence of $H_{c2}(T)$ in multi-gap/band superconductors is characterized by a pronounced upward curvature near to T_c. This particular deviation of the WHH model is associated the interband coupling, and can be stronger with the ratio between Fermi velocities in each band [35, 36, 37].

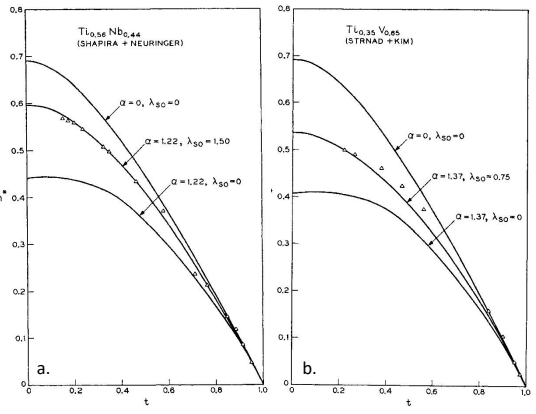

Figure 1.C Plots of $H_{c2}(T)$ for the alloys $Ti_{0.56}Nb_{0.44}$ and $Ti_{0.356}V_{0.65}$. Triangles are the experimental data. Continuous different lines are the WHH model with different fit parameters [34]. In the weak coupling BCS limit, the slope of H_{c2} is constant near T_c.

Quantum Tunneling in Superconductors

Tunneling spectroscopy is a good experimental method to probe the density of states. This technique was pioneered by Giaever [38] who used it to confirm the density of states and temperature dependence of the energy gap predicted by BCS (see Fig. 1.11). In a normal-normal junction, the tunneling current has an ohmic behavior for all ranges of voltage and temperature; i. e., the tunneling conductance has a well defined value σ_{nn} (see red lines in Fig. 1.11). By contrast, in a normal-superconductor, at $T = 0$ K, there is no tunneling current until $|E| \geq \Delta$ (see continuous blue lines in Fig. 1.11).

Giaever, by applying a bias voltage between a superconductor and a metal, separated by a thin insulator of some Angstrom, shows that the tunneling current as a function of the bias

voltage has a non linear behavior at energies close to the energy gap predicted by BCS. In particular, taking the derivative of the tunneling current with respect to the voltage, i.e., the tunneling conductance, shows clearly that the density of states at the Fermi level is drastically changed when a metal becomes a superconductor, the change being symmetric with respect to the Fermi level. The curve resembles the BCS density of states for quasi-particle excitations (see Fig. 1.11).

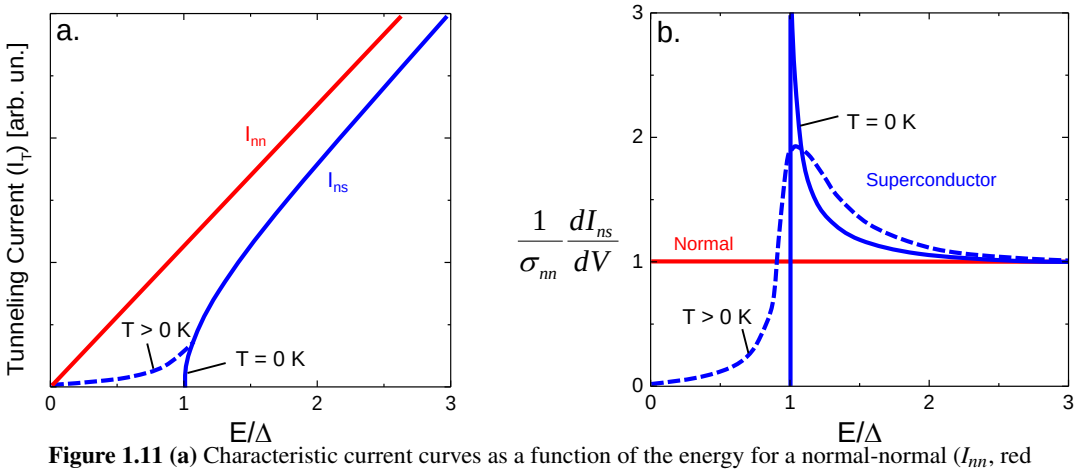

Figure 1.11 (a) Characteristic current curves as a function of the energy for a normal-normal (I_{nn}, red line) and a normal-superconductor (I_{ns}, blue line) tunnel junctions. The effect of the temperature is shown in the I_{ns} for $T = 0$ K (continuous line) and $T > 0$ K (dashed line). **(b)** Tunneling conductance dI/dV for the curves shown in **(a)** normalized to the conductance from normal-normal junction σ_{nn}. At $T = 0$ K the dI_{ns}/dV reflects the superconducting density of states (continuous blue line) with divergences at $|E| = \Delta_{BCS}$, whereas at $T > 0$ K, it has rounded-shape as a consequence of the temperature broadening (dashed blue line).

1.3 Superconducting properties by Scanning Tunneling Microscopy

The invention of the scanning tunneling microscope (STM) in 1981 by Binnig and Rohrer at IBM Zurich [39], was the turning point to reveal the electronic properties in materials at local scale. The STM can be used to measure spatial variations of the superconducting density of states caused, for example, by vortices.

Hess et. al., in 1989 [19, 40] studied the vortex lattice in 2H-$NbSe_2$, showing with great detail the internal electronic structure of the vortex core. The electronic density of states in a vortex decays continuously over distances of the order of coherence length ξ.

Hess reported that the spatial variation of the density of states in 2H-$NbSe_2$ has a peculiar hexagonal symmetry. The conductance maps at E=E_F shown a six fold vortex core star shape. In addition, they found a peak in the tunneling conductance curves very close to the Fermi level at the center of the vortex cores. These results show the existence of a rich phenomenology as a consequence of the intrinsic electronic properties of the material.

The peak evidenced the presence of the lowest energy bound state generated inside the vortex cores of this clean type II superconductor (see Fig. 1.12). It was predicted by Caroli et. al., in 1964 [41]. The origin of the bound states for quasiparticles generated in the vortex cores can be understood by considering the vortex core as a normal region surrounded by a superconducting one. The vortex normal core surrounded by a superconductor behaves as a potential well for quasiparticles with energies below the Δ. The potential well shape is determined by the size of the superconducting gap and how it closes the vortex core in a radius of ξ.

Since Hess' pioneering work, vortex lattices and vortex cores have been a matter of intense

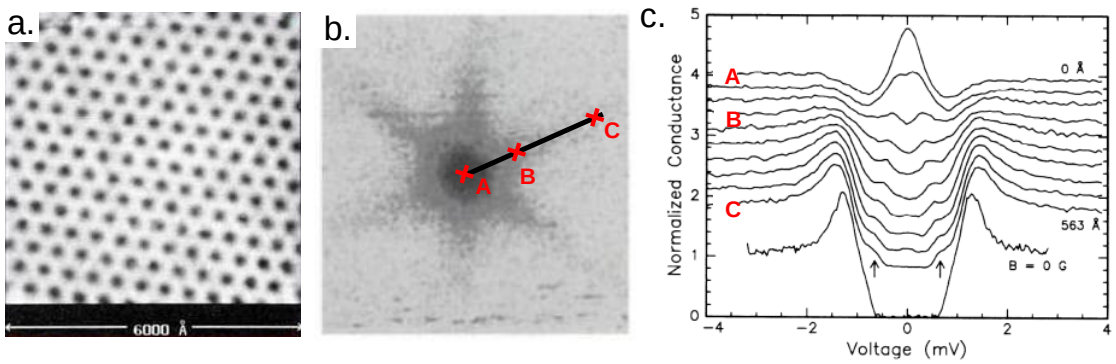

Figure 1.12 (a) First tunneling spectroscopy map of the vortex lattice by Hess et. al. in 2h-$NbSe_2$ at 1 T and 1.8 K [19]. **(b)** Image of a isolated vortex at 0.03 T and 0.3 K. It shown the particular variation of the density of states whose spatial dependence has hexagonal symmetry. **(c)** Tunneling conductance curves as a function of the position taken from the outside to the vortex center (black line in **(a)**). The curves evidence the spacial and energy dependence of the bound states. At the vortex center (A) appears a peak centered at the Fermi energy due to the localized states at lower energies.

research in the past two decades. Mostly, the direct real-space visualization of the vortex lattice has being made using STM. As a result, diverse vortex images and the internal structure of vortices, have revealed features of Fermi surface and symmetries of the superconducting gap. In addition, STM experiments on mixed phase have been focused in the study of the collective behavior of the vortex lattice in different materials and conditions, the crystal lattice influence and the observation of vortex lattice melting.

Diverse theoretical and experimental groups have considered challenging lines of work, which include imaging vortices in nanostructures, multiband and heavy fermion superconductors, single layers and van der Waals crystals, studying current-driven dynamics and the liquid vortex phases. Moreover, specific experimental tools are required for its measurement, and the only one which allows to view them and study their spatial distribution is STM.

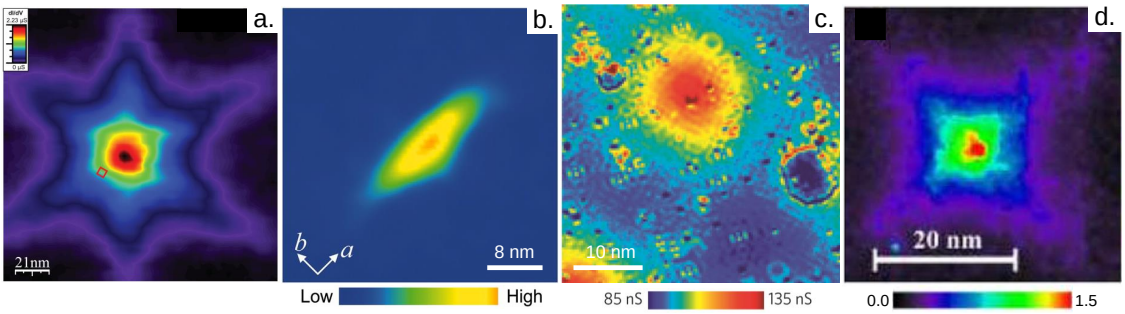

Figure 1.13 Vortex cores in different superconducting materials by scanning tunneling spectroscopy. The vortex shapes are highly dependent of the superconducting properties, structural symmetries and other electronic properties of the compound. **(a)** A six peaks star vortex shape in the anisotropic superconductor 2H-$NbSe_2$ at 0.03 T and 100 mK [42]. **(b)** A ellipsoidal vortex shape in the iron-based superconductor, iron selenide (FeSe) at 1 T and 0.4 K [43]. **(b)** A circular vortex shape in the heavy fermion superconductor $CeCoIn_5$ at 1.5T and 245 mK[44]. **(d)** A four peaks star vortex shape in the borocarbide superconductor YNi_2B_2C at 0.3 T and 150 mK [45].

1.4 Fermi surface features from tunneling conductance measurements.

A direct measure of the superconducting gap structure can be obtained by tunneling microscopy. As I will describe in next section, the tunneling conductance gives the density of states $N_S(E)$ as a function of the energy of the sample. In a superconductor, the tunneling conductance can be modified by different ways: multiband features, superconducting gap symmetries, crystal structure and temperature.

Figure 1.14 shows the Fermi surface of the multiband superconductor MgB_2 and how some features of this structure can be derived from scanning tunneling microscopy data.

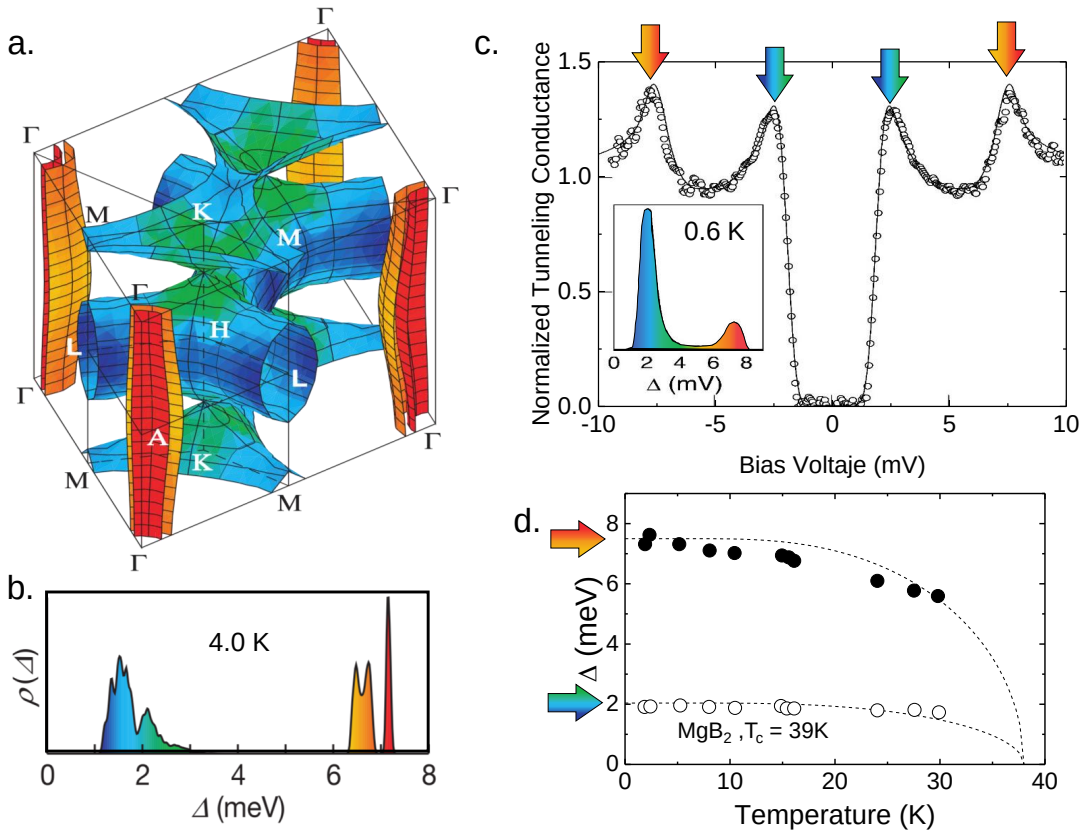

Figure 1.14 MgB_2: Example of the relation between the Fermi surface, tunneling conductance and the superconducting energy gap. **(a)** Superconducting energy gap on the Fermi surface at 4 K given using a color scale. **(b)** Distribution of gap values at 4 K. The Fermi surface of MgB_2 consists of four distinctive sheets. Two σ sheets (cylinders), derived from the σ-bonding $p_{x,y}$ orbitals of boron, are shown split into eight pieces around the four vertical Γ-Γ lines. Two π sheets (webbed tunnels), derived from the π-bonding p_z orbitals of boron, are shown around *K*-*M* and *H*-*L* lines (upper and lower *K*-*M* lines are equivalent). The superconducting energy gap is ~ 7.2 meV on the narrower σ-cylindrical sheet, shown in red, with variations of less than 0.1 meV. On the wider σ cylindrical sheet, shown in orange, the energy gap ranges from 6.4 to 6.8 meV, having a maximum near Γ and a minimum near A. On the π sheets, shown in green and blue, the energy gap ranges from 1.2 to 3.7 meV. **(c)** Normalized tunneling conductance of MgB_2 as a function of the bias voltage at 0.6 K. The double-peak structure represents the two gaps associated at each band $\Delta_\sigma = 7.1$ meV and $\Delta_\pi = 2.2$ meV, the continuous line is the fit with the contributions of each band; inset shows the distribution values of the superconducting gap used to fit the experiment (notice the changes respect to the distribution at 4K). At high-temperatures, the electronic features are governed by the band with the larger gap while low-temperature behavior depends on the band with small gap. bf (d) Energy gaps, corresponding to the peaks (shoulder) position evolution with temperature. In **(c)** black and open circles correspond to Δ_σ and Δ_π respectively; the dashed lines are the BCS fit [46]. With the same color scale as in FS, big arrows are a guide to associate the tunneling data with the features of the Fermi surface.

1.5 e^--e^- correlations and how they change the electronic properties close to the FS

The effects of impurities in a metal will depend on the atomic nature of the impurity, which can belong to three main groups: transition metals, rare earths or actinides. These groups are characterized by elements whose atoms have partially filled subshells (d in transition metals and f in rare earths or actinides), thus, their electrons are very localized, and behave as localized magnetic moments.

Several intermetallic compounds have elements with a partially filled f-shell, whose electrons interact with the s, p or d conduction electrons. The electrons in the partially filled f-shell often has magnetic moments at room temperature. Decreasing temperature reduces the magnetic entropy by the interaction with the conduction electrons causing that some thermodynamic and transport properties do not follow the behavior purposed by the free-electron theory. These experimental results can be understood by assuming that the conduction electrons behave as if they had an effective mass up to 1000 times the free-electron mass. This large effective mass shows that electronic correlations can considerably modify the properties of some solids with respect to expectations from usual bandstructure considerations.

The fusion between the heavy fermion and superconductivity was established in 1979 (almost two decades posteriori of the BCS-Theory) by the discovery of superconductivity in $CeCu_2Si_2$ [31]. The event marked the turning point in the description of the superconductivity as pairing conduction electrons mediated by phonons.

1.5.1 Kondo Effect

The electrical resistance of pure metals habitually decreases with reducing temperature. This is a consequence of electron scattering due to lattice vibrations, which are gradually attenuated when decreasing the temperature. However, already in the earliest 1930s it was discovered that, in some metals containing magnetic impurities, the electrical resistance increases again below a certain temperature follow a logarithmic behavior [48, 49, 50]. Figure 6.A shows this effect for Fe diluted in Cu [47]. In 1964, J. Kondo [51, 52] pointed out how these experimental observations can be understood considering an antiferromagnetic (AFM) interaction between a localized spin and an itinerant spin bath with a spin-spin exchange coupling $J < 0$. This interaction leads, at temperatures below a characteristic Kondo temperature, T_K, to a screening of the localized magnetic moment (see inset in Fig. 1.15 (a)) and results in a stable, non-magnetic singlet ground state [48]. After Kondo's description, the interaction is known as "Kondo effect" and if the localized magnetic atoms are arranged in a dense periodic array, they are called Kondo lattice (Fig. 1.15 (b)).

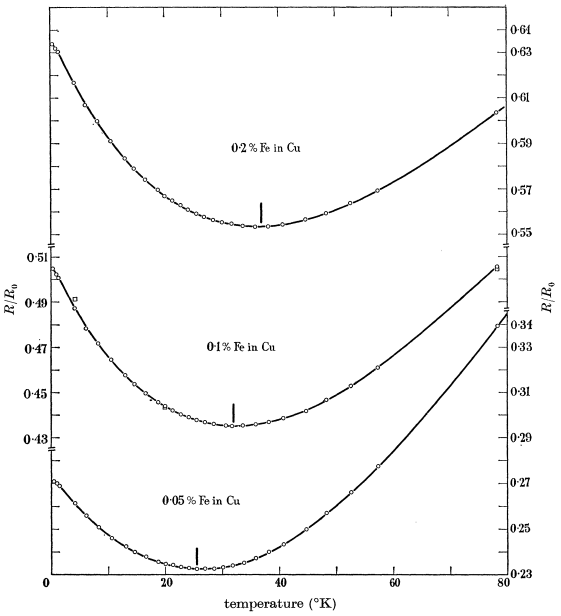

Figure 6.A The Kondo effect in samples containing magnetic impurities (Fe) diluted in a non-magnetic metal (Cu). The resistivity increases below a concentration-dependent temperature called Kondo temperature T_K [47].

The Kondo effect has been studied by STM. Several groups have demonstrated that it can be observed on metals with diluted magnetic impurities and others heavy-fermions compounds [53, 54, 55, 56, 57, 58, 59, 60].

Usually the tunneling spectrum produced by a single Kondo impurity has an asymmetric line shape respect to the Fermi level (Fig. 1.15 (a)) and is known as Fano resonance [61].

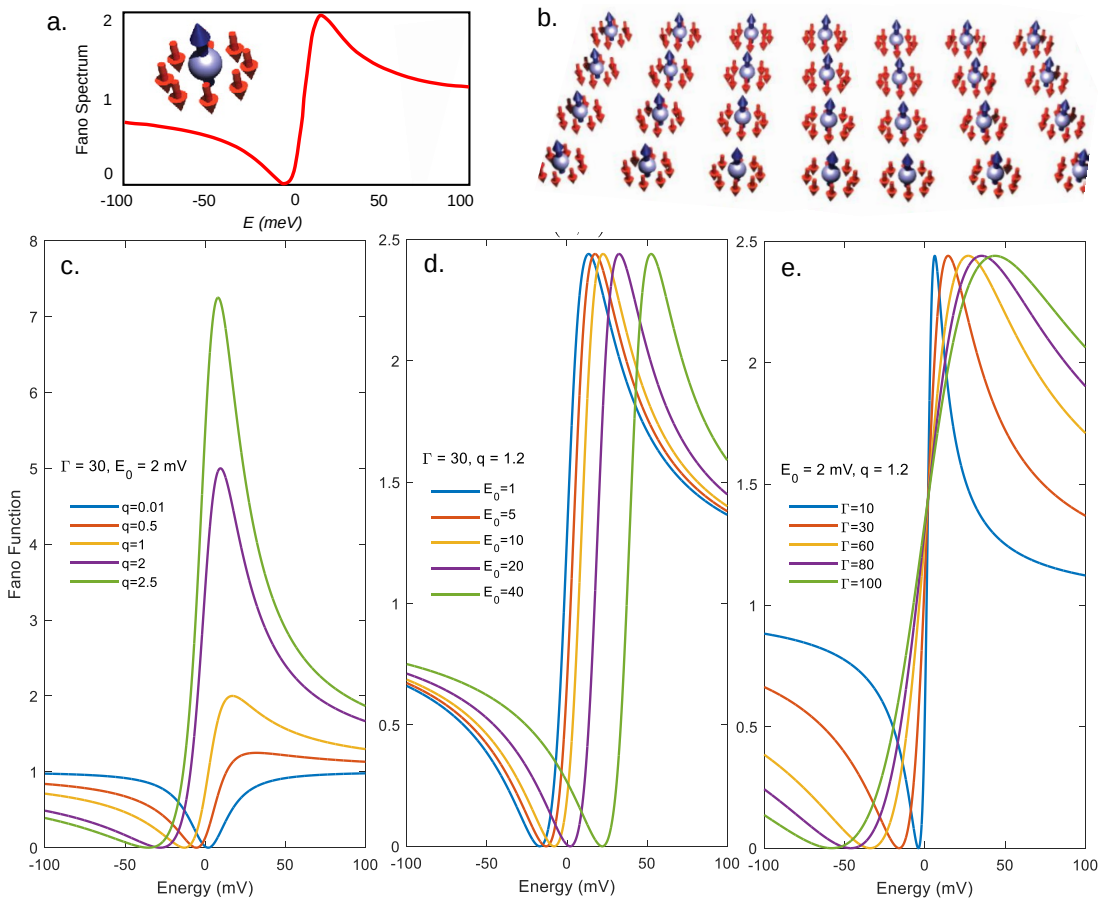

Figure 1.15 (a) (Inset) Schematic representation of a single-impurity Kondo effect, the localized magnetic atom/spin (blue) is screened by the conduction electrons (represented in red). Plot shows a typical Fano tunneling conductance spectrum $\sigma(E)$ expected near the localized magnetic atom. **(b)** Schematic of a Kondo lattice [58]. **(c-d)** Set of curves calculated with the Fano equation 1.24 for different q, Γ and E_0 values respectively.

1.5.2 Fano Resonance

The STM Fano resonance in a Kondo lattice occurs due to the interference of two-tunneling signals, one, associated with the itinerant conduction electrons and, other linked to the localized magnetic impurity. The tunneling conductance spectrum can be parametrized by the so-called Fano function [61, 48].

$$\sigma_{Fano}(E) = \frac{[2(eV - E_0)/\Gamma + q]^2}{1 + (2(eV - E_0)/\Gamma)^2} \tag{1.24}$$

being E_0 the resonance Energy and Γ the resonance width given by [62, 56, 59]

$$\Gamma = 2\sqrt{(\pi k_B T)^2 + 2(k_B T_K)^2} \tag{1.25}$$

q represents the ratio between two tunneling channels. Figures 1.15 (c-d) depict the asymmetry of the Fano signal for different values in the parameters E_0, Γ and q. The thermal broadening in

the tunneling measure will be the convolution with the derivative of the Fermi distribution.

$$\sigma_{Fano}(E,T) = \int_{-\infty}^{+\infty} \sigma_{Fano}(E) \frac{\partial f(E_F) - eV, T}{\partial V} dE \tag{1.26}$$

1.5.3 Hybridization of Heavy and Light Bands

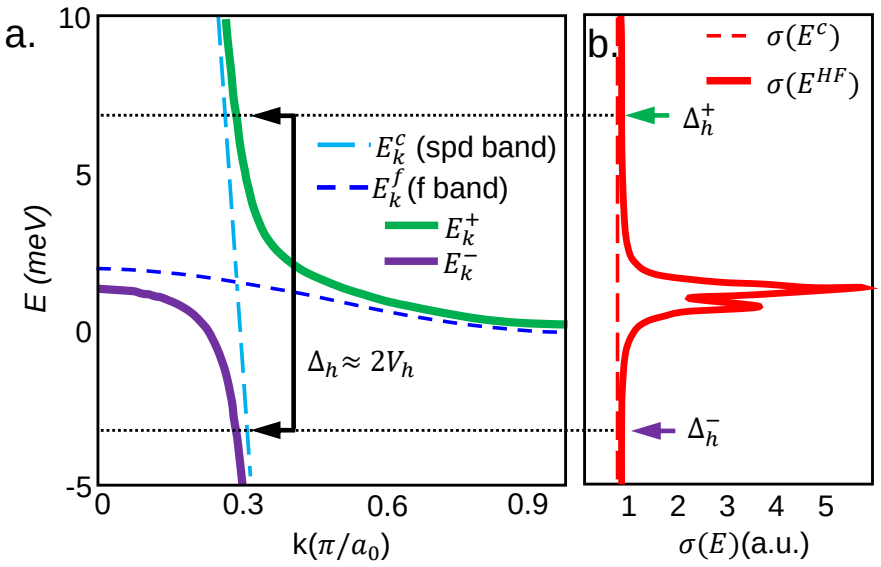

Figure 1.16 (a) Schematic representation at $T \approx 0$ of a simple heavy-fermion band structure in k-space. The dashed lines represent the (light) hole-like conduction spd-electron band E_k^c and the (heavy) localized f-electron band E_k^f. The two heavy-fermion $E_k^{+/-}$ bands are indicated by solid lines, with the energy range of their avoided crossing, the hybridization gap Δ_h, as shown. **(b)** Example of the density of states $\sigma(E)$ for a heavy-fermion system as shown in **(c)**. Δ_h can be determined in r-space by identifying the energy range between $\Delta_h(r) = \Delta_h^+(r) - \Delta_h^-(r)$ within which the $\sigma(E)$ is perturbed form its structure before the heavy-fermion bands appeared [57, 60, 58]

The emergence of the heavy-fermion state in a Kondo lattice (Fig. 1.15 (b)), can be considered as a result of the hybridization of two electronic bands: one light band due to the delocalized conduction spd-electrons and one heavy band originating from localized f-electrons [58, 63, 64, 56, 57, 59, 60]. The resulting electronic band-structure is represented schematically in Figure 1.16. Here the conduction hole-like band E_k^c (light band) splits into two distinct heavy bands $E_k^{\pm}$ within an energy range often referred to as the "hybridization energy" Δ_h.

This energy range is determined by the strength of the matrix element $V_h \approx \Delta_h/2$ (such that $\Gamma \propto \langle |V_h|^2 \rangle$ [57, 65]) for the quantum conversion of a f-electron into an conduction electron and vice versa. The value of Δ_h is defined quantitatively in k-space as the energy-separation between the heavy-fermion bands at the points where $E_k^{\pm}$ intersects the light conduction band (Fig. 1.16 (a)). Equivalently, Δ_h in r-space is defined as the energy range within which changes occur in the density-of-states due to appearance of the heavy-fermion bands (horizontal arrows in Fig. 1.16 (b)). Diverse authors have noted that Δ_h is the energy range of a quantum mechanical avoided crossing in k-space (Fig. 1.16 (a-b)) [58].

Recently, by using spectroscopic imaging scanning tunneling microscopy (SI-STM), it has become possible to detect both the characteristic k-space and r-space signatures of this heavy-fermion hybridization gap [58, 56, 57, 59, 60]. The emergence of the band of heavy quasiparticles near the Fermi level energy, is understood as a result of the hybridization of the localized f-electrons with conduction electrons[66, 67].

1.6 SC in Presence of Strong Electronic Correlations and URu_2Si_2

After 1957 the properties of superconductors were typically analyzed within the context of the BCS-Theory [28, 29]. Two decades posteriori the discovery of superconductivity in the heavy-fermions UBe_{13} [68] and $CeCu_2Si_2$ [31] mark the turning point in the description of the superconductivity as pairing conduction electrons mediated by phonons.

Thermodynamic and transport properties have long provided evidence for unconventional superconductivity in a variety of Kondo lattice systems [66, 67]. The magnitude of energy scales departs enormously from the BCS theory assumptions, suggesting that the phonon-coupling is not the pairing mechanism of the quasiparticles with enhanced effective masses.

A review by White et. al. [67], summarizes the general features of the superconducting heavy fermion compounds up to January of 2015. The superconducting states in the reported materials are generally characterized by: (1) Critical temperatures usually of order 1 K or lower, (2) Cooper pairs formed by heavy quasiparticles as inferred from larger jumps of order γT_c in specific heat at T_c; (3) very large initial slopes $(dH_{c2}/dT)_{T_c}$ near T_c in the upper critical field; (4) large London magnetic penetration depth λ relative to the coherence length ξ, thus $\kappa = \lambda/\xi \gg 1/\sqrt{2}$ (i.e. they are extreme type-II superconductors); (5) line or point nodes in the superconducting gap; (6) some of them exhibit evidence for multiple superconducting energy gaps [69].

Part of the challenge in the physics of the heavy-fermion superconductors has been the inability of spectroscopic measurements to probe the development of a superconducting gap out of heavy quasiparticles, due to the lack of understanding of the properties at the surface of these materials and the needed high resolution in energy [66].

Here we provide results in URu_2Si_2 that contribute to this subject.

2 - Experimental Techniques

Muchos años después, al frente del pelotón de fusilamiento, el coronel Aureliano Buendía había de recordar aquella tarde remota en que su padre lo llevó a conocer el hielo.
Cien Años de soledad.
Gabriel García Márquez

Many fundamental properties of liquid and solid matter have been found and/or understood after matter was cooled to low temperatures. Among these properties are the quantization of lattice vibrations (phonons), the linear temperature dependence of the specific heat of conduction electrons, superconductivity, superfluidity and many aspects of magnetism. Even the studies on the Higgs Boson are currently done using low temperature superconducting technology at the LHC.

In this thesis I have used scanning tunneling microscopy (STM) at low temperatures to investigate the local properties of several topical superconductors. Low temperatures give access to quantum phenomena and micro-eV energy resolution and STM provides the spatial resolution down to atomic scale. This makes STM at low temperatures a unique tool to study the local electronic properties of macroscopic quantum states such as superconductivity.

This chapter is divided into six parts. Part one presents an overview of the experimental setup. The second part deals with the basic physics behind the quantum properties of the ^{3}He-^{4}He mixture, the cryogenic system and the 3-axis superconducting magnet. The third part is devoted to describe the principles of the STM and the modes of operation to acquire topography/spectroscopy maps. In the fourth part, I will describe the homemade microscope, including its positioning stage and the *in situ* cleavage systems that were implement in the course of this thesis. In the fifth part, I will briefly discuss the sensitivity to the mechanical and electrical noise in our measurements. Finally, I will present the crystal growth methods by which we have obtained high quality single crystals of the superconducting materials studied in this Thesis.

2.1 Overview of the Experimental Setup

The experimental set up consists of a home-made scanning tunneling microscope anchored to the coldest point (the mixing chamber) of a dilution refrigerator Kelvinox MX100 with effective base temperature of 100 mK. This is inserted into a home-made 3-axis superconducting magnet that allows applying vectorial fields up to 5 T in the out-of-plane direction and up to 1.2 T in any in-plane orientation.

This set-up was built it up during a previous PhD thesis in the group [70] and has been further developed during this thesis by improving energy/spatial resolution and by implementing new functionalities. Along this chapter I will describe the important parts of the experimental set up putting emphasis on those aspects that have been worked out during this thesis.

2.2 Very Low Temperatures

In the race to reach the zero absolute in science labs, many refrigeration methods compete. In particular, the milikelvin temperature range is completely dominated by ^{3}He-^{4}He dilution refrigeration method [71]. This technique is based on: *the dilution of the rare isotope* ^{3}*He by the common isotope* ^{4}*He*.

The ^{3}He-^{4}He dilution refrigeration technique is very versatile and has important advantages over other cooling methods. It allows maintaining continuously temperatures in the milikelvin range with large cooling power (hundreds of μW below 0.3 K). This has two-fold positive effect on our STM experiments. First, by reducing temperature to a few milikelvin, we decrease thermal energy (k_BT) to a few μeV allowing for sub-meV energy resolution. This is very important to resolve details in the electronic structure of low critical temperature superconductors with characteristic energy scales of 1 meV or below. Second, it allows for long-term experiments at base temperature enabling measurements of detailed spectroscopic maps during several days. Also, unlike other cooling methods such as adiabatic demagnetization refrigerator, the dilution refrigerators can be operated under magnetic fields which have been extensively used in this thesis.

I will start by discussing the main properties of ^{3}He-^{4}He mixture.

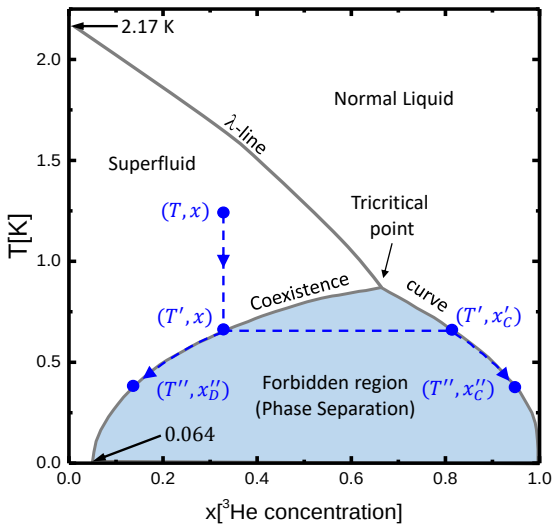

Figure 2.1 Phase diagram of ^{3}He-^{4}He mixture. Above the coexistence curve, the λ-curve defines if the liquid is superfluid or normal. The tricritical point (T = 0.86 K), establishes the temperature where the liquid separates into two phases, one being rich in ^{3}He (concentrated phase) and the other rich in ^{4}He (diluted phase) [72].

2.2.1 Properties of ^{3}He - ^{4}He Mixture

Figure 2.1 shows the phase diagram of ^{3}He-^{4}He mixture in the (T,x)-plane where x is the concentration of ^{3}He. Above the coexistence curve the liquid is superfluid or normal, depending on whether the point (T,x) is on the left or right side of the λ-line, respectively. At the coexistence curve the liquid spontaneously separates into two components, the concentrated phase (rich in ^{3}He), and the dilute phase (rich in ^{4}He). Because of its lower density the concentrated phase floats on top of the dilute phase. Since the enthalpy of ^{3}He in the two phases is different, the *evaporation* of ^{3}He from the concentrated phase into the dilute phase may provide highly effective cooling [72].

A typical cooling process starts, for example, at the point (T,x) (see Fig. 2.1) in the single phase superfluid region and then, lowering temperature and keeping x constant we reach the coexistence curve at (T',x) where the two phases begin to form. On further cooling from T' to T'' the concentration of ^{3}He increases in the upper phase while the dilute phase becomes richer in ^{4}He. The point representing the dilute phase moves along the left branch of the coexistence curve to (T'',x''_D) while the (T,x) condition of the concentrated phase moves from (T',x'_C) to $(T'',x'_C\prime)$ following the right branch of the coexistence curve.

We can see in Fig. 2.1 that below $\sim$0.1 K the concentrated phase is essentially pure ^{3}He $(x_c \approx 100\%)$ while in the dilute phase, x_D varies slightly from 7% at 0.1 K to 6.4% at 0 K. That the concentration of ^{3}He in the dilute phase, even at $T = 0$ K, remains finite, it is of utmost importance for the practical operation of a dilution refrigerator.

The explanation of the finite solubility of ^{3}He in ^{4}He at $T = 0$ K requires a detailed quantum mechanical description. Many textbooks and reviews have a rigorous theoretical description to explain the dilution of ^{3}He in ^{4}He [72, 71, 73, 74]. However, some fundamental concepts are enough to understand the process, which I will describe briefly.

At temperatures below 2.17 K, liquid ^{4}He is a superfluid that obey the Bose-Einstein statistics and can be treated as an inert liquid. In contrast, ^{3}He has a nuclear spin of $1/2$. It is described by Fermi-Dirac statistics and can be regarded as a normal Fermi liquid. Experimental measurements show that the thermal behavior of dilute ^{3}He in ^{4}He can be calculated from the properties of an ideal Fermi-Dirac gas, considering a slight variation of the effective mass of the ^{3}He atoms as a function of the ^{3}He concentration [72].

In equilibrium, the partial chemical potentials of ^{3}He (and ^{4}He) in both phases are equals, i.e.

$$\mu_{3C}(T,x_C) = \mu_{3D}(T,x_D) \tag{2.1}$$

hence $\mu_{3C} = G_{3C} = H_{3C}\text{-}TS_{3C}$ and $\mu_{3D} = (\partial G_{3D}/\partial n_3)_{T,P,n_4}$[1]. At $T = 0$ K, the energy required to remove one ^{3}He atom from the concentrated phase into vacuum, is equal to the latent heat of evaporation of ^{3}He:

$$\frac{\mu_{3C}(0)}{N_A} = -\frac{L_{3C}(0)}{N_A} \tag{2.2}$$

where N_A is Avogradro's number. In the dilute phase, the binding energy of one of ^{3}He atom in liquid ^{4}He at $T = 0K$ and $x_D = 0$ can be written as follows

$$\frac{\mu_{3D}(0)}{N_A} = -\varepsilon_{3D}(0) \tag{2.3}$$

where $-\varepsilon_{3D}(0)$ represents the minimum value of translational energy of an ^{3}He atom in the dilute phase (see Fig.2.2a).

[1] Subscrips 3, 4, C and D, refer to ^{3}He, ^{4}He, concentrated phase and dilute phase, respectively. Small capitals denoted molar quantities and n represents the number of moles

Due to the identical electronic structure of the Helium isotopes, the Van der Waals forces between them are identical. However, the ^{3}He atoms have a larger zero-point motion than the ^{4}He atoms due to their smaller mass. Consequently, in the liquid phase ^{3}He atoms occupy a bigger volume than ^{4}He atoms. Thus, a single atom of ^{3}He will be more strongly bound into liquid ^{4}He (due to the smaller distance or larger density) than into liquid ^{3}He, that is $\mu_{3D}(0) > \mu_{3C}(0)$, or,

$$-\varepsilon_{3D}(0) > -\frac{L_{3D}(0)}{N_A} \tag{2.4}$$

This condition shows that the ^{3}He will dissolve across the phase boundary into superfluid ^{4}He at $T = 0K$ as it is indicated in Fig. 2.2. However, the amount of ^{3}He soluble in ^{4}He has a limited value. That is because the Pauli principle restricts the occupation of translational kinetic energy to two quasiparticles per state as shown schematically in Fig. 2.2a. Thus, we have that the chemical potential of a ^{3}He atom in diluted ^{3}He-^{4}He (at $T = 0K$) increases with the concentration of ^{3}He atoms (x_D) as

$$\frac{\mu_{3D}(0,x_D)}{N_A} = -\varepsilon_{3D}(0,x_D) + k_B T_F(x_D) \tag{2.5}$$

where $k_B T_F(x_D) = (\hbar/2m^*)(3\pi x_D N_A/V_m)^{2/3}$ is the Fermi energy of an ideal gas of fermions with effective mass m^* and concentration x_D; this result is illustrated in Fig. 2.2b. If we continue increasing the ^{3}He concentration, the binding energy of a ^{3}He atom in a dilute phase will reach the binding energy of a ^{3}He atom in pure liquid ^{3}He. At this point Eq. 2.1, will be

$$-\frac{L_{3D}(0,x_D)}{N_A} = -\varepsilon_{3D}(0,x_D) + k_B T_F(x_D) \tag{2.6}$$

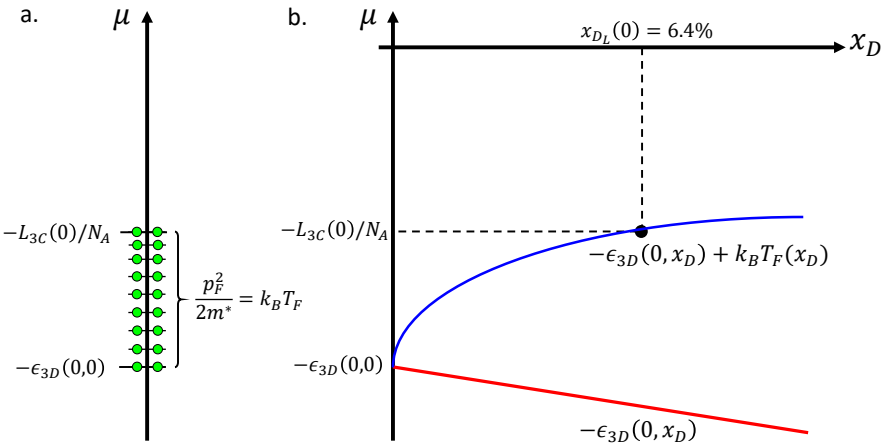

Figure 2.2 (a) Oversimplified energy diagram of the ^{3}He quasiparticles (green dots) to describe that the Pauli principle restricts the occupation of translational states (horizontal lines) to two per state until the system energy equals the chemical potential of pure ^{3}He . **(b)** Chemical potential of a ^{3}He atom in concentrated phase and in the dilute phase as a function of the ^{3}He concentration x_D. In the dilute phase the chemical potential is increased by $k_B T_F(x)$ (blue line). At $x_{D_L} = 6.4\%$ the chemical potential of ^{3}He in ^{4}He reaches the binding energy of a ^{3}He atom in pure liquid ^{3}He [71, 72, 74].

The limit concentration x_{D_L} for which the chemical potentials of the two liquids become equal, is obtained by solving Eq. 2.6; the equilibrium value, at $T = 0K$ is $x = 6.4\%$.

2.2.2 The ^{3}He - ^{4}He Dilution Refrigerator

Figure 2.3 shows the main components of a dilution refrigerator and a flow diagram for the ^{3}He-^{4}He mixture. The phase separation occurs in the mixing chamber and cooling power is produced

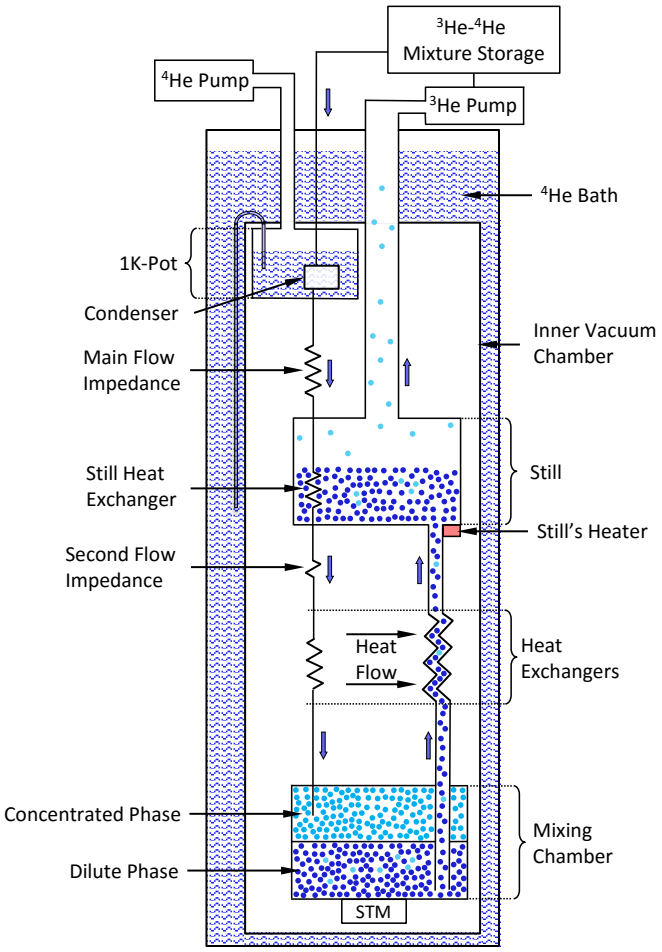

Figure 2.3 Schematic diagram of a ^{3}He-^{4}He dilution refrigerator. The STM is anchored to the coldest part of the cryostat, the *mixing chamber*.

by the dilution of ^{3}He atoms from the concentrated phase into the dilute phase. This process is, in many aspects, similar to a usual evaporation, where the concentrated phase corresponds to ^{3}He liquid and and the dilute phase to ^{3}He vapor. The continuous dissolution of ^{3}He atoms from the concentrated to the dilute phase is obtained by circulating ^{3}He by means of a pump.

The cooling process starts when the ^{3}He-^{4}He mixture at room temperature ($T = 300K$) enters the cryostat at a pressure of a few hundred millibar ($P = 0.42Bar$). Next it is precooled and liquefied in the *condenser* attached to the *1K-pot* at $T_{1K} \approx 1.2 - 1.5$ K. The *1K-pot* is a vacuum pumped ^{4}He bath (as decreasing the pressure of the ^{4}He reservoir depresses its boiling point). The pressure of ^{3}He is kept sufficiently high for condensation to occur by means of a flow impedance. The ^{3}He liquid flows through different *heat exchangers*, where it is cooled by the ^{3}He which flows upward in the dilute phase. Finally, the ^{3}He enters the *mixing chamber* where it is dissolved from the concentrated phase through the phase boundary into the dilute phase. The heat necessary for moving ^{3}He through the phase boundary is the effective cooling power of the dilution refrigerators.

The continuous dilution of ^{3}He atoms in the *mixing chamber* occurs due to a pumping system at room temperature connected to the *still*. The gradient in the ^{3}He concentration produced by pumping creates an osmotic pressure between the *mixing chamber* and the *still*, which moves the ^{3}He from the concentrated to the dilute phase, and then from the *mixing chamber* to the *still*. Thus, the ^{3}He leaves the *mixing chamber* in the dilute phase. As we explained before, the diluted

upward flowing ^{3}He cools the downward flowing ^{3}He via the *heat exchangers* until it enters the *still*. In the *still* ($T_s \approx 0.7K$), the ^{3}He flows through superfluid ^{4}He which can be considered as inert liquid [71]. This process occurs because of the vapor pressure of ^{3}He is much higher than the vapor pressure of ^{4}He [2]. Therefore, the *still* operates like a distillation chamber, evaporating almost pure ^{3}He. To maintain a steady flow of ^{3}He, external heating is applied by the *still heater*. Finally, the evaporated ^{3}He is compressed by the pumps ($\approx$ few hundred mBar) and returned back into the refrigerator, completing the cycle.

2.2.3 Cryogenic Setup

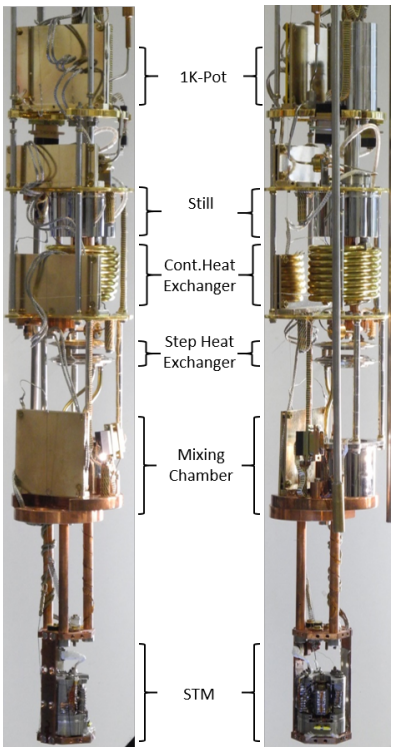

Figure 2.4 Photographs of the dilution refrigerator showing the different cooling stages for the ^{3}He-^{4}He mixture. The shiny rectangular plates at each stage are used to the thermalization of the wires for the electrical signals. The STM head is anchored to the coldest part (*mixing chamber*).

The cryogenic setup consists of a standard dilution refrigerator Oxford-Kelvinox^{TM}MX100, with base temperature 25 mK and 100 μW cooling power at 100 mK (Fig. 2.4). The dilution refrigerator is housed inside an *inner vacuum chamber (IVC)* made of Al. The *IVC* consists of a conventional indium sealed circular closed tubing assembly, which is immersed into liquid helium bath inside an super-insulated 100 L ^{4}He dewar (See Figs. 2.6 and 2.10). The liquid helium level is usually between 80 L and 30 L. The lower limit is imposed by the position of the *1K-Pot* tube which is located well below the upper flange of the *IVC*. The helium pick-up capillary is vacuum insulated to allow for helium flow into the *1K-Pot*, as usual in refrigerators of the type of Ref. [76]. This has the advantage that, with the same length, more space is left free for the experiment.

In the course of this thesis, we have designed and built a new sliding seal between the dilution refrigerator an the super-insulated 100 L ^{4}He dewar made of stainless steel much shorter than the one used before. In addition the free space at the upper part of the dilution refrigerator was filled and covered with Ethylene-vynil acetate (EVA), also known as poly(ethylene-vynil

[2] For example at $T \approx 0.8K$ the vapour pressures are $P_{^3He} \approx 4mBar$ and $P_{^4He} \approx 13\mu bar$ [75]

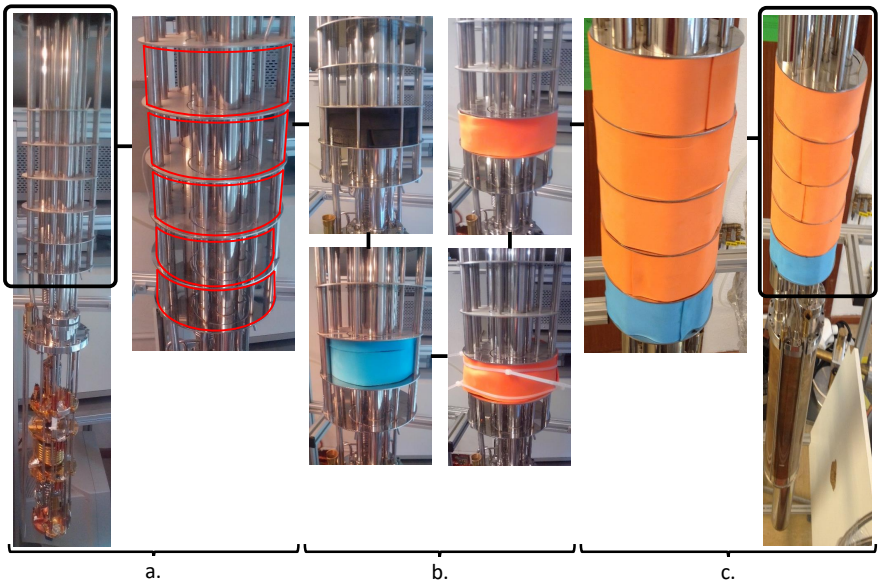

Figure 2.5 In the course of this thesis, the free space at the upper part of the dilution refrigerator, marked with the red boxes in **(a)**, was filled and cover with Ethylene-vynil acetate (EVA) (black, orange and blue materials in **(b)**. As a result **(c)**, we reduced the ^{4}He consumption and thus, the time to perform longer measurements was increased.

acetate)(PEVA). Figure 2.5 shows photographs of the dilution refrigerator before and after fill it in with EVA. These two improvements, helped to further reduce the helium consumption, being now a 20% less than previously. Thanks to these modifications we increased the time in between transferring operations of ^{4}He liquid from 3 days up to 4.5 days making possible to perform longer measurements.

Figure 2.6 shows a photography of the experimental setup used to operate the dilution refrigerator. The flux control of the ^{3}He-^{4}He mixture during the cooling process is monitored continuously by a gas handling system (e-f). The system, besides manometers and valves, has a series of filters and a Nitrogen cold trap (d) to clean the ^{3}He before to reenter on the fridge at concentrate phase. The pumping pipes from the pumping room, 5 m away to the fridge, are wide diameter stainless steel tubes connected in series with at least 2 m long silicon hoses reinforced with a steel spiral (h). We use the hoses armorvin^{TM} described in reference [77]. These hoses go through one sand box (c) to reduce the mechanical vibration transmitted by pumping. Between the sandbox and the cryostat, we continue with 1 m long stainless steel flexible hoses covered by rubber shells. Therefore, the ^{3}He-^{4}He mixture is pumped without any remarkable effect on the operation of the dilution refrigerator. To decrease the sensitivity to acoustic noise, we glued a sound insulating foam to the to the outside of the nitrogen-free dewar (a). After few days, the nitrogen trap is cleaned to reduce contamination due to degassing.

Temperature control is made using a LakeShore370^{TM}[78] (see (f-g) in Fig. 2.14). We use Ruthenium Oxide RX-202A [79] sensors in the *1K-Pot*, the *Still* and the *Mixing Chamber* stages of the dilution refrigerator. One additional sensor is located on the STM holder. A constantan wire wound close to the mixing chamber is used as the heater to control temperature.

The wires for thermometry and STM signals are inserted into tubing connected to the low temperature vacuum chamber. On top, at room temperature, they are soldered to the electrical vacuum feed through connection ((b) in Fig. 2.6). An important point to reach the lowest possible temperature in the system, is the correct thermalization of all components inside the cryostat. Our system has 16 wires with steel shielding mesh which transport the electrical signals: temperature measurements, STM control and data acquisition. These signals came from external

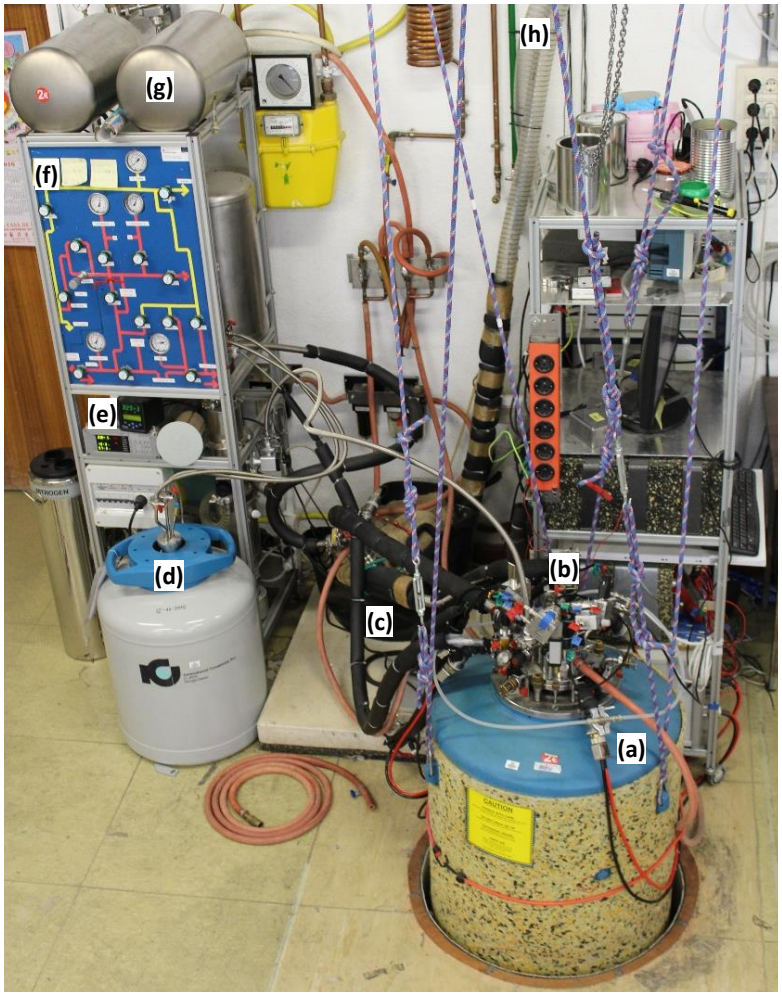

Figure 2.6 *Overview of the experimental Setup I: Equipment used to operate the dilution the dilution refrigerator.* **(a)**. A super-insulated Dewar of 100 L of capacity hangs from the roof by a system made up by ropes and anti-vibration ceiling hangers (see Sec. 2.6). **(b)**. Upper part of the ^{3}He-^{4}He dilution refrigerator, STM and 3-axis superconducting magnet connectors. **(c)**. Sand box on a 30×30×8 cm^3 concrete plate, used to reduce mechanical vibrations transmitted by the pumping lines on hoses. **(d)**. A 35 L Dewar and Nitrogen trap. **(e)**. High and low pressure monitors. **(f)**. Gas handling system. **(g)**. ^{3}He-^{4}He mixture containers. **(h)**. Hoses to connect the ^{3}He-^{4}He dilution refrigerator to the pumping room.

connectors at room temperature to the STM at the base temperature. According to the thermal stages, we divided the wiring thermalization process in four steps as we shown in figure 2.4. Each thermalization stage has two copper plates (covered with a gold layer of 6 μm thick) screwed on each level; the wires are clamped between the plates in a zigzag form. This method allows a faster wire thermalization in comparison with standard procedures which winds the wire around a cylindrical bar putting only one side of the wire in contact with the cold point. With this arrangement the effective cooling area is twice due to all external surface of the wire is in contact with the cold point. This has allowed us to reduce the wire length without producing any thermal leaking to improve transport of electric signals.

2.3 3-Axis Superconducting Magnet

We have used a home-made three axis magnet consisting of five coils, one solenoid for z axis and two sets of split coils for the XY plane. The five coils are mounted in an Al cage. Figure 2.7

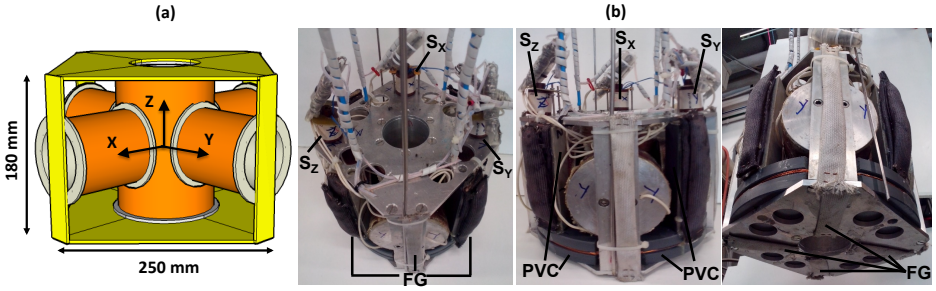

Figure 2.7 (a). Schematic view of the three axis magnet. One long coil is used to generate the z-axis magnetic field. For the in-plane field, we use two crossed split coil systems centered on the z-axis coil. The support is made of Al. Each coil is connected to a superconducting switch (S_x, S_y, S_z). **(b)**. Photographs of the magnet showing the PVC and fiber glass mesh pieces.

shows a schematic diagram and three photographs showing different views of the magnet.

In the course of this thesis, the free space in between coils has been filled using Polyvinyl Chloride (PVC) and fiber glass mesh, in order to eliminate as far as possible unused liquid helium volume around the magnet.

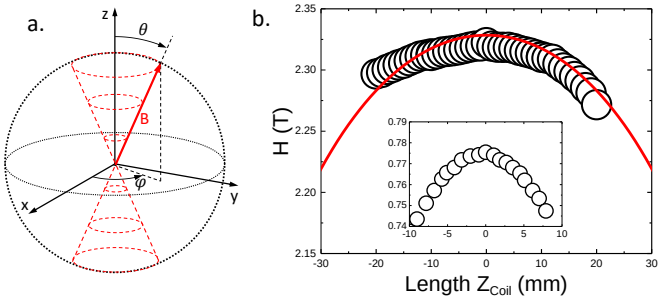

Figure 2.8 (a). Representation of the effective volume of the magnetic field (red cone). In **(b)** we show the magnetic field vs z-axis position, with respect to the center of the magnet when the z-coil is energized (50 A), (main panel) and when the x or y coils are energized (75 A, inset). Red line is a guide to the eye.

We reach a maximum magnetic field of 5 T in the z axis and 1.2 T in the x-y plane, using a current of about 100 A. This gives a tilted magnetic field of 5 T at a cone with opening angle of 13.5° around z as we show in Figure 2.8(a). The cone increases its opening angle towards lower fields on the z-axis coil, and we reach the full three dimensional vector capability for fields below 1.2 T. We have measured the magnetic field as a function of the distance and find a homogeneous field within a sphere of 0.5 cm radius around the center of the coil system of 0.2% for the magnetic field along the z axis, and of 1% for the magnetic field in the plane (Fig. 2.8 (b)). The three coil systems are equipped each with a persistent mode switch (S_x, S_x and S_z, Fig. 2.7b), which allows maintaining the magnetic field constant when the liquid helium is above the magnet. The magnet is immersed in liquid helium and hangs from a room temperature flange using four stainless steel bars 4 mm in diameter which connect it to main support of the magnet (Fig. 2.10(a)). The magnet is energized using a power supply which has three independent current sources; each one has a commuted internal commercial stage of 5 V 100 A, followed by a voltage to current converter consisting of a stage providing linear regulation which uses MOSFET power transistors. Figure 2.9 shows schemes of the circuits and photographs of the power supply. The power supply was designed and made at SEGAINVEX mostly by M. Cuenca.

When we modify the magnetic field, we heat all three persistent mode switch heaters, with a liquid helium consumption of 1.5 L/h. For STM experiments, we usually work in the persistent mode, with the switch heaters off. So, during normal operation, the liquid helium consumption

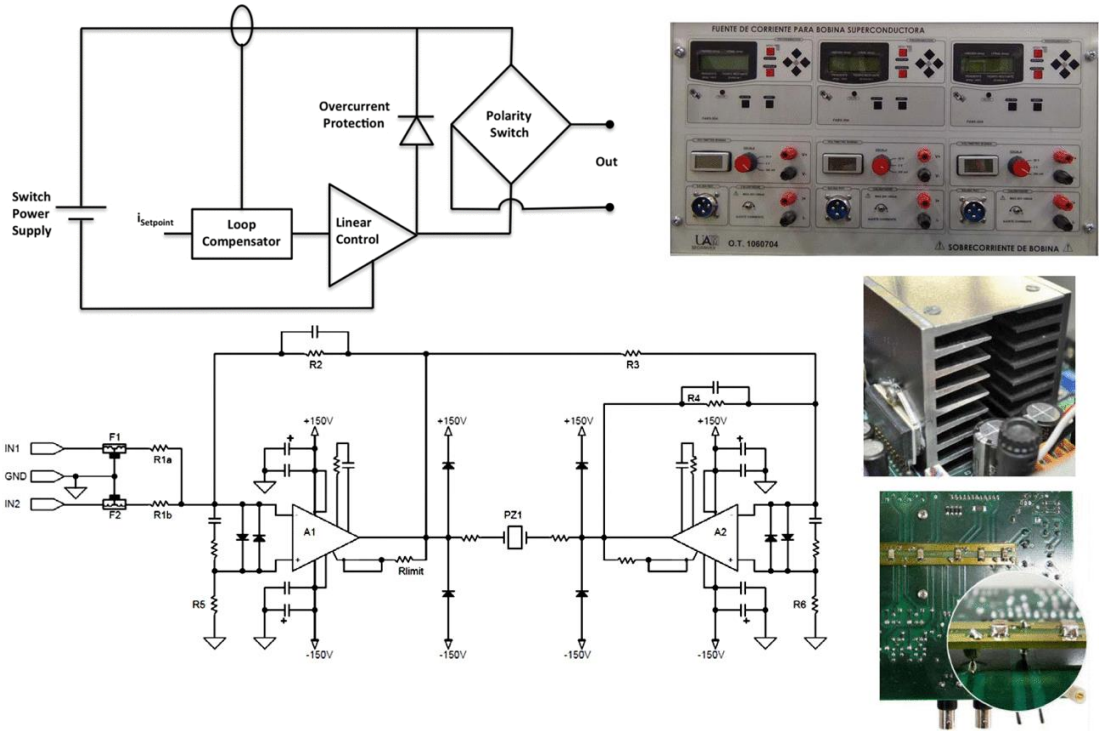

Figure 2.9 (Upper panel) A scheme (left) and a photograph (right) of current power supply. It is rather compact, 50 cm high and 80 cm long. (Lower panel) A basic scheme for high voltage amplifiers (A1 and A2) in opposition to drive the piezo (left). This is the most simple arrangement, and includes filters at the entrance and basic overvoltage protection. It takes utmost care of the ripple of the power supply, and of the temperature control. The amplifiers are cooling by using a large refrigerator (middle right panel). A motive of the high voltage power supply bus is shown in the lower right panel. Details of power supply in Ref. [80].

is below 0.7 L/h and the hold time of the cryostat is of 4.5 days.

2.4 Scanning Tunneling Microscopy-Spectroscopy

The scanning tunneling microsocopy (STM) invented in 1981 by Gerd Binnig and Heinrich Rohrer at IBM in Zürich [82] is the emblematic beginning of our hands and eyes reaching the nanoscale level. The STM operation relies on two simple ideas: the tunnel effect and the piezoelectric effect. In this section, I will briefly describe the basic theory of the STM and the experimental procedures to obtain topography images and spectroscopy maps.

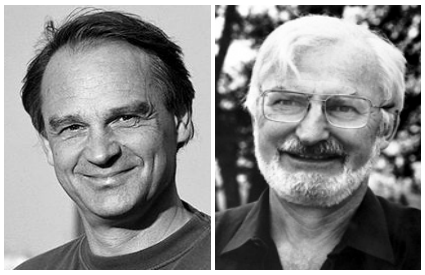

G. Binnig and H. Rohrer, Nobel Prize in Physics (1986) *"for their design of the scanning tunneling microscope"* [81].

Tunneling Current and Conductance

The phenomenon behind STM is the quantum tunneling of electrons between a sharp metallic tip and a conducting sample separated by a thin insulating barrier.

Quantum tunneling was developed from the study of semiconductors and the development of transistor and diodes. Pioneering work by L. Esaki, I. Giaver and B. Josephson [83, 38, 84] led to the acceptance of electron tunneling in solids. In 1961 Bardeen [85] proposed the tunneling Hamiltonian formalism which provides the framework to understand the single-particle and pair tunneling phenomena. In 1983 (2 years after the invention of the STM) Tersoff and Hamann

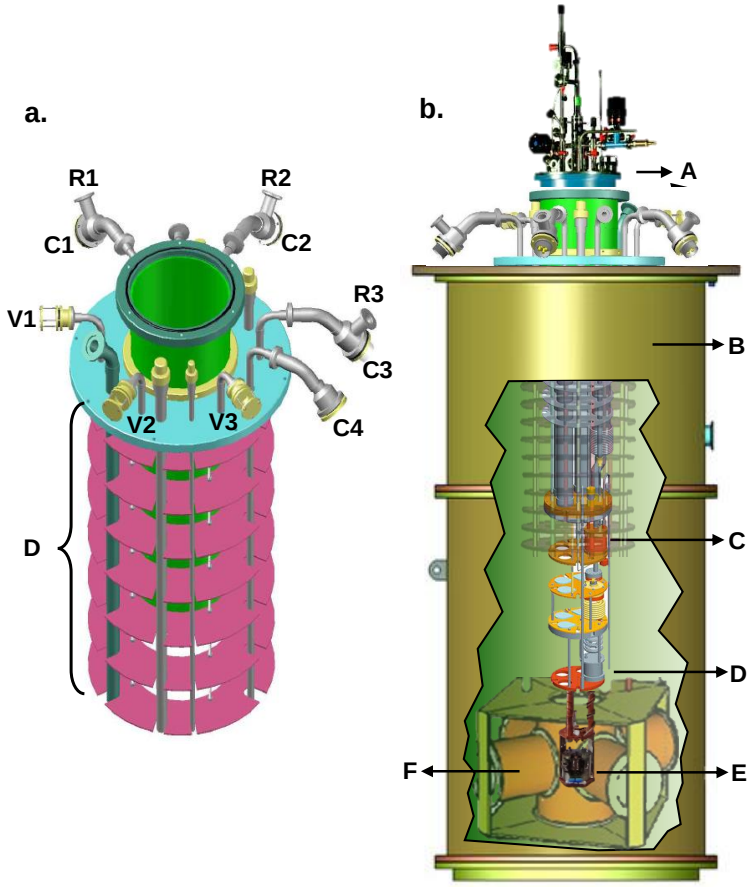

Figure 2.10 (a). Magnet support system with the upper cable connectors (C1-C3 for current supply and C4 for diagnosis of the coil and temperature measurement), helium recovery points (R1-R3), and security valves (V1-V3). We use several stainless steel screens (D). All tubes have small lateral holes to avoid Taconis vibrations. **(b)**. The whole cryostat (see Figs. 2.6 and 2.14): the dilution refrigerator (A) hangs from the top, the dewar (B), the 1K pot (C), the mixing chamber (D), the STM's body (E), and the superconducting coils (F).

[86] applying the Bardeen formalism found that the level of the tunneling current is proportional to the local density of states of the sample and exponentially dependent on the distance between the tip and the surface.

The figure 2.11 represents a tunnel process between the tip and the sample. When a positive voltage $+V$ is applied across the barrier (tip biased by a positive voltage), electrons will flow out of the filled states of the sample into the empty states of the tip and viceversa. Therefore, we have two tunneling process one from the tip to the sample and other from the sample to the tip. If we measure respect to the Fermi level of the sample we have the following expressions

$$I_{Tip-Sample}(V) = 2e\frac{2\pi}{\hbar}\int_{-\infty}^{+\infty}|M_T|^2 \underbrace{N_T(E)f(E)}_{\substack{\text{number of filled tip states}\\ \text{for tunneling from}}} \underbrace{N_S(E-eV)[1-f(E-eV)]}_{\substack{\text{number of empty sample states}\\ \text{for tunneling to}}} dE \quad (2.7)$$

$$I_{Sample-Tip}(V) = -2e\frac{2\pi}{\hbar}\int_{-\infty}^{+\infty}|M_T|^2 \underbrace{N_S(E-eV)f(E-ev)}_{\substack{\text{number of filled sample}\\ \text{states for tunneling from}}} \underbrace{N_T(E)[1-f(E)]}_{\substack{\text{number of empty tip}\\ \text{states for tunneling to}}} dE \quad (2.8)$$

where e is the electron charge, $\hbar$ is the Planck constant, $|M_T|$ is the matrix element or transmission probability, $N_{T(S)}$ is the density of states (DOS) of the tip (sample) and $f(E)$ is the Fermi

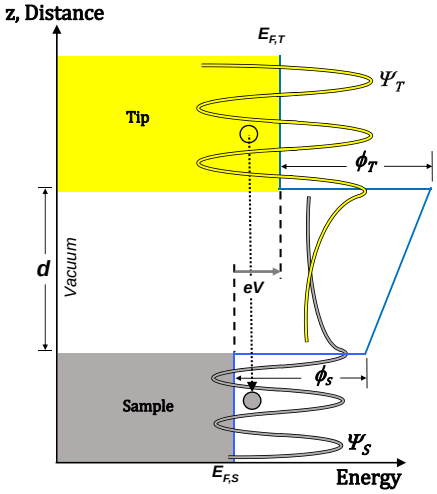

Figure 2.11 Tunneling process between the tip and sample across a vacuum barrier of width d. The electron wave functions ψ_T and ψ_S decay exponentially into vacuum with a small overlap, allowing electrons to tunnel from one electrode to the other. When a positive bias voltage $+eV$ is applied to the tip, electrons tunnel from the tip into unoccupied sample states.

distribution respect to the Fermi level at a temperature T:

$$f(E) = \frac{1}{1 + e^{\frac{E-E_F}{k_B T}}} \tag{2.9}$$

Thus, the total tunneling current I_T is the sum of these contributions $I_{Tip-Sample}$ and $I_{Sample-Tip}$

$$I_T = \frac{4\pi e}{\hbar} \int_{-\infty}^{+\infty} |M_T|^2 N_T(E) N_S(E-eV)[f(E) - f(E-eV)]dE \tag{2.10}$$

Note that the total current is proportional to the overlap between the two densities of states, the tunneling matrix element and the Fermi distributions difference. To simplify this expression we can use several physical reasoning. First, all measurements made in this thesis were done using tips made of non-superconducting (normal) metals, mainly gold but also tungsten at low bias voltage (a few meV). Within this energy range $N_T(E) = constant = N_T(0)$, hence

$$I_T = \frac{4\pi e}{\hbar} N_T(0) \int_{-\infty}^{+\infty} |M_T|^2 N_S(E-eV)[f(E) - f(E-eV)]dE \tag{2.11}$$

Second, $|M_T|$ is the transmission probability expected for the single-particle current in the normal direction to the plane of the junction, through a surface Ω lying entirely in the barrier region [87].

$$M_T = \frac{\hbar^2}{2m} \int_\Omega [\Psi_T^* \nabla \Psi_S - \Psi_S \nabla \Psi_T^*] dS \tag{2.12}$$

where Ψ_T (Ψ_S) are the tip (sample) electron wave functions. Bardeen discussed the tunneling from a many-particle point of view and showed that it is plausible to treat the matrix element M_T as a constant [85]. Then, Eq. (2.11) gives

$$I_T \approx \frac{4\pi e}{\hbar} |M_T|^2 N_T(0) \int_{-\infty}^{+\infty} N_S(E-eV)[f(E) - f(E-eV)]dE \tag{2.13}$$

Third, we assume that the vacuum barrier is a unidimensional square barrier of width d. Using the basic theory for vacuum tunneling [88, 89, 90, 91] we have that the wave functions decay

exponentially inside the barrier

$$\begin{aligned}\Psi_T(z) &= \Psi_T(0)e^{-\kappa z}\\ \Psi_S(z) &= \Psi_S(0)e^{-\kappa(d-z)}\end{aligned} \tag{2.14}$$

with

$$\kappa = \sqrt{\frac{2m\phi}{\hbar^2}} \approx 0.5\sqrt{\phi(eV)}\mathring{A}^{-1} \tag{2.15}$$

where m is the electron mass and ϕ, in general, is a work function [89]. Thereby, the matrix element (the tunneling probability throught a square barrier) is proportional to $|M_T|^2 \propto e^{-2\kappa d}$. By including this new assumption in Eq. 2.13 we find that

$$I_T \propto e^{-2d\sqrt{\frac{2m\phi}{\hbar^2}}} \tag{2.16}$$

thus, the tunneling current I_T depends exponentially on the tip-to-sample spacing d. The work functions for typical metals (Au, Pt, W) are around $\phi \approx 5$ eV, which gives a value of the decay constant $\kappa \approx 1\ \mathring{A}^{-1}$ (i.e. $e^2 \approx 10$ times per $\mathring{A}$), which means that a variation of 1 Angstrom in the electrode spacing d, produces a tunneling current decaying about one order of magnitude.

In summary, under these three simplifications, the tunneling current is proportional to

$$I_T \propto \frac{4\pi e}{\hbar} e^{-2d\sqrt{\frac{2m\phi}{\hbar^2}}} N_T(0) \int_{-\infty}^{+\infty} N_S(E-eV)[f(E)-f(E-eV)]dE \tag{2.17}$$

Tunneling Conductance and Superconducting DOS at Low Temperatures

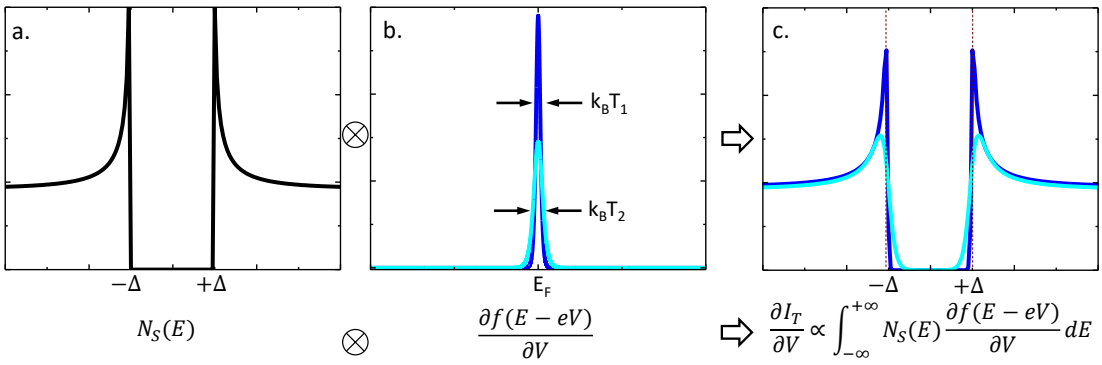

Figure 2.12 Effect of the temperature on superconductor-normal metal tunneling process. **(a)** As we show in the previous chapter, the BCS superconducting DOS has a gap in the excitation spectrum of Δ on each side of the Fermi level and characteristic singularities in $N_S(E)$ for $E = \pm\Delta$ (Eq. 1.23). **(b)** Examples of the temperature dependence of the derivative of the Fermi distribution at low temperatures with $T_1 < T_2$ and a cut off widths of k_BT. **c**. The tunneling conductance is the convolution between **(a)** and **(b)**. As a result, we have a thermal broadening in the DOS. At very low temperatures the tunneling conductance is a direct measurement of the superconducting DOS [92].

One of the most important tunneling experiments arises when we study a superconducting sample with a tip made of a normal metal. The importance of the temperature in this kind of tunneling process can be appreciated by taking the derivative of the tunneling current with respect to the voltage; the result is defined as the *tunneling conductance* σ and can be written in the form

$$\sigma(V) = \frac{dI_T}{dV} \propto \int_{-\infty}^{+\infty} N_S(E)\frac{\partial f(E-eV)}{\partial V}dE \tag{2.18}$$

Thus, the tunneling conductance is proportional to the convolution between the density of states (DOS) of the sample and the derivative of the Fermi distribution.

In Figure 2.12 we represent the effect of the temperature on the BCS superconducting DOS (Fig. 2.12 a). At low temperatures the derivative of the Fermi distributions is a bell shaped symmetric curve centered at the Fermi level with a cut off width of k_BT (Fig. 2.12 b). As a result, we have a thermal broadening in the tunneling conductance (Fig. 2.12 (c)). As the temperature $T \to 0$ K the function $\partial f(E-eV)/\partial V \to \delta(E-eV)$, the Dirac delta function. In this case, eq. 2.18 becomes

$$\sigma(V) = \frac{dI_T}{dV}\Big|_{T\to 0} \approx N_S(E = eV) \tag{2.19}$$

Thus, in the limit of low temperatures, a measurement of tunneling conductance provides the density of states of the superconductor.

With this new capability, the STM becomes a STS *Scanning Tunneling Spectroscopy: a tool to visualize the density of states at local scale as a function of the energy on the sample*.

In the next section I will show how we can control the movement of the tip on a surface and the methods to obtain topography and spectroscopy maps.

2.4.1 STM: Topography and Spectroscopy

Basic elements in a STM

Figure 2.13 shows the basic elements in a scanning tunneling microscope. A probe tip is made of Au, or Pt-Ir alloy, is attached to a piezotube which consists of three mutually perpendicular piezoelectric transducers: $\pm x$-piezo, $\pm y$-piezo and z-piezo. A piezoelectric material expands or contracts in response to an applied voltage. Therefore, by applying a triangular voltage on the $\pm x$-piezo and a voltage ramp on the $\pm y$-piezo, the tip scans on the xy-plane. Using the z-piezo, the tip and the sample are brought to within a few angstroms of each other.

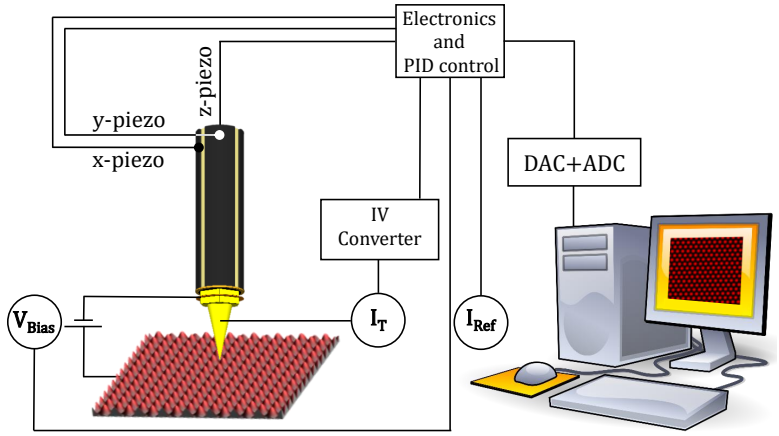

Figure 2.13 Schematic diagram of the scanning tunneling microscope. The tunneling current I_T is measured and compared with a reference current I_{ref}. The bias voltage V_{bias} produces a net tunneling current flow. All the signals (generated/received) are controlled mainly by an analog PID control. The ADC and DAC allow controlling all the signals needed for the operation of the STM.

A bias voltage (V_{bias}), applied between the tip and the sample, produces the tunneling current flow. The tunneling current passes through a IV converter with a gain of 10^8 to 10^9 V/A, to become a voltage. The signal is compared with a reference tunneling current I_{ref}. The condition $I_{tunn} = I_{ref}$ is kept by continuously feedback-adjusting the tip z-piezo-position during the scan.

The feedback is controlled by a Proportional-Integral-Derivative (PID). The analog-to-digital converter (ADC) and a digital-to-analog converter (DAC) connected to a 96-bits digital I/O interface card (DIO-96) installed in the PC, allow generating and receiving all the signals needed in the STM operation.

Figure 2.14 shows a second photography of the experimental setup, focused on some of the items which help to control the temperature, data acquisition and the STM operation. As I had described previously, the STM is anchored to mixing chamber of the dilution refrigerator and housed inside an *inner vacuum chamber (IVC)*. The system is immersed into an super-insulated ^{4}He dewar (a). The wires for STM signals on top, at room temperature, are soldered to the electrical vacuum feed through connection (b). The PID, the I_{ref} control (c), the IV converter (not shown, behind (c)), the temperature controller (f-g) and the PC (h) are energized by the power supplies (e) which are grounded to a point uncoupled from the building (exactly under the dewar).

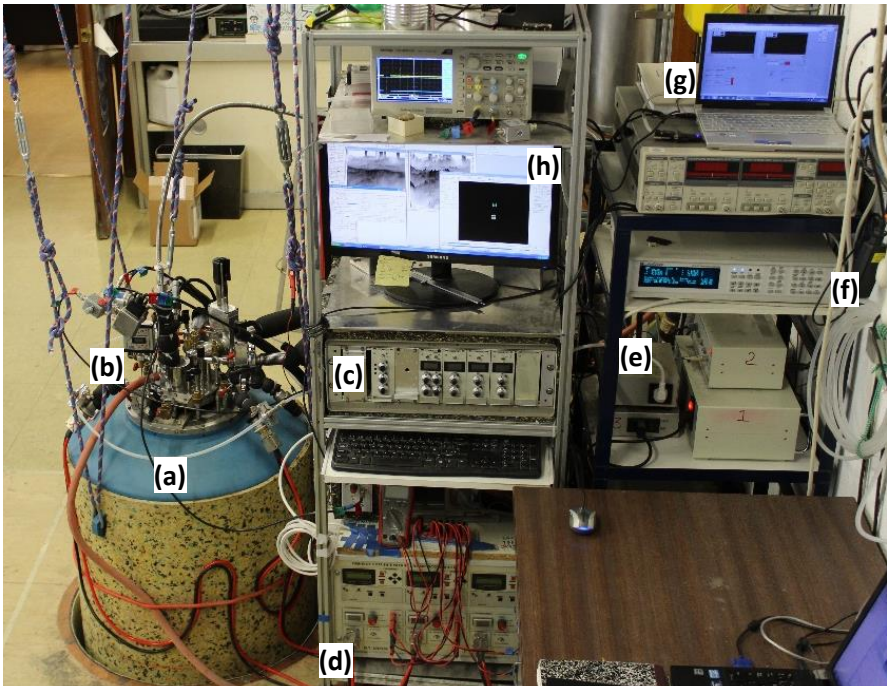

Figure 2.14 *Overview of the experimental Setup II: Equipment to control the temperature, data acquisition and the STM operation.* **(a)** A super-insulated Dewar of 100 L of capacity. **(b)** Insert connections and upper part of the ^{3}He-^{4}He dilution refrigerator. **(c)** Electronics to control the PID, the I_{ref} and the IV converter (not shown, behind (c)). **(d)** 3-Axis Magnet power supply which has three independent current sources. **(e)** Power supplies to STM control. **(f-g)** Temperature controller and PC monitor. **(h)** Monitor of the main PC.

Tip positioning

As mentioned above, the tip positioning is controlled by a piezotube whose working principle is based on the piezoelectric effect: the property of certain materials to change its size in response to an applied voltage. The tip is screwed at one of the ends of the piezotube while the other extreme is fixed to the STM body. The piezotube has 5 electrodes: 4 outside $V_{\pm x}$, $V_{\pm y}$ and one single for V_z (Fig. 2.15). The motion in each direction Δx, Δy, Δz is determined by

$$\Delta x[\mathring{A}] = \Delta y[\mathring{A}] = \frac{0.9 d_{31} L^2 V_{x,y}}{d_m t} \tag{2.20}$$

$$\Delta z[\mathring{A}] = \frac{d_{31} L V_z}{t} \tag{2.21}$$

where L is the length of the piezotube, t its thickness, d_m is the average of the inner and outer diameters, d_{31} is a constant of the ceramic material and V is the applied voltage.

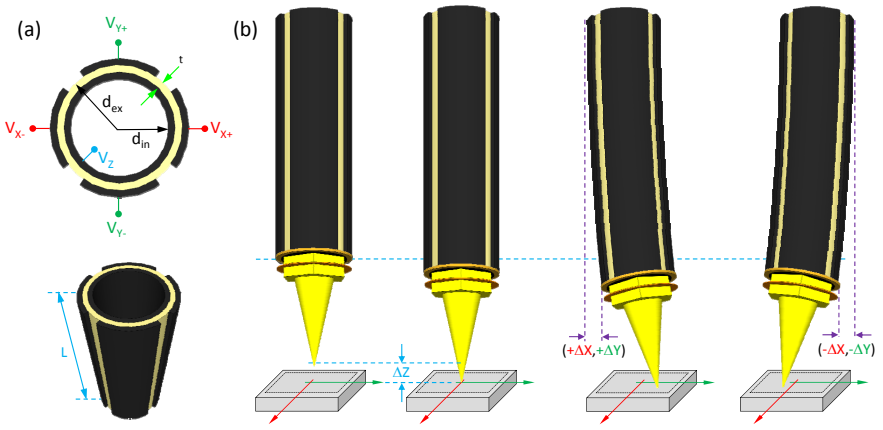

Figure 2.15 (a) Electrodes (black) and geometry of a a ceramic (yellow) piezotube. The voltages are applied to the x, y and z electrodes to produce a positive stress (pressure) or negative stress (tension). At equilibrium the distribution of stress and strain establishes a total torque. **(b)** The deflection of the piezotube in each direction ($\pm\Delta x$, $\pm\Delta y$, $\pm\Delta z$) depends on the geometry of the piezotube and the applied voltages according to the expressions 2.20 and 2.21. The tip (yellow cone) is screwed at one of the ends of the piezotube.

In this thesis I prepared a new piezotube with $L = 18$ mm, t = 0.381 mm, d_m=2.667 mm and d_{31} (4.2K)=0.31 Å/V [93]. This gives scan ranges of Δx=Δy= 90 Å/V and Δz = 12 Å/V. The maximum scanning window and largest displacement in z-direction are limited by the maximum voltage we can apply using our home-made electronics (V_{max} = 230V). These are respectively $\Delta x_{max} = \Delta y_{max} = 2\mu m$ and $\Delta z_{max} = 300$ nm

Topography Maps

The two different modes to obtain a topography map are: *scanning at constant current* and *scanning at constant height*.

Scanning at constant current (Fig. 2.16 left): the tip probes the surface while the tunneling current I_T is kept constant by continuously feedback-adjusting the tip z-position during the scan. The change of the tip height is recorded. This is the mode used to acquire all the topography images shown in this work.

Scanning at constant height (Fig. 2.16 right): the tip probes the surface while the vertical position of the tip z is kept constant (feedback-adjusting the tip z-position turned off). This mode is limited to samples with surface corrugations of a few Angstroms, to avoid collisions of the tip with defects on the surface (bumps, protrusions).

Spectroscopy Maps

Figure 2.17 represents a measurement of an spectroscopy map where a current versus voltage curve (I-V curve) is recorded at each pixel on a xy-area (Fig. 2.17a). A reference tunneling current I_{ref} is kept constant by continuously feedback-adjusting the tip z-position during the scan. On each pixel the feedback-adjusting control is turn off and a I-V curve is measured, then the feedback-adjusting control is turned on and the tip moves to the next pixel keeping reference tunneling current I_{ref} constant. The procedure is repeated consecutively on all scan window (Fig. 2.17b). The conductance at each pixel $\sigma(V) = dI/dV$, is obtained by numerical differentiation of I with respect to V (Fig. 2.17c). Finally, we can build spectroscopy maps at specific voltages if we represent the conductance at that specific voltage as a function of the xy-position (Fig. 2.17d). While a topography map can be obtained on the times scale of several minutes, a spectroscopy

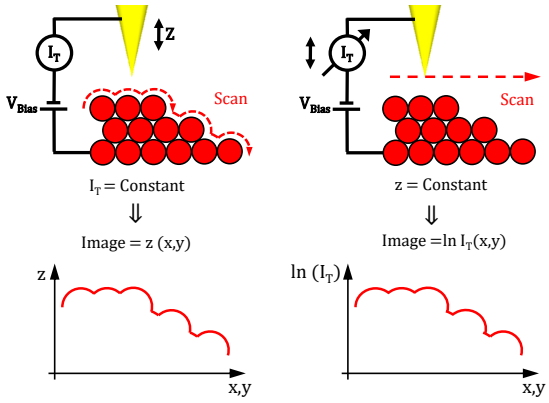

Figure 2.16 Schematic representation of the STM operating modes: scanning at constant current (*left*), and scanning at constant height (*right*). As the tip scans on the surface of the sample, the tunneling current will vary according to the tip-sample distance: tip on top of an atom (high-$I_T \Rightarrow z$-smaller), or, tip in between atoms (low-$I_T \Rightarrow z$-larger) [87].

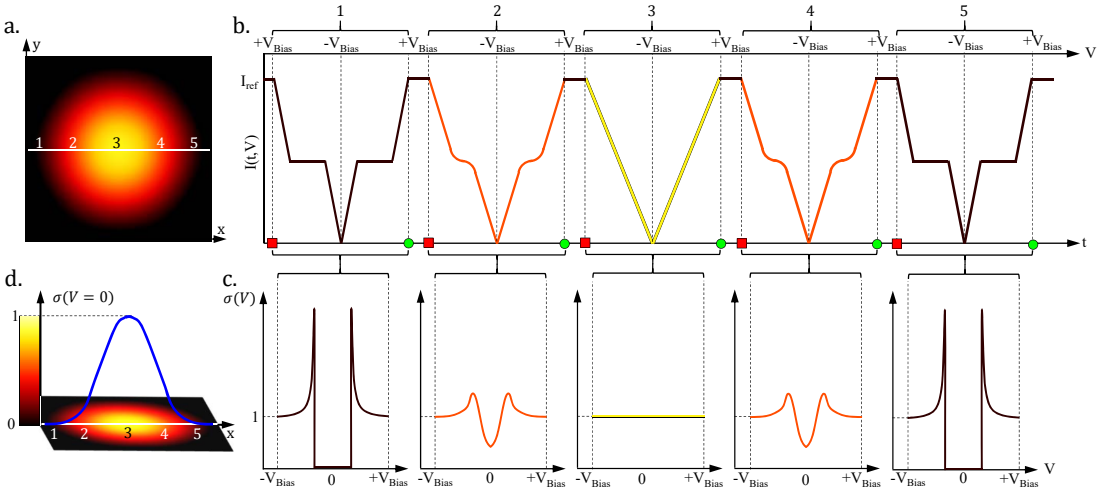

Figure 2.17 Example of the spectroscopy map in a xy-region with a circular shape BCS superconducting vortex **(a)** where the superconducting signal (black) gradually disappear (red to yellow). The tunneling current is measured as a function of the bias voltage **(b)** at each point while the tip is scanned in the x-direction across the white line in **(a)**. Two curves are measured at each point (from 1 to 5) by ramping the voltage from positive to negative values and vice-versa. Turn on and turn off the control is represented on the temporal axis as green circle and red square. The conductance $\sigma(V)$ curves at each point are obtained by the numerical derivative of the average of the two I-V curves at each point **(c)**. From these data we can represent a conductance profile (blue line) at zero bias voltage along the white line in **(d)**.

map may require longer periods of about several hours or even days.

An example of topography and spectroscopy measured simultaneously

The two previous subsections can be summarized as: in the topographic mode, we mapped the surface of the material via the dependence of the tunneling current upon the tip-to-sample distance, while in the spectroscopy, the DOS of the sample is collected measuring the tunneling conductance at local scale. Thus, the advantages of a STM, as a surface technique to characterize the structural and electronic properties of a system, lie on the coupling of these two features.

An example of the simultaneous topography/spectroscopy maps measured during this thesis is shown in Fig. 2.18. The measurements were obtained on the isotropic superconductor β-Bi_2Pd at 100 mK and 0.2 T (perpendicular to the window) with I_{ref} = 10 nA. Color contrast in

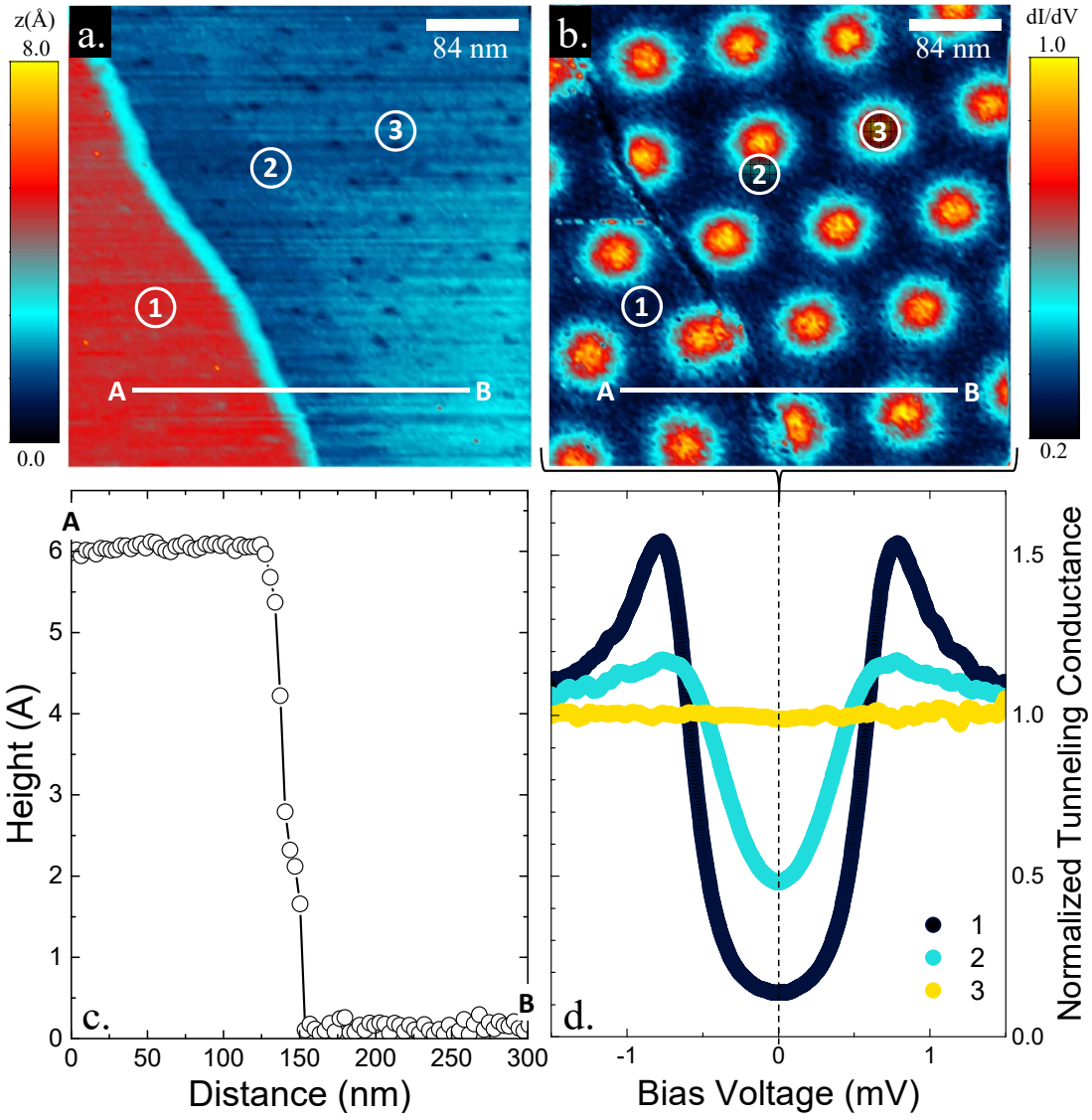

Figure 2.18 (a). Topography and **(b)** spectroscopy map at V = 0mV, measured simultaneously in the superconductor β-Bi_2Pd at 100 mK, 0.2 T (perpendicular to the surface). From the topography we measure a profile **(c)** between the surfaces labeled as **A** and **B** (white line in **(a)** and **(b)**). **(d)** shows some normalized tunneling conductance curves measured on the points ①, ② and ③. Vertical color bar scales in **(a)** and **(b)** give the contrast in height and conductance for the topography and spectroscopy respectively.

topography (Fig. 2.18a) allows distinguish two flat surfaces, A and B, whose separation height is 6 Å (Fig. 2.18c). At 0.2 T a vortex lattice forms in this material that can be imaged using the STM as shown in the spectroscopy map in Fig. 2.18b. This was made at V = 0 mV, thus the contrast is given by changes in the conductance curves from inside to outside of the vortices at the Fermi energy (Fig. 2.18d). It is easy to see that both images have been taken simultaneously over the same region. Note that the border line between A and B surfaces (cyan in the left panel, dark blue in the right panel) is clearly identified in both images.

Hence, we can map the tunneling current on a surface as a function of 4 variables: 3 spatial directions and energy, i.e. x, y, z and V. As a result, we can establish the operation modes of a STM and extract topographic and spectroscopic data at local scale.

2.5 Our Microscope

The STM used in this thesis was designed and built with the collaboration of the SEGAINVEX workshop [70], on the basis of preceding microscopes installed at the LBTUAM [90, 94]. It is made of titanium. It is a lightweight material (a 40% lighter than iron), it is a paramagnetic material (it is not affected by magnetic fields) and it has a thermal expansion similar to the piezoelectric materials used in the STM (to avoid problems due to thermal stress when changing temperature). Figure 2.19 shows a schematic diagram and two photos of the STM's body. One of the ends of the piezotube is screwed inside of a mobile titanium prism **A** which is held with a spring **G** to the rear part of the STM's body (see Fig.2.19c).

Shear piezostacks **B** at two sides of the prism (glued to STM's body) are used to drive the coarse vertical motion of the tip. Each piezostack consists of five shear plates with size $10 \times 5 \times 0.5$ m^3 from Ferroperm glued with Stycast. The inertial motor is driven a ± 130 V sawtooth signal.

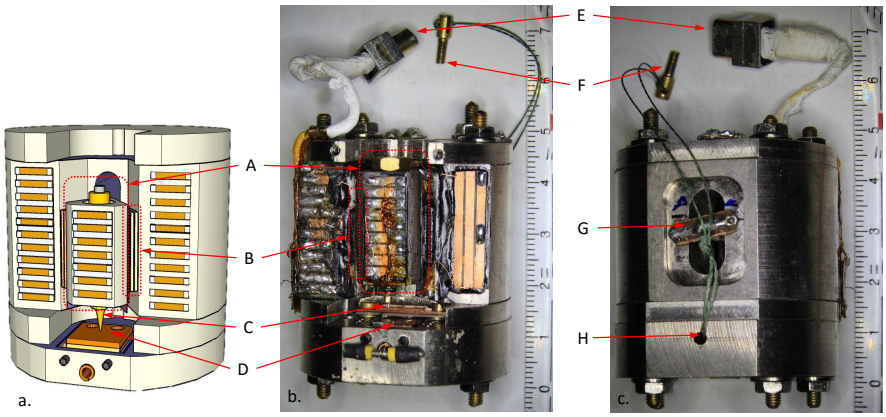

Figure 2.19 Schematic diagram **(a)** and photographs, front **(b)** and rear **(c)**, of the STM's body. The mobile titanium prism is shown inside of the dashed line square **A**. The piezo stacks **B** allow the vertical movement of the prism which houses the piezotube connected to the tip **C**. The sample holder **D** is screwed to a slider. All the signals goes thought a 9 pin connector **E**. A screw **F** joins the piano wire with the Kevlar® rope connected to the slider thought the hole **H**. **G** is the end of the spring which held the mobile titanium prism to the STM's body.

During this thesis, STM connections were improved in the last thermalization stage of the wiring.A special connector was soldered to the STM's body (**E** in Fig. 2.19) to reduce time needed to prepare the experiment at ambient conditions and avoid sample/tip contamination from waste elements of the welder process.

Sample positioning stage

The sample is mounted on a horizontal linear positioning stage which can be moved macroscopically in a range up to a cm and with an accuracy down to the tens of nm. The position of the tip over the sample as set at room temperature does not change more than a few micrometers when cooling down. The same stage can be used to approach a hard single crystalline sample to a knife and cleave it, or break it, *in-situ* as described below [94].

The positioning device consists of a sample holder screwed on a slider fixed to a frame which is firmly screwed into lower part of the microscope. The forward or backward movements of the slider are driven by a screw fixed at the upper part of the dewar and glued on the upper end of the piano wire. The whole system is attached (using Kevlar® ropes) to a copper support in good contact with the mixing chamber of the dilution refrigerator in such a way as to impede motion of the microscope when pulling on the slider [94]. Figure 2.20 describes with more detail the sample positioning mechanism by the forward or backward movements of the slider.

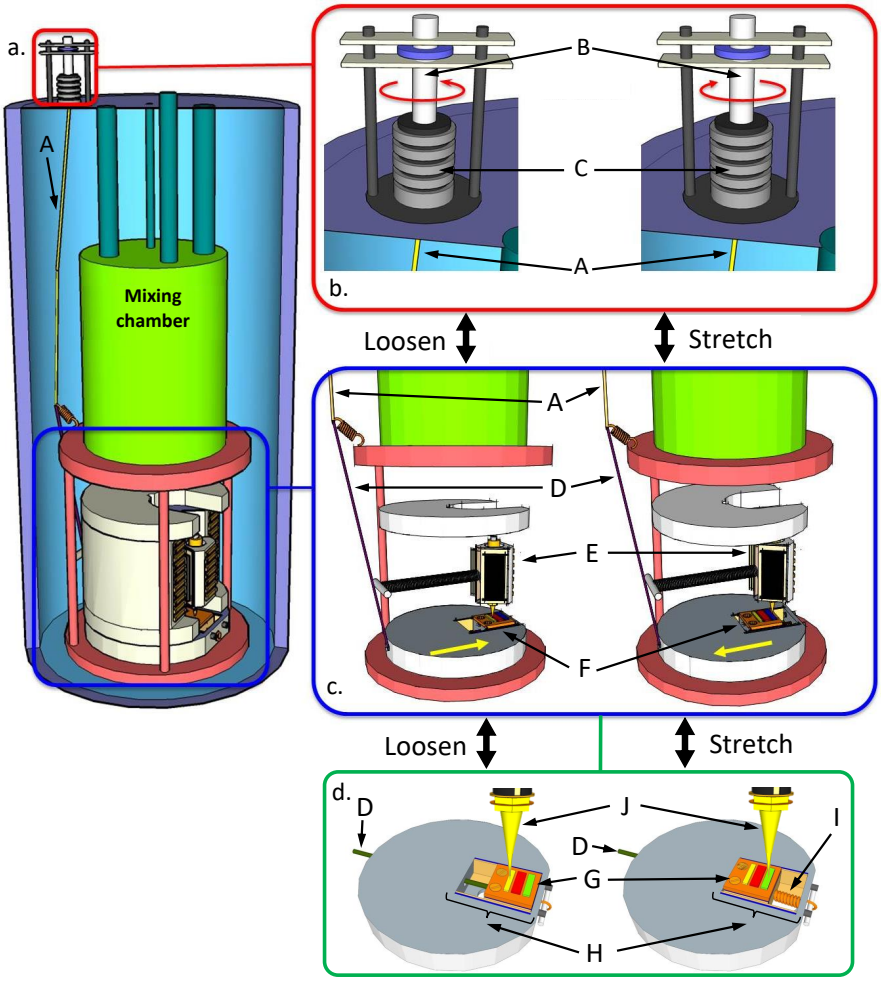

Figure 2.20 (a). Schematic representation of the positioning mechanism in the STM. The STM's body is anchored in a cooper support which is connected to the mixing chamber. The piano wire **A** (made of tempered high-carbon steel) is glued on a screw **B** fixed at the upper part of the dewar, and attached to the slider by a Kevlar® rope **D**. **(b)**. *Detail of the upper part of the system*: the screw **B** insides of a metallic bellows **C** stretch or loosen the piano wire **A**. **(c)**. *Sample holder movement*: the tension of the piano wire **A** is transmitted by a Kevlar® rope **D** connected to the slider **F**. As a visual aid, the mobile titanium prism and the spring to support it to the rear part of the STM's body is represented **E**. **(d)**. *Detail of how the sample positioning mechanism allow to measure different samples*: the samples (yellow, green and red) are glued on the sample holder **G** which is screwed on the slider **F**. The Kevlar rope **D** serves to pulls on the slider which moves on Alumina track covered by graphite **H**. The relative xy-position of the tip **J** and the samples will depend on the equilibrium between the tension on the Kevlar rope and the restoring force of the spring **I**.As we did with the wiring for the STM signals, which is thermalized at the different thermal stages (described in sec. 2.2.3), the piano wire has been welded to specific positions of the refrigeration cycle to avoid themal losses (Not shown here).

Cryogenic Cleavage Methods

During this thesis two cryogenic cleavage methods where implemented and tested. The first method is shown in Fig. 2.21, it was designed to cleave hard samples in situ. In this cleaving process, a ceramic blade is fixed with two screws to the bottom part of the STM. The Kevlar® rope is pulled to move the sample holder backwards. The sample hits the ceramic blade and it breaks. Then the piano wire is loosened and the sample holder returns to its initial position by the restoring force of the spring (**I** in Fig.2.20). The method was probed by first time in this experimental setup on the heavy fermion compound URu_2Si_2. All the topography/spectroscopy images shown in the chapter 6 were obtained after breaking different samples of URu_2Si_2 at 4.2

K.

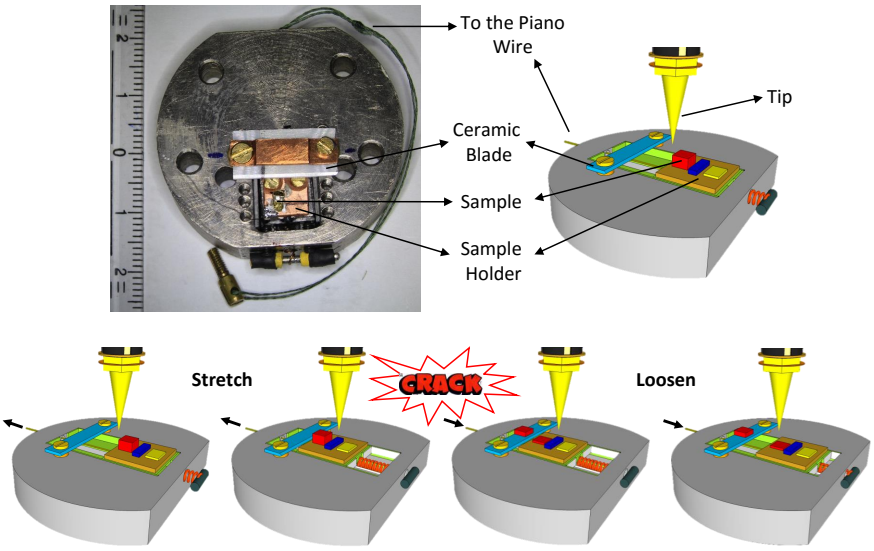

Figure 2.21 Photography (scale in mm) and schematic diagram of the stage to cleave samples by means of a ceramic blade. Pulling the Kevlar rope the sample hits the ceramic blade and it breaks. This mechanism was implemented in the course of this thesis and allows to get clean surfaces *in-situ* on hard samples. The method was 90% successful cleaving URu_2Si_2 samples (see Charter 6).

This method was successful 90% of the times; the remaining 10% was due to failures after the sample's cleavage. Sometimes, the broken sample remained blocked under the ceramic blade, thus, the restoring force of the spring (**I** in Fig.) was not enough to move the slider to the equilibrium position with respect to the tip. In other experiments, a piece of the broken sample jumped and hit the tip; as a result, the tip was bent and contaminated. In another case was because a piece of the broken sample jumps to the Alumina track, thus, the motion of the slider was blocked.

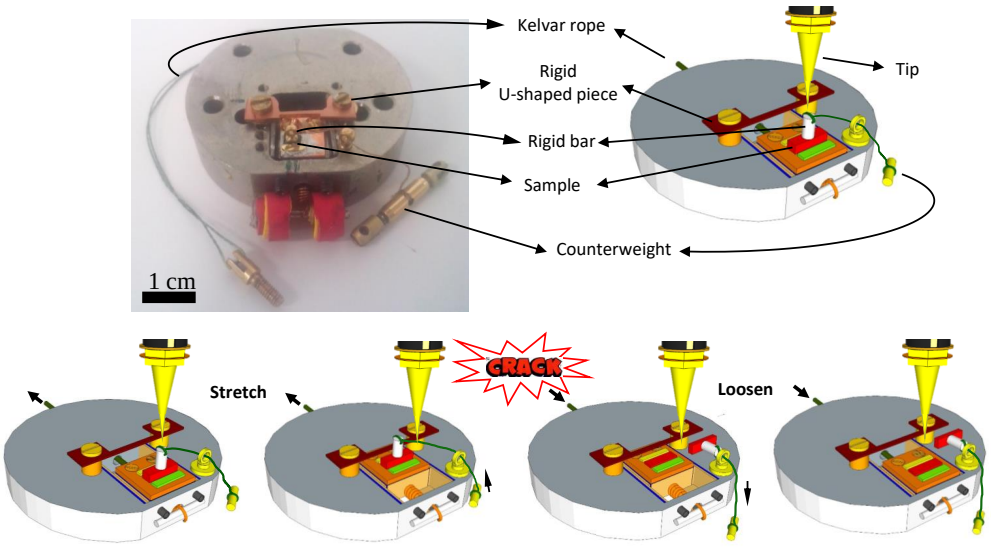

Figure 2.22 Photography and schematic diagram of the stage to cleave samples by means of gluing a tiny rigid bar on the sample. Pulling the Kevlar rope the tiny rigid bar hits a rigid U-Shaped piece and it breaks. This mechanism was implemented in the course of this thesis and allows to get clean surfaces *in-situ* on layered samples.

The second method is shown in Fig. 2.22, it was designed to cleave layered samples in situ. In this cleaving process, a tiny rigid rod (size similar to the sample's size) is glued on top of the sample. The Kevlar® rope is pulled to move the sample holder backwards. The tiny rod hits a rigid U-Shaped piece and it breaks, then the piano wire is loosened and the sample holder returns to its initial position by the restoring force of the spring **I** in Fig.2.20. The counterweight avoids that the tiny rigid bar and the glued piece of the broken sample, hit the tip or block the Alumina track of the slider.

The method was used in the layered compounds $La_{1-x}Ce_xSb_2$ [95], $Rh_9In_4S_4$ (see Charter 5) and recently in $Bi_2Sr_2CaCu_2O_{8+\delta}$.

2.6 Some Mechanical and Electrical Noise Considerations

In this thesis we have improved the mechanical isolation of the experimental setup to decrease sensitivity to vibrations by two ways.

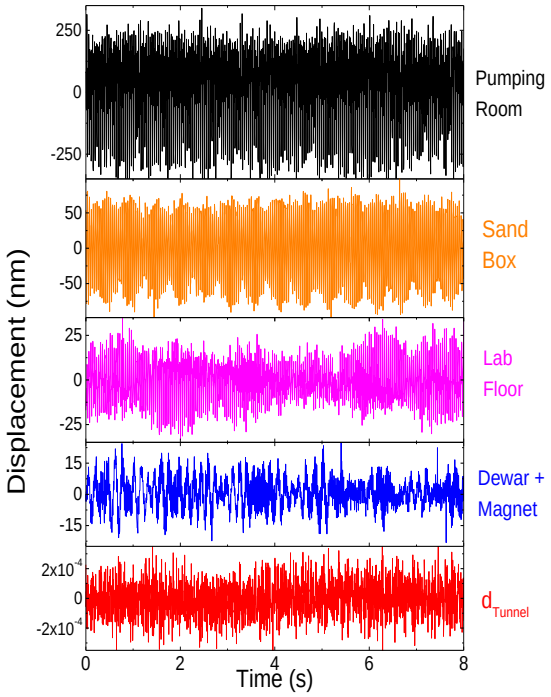

Figure 2.23 Displacements induced by vibrations at different parts of the dilution refrigerator experimental set-up. Upper four curves are taken using an accelerometer. Lower curve is obtained by measuring the STM current as a function of time without the STM feedback loop.

We first reduced the mechanical noise using the new sliding seal between the dilution fridge and the dewar, followed by the covering of the free space at the upper part of the dilution refrigerator (described in section 2.2.3); these improvements decrease the vibrations inside dewar produced by the ^{4}He evaporation.

We further improved the mechanical noise isolation by optimizing the hanging system of the dewar at the ceiling of the lab (see the ropes in Figs. 2.6 and 2.14). We decided to change the old ropes by new ones with a higher linear density (almost twice mass). A massive rope has a higher attenuation coefficient, thus, the energy density and the amplitude of the transmitted vibrations decrease; as a result, the transmitted vibration are reduced to $\sim$70% in comparison with the less massive rope. In addition, we have decoupled the joint between the roof and the rope by a TRAXIFLEX® antivibration ceiling hanger [96]. The TRAXIFLEX® hanger system comprises

two metallic U armatures joined by two bonded rubber blocks. It has a nominal charge of 20-80 daN and natural frequency from 8 to 10 Hz [96].

After the implementation of these improvements for the mechanical isolation, we have made a quantitative analysis of the mechanical noise level. In figure 2.23 we show measurements of the noise level at different points of the experimental setup. We measure the vertical displacement with an accelerometer in different positions and then the displacement of the tip with respect to the sample in the STM's body. In the room where all pumps needed to operate the dilution refrigerator are located, we find vibration amplitudes of 300 nm as measured on top of the pumps.

The vibration level on the laboratory floor is somewhat larger, of about 25 nm, and is due to residual motion of the base of the building and to acoustical noise. To reduce the part corresponding to acoustical noise, we glue Copopren^{TM} to the outside of the dewar. To reduce further the sensitivity of the STM's body to vibrations, we pose the microscope on fiberglass on top of its support anchored at the mixing chamber.

We measure the vibration of the tip over the sample using the tunneling current with the expression (eq. 2.16). We use tip and sample of gold, thus $\phi \approx 5$ eV (the work function of Au), and find values below 0.2 pm at 100 mK with the dilution refrigerator operating and the magnet energized (see Fig. 2.23). The voltage noise level of the electronics used ((c-f) in Fig. 2.14) produces displacements of the piezotube below pm at 100 mK value (using a piezotube of with 90 Å/V in the x-y plane) [80]. Thus, noise in the tunneling current is due to residual vibrations.

2.7 Crystal Growth

The superconducting systems studied in this thesis are single crystals grown by our group and crystals from collaboration with other researchers.

I participated in the growth of single crystals of the β-Bi_2Pd (Chapter 3 and 4) at the crystal growth facility of the Low Temperatures Laboratory at Universidad Autónoma de Madrid (Spain) [97].

Single crystals of the $Rh_9In_4S_4$ were obtained thanks to the collaboration with the Professor Paul Canfield from Ames Laboratory and Iowa State University (USA) [98].

The single crystals of $Rh_9In_4S_4$ (Chapter 5), were obtained by the solution growth technique [99, 100]. Figure 2.24 summarizes the main steps to grow a crystal by this technique. In this method the components of the desired compound are put in a crucible of aluminium oxide (Al_2O_3). The crucible is sealed in a quartz ampoule under a controlled atmosphere, sometimes with a small excess of elements whose function is encourage the crystal growth. Then, the quartz ampoule is heated from room temperature to temperatures slightly above the saturation temperature, following different thermal cycles long enough to form a complete solution. In most of the cases, the crystal formation started by spontaneous nucleation. Finally, the reaction is stopped and the ampoule is cooled down to room temperature by quenching or by centrifugation in order to allow the desired material to precipitate.

Single crystals of URu_2Si_2 were obtained thanks to the collaboration with the Professor Dai Aoki from INAC/SPSMS, Grenoble (France).

The single crystals of URu_2Si_2 (Chapter 6) were grown by the Czochralski method [101]. In this technique, the top of a seed crystal is molten and fed with molten liquid of a source compound. The crystal is slowly pulled out of the melt as it grows, by a rotating rod keeping constant the melt temperature. The quality of the crystal will depends strongly on the control of the temperature gradients, rate of pulling and speed of rotation [102]. Figure 2.25 shows the essential features of the Czochralski process and photographs of a few of the high quality single crystal of URu_2Si_2 studied in this thesis.

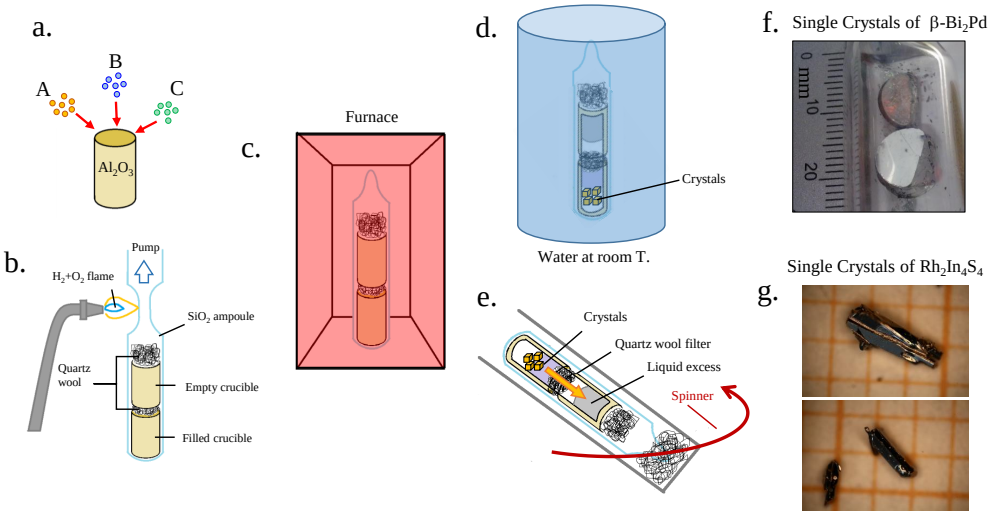

Figure 2.24 (a). Stoichiometric amounts of the elements which form the desired compound, represented by A, B and C, are put in crucibles of Aluminum oxide. Then, they are encapsulated with quartz wool and sealed in a quartz ampoule under a controlled atmosphere **(b)**. According to the phase diagram of the wanted material, the sealed ampoule goes through a thermal cycle **(c)**. Thus, the basis elements react and precipitate the solution which will originate the crystal. Finally the reaction is stopped cooled the ampoule by quench **(d)** or by centrifugation **(e)**. **(f)** and **(g)** show photographies of β-Bi_2Pd and $Rh_9In_4S_4$ compounds respectively (grid in mm). The β-Bi_2Pd single crystals were obtained by quench in water at room temperature whereas the $Rh_9In_4S_4$ samples were obtained by centrifugation [97, 98].

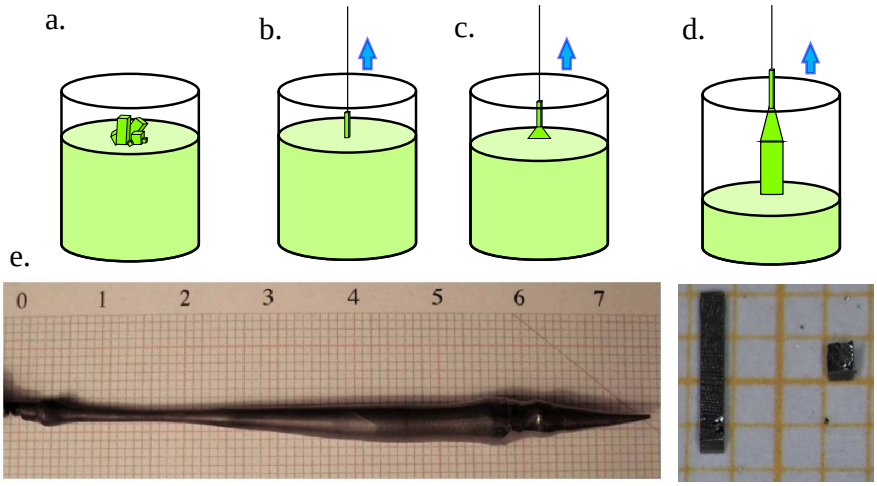

Figure 2.25 (a). A crucible is heated until the synthesis of the basis elements occurs. **(b)**. A seed crystal of the desired compound is rotated and slowly withdrawn from the melt, beginning the crystal growth. **(c-d)**. Controlling the temperature gradients, rate of pulling and speed of rotation, it is possible to extract a large, single-crystals. **(e)**. Photographies of high quality single crystals URu_2Si_2 grown by the Czochralski method [101] (grids in mm).

3 - β-Bi_2Pd: Single-gap & Multi-band SC

"Tell your son to stop trying to fill your head with science- for to fill your heart with love is enough"
The Pleasure of Finding Things Out" (1981)
R. Feynman

Multiband superconductivity was proposed theoretically in 1959 [33]. Wide spread experimental support to this picture came after the discovery of superconductivity in MgB_2 [103]. Soon after the publication of the first papers on superconductivity in this compound, a very small superconducting gap was observed by tunneling spectroscopy [104]. Theory immediately reacted by proposing two-band superconductivity, with one gap smaller and another gap slightly above the BCS value ($1.76k_BT_c$) [105, 106, 107]. Later measurements showed two well defined superconducting gaps in the tunneling spectroscopy [46] and in a number of other measurements [108, 109, 110]. Since this discovery, multigap and multiband superconductivity have been conceptually linked together, suggesting that materials showing different Fermi surface sheets could also have different superconducting gaps in each sheet. However, the role of interband scattering remains unclear. In particular, it is unknown what are the specific properties of a material with multiple Fermi surface sheets and a single superconducting gap.

This chapter show how superconducting features are modified by a multiband Fermi surface from the tunneling spectroscopy and vortex lattice imaging in β-Bi_2Pd. The first part provides an overview on the effects by which a gap material can be identified, describing how the multi-gap properties have been established by comparison with a single-gap BCS predictions. The second part exposes a general description of the Bi-Pd family focusing on the previous reports in β-Bi_2Pd. The third section is dedicated to show experimental results in β-Bi_2Pd. I will show how the scanning tunneling results on the superconducting and mixed phase, classify β-Bi_2Pd as a single gap superconductor. Finally, the fourth section presents the discussion on our experimental results, closing the chapter with some concluding remarks.

3.1 Superconductivity in systems with multiple bands crossing the FS

Two-gap superconductivity was proposed theoretically by Suhl, Matthias and Walker in 1959, "*as an extension of the BCS theory to the case where two bands ... overlap*" [33]. In a single gap BCS theory, a Cooper pair is the result of coupling between electrons of the same band. In multiband superconductors, eletrons from different bands can interact through electron-phonon coupling mechanism. This results in the mixture of the electronic properties between bands producing what is known as interband scattering. In a hypothetical multiband superconductor without interband scattering, one superconducting gap emerges in each band with different values and critical temperatures, according to the BCS expression $k_B T_{ci} = \Delta_i/1.76$ (i number of bands). Thus for a two-band superconductor, when the mixing between bands is ignored, two independent BCS gaps Δ_1 and Δ_2, with two different critical temperatures open over the Fermi surface. Turning on the interband scattering, produces a strong deviation in the theoretical critical temperature for the smaller gap (T_{c1}). Above T_{c1} the band with larger gap induces superconductivity in the band with smaller gap, increasing the value of T_{c1} up to T_{c2}. Thus, the temperature dependence of the smaller gap above the hypotetical T_{c1} is peculiar and does not follow the behavior expected within BCS theory [90, 111]. This description is schematically represented in Figure 3A. When interband scattering is strong enough it can even make equal the superconducting properties in the two bands, destroying completely the multigap superconductivity.

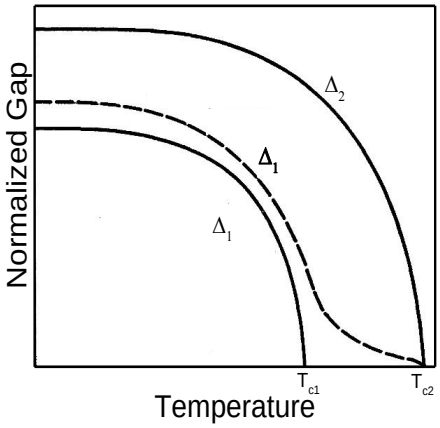

Fig. 3.A The energy gaps Δ_1 and Δ_2 as a function of the temperature in a hypothetical two band superconductor. The solid lines would be possible without interband coupling, following the BCS theory with different critical temperatures T_{c1} and T_{c2}. As a result of the interband coupling, the smaller sized superconducting gap survives up to the critical temperature T_{c2} (Δ_1 dashed line). Increasing the interband coupling, the kink vanishes gradually and both gaps merge into one as within single gap BCS theory. [90, 33].

Results in two-band superconductors

Tunneling spectroscopy of known two-gaps superconductors

A direct measurement of the superconducting gap structure can be obtained by tunneling microscopy. As we described previously, the expression Eq. 2.19 gives the density of states $N_S(E)$ as a function of the energy of the sample. In a two-band superconductor, the tunneling conductance can be modeled by $N_S = n_1 N_1 + n_2 N_2$, with N_i density of states of the different bands and n_i their relative contribution to the tunneling current ($n_1 + n_2 = 1$).

Figure 3.1 shows the tunneling spectroscopy signals and the superconducting gaps in three multigap superconductors. The peaks in MgB_2 reveal the two gap signature (Fig. 3.1(a)); the small gap is associated with the π-band ($\Delta_\pi = 2.2$ meV) while the larger gap is linked to the σ-band ($\Delta_\sigma = 7.1$ meV) [46]. The temperature-dependence of tunneling spectra shows that both superconducting gaps follows the BCS behavior and disappear at 39K (Fig. 3.1(d)). In contrast, the tunneling conductance in the dichalcogenide 2H-NbS_2 shows only one peak with and a shoulder at lower voltage (Fig. 3.1(b)). In this case, there is a distribution of gaps with maxima at $\Delta_2 = 0.97$ meV. These values are obtained by the derivative of the conductance curve $d\sigma/dE$, (inset Fig.3.1b) whose temperature evolution shows that both gaps disappear at $T_c = 5.7$ K (Fig. 3.1(e)) [112]. Finally, as in MgB_2, the tunneling spectroscopy signal in the iron-based material $Ba_{0.6}K_{0.4}Fe_2As_2$, shows a clear two-gap structure (Fig. 3.1(c)) [113], showing one gap at $\Delta_1 = 12.5$meV and another one at $\Delta_2 = 5.5$meV (Fig. 3.1(f)) [114]. A similar result has been found recently in the LBTUAM for the compound $CaKFe_4As_4$ (see [115, 116]).

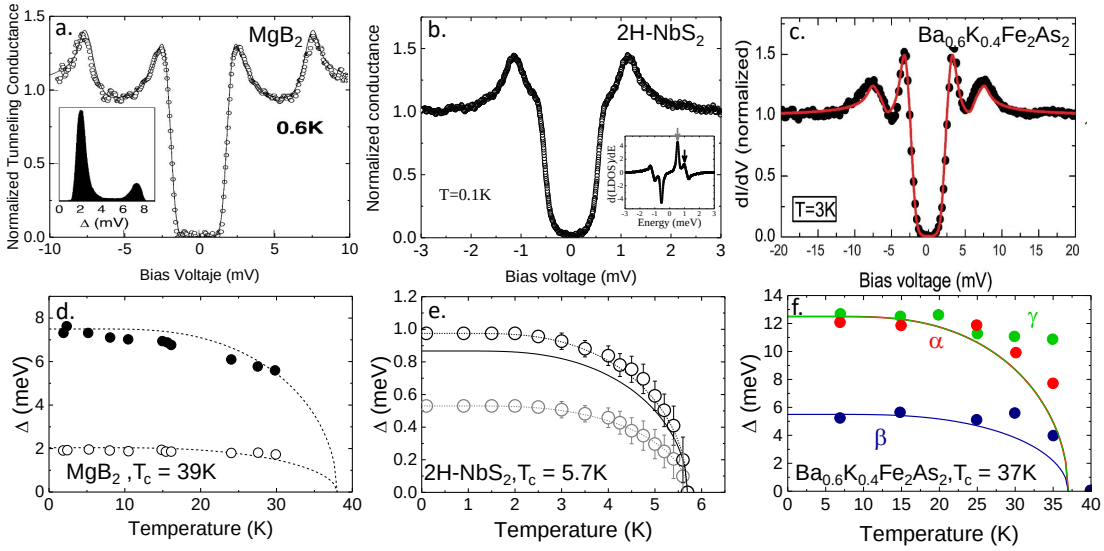

Figure 3.1 (*Upper panel*) Normalized tunneling conductance of MgB_2 **(a)**, 2H-NbS_2 **(b)** and $Ba_{0.6}K_{0.4}Fe_2As_2$ **(c)**, as a function of the bias voltage. In MgB_2, the double-peak structure is associated with two gaps $\Delta_\sigma = 7.1$ meV and $\Delta_\pi = 2.2$ meV, the continuous line is the fit with the contributions of each band; inset shows the distribution values of the superconducting gap used to fit the experiment. The peak+shoulder structure in 2H-NbS_2 and its derivative (inset) corresponds to two-gap scenario with a distribution of gaps with a maxima at $\Delta_2 = 0.97$ meV. The two peaks in $Ba_{0.6}K_{0.4}Fe_2As_2$ reveals the multigap signature with $\Delta_1 = 12.5$meV and $\Delta_2 = 5.5$meV. (*Lower panel*) Temperature dependence of the superconducting gaps obtained from the energy position of the peaks (shoulder) at each temperature. In **(d)** black and open circles correspond to Δ_σ and Δ_π respectively; the dashed lines are the BCS fit. In **(e)** black and gray circles correspond to the features associated with Δ_1 and Δ_2. In **(f)** the color circles are related with the α, β and γ sheets of the Fermi surface, the continuous lines are the BCS fits. Plots from references [46, 112, 114, 113]

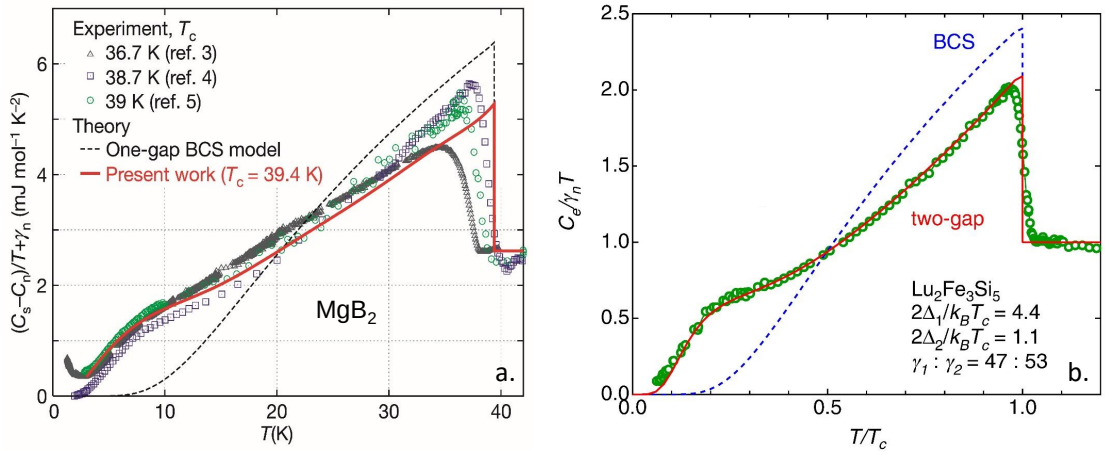

Figure 3.2 Temperature dependence of the normalized electronic specific heat for MgB_2 (a.)[117] and $Lu_2Fe_3Si_5$ (b.)[118]. Dashed and solid lines are the BCS normalized specific heat corresponding to $2\Delta(0)/k_BT_c = 3.54$ and two-gap fit respectively. In both cases, the BCS deviation reveals the multigap behavior.

Specific Heat

Measurements of the specific heat in multiband superconductors have exposed remarkable deviations from the BCS standard curve (see for example [119]). Those striking features are the jump magnitude at T_c, a fast increase at low-temperature and a small kink (shoulder or peak) in between. Figure 3.2 shows the measured and calculated electronic contribution of the specific

heat in two multigap superconductors, MgB_2 [117] and the ternary-iron silicide $Lu_2Fe_3Si_5$ [118].

In both cases The experimental data are plotted together with the BCS curve and a two band model which fits the experimental data. A direct comparison between BCS theory and measurements allows differentiating the already mentioned three characteristic features of a two-band specific heat curve: a small jump at the transition temperature ($\sim$1.2 in MgB_2, and, $\sim$1 in $Lu_2Fe_3Si_5$), a large hump inconsistent with one gap BCS model (at about $0.25T_c$ in both compounds) and a fast increase at low temperatures. .

Different authors conclude that the specific heat of two-band superconductor is governed at high-temperature by the band with the larger gap while low-temperature behavior is governed by the band with small gap [111, 117, 118]. In between the specific heat is determined by an overlapping, smoothed by the interband coupling, which results in a shoulder or kink [120].

Upper critical magnetic field

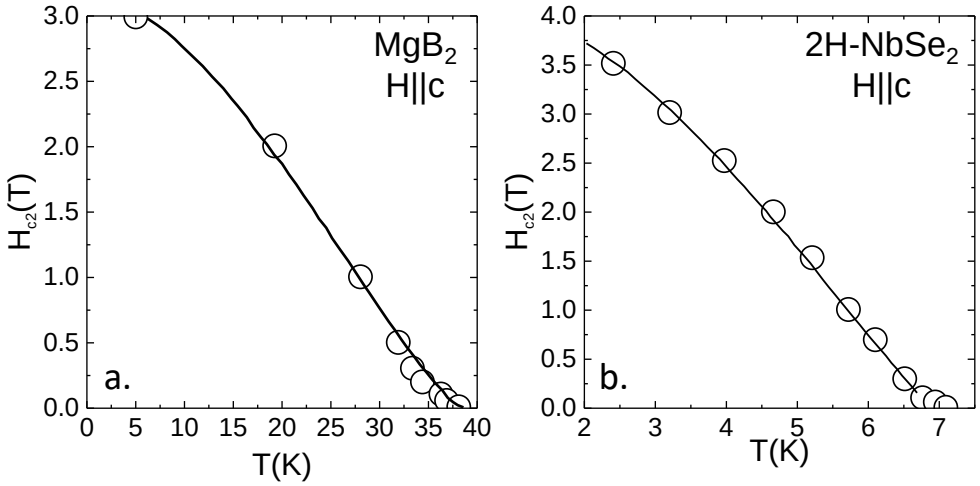

Figure 3.3 Temperature dependence of the upper critical field H^c_{c2} for MgB_2 **(a)** and 2H-$NbSe_2$ **(b)** [37]. The symbols indicate the experimental data. The solid lines are the two-band model using the theory described in references [36, 37, 121]. The positive curvature near the transition temperature reveals remarkable deviation from the WHH model; this feature is considered as indication or confirmation of two-band superconductivity. It is easy to observe the change of the slope dH_{c2}/dT close to T_c. This effect changes from sample to sample, and it is linked to the interband/intraband coupling and the Fermi velocities of each compound.

It has been also shown that the temperature dependence of the upper critical field can be related to the properties of the Fermi surface and multigap superconductivity (see introduction). In a simple BCS superconductor and at zero temperature $H_{c2} = \Phi_0/2\pi\xi^2$ and $\xi = \hbar v_f/\pi\Delta$ (see introduction). Thus, different gap values and Fermi velocities lead to different H_{c2} at zero temperature. In a multiband superconductor with different v_F, this gives two "effective" upper critical fields. This influences the temperature dependence of H_{c2}. Close to T_c, one band dominates, often the one that has the highest Fermi velocity (largest coherence length), leading to an extrapolation of H_{c2} to zero temperature that is small. At lower temperatures, the other band with a smaller Fermi velocity (smaller coherence length) has a larger contribution, leading to a high value of H_{c2}. This can be put into quantitative terms by an extension to the classical WHH theory to multiband systems. This extension was described in Refs. [36, 37, 121, 122, 123, 124] and used to explain the multiband characteristics of MgB_2, 2H-$NbSe_2$ and 2H-NbS_2.

Figure 3.3 shows the temperature dependence of $H_{c2}||c$ in two-gap/band superconductors which have been measured previously at LBTUAM: magnesium diboride MgB_2 and the dichalcoagenide 2H-$NbSe_2$ [37]. It is easy observed the pronounced upward curvature near to T_c. In

all cases, the experimental results have been fitted to a two-gap model described in detail in references [36, 37, 121].

This behavior has been observed in many different compounds, including heavy fermions, borocarbides, and Fe-based superconductors [125, 126, 127, 128, 129].

3.2 The Bismuth-Palladium Family

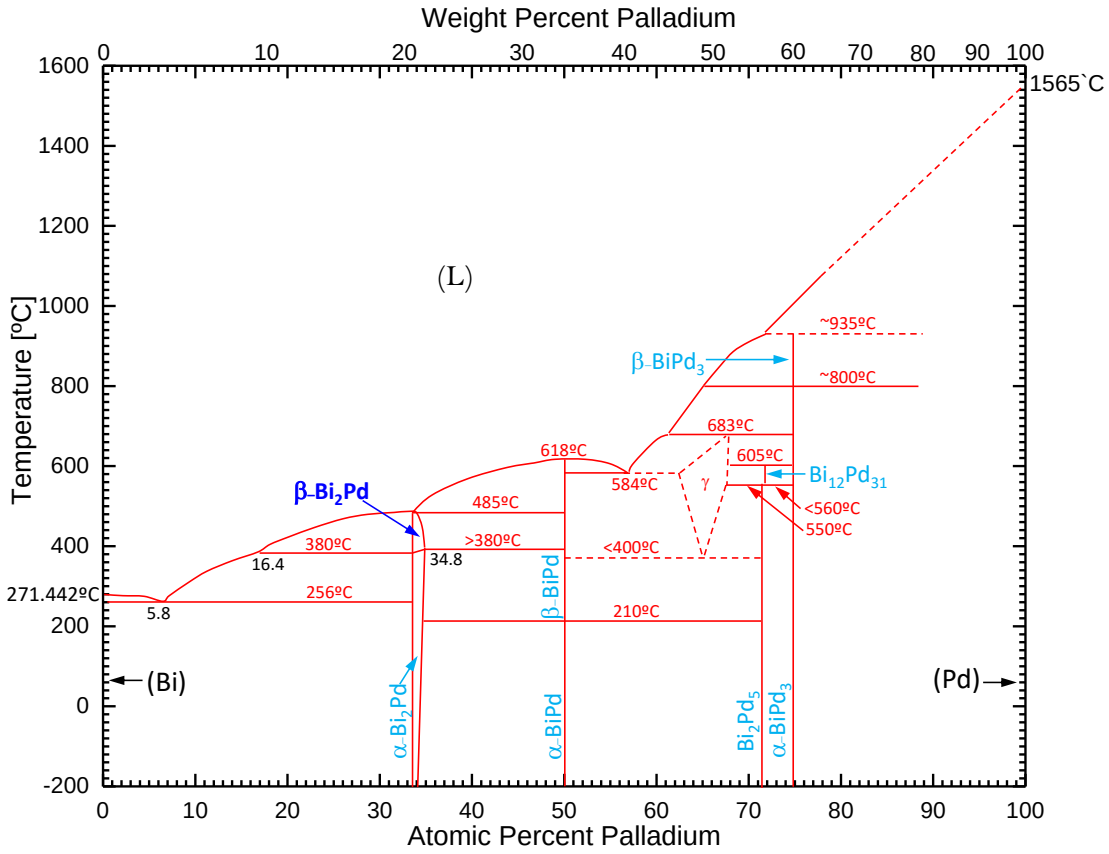

Figure 3.4 Phase Diagram of Bismuth and Palladium system. We remark the special stoichiometric composition and temperature ranges were the β-Bi_2Pd is stable (dark blue)

Figure 3.4 shows the binary phase diagram of *Bi-Pd* consolidated by Okamoto [130]. It summarizes the data from thermal analysis [131, 132], thermal metallography [133] and X-ray analysis [134]. The equilibrium phases are (1) liquid, L; (2) rhombohedral solid solution, (Bi); (3) tetragonal β-Bi_2Pd; (4) monoclinic α-Bi_2Pd; (5) orthorhombic phase, β-BiPd; (6) monoclinic α-BiPd; (7) γ phase or Bi_3Pd_5; (8) monoclinic Bi_2Pd_5; (9) orthorhombic $Bi_{12}Pd_{31}$, (10) β-$BiPd_3$; (11) orthorhombic α-$BiPd_3$; and (12) the fcc solid solution (Pd).

Among the different Bi-Pd phases, recently, attention has been focused on two of them: the noncentrosymmetric BiPd ($T_c \approx 3.8$ K) [135, 136, 137] and the centrosymmetric β-Bi_2Pd ($T_c \approx 5.0$ K) [138, 139, 140], both have been proposed as possible topological superconductors [141, 142, 143].

Efforts have been concentrated on the structural and electronic characterization on bulk properties of the β-Bi_2Pd. However, atomic scale characterization in normal and superconducting state on β-Bi_2Pd has not been reported, prior to our work. This was our main motivation and the starting point of our study of this compound.

3.3 Crystal structure and Fermi surface of β-Bi_2Pd

The review by Matthias et. al. [138] makes an overview of the binary superconducting compounds found until 1963. Among the Bi-Pd alloys that were identified, β-Bi_2Pd was reported by Zhuravlev in 1957 with a transition temperature of 4.25 K [132]. The Zhuravlev's work also remarks that β-Bi_2Pd crystallizes in a tetragonal lattice, space group $I4/mmm$, with constants $a = 3.362(1)\AA$ and $c = 12.983(1)\AA$. This structure can be schematically described as a stacking of square bilayers of Bi joined by a Pd layer in the sequence $...Pd/Bi/Bi/Pd/Bi/Bi/Pd...$ along the z as shown in Figure 3.3 A. Subsequent reports showed that, by improving the crystal quality, the transition temperature of β-$Bi2_2Pd$ can be increased. Figure 3.5(a) shows the dependence of the resistivity on a single crystal of β-$Bi2_2Pd$ reported by Imai *et.al.* [139], with a critical temperature of 5.4 K.

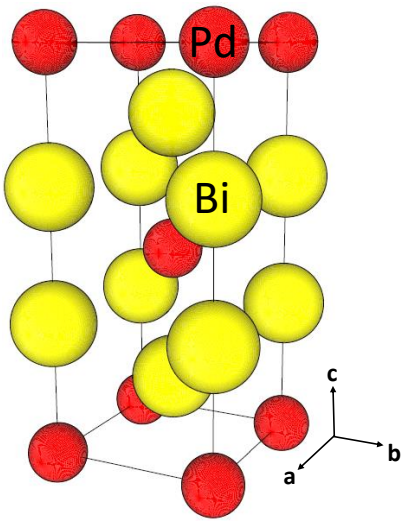

Figure 3.3 A Schematic crystal structure of β-Bi_2Pd [132].

β-Bi_2Pd: Fermi Surface

The electronic band structure and the Fermi surface (FS) of β-Bi_2Pd have been examined theoretically and experimentally [140, 142]. The calculated FS shape (Fig. 3.5(b)) is determined completely by Pd $4d$ and Bi $6p$ orbitals which yield to a unusual 2D/3D type of multi-sheet FS. The FS can be divided in four main structures: a 2D hole-like sheet with the shape of a deformed cylinder (shiny green color in Fig. 3.5(b)) parallel to k_z direction; a small closed hole-like pocket centered at Γ-point, electron-like 3D pockets which overlap in some regions the pseudo-cylinder and extends to the corners of the Brillouin zone, and finally, one small pocket (along P-X) inserted into the electron-like 3D pocket [140].

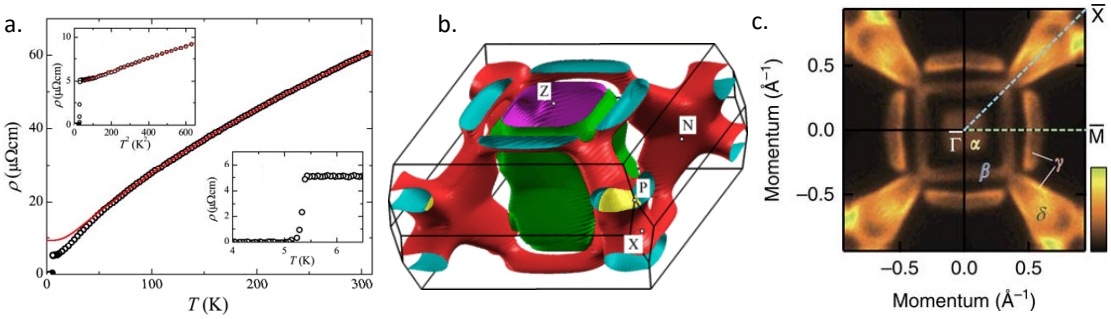

Figure 3.5 (a) Temperature dependence of the resistivity ρ in a β-Bi_2Pd crystal with a residual resistivity ratio [RRR, $\rho(T = 300K)/\rho(T = 6K)$] of 12 [139]. Insets show ρ near T_c and ρ at temperatures less than 25 K plotted as a function of T^2. Red line is a fit proportional to T^2. **(b)** Calculated Fermi surface of β-Bi_2Pd shown with the first Brillouin zone [140]. **c.** Fermi surface of β-Bi_2Pd recorded by angle-resolved photoemision spectroscopy (ARPES). Two electron-like and two hole-like Fermi surfaces are denoted by α, β and γ, δ, respectively [142].

An important conclusion of the electronic band calculation, is that there are anisotropies of chemical bonding which originate that Bi/Bi layers are less coupled that the adjacent Bi/Pd sheets. As I will describe in next sections, the cleaving procedure can be understood within this

chemical bonding framework.

Recently, the FS has been mapped experimentally by angle-resolved photoemision spectroscopy (ARPES). The result, shown in Fig. 3.5(c), mostly well agrees with the 2D projection on the k_xk_y-plane of the calculated bulk FS [142].

All references reviewed previously to our work point out the β-Bi_2Pd as a multigap superconductor. Band structure calculations have suggested that multiple FS should lead to multiple gap superconductivity [140]. Macroscopic measurements reported by Imai et. al. [139] also appeared to be consistent with multigap scenario. In particular, specific heat data have shown a rather peculiar temperature dependence that the authors interpreted as two gap features. In addition, upper critical field measurements as a function of temperature shown a positive curvature near T_c that again was reported as a signature of multigap superconductivity. Our STM work discards this hypothesis and has allowed to distinguish between multiband and multigap superconductivity.

3.4 Growth and characterization of β-Bi_2Pd crystals

To grow β-Bi_2Pd we use the flux-growth method described in section 2.6.2 (Fig. 2.24) with a slight excess of Bi [99, 100]. According to the phase diagram, we grew the samples from high-purity Bi (Alfa Aesar 99.99%) and Pd (Alfa Aesar 99.95%). Bi and Pd were introduced in quartz ampoules and sealed at 140 mbar of He gas. Then, the ampoules were heated from room temperature to 900°C in 3 h, maintained 24 h at this temperature, slowly cooled down to 490°C in 96 h and finally cooled down to 395°C in 200 h. This temperature is about 15°C above the temperature for the formation of the α-Bi_2Pd phase (see Fig. 3.4) [130]. To avoid formation of the α phase, we quenched the crystals down to ambient temperature by immersion in cold water. We obtained large crystals of $5\times5\times3$ mm^3 similar to those ones shown in inset of Fig. 3.6(a)[1].

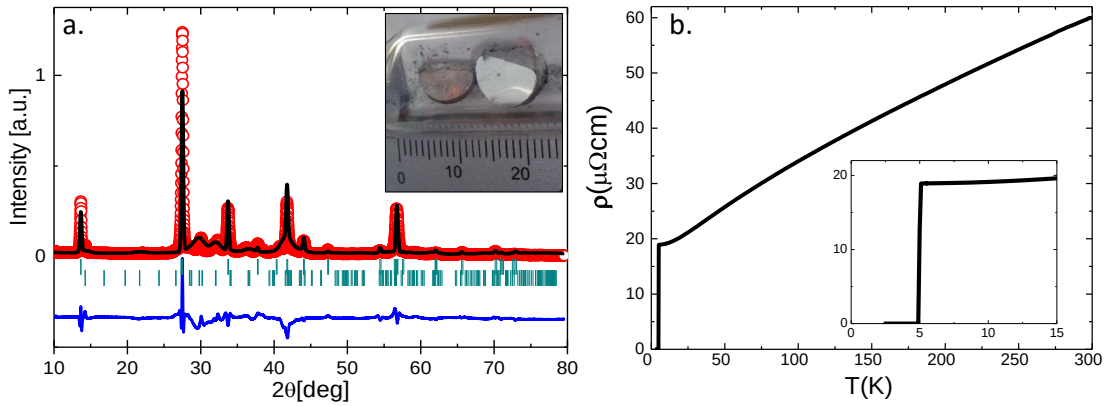

Figure 3.6 (a) Powder diffraction pattern of β-Bi_2Pd. Red symbols are the experimental points. The black line is the best fit to β-Bi_2Pd diffraction pattern [144]. Residuals are given by the blue line. The two series (upper and lower) of vertical green strikes represent, respectively, the position in 2θ scale of the reflections from the β-Bi_2Pd (*I4/mmm*) and α-Bi_2Pd (*C12/m1*) phases. Inset shows a photograph of twoβ-Bi_2Pd crystals, scale in mm. **(b)** Resistivity vs. Temperature of the crystal β-Bi_2Pd from 300 K to 2 K. The inset shows the sharp superconducting transition.

X-Ray Characterization

We made x-ray diffraction on β-Bi_2Pd crystals milled down to powder (Fig.3.6(a)), using x-rays with wavelength 1.54 $\AA$. We find β-Bi_2Pd (I4/*mmm*, see Ref. [132]) with refined lattice parameters $a = b = 3.36(8)\AA$ and $c = 12.97(2)\AA$ and no trace of α-Bi_2Pd. We made in total

[1]The growth of β-Bi_2Pd crystals was done in the Laboratorio de Preparación de Muestras at Laboratorio de Bajas Temperaturas, Departamento de Física de la Materia Condensada, Universidad Autónoma de Madrid.

twelve growths, varying slightly the conditions for the quench, growth temperature, and initial composition, and obtained always crystals with a resistivity versus temperature very similar to the one shown in the inset of figure 3.6(a).

Resistivity

The temperature dependence of the resistivity is shown in Figure 3.6(b). The superconducting transition in our sample occurs at 5 K. Previous resistivity measurements in this material reported a slightly higher value of T_c (around 0.3 K larger) and a residual resistivity three times smaller than the one found here [139]. From the residual resistivity of our samples ($\rho_0 = 18\mu cm$), we calculated the mean free path ℓ, using the Drude's formula $\rho_0 = \hbar(3\pi^2)^{1/3}/e^2n^{2/3}\ell$ [145, 146], where n is the density of carriers. We have assumed $n = 1.55 \times 10^{22} e/cm^3$ and found ℓ = 15.3 nm. As I will describe in the next sections, since the superconducting coherence length $\xi = 23$ nm is bigger than ℓ, β-Bi_2Pd lies in the regime of the dirty limit.

Upper critical field by Susceptibility and Resistivity

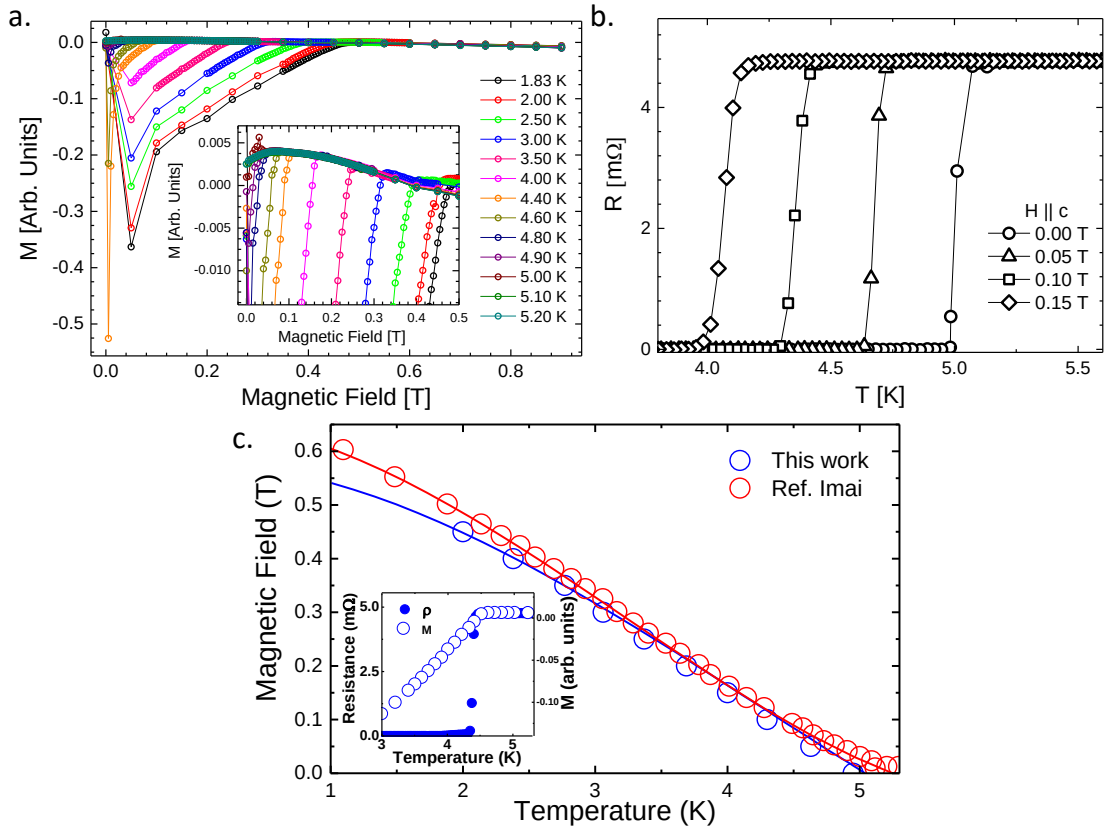

Figure 3.7 (a) Susceptibility vs. temperature of the crystal β-Bi_2Pd. The inset shows the sharp in the superconducting transitions. **(b)** Temperature dependence of the resistivity of a β-Bi_2Pd single crystal in a magnetic field parallel to the c-axis. **(c)** $H^c_{c2}(T)$ in our sample of β-Bi_2Pd with a residual resistivity of 18 $\mu\Omega$cm (open blue points) and $H^c_{c2}(T)$ in sample of Ref. Imai et.al., [139] with a residual resistivity of 5 $\mu\Omega$cm (open red points). Lines are fits to each $H^c_{c2}(T)$ using the parameters explained in the discussion section (Table 3.1). Note that the upper critical field remains nearly the same, although the mean free path varies by a factor of four. In the inset, we show the transition in resistance and susceptibility in our sample at a magnetic field of 0.1 T. The transitions remain sharp and well defined throughout the phase diagram.

The upper critical field parallel to the c-axis ($H^c_{c2}(T)$) was measured using susceptibility and resistivity as a function of temperature (Fig. 3.7 (a) and (b)). We compared results with available data in a sample with a larger mean free path [139] (Fig. 3.7 (c)). A smaller mean

free path leads to a shorter coherence length and hence to an increased $H^c_{c2}(T)$, also in multigap superconductors, see for instance MgB_2 [147, 148, 149, 150, 151]. Here, however, we do not observe such an increase in $H^c_{c2}(T)$ and instead we find slightly smaller $H^c_{c2}(T)$.

To explain our result, we have calculated $H^c_{c2}(T)$ using the same multiband approach of Refs. [36, 37, 121, 124]. We simplify the Fermi surface by using a two-band description, with differing Fermi velocities $v_{F,i}$, electron-phonon coupling λ_{ij} and electron scattering parameters $\tau_{i,j}$ (with subindices i,j for each band). We assume that the intraband and interband electron-phonon coupling constants λ_{ij} are connected together as $\lambda_{11} = \lambda_{11} = \lambda_{21} = 1$ and $\lambda_{22} = \lambda_{12} = 0.3$. The superconducting gap has then the same value in both bands. This agrees with our zero-field tunneling spectroscopy result as shown below (see Fig. 3.9(a)).

We assume that the conductivities of each band are equal $\rho_1 = \rho_2$ and we deduce the relaxation rate for each part of the Fermi surface using $\tau_i = \frac{\rho_i \gamma_i v_{Fi}^2}{V_{mol}}$. Where V_{mol} is the molar volume, $\gamma = 13mJ/K^2$ the Sommerfeld coefficient and ρ the resistivity. Moreover, $\lambda_{12}/\lambda_{21}$ is given by the ratio of the density of states in both bands. With γ we deduce γ_i from the choice of the λ_{ij} . We also assumed that the relaxation rate is isotropic and that each τ_i is split into intraband and interband scattering, parametrized by an additional coefficient, α_i, such that $\tau_{i,j} = \alpha_j \tau_i$, with $\alpha_1 + \alpha_2 = 1$.

Parameters for the calculation of H_{c2}(T)

Sample	v_{F1}	v_{F2}	$\gamma\,(mJ/K^2mol)$	ρ ($\mu\Omega$ cm)	T_c (K)	α_1	α_2
This work	0.09	0.38	13	18	5.07	0.2	0.8
Ref. Imai [139]	0.09	0.38	13	5	5.35	1	1

Table 3.1 Parameters used to calculate the temperature dependence of the upper critical fields $H_{c2||c}$ in samples used in this work and in samples of Ref.[139] (Fermi velocities are given in units of 10^6 m/s).

The introduction of interband scattering $\tau_{12} \neq 0$ is needed to decrease the sensitivity of $H_{c2}(T)$ to the mean free path ℓ and obtain similar values of $H_{c2}(T)$ when ℓ is decreased. In Table 3.1, we give the list of parameter values used to fit the two sets of data. We neglect interband defect scattering for the data of Ref. [139]. This provides an excellent fit to the $H_{c2}(T)$ data of Ref. [139] (Fig. 3.7(c)). If we simply decrease the mean free path to try to fit $H_{c2}(T)$ in our sample, we find an increase of the upper critical field. Only when allowing for interband scattering, with $\tau_{ij} \neq 0$ for $i, j \neq 0$, we find that $H_{c2}(T)$ does not increase when the mean free path is decreased. An intraband decrease of the mean free path invariably leads to a decreased coherence length and an increased upper critical field, but interband mixing can lead to similar values of the upper critical field. Introducing interband scattering, we obtain an excellent fit of our data, with an upper critical field that does not increase with decreased mean free path as shown by experiments (Fig. 3.7(c)).

Specific Heat

As it was described at the beginning of this chapter, the specific heat in multigap superconductors have shown remarkable deviations from the BCS predictions: the magnitude of the jump at T_c, a quick increase at low-T and a small shoulder in between. To check these features in β-Bi_2Pd, some of the samples synthesized at LBTUAM were analyzed by the group of Prof. P. Samuely at Centre of Low Temperature Physics in Kosice (Slovakia) and published in the Ref. [152].

They measured the temperature dependence of the specific heat using an ac technique [153, 154]. The specific heat transition of our samples is sharp, of about 30 mK width [152]. Figure 3.6 B depicts the specif heat of the sample at 0 T and 1 T while sweeping the temperature. The main panel shows total specific heat C/T of the sample. In the zero-field measurement a clear superconducting anomaly is observed close to 5 K, whereas in 1 T superconductivity is completely suppressed. Thus subtracting both measurements we obtain the electronic contribution to the specific heat. The resulting electronic specific heat (inset Fig. 3.3 B) was compared with the so-called α-model [155] based on the BCS theory (blue line in the inset). The fit reproduces very well the jump at the anomaly as well as the overall shape of the measured curve. It is obvious that in these data there is no sign of any additional hump or other manifestation of expected second energy gap.

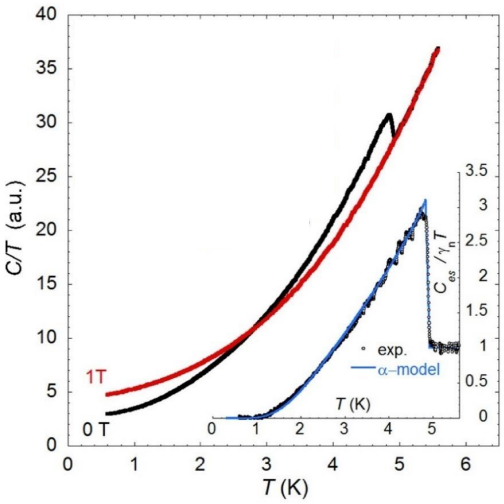

Figure 3.6 B Specific heat vs. temperature at 0T and 1T of one of the crystals β-Bi_2Pd grown at LB-TUAM. The inset shows the normalized electronic specific heat showing the sharp jump in the superconducting transition. The continuous blue line is the theoretical curve based on the BCS theory. The result was published in ref. [152].

3.5 STM/S on β-Bi_2Pd at zero magnetic field

Atomic Lattice of β-Bi_2Pd

We make the STM measurements in a sample roughly 1-mm thick, which was cleaved using a scotch tape at ambient conditions after gluing it using silver epoxy to the sample holder. We use an Au tip cleaned by repeated indentation on an Au sample as described in Ref. [156]. Usually, the bias voltage is kept at 10 mV or below, and the tunneling conductance is of a few tenths of microsiemens.

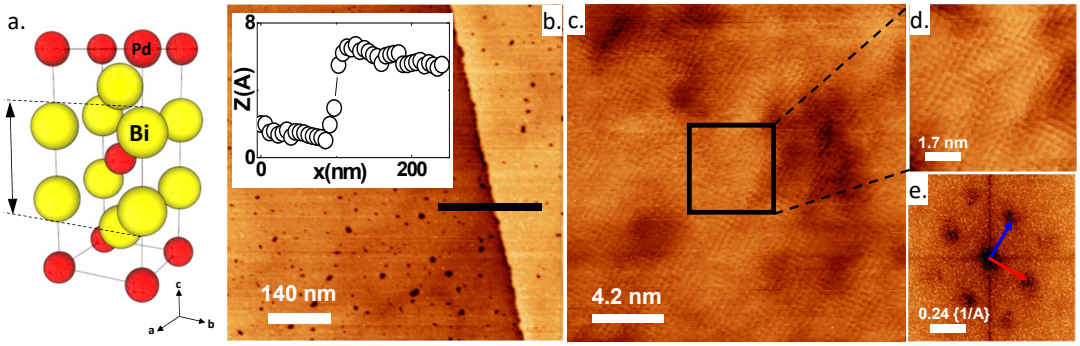

Figure 3.8 Surfaces of β-Bi_2Pd at different length scales. Images are taken at a bias voltage of 10 mV and conductance 0.1 μS at 0.15 K. **(a)** Lattice structure, highlighting the cleaving plane with distance between two successive planes $d = 6.5\mathring{A}$ as shown in **(b)**. The inset in **(b)** shows a cut through a line with a step edge whose size corresponds to the distance between cleaving planes. The corresponding distance is shown by an arrow in **(a)**. **(c)** and **(d)** show images with atomic resolution, giving the square atomic Bi lattice. In **(e)** is shown the Fourier transform of **(c)**. Blue and red arrows give crystalline axis.

Figure 3.8(b) shows a $0.7 \times 0.7\ \mu m^2$ topography image at 0.15 K, where a small step edge is clear. The step edge (inset) is of 6.5 $\mathring{A}$ height, which corresponds to the distance between adjacent Bi-Pd groups (black arrow in Fig. 3.8(a)). In Fig. 3.8(c,d), we show atomic resolution topography images taken on the surface of the sample at 0.15 K. We find indeed a square atomic

lattice. The Fourier transform of the topography images (Fig. 3.8(e)), gives a lattice parameters of $a = b = 3.3\mathring{A}$. Thus we conclude that the surfaces in Fig. 3.8 are made out of the square Bi lattice.

Density of States and Superconducting Gap in β-Bi_2Pd

From the tunneling conductance curves at low temperature, the single-gap character of β-Bi_2Pd emerges. Figure 3.9 shows the tunneling conductance versus bias voltage as a function of temperature. At 0.15 K, (Fig. 3.9(a)) we find clear superconducting quasiparticle peaks and no conductance at zero and low bias. We can fit our data using single-gap BCS theory and $\Delta = 0.76$ meV (Fig. 3.9(b)). We need to add small additional broadening, with a Gaussian distribution of width 30 μeV. The temperature dependence of the tunneling density of states can be fitted just by varying Δ with temperature and shows that superconductivity disappears at about 5K and that the obtained Δ(T) follows well the single-gap BCS theory (Fig. 3.9(c)).

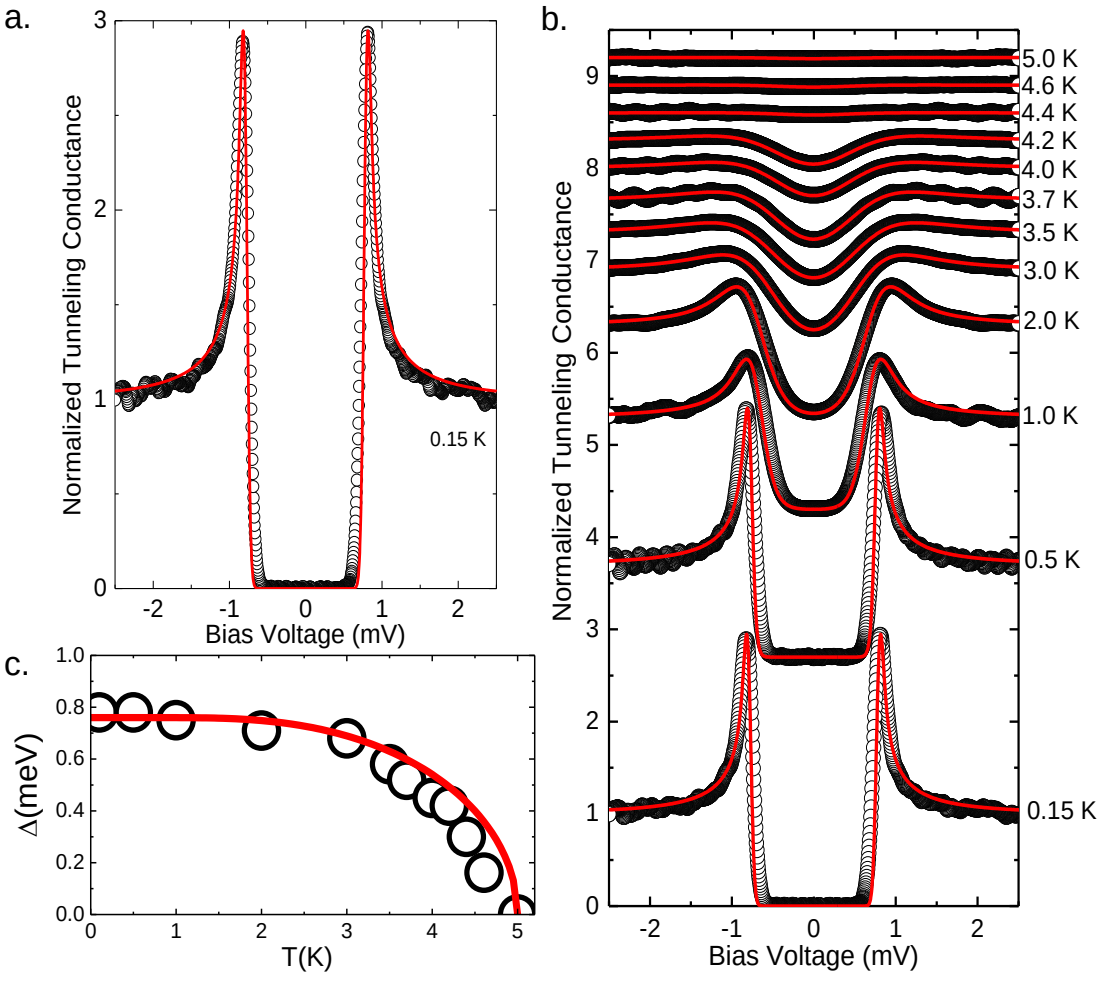

Figure 3.9 **(a)** Normalized experimental tunneling conductance β-Bi_2Pd (black dots) at 150 mK. Red lines are the fits to *s*-wave BCS expression. The well defined quasiparticle peaks ($|\Delta|$ = 0.76 meV) and the absence of shoulders, kinks or additional peaks at other energies (see Fig.3.1), reveal that one-gap scenario to describe the evolution of the DOS in βBi-$_2$Pd. **(b)** Temperature dependence of the experimental conductance of β-Bi_2Pd (black dots) and fits to s-wave BCS expression (red curves). **(c)** Evolution of the superconducting gap versus temperature. Red line is the fit to the BCS theory with $2\Delta = 3.52 k_B T_c$

3.6 STM/S on β-Bi_2Pd under magnetic fields

As I described in the Chapter 2, if we study a superconducting sample with a normal tip metal at low temperatures, the conductance curve $\sigma(V)$ reflects the superconducting density of states of the sample. Thus, the vortex lattice can be obtained by the spatial variation of the $\sigma(V)$ through the vortex core. We have started the analysis of the vortex lattice in β-Bi_2Pd applying magnetic fields parallel to the *c-axis*. Figure 3.10 shows vortex lattice images from 5 to 500 mT. A hexagonal Abrikosov lattice is observed in all images. The intervortex distance is modified as expected for the hexagonal vortex lattice $d_\Delta = 1.075\sqrt{\frac{\Phi_o}{B}}$ (with Φ_0 being the flux quantum) [15].

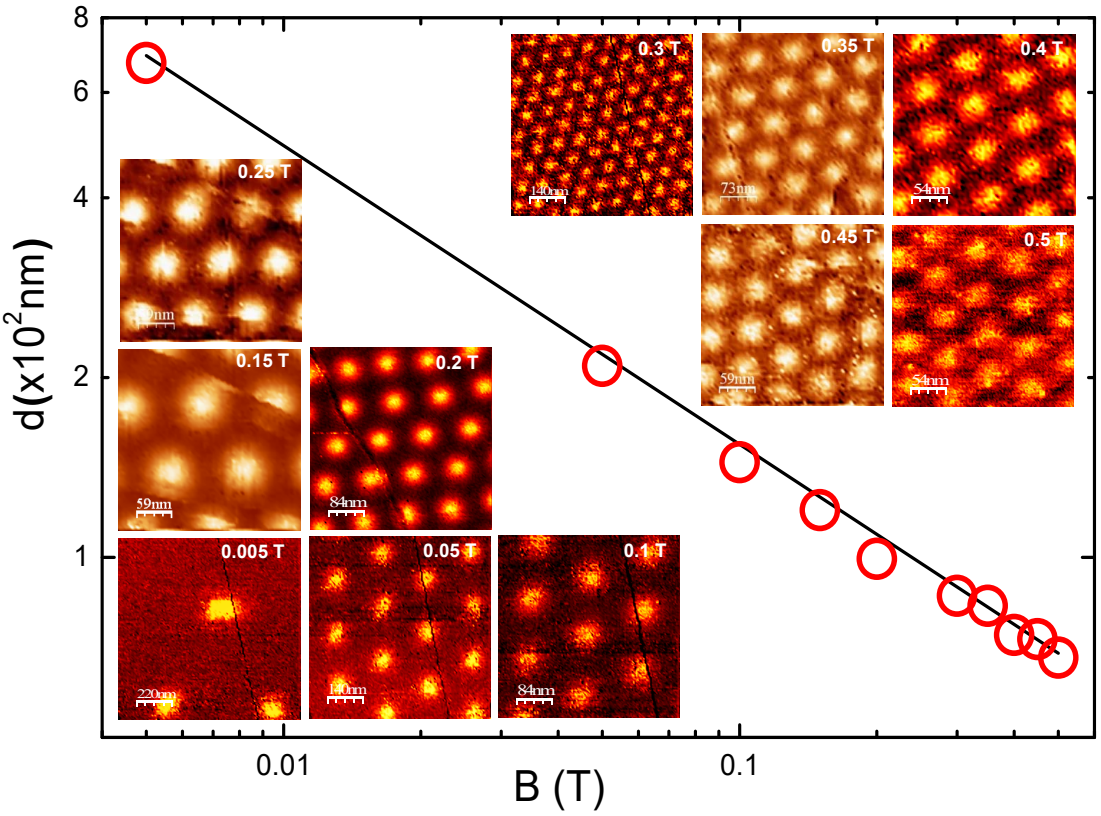

Figure 3.10 Intervortex distance obtained from the zero bias conductance maps in β-Bi_2Pd at 150 mK and magnetic fields parallel to the *c-axis* (red circles). The continuous line is the expected intervortex distance for hexagonal lattice $d_\Delta = 1.075\sqrt{\frac{\Phi_o}{B}}$ (with Φ_0 being the flux quantum).

Vortex Lattice Orientation

From Figure 3.10 we found no relation between the orientation of the vortex lattice with step edges or other defects in the sample. Instead, we find that the orientation of the vortex lattice is determined by the underlying crystalline lattice (blue and red arrows in Fig. 3.11). One of the three main vortex lattice directions is always parallel to one of the two crystalline axes. This gives two equivalent orientations for the hexagonal vortex lattice at any magnetic field.

Figure 3.12 (right panel) shows that we can find two orientations of the vortex lattice in different locations of the sample at a fixed magnetic field. They are observed in different scanning windows separated by several tens of microns. This shows that the typical domain size is of a few microns. Thus the hexagonal vortex lattice is broken up into two domains each with one main axis of the vortex lattice oriented along one crystal axis. The spatial distribution of domains is random and most likely determined by the pinning landscape. Figure 3.12 *(left panel)* shows

a schematic representation of the interaction between a square crystal lattice and a hexagonal vortex lattice. As a result, two equivalent orientations of the vortex lattice are determined by the symmetry of the crystal. Our results in β-Bi_2Pd, show that this dichotomy is not affected by the magnitude of the magnetic field (Fig. 3.12 *(right panel)*).

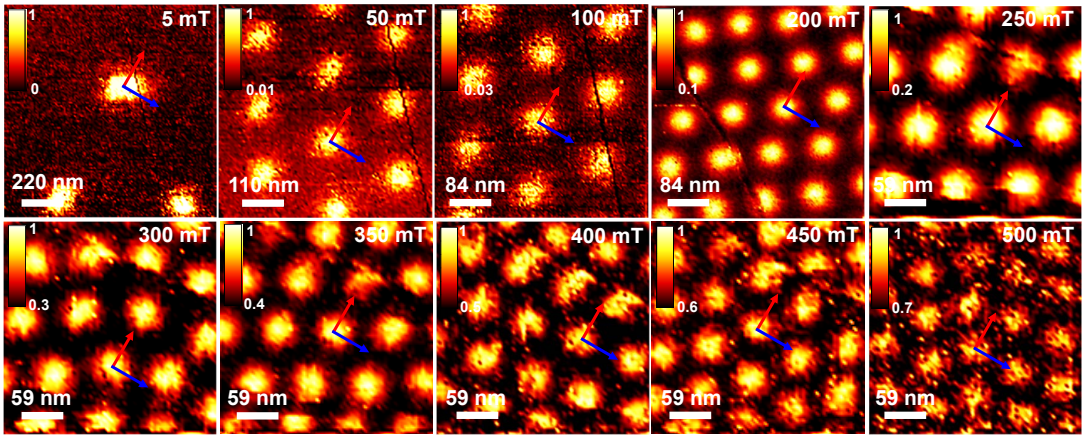

Figure 3.11 The vortex lattice as a function of the magnetic field applied parallel to the *c-axis* in β-Bi_2Pd. The vortex lattice has a hexagonal symmetry for all values of the magnetic field. The images were taken at 150 mK and the magnetic field was increased up to H_{c2} = 0.6 T. Contrast in the zero-bias conductance is shown by the color scale. The crystalline orientation is shown as red and blue arrows in each panel.

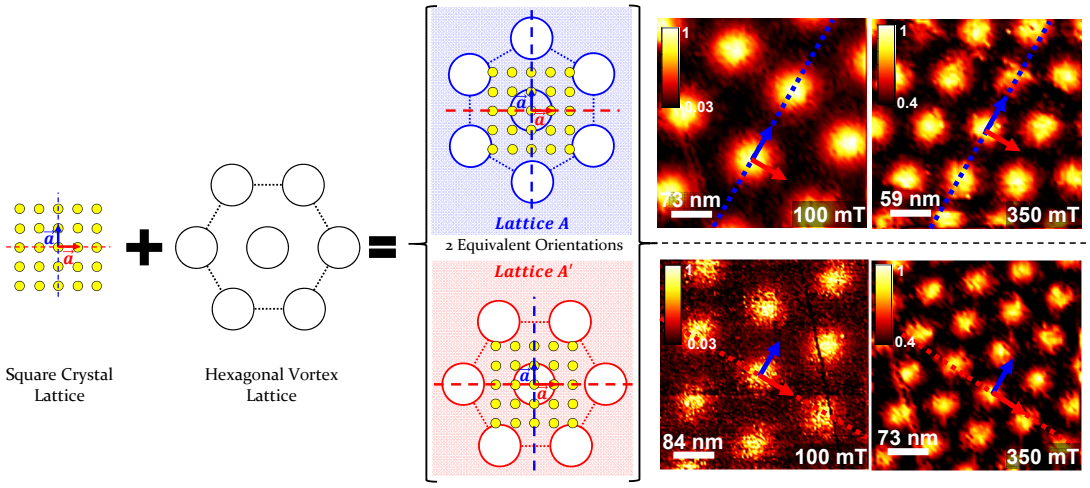

Figure 3.12 *(Left panel)* Schematic representation of how the atomic lattice (yellow circles) influences the vortex lattice orientation (gray circles). The square crystalline symmetry (red and blue arrows) determines two equivalent orientations of the vortex lattice: *Lattice A* or *Lattice A'*. Therefore, one of the main axis of the vortex lattice is always parallel to one of the crystalline directions. *(Right panel)* Vortex lattice at two different magnetic fields at 150 mK. In each magnetic field, we show two vortex images obtained at different scanning windows. Note the change in the orientation with respect to the atomic lattice, as marked by red and blue arrows. Contrast (zero-bias conductance) is shown with the color scales.

The relationship between the symmetry and orientation of the vortex lattice with respect to the crystal lattice has been discussed in detail before. In 2H-$NbSe_2$, the vortex lattice is oriented parallel to the hexagonal crystal lattice [42, 40]. In the nonmagnetic nickel borocarbide $LuNi_2B_2C$, when the magnetic field is applied along the c axis of the tetragonal crystal structure, the vortex lattice is square at high fields, with a side along or in between the axis of the in-plane crystalline directions. The low-field hexagonal vortex phase preserves this orientation,

showing two hexagonal domains, oriented along one of the two in-plane crystalline directions [157, 158, 159, 160, 161]. The interaction between crystal and vortex lattices is mediated by nonlocal effects, which introduce terms in the vortex-vortex interaction whose in-plane behavior depends on the shape of the Fermi surface [157, 158, 159, 160, 161, 162, 163].

In β-Bi_2Pd, the vortex lattice is hexagonal and oriented along the in-plane directions of the square crystal lattice [100] and [010]. This shows that the anisotropy of the Fermi surface and of the vortex-vortex interaction is also oriented along the same directions. Thus the anisotropy of the in-plane electronic properties, with the square fold Fermi surface, influences the vortex lattice orientation in β-Bi_2Pd.

Magnetic Field dependence of Intervortex Density of States.

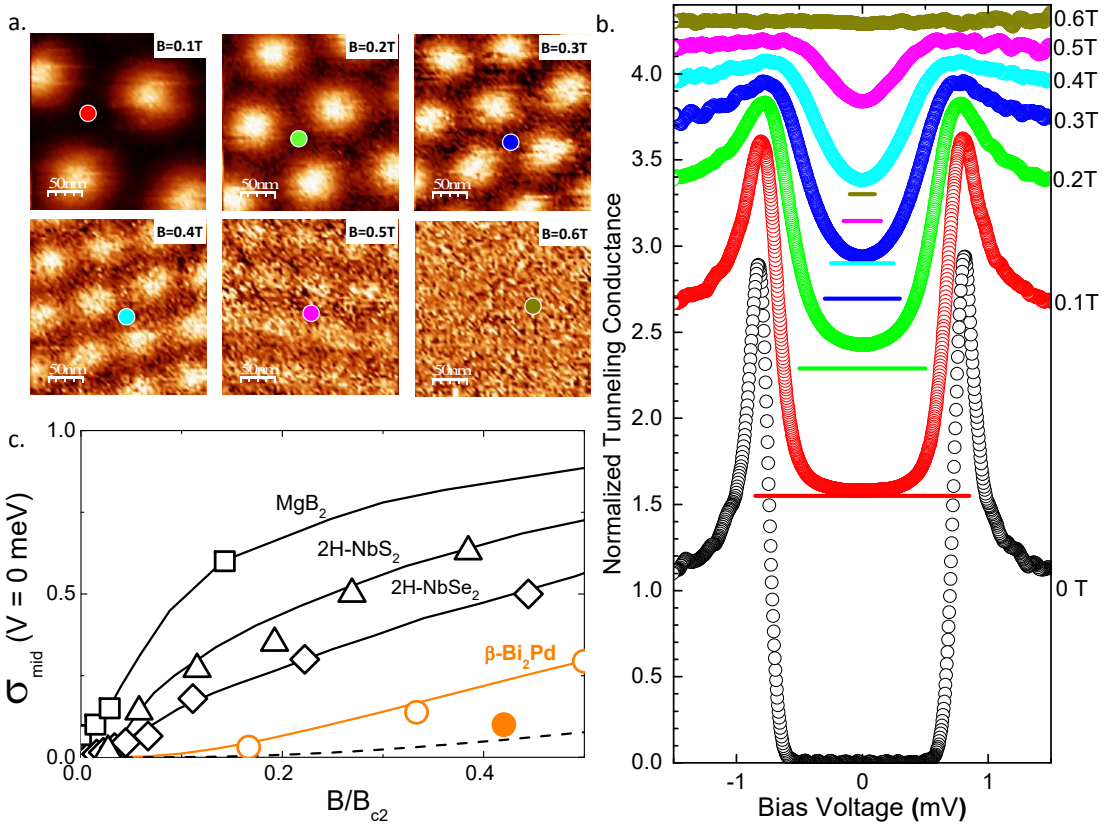

Figure 3.13 a. The vortex lattice as a function of the magnetic field applied parallel to the *c-axis* at 0.15 K in β-Bi_2Pd from 0.1 T to $H_{c2}^{c} = 0.6T$. **b.** Magnetic field dependence of the full normalized tunneling conductance $\sigma_{mid}(V)$ obtained at the center point between vortex cores of images shown in **a.**. Curves are shifted vertically for clarity. Horizontal lines provide the zero conductance value for each magnetic field. In **c.**. we show the magnetic field dependence of the zero-bias tunneling conductance σ_{mid} exactly in-between vortices (line is a guide to the eye) when the field is applied along the c axis (open orange points) and when the field is applied along the plane (filled orange point). Data from 2H-$NbSe_2$ (diamonds), 2H-NbS_2 (triangles) and MgB_2 (squares) (lines are guides to the eye) are from [164, 157, 112, 42].

To analyze the magnetic field dependence of the density of states on the mixed state in β-Bi_2Pd we varied the magnetic fields parallel to the *c-axis* from 0T until the value where the superconducting signal disappears i.e., to the upper critical field H_{c2}. Figure 3.13(a) shows how increasing the magnetic field, the number of vortices increases until the overlapping between cores suppresses the superconducting features. On each conductance map, we look for the point where the tunneling conductance has the minimum value at zero bias voltage. To establish this point, we measure the vortex lattice on different zones of the sample at the same magnetic field.

From the images we check at each pixel the IV curve and choose the curves where the tunneling conductance has the minimum value at zero bias voltage. In all cases this pixel coincides with the geometrical center in between three vortices. From these measurements we obtain the tunneling conductance exactly between three vortices (colored circles on the spectroscopy maps Fig. 3.13 (a)). The curves are shown in Fig. 3.13 (b). We found an upper critical magnetic field of $H_{c2} = 0.6$ T which coincides with the value reported previously by susceptibility and resistivity measurements (See Fig. 3.7). Using the Ginzburg-Landau relation ($H_{c2}(T = 0\ K) = \frac{\Phi_0}{2\pi\xi^2}$) the coherence length is ξ = 23 nm. As I reported already in previous sections, the coherence length $\xi = 23$ nm is bigger than ℓ, thus β-Bi_2Pd lies in the regime of the dirty limit.

To characterize with more detail the mixed state, we compare the evolution of the zero-bias tunneling conductance exactly between three vortices σ_{mid} with the dependence obtained in other well known superconductors (Fig. 3.13 (c)). We found that the increment of σ_{mid} is smaller than the increase found in 2H-$NbSe_2$, 2H-NbS_2 and MgB_2 but larger than the increase expected for a single-gap s-wave superconductor (dark dashed line in Fig. 3.13(c)).

To analyze the strongest increase in vortex core overlap in β-Bi_2Pd, we compare in Table 3.2 its superconducting gap and the Fermi velocities values with those in superconductors that show pronounced multigap behavior, MgB_2, 2H-$NbSe_2$, and 2H-NbS_2 (see Fig. 3.13(c)). MgB_2 is the compound where the two gaps are more separated in energy, being the larger gap (Δ_1) a factor of three higher than the smaller gap (Δ_2) [46]. In 2H-NbS_2, the ratio between the two gaps is around two [112]. The same gap ratio is found in 2H-$NbSe_2$, although in this material there is a sizable in-plane gap anisotropy with a wide distribution of gap values [42, 165, 156, 166]. The vortex core overlap is smaller in 2H-$NbSe_2$ than in 2H-NbS_2 (Fig. 3.13(c)). The anisotropy in the Fermi velocity is of the same order in 2H-$NbSe_2$ and 2H-NbS_2 than in MgB_2 [36, 37, 112, 124, 164, 157, 167]. Yet, the vortex core overlap is the highest in 2H-NbS_2, which has also more pronounced multigap properties.

	FS parameters from H_{c2}(T)		Δ (meV)	
Compound	v_{F1} (10^6 m/s)	v_{F2} (10^6 m/s)	Δ_1	Δ_2
MgB_2	0.29	0.9	7.1	2.2
2H-NbS_2	0.155	3.1	0.97	0.53
2H-$NbSe_2$	0.055	1	1.2	0.75
β-Bi_2Pd	0.09	0.4	0.75	0.75

Table 3.2 Fermi velocities and superconducting gaps in multiband superconductors and the samples β-Bi_2Pd of this work. Data from [36, 37, 46, 112, 42, 157, 164, 124].

The strongest increase in vortex core overlap is thus produced by multiband superconductivity. In β-Bi_2Pd, the vortex core overlap is closest to a single isotropic superconducting gap, yet it lies sensibly above expectations. Thus the highly anisotropic Fermi surface (Figs. 3.5(b,c)) produces a small but sizable effect on the intervortex electronic density of states. As I previously described, β-Bi_2Pd has a Fermi surface with two nearly cylindrical sheets and two 3D sheets, derived from Pd-4d and Bi-6p states [140, 141]. Thus, states from both Pd and Bi contribute to the density of states at the Fermi level, and in particular anisotropic $4d_{xy+yz}$ orbitals. We should note that the tunneling spectroscopy data at the surface is often mostly influenced by the quasi-2D nature of a large part of their Fermi surface, possible favoring contribution for the in-plane states. However, the strong anisotropy of $4d_{xy+yz}$ orbitals most likely favors interband scattering. This suggests that the interband scattering provides tunneling spectroscopy results in β-Bi_2Pd giving information about large parts of the Fermi surface, although this requires confirmation by detailed calculations of the tunneling conductance at the surface.

The influence of multiband effects on the mixed phase properties of β-Bi_2Pd also explains

the lack of increase of H_{c2} with the mean free path shown in Fig. 3.13(c). In β-Bi$_2$Pd, T_c is practically not modified by scattering and the gap is already nearly isotropic (see Fig. 3.9(a)), but $H_{c2}(T)$ behavior shows the influence of multiband Fermi surface properties and interband scattering.

The spatial dependence of the superconducting density of states in and around vortices shows that the gap fully closes inside the vortex core (Fig.3.14 (a)). We do not observe signatures of Caroli-de Gennes-Matricon Andreev core states [42, 40, 41]. On the other hand, the in-plane coherence length from the upper critical field $H_{c2}(T = 0\ K) = \frac{\Phi_0}{2\pi\xi^2}$ yields $\xi = 23$ nm. The mean free path in our samples is $\ell = 15.3$ nm. Thus $\ell < \xi$ and Caroli-de Gennes-Matricon states are smeared by defect scattering [146].

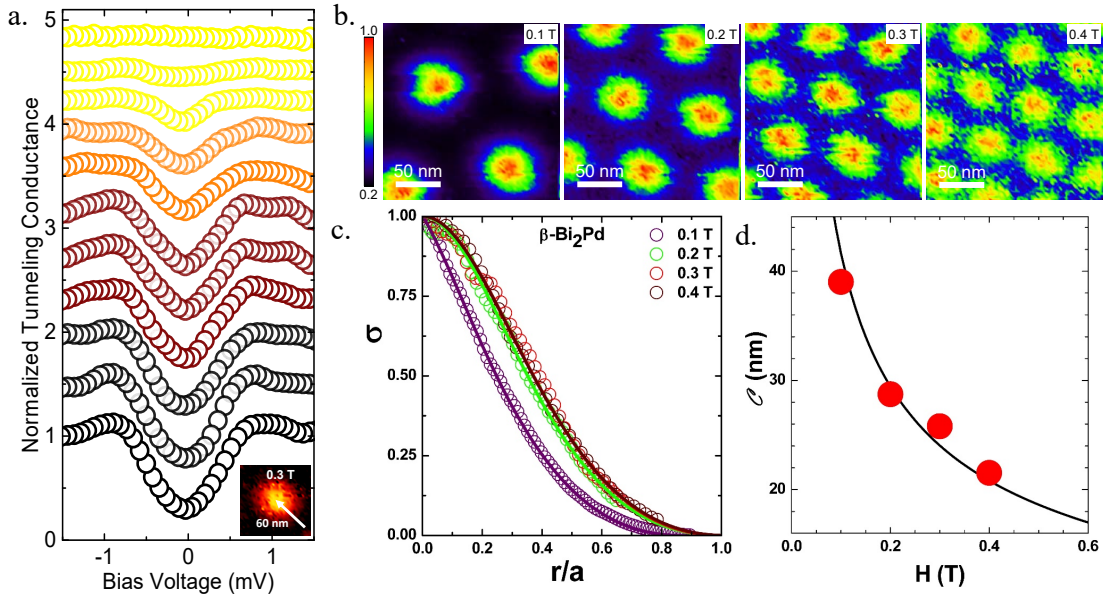

Figure 3.14 (a) The tunneling conductance vs. bias voltage when entering a vortex core at 0.3 T along the path shown by the white arrow in the inset (one curve each 6 nm approximately). **(b)** Vortex lattice images at different magnetic fields parallel to c-axis at 150mK in β-Bi$_2$Pd. **(c)** Tunneling conductance σ of Eq. 3.2 vs distance r from the vortex center, normalized to the cell radius a. Data have been obtained from images of vortices of **(b)**, averaged over the angle for each r and normalized as described in the text. **d.** The core size $\mathscr{C}$ of Eq.3.3 vs H. Dots are the values of $\mathscr{C} = \eta a$ obtained from the fits of the curves shown in **(c)**. The line is $\mathscr{C}$ calculated with $\eta \approx 0.5$ found in the fits.

We further studied the spatial distribution of the density of states (DOS) at zero bias $N(r)$ in the mixed state at magnetic fields parallel to the c-axis. Fig. 3.14(b) shows the vortex lattices analyzed. To obtain tunneling conductance versus distance from the vortex center, we select single vortices out of zero-bias conductance images and evaluate angular averages of the normalized conductance σ_0 for each r. We define σ as:

$$\sigma = \frac{\sigma_0(r) - \sigma_0(r^*)}{\sigma_0(0) - \sigma_0(r^*)} \tag{3.1}$$

where r^* is the distance from the vortex center to the point where the tunneling conductance is minimum (in the hexagonal lattice, the center of an equilateral triangle). The magnetic field dependence of the conductance profiles σ as a function of the distance r (Fig. 3.14(b)) have been fitted to a single gap analytic model described by Ref. [168].

$$\sigma = 1 - \frac{\rho^2(1+\eta^2)}{\rho^2+\eta^2} exp \frac{\eta^2(1-\rho^2)}{1+\eta^2} \tag{3.2}$$

where $\rho = r/a$ and $\eta = \mathscr{C}/a$; a is the radius of a circle unit cell within the Wigner-Seitz approximation of the hexagonal vortex lattice, such that $\pi a^2 = \phi_0/H$, H is the magnetic field and $\mathscr{C}$ is the vortex core size.

Figure 3.14(c) shows the field dependence of the extracted core size $\mathscr{C}$ treating η as a fit parameter. The fits yield values of η around 0.50 in a field range where H changes by a factor of 4. Since $\eta \approx$ const, we have

$$\mathscr{C} = \eta a = \eta \sqrt{\frac{\phi_0}{\pi H}} \tag{3.3}$$

Hence, the core size $\mathscr{C}$ varies with applied field as $1/\sqrt{H}$, the dependence deduced from the muon spin rotation (μSR) data on many materials [169]. This is highlighted by the red points in Fig. 3.14(d).

The theory of Ref. [167] suggests that in large fields the coherence length as a function of field should behave as $\xi \approx A/\sqrt{H}$. In particular, this relation should hold at the upper critical field H_{c2}. This gives the constant $A = \sqrt{\phi_0/2\pi}$ so that we have

$$\xi = \sqrt{\frac{\phi_0}{2\pi H}} \equiv \xi_H. \tag{3.4}$$

The core size, therefore, is

$$\mathscr{C} = \eta a = \eta \sqrt{\frac{\phi_0}{\pi H}} = \eta \sqrt{2} \xi_H \tag{3.5}$$

Using $\eta \approx 0.5$ obtained by the fits, we find $\mathscr{C} \approx 0.7\xi_H$. Equation 3.5 implies that the order parameter and density of states distributions within vortex lattice in large fields of single band materials are governed by a *universal length* ξ_H of Eq.3.4. As $H \to H_{c2}$, ξ_H reaches the value of the standard coherence length $\xi_{c2} = \sqrt{\phi_0/2\pi H_{c2}}$. Therefore our experimental results can be reproduced by the theory proposed by Ref. [168].

This result has been compared with the multigap superconductors 2H-$NbSe_{1.8}S_{0.2}$ and 2H-NbS_2 in Ref. [168]. Whereas in multigap cases $\mathscr{C}$ remains H independent and can be analyzed using a two gap model, in β-Bi_2Pd the $1/\sqrt{H}$ core dependence, follows the predicted behavior for a single gap superconductor proposed by Kogan et. al. [167]. This evidence reinforces our first spectroscopy data about β-Bi_2Pd as a sigle gap superconductor.

3.7 Concluding Remarks

We have synthesized and characterized at local scale and low temperatures (0.15 K) single crystalline samples of the superconductor β-Bi_2Pd.

We have observed a single superconducting gap from the zero-field tunneling conductance and found that the hexagonal vortex lattice is locked to the square atomic lattice as expected in crystalline superconductors with anisotropic Fermi surfaces.

By discussing tunneling spectroscopy, $H_{c2}(T)$, vortex lattice and vortex profiles we have shown that β-Bi_2Pd is a multiband superconductor with a single superconducting gap. We have observed that the shape of the superconducting vortices in the compound Beta-Bi2Pd does not match with the single superconducting gap we measure at zero field. We have found that this is due to the multiband properties of the Fermi surface of Beta-Bi2Pd. Previous results have associated multiple bands with multiple superconducting gaps, almost invariably. Our data in β-Bi_2Pd show that this view is not fully correct. Only weakly connected bands allow for multigap superconductivity. We conclude that the mixed phase of superconductors is strongly modified in multiband Fermi surface materials, even when the zero-field superconducting tunneling conductance is not.

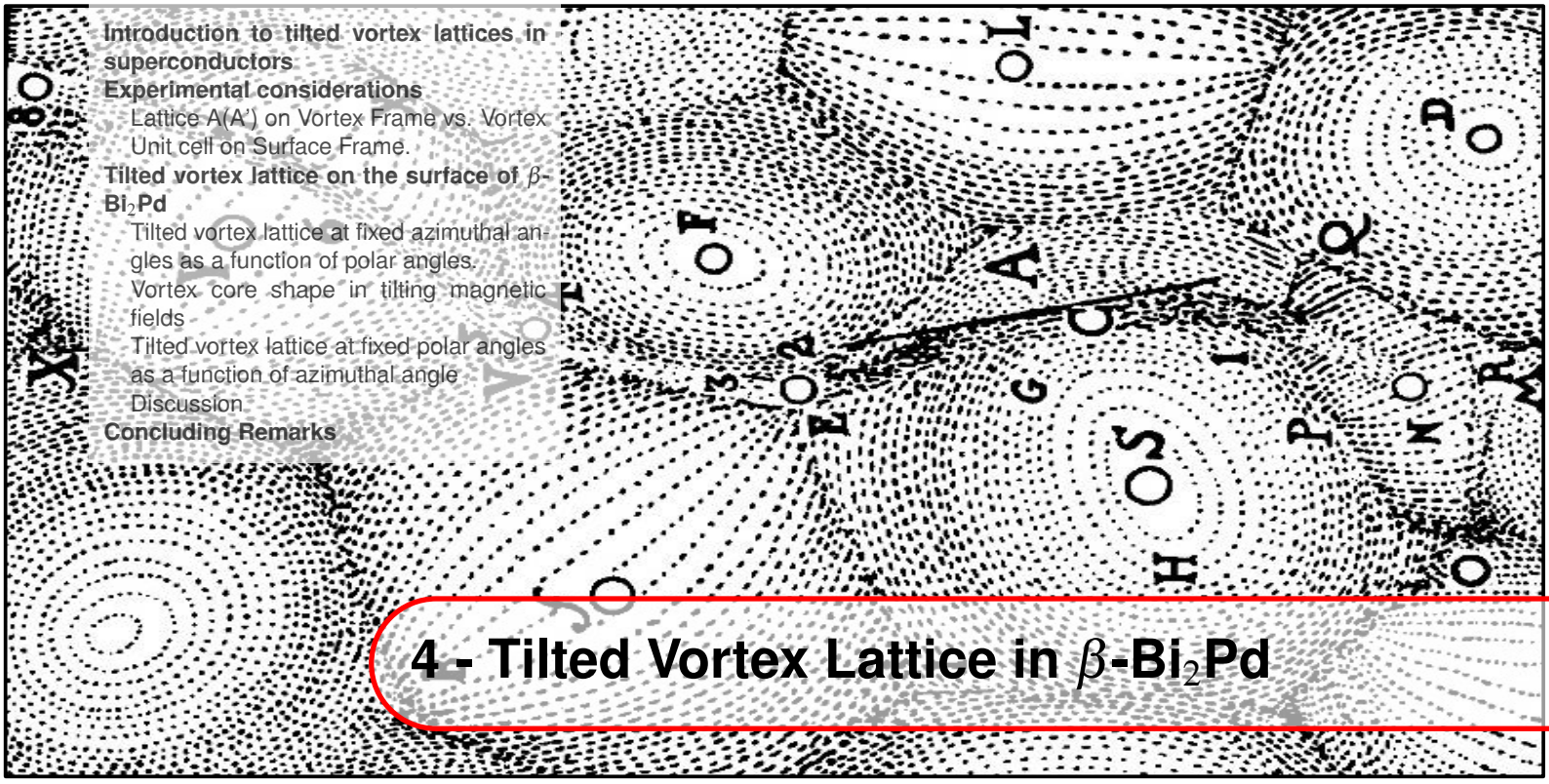

4 - Tilted Vortex Lattice in β-Bi_2Pd

Top image: "Celestial vortices".
René Descartes, The World, (1633)

"The celestial matter in which the Earth is embedded moves faster at one side of the planet than at the other, and this gives the Earth a "spin" or rotation, which in turn sets up a centrifugal effect, creating a small vortex around itself, in which the Moon is carried... The universe, as Descartes represents it, consists then of an indefinite number of contiguous vortices, each with a sun or star at the center and planets revolving around this center..."[170]

Type-II superconductors are characterized by the presence of quantized vortices. Vortices are flux tubes oriented parallel to the magnetic field direction each carrying a flux quantum. In anisotropic superconductors, the vortex lattice changes its properties as a function of the magnetic field orientation with respect to the main high symmetry directions. This produces vortex lattices whose symmetry and orientation are not well understood.

Here we have measured the tilted vortex lattice in the isotropic superconductor β-Bi_2Pd using Scanning Tunneling Microscopy.

This chapter is organized in the following manner. Section 1 presents a brief introduction to the tilted vortex lattice and its relation with crystal anisotropies. In section 2 we introduce the method used to analyze our experimental results. Section 3 begins with a description of the procedures followed to acquire the spectroscopy maps and then focuses on the results at different orientations of the magnetic field. We observe for the first time that vortices bend when reaching the surfce. We also show that non-local effect influence the behavior of the tilted vortex lattice for low tilt angles. We find that the symmetry and orientation of the tilted vortex lattice within the bulk is influenced by a new contribution to the intervortex repulsion at the surface that has not been considered so far.

4.1 Introduction to tilted vortex lattices in superconductors

As it was described in the first chapter, type-II superconductors allow a partial penetration of magnetic fields by introducing flux-quantized lines. These flux lines penetrate the sample as periodic arrangements, *i. e.*, vortex lattice [15]. The structure and organization of superconducting vortex lattice reveals unequivocally the crystalline anisotropy of the host material. As a consequence, equilibrium properties of the vortex lattice, under tilted magnetic fields are determined by bulk properties. Figure 4.0 shows schematically the expected behavior of the tilted vortex lattice in isotropic and anisotropic layered superconductors. In isotropic superconductors, the repulsion between vortices leads to a hexagonal vortex lattice which is independent of tilt angle (Fig. 4.0 (a-b)). The situation is rather different in extremely anisotropic superconductors where a rich variety of vortex structures have been proposed and observed for the magnetic field tilted with respect to the *c*-axis [171, 172, 173] (Fig 4.0 (c-f)). These superconductors have a layered crystalline structure where the interlayer distance is of the same order or above the out of plane (*c*-axis) coherence length. When the field is perpendicular to the planes, vortices are uncoupled along the *c*-axis, giving rise to the so-called pancake vortices. When rotating the magnetic field to be parallel to the planes, Josephson vortices appear. These are different from the conventional Abrikosov vortices. Abrikosov vortices are located in the superconducting condensate and are characterized by having normal cores, where the superconducting density of states disappears at the scale of the coherence length. Instead, Josephson vortices do not have a core. Supercurrents circulate around its vortex center which is situated inside a Josephson barrier. Intermediate situations appear when the magnetic field orientation is in between the planes and the *c*-axis forming crossing lattices where the interference between both lattices may even produces small displacements of the pancake vortices (Fig 4.0 (e)). For certain values of tilting, the Josephson vortices arrange vertically intercepted by unidimensional chains of pancake vortices forming 1D vortex chains (Fig 4.0 (f)).

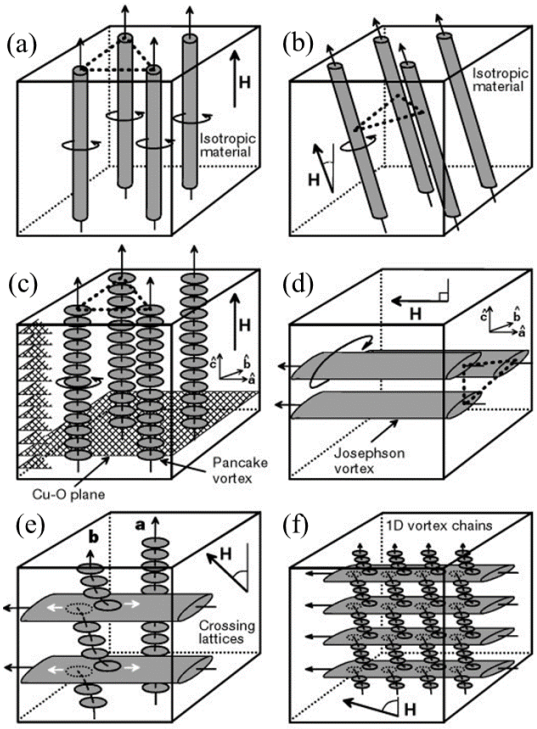

Figure 4.0 Schematic comparison of vortex lattice in isotropic and anisotropic layered superconductors. *(Top panel)* **(a)** and **(b)** show an isotropic superconductor for perpendicular and tilted fields *(Top panel)***(c-f)** Vortex lattice in a very anisotropic superconductor showing pancake vortices under perpendicular field), Josephson vortices for in-plane field, and crossing vortex lattices and 1D vortex chains for intermediate orientations [171].

Tilted vortex lattices have been studied in anisotropic type II superconductors using STM [174, 175], Bitter decoration [176], scanning Hall probe microscopy [171] and neutron scattering [177, 178]. The early experimental work was focused on the superconductor 2H-$NbSe_2$ [174, 175] followed by other layered compound, such as $Bi_2Sr_2CaCu_2O_\delta$ that reported the rich variety of vortex structures discussed above[172, 173].

In the moderate anisotropic superconductor 2H-$NbSe_2$ the tilted vortex lattice has been studied by either neutron scattering experiment[177] and direct observation through STM [174]. Neutron scattering experiments show that when tilting the field from parallel to the c-axis to an in-plane direction, the hexagonal vortex lattice distorts forming an elongated hexagon[177]. This observation was in agreement with the Ginzburg-Landau theory for anisotropic superconductor

which predicts that the distortion is given by the anisotropy of the upper critical field and the effective mass ratio [179]. The same result was reproduced by STM experiments where, however, several deviations with respect to the expected behavior at very large tilting angles, such as chain-like and distorted lattice patterns, were observed[174, 175].

Other results were obtained, for instance, in superconducting Nb through neutron scattering experiments[180]. In the form of high purity single crystals, it is nearly a type I material showing a Shubnikov phase above about hundreds gauss. The bulk vortex lattice shows a variety of transitions, including two-fold structures breaking the crystalline four-fold rotation symmetry and scalene unit cells. The observed behavior is attributed to non-local contributions to the vortex interaction and the influence of the strongly band dependent and anisotropic Fermi surface of Nb.

More recently, new work on the tilted vortex lattice in 2H-$NbSe_2$ was performed in the Laboratorio de Bajas Temperaturas to study the shape and the internal electronic structure of the tilted vortex cores in this material [181]. The STM data have been compared to a microscopic model for the tilted vortex which shows that surface screening currents lead to an important modification of the shape of tilted vortex core. Also, rotating magnetic fields may induced structural changes in the vortex lattice in both isotropic and anisotropic superconductors.

All this work has left a very simple question opened: does the tilted vortex lattice of an isotropic superconductor behave as expected and schematically shown in Fig 4.0 (b)?

This was our main motivation to initiate this work. In this thesis, we have performed a detailed study of the tilted vortex lattice in the isotropic superconductor β-Bi_2Pd. We have found that the orientation of the tilted vortex lattice can be modified by non local effects and a new contribution to the intervortex interaction at the surface that was not previously considered.

4.2 Experimental considerations

Before presenting our experimental results, it is convenient to discuss how the tilted vortex lattice can be studied at the surface using STM. Also, I will present the different configurations that are expected when tilting the vortex lattice of β-Bi_2Pd.

Vortex frame vs. surface frame

We need two reference frames to analyze the tilted vortex lattice at the surface with respect to the crystalline structure and the direction of the applied magnetic field [175]. In figure 4.1 we define vortex lattice and surface lattice frames as well as the angles and directions used in the analysis of the experimental data. The vortex frame (yellow) gives the vortex lattice at a plane perpendicular to the applied magnetic field. The surface frame (gray) provides the projection of the vortex lattice to the surface. This gives elongated hexagons at the surface that we describe using vectors $\vec{d}_1$ and $\vec{d}_2$ with

$$\vec{d}_1 = \frac{d_0}{\cos\theta}\hat{i} \tag{4.1}$$

$$\vec{d}_2 = \frac{d_0}{2}\left(\sqrt{3}\hat{i} + \frac{1}{\cos\theta}\hat{j}\right) \tag{4.2}$$

where d_0 is the intervortex distance in the vortex frame.

The polar angle and azimuthal angles are θ and φ respectively. In this work, as the material is nearly isotropic, we can take as a starting hypothesis that the bulk vortex lattice remains hexagonal at all tilts. As I will show below, our data confirm this point. In particular, the vortex density and main vectors of the vortex lattice follow expectations for a tilted vortex lattice in an isotropic material.

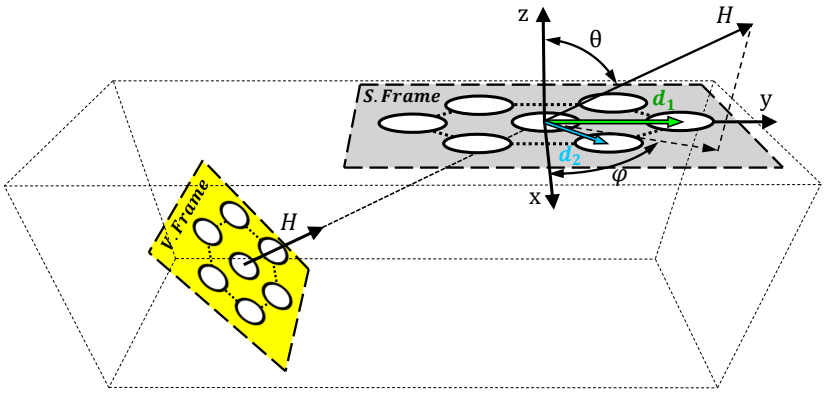

Figure 4.1 Schematic representation of the vortex lattice frame (yellow) and its projection to the surface (gray) [175]. Black arrow shows the direction of the magnetic field **H**, tilted by the polar angle θ and the azimuthal angle φ. The arrows with coordinates x, y, z provide the reference surface frame. $\vec{d}_1$ and $\vec{d}_2$ characterize the positions of the vortices in the surface reference frame.

4.2.1 Lattice A(A') on Vortex Frame vs. Vortex Unit cell on Surface Frame.

As I described in section 3.4 the vortex lattice under magnetic fields parallel to the c-axis in β-Bi_2Pd has two possible orientations with respect to the crystalline lattice, at each one the vortex lattice being locked to one of the crystalline axis: Lattice A and A' (see figures 3.11 and 3.12).

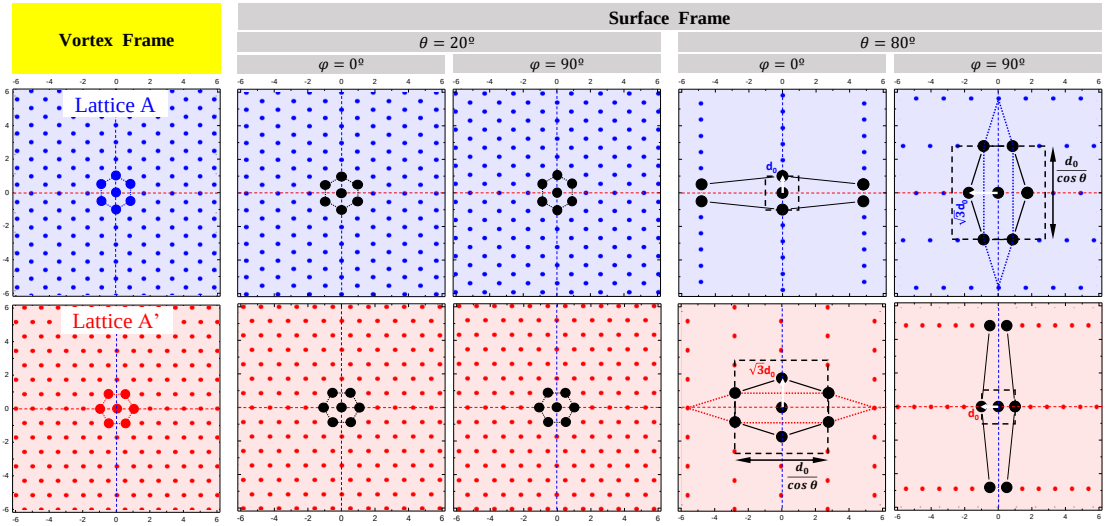

Figure 4.2 Calculated patterns of vortex lattices A and A' on the vortex frame and the surface frame when the magnetic field is tilted by $\theta = 20°$ and $\theta = 80°$ as a function of two in-plane directions $\varphi = 0°$, $\varphi = 90°$ (black arrows). Black dots and lines mark the arrangement of nearest neighbors of the surface vortex lattice. Blue and red dotted hexagons at $\theta = 80°$ highlight the projection of the primitive unit cell in the vortex frame. We mark the smallest intervortex distance with white arrows. The dotted line squares will be useful for discuss our results. Horizontal and vertical scales are normalized to the intervortex distance on the vortex frame d_0.

In order to better describe the results obtained in this work, it is useful to visualize the possible vortex lattice configurations at the surface when tilting the magnetic field. Fig. 4.2 show the two lattices A and A' and how these are projected to the surface for different polar and azimuthal orientations. In the left panels, we represent two lattices in the vortex frame whereas middle and right panels show the corresponding lattices in the surface frame for, respectively, low ($\theta = 20°$) and large ($\theta = 80°$) polar angle as a function of two in-plane directions ($\varphi = 0°$,

$\varphi = 90^\circ$). The arrangement of nearest neighbors on the surface frame is represented by black hexagons. Background colors mark the orientation of the vortex lattice in the vortex frame, either A (blue) or A' (red).

For low polar angles, the expected patterns at the surface are very similar for either A or A' lattice and nearly independent of the azimuthal orientation of the magnetic field. The polar angle is very small and the distortion of the surface hexagonal lattice is minor, maintaining a regular hexagonal symmetry. In contrast, at large polar angles, depending on the azimuthal orientation of the tilted magnetic field, there are two options, which appear alternatively. Either the surface lattice is strongly distorted (upper left and lower right panels of the surface frame at $\theta = 80^\circ$), or not (upper right and lower left panels of the surface frame at $\theta = 80^\circ$). Note that, in the latter case, for the less distorted surface lattices, the nearest neighbors of the surface vortex lattice (black points) do not coincide with the geometrical projection of the primitive cell at the vortex frame (given by the dotted blue and red hexagons in upper right and lower left panels of the surface frame at $\theta = 80^\circ$). In the following, I always refer to the arrangement of nearest neighbors of the surface vortex lattice to discuss the experimental results.

As can be seen, for large polar angles the smallest intervortex distance in the surface frame increases from d_0 (the intervortex distance on the vortex frame) for the most distorted lattice to $\sqrt{3}d_0$ for the less distorted lattices. The dotted squares in the left panels of Fig. 4.2 will be use to analyze the experimental results.

4.3 Tilted vortex lattice on the surface of β-Bi_2Pd

To make the STM measurements, we mounted the samples of β-Bi_2Pd with the c-axis of the tetragonal crystal structure parallel to the z direction of the magnetic field. The other two crystalline orientations with respect to x and y of the magnet are found by scanning the surface with atomic resolution and finding the square Bi lattice shown in Figures 3.11 and 3.12. All the spectroscopy maps presented in this chapter were measured at 150 mK and 1 nA. We obtain vortex lattice images by making maps of the zero bias conductance. Data are usually taken in field cooled conditions, although, due to the weak vortex pinning of this material, we find the same results when changing the magnetic field at low temperatures. Each time we changed the orientation of the magnetic field we made a topography image to obtain the relative orientation between the atomic and vortex lattice. No filtering or image treatment is applied to the conductance maps shown in this chapter.

4.3.1 Tilted vortex lattice at fixed azimuthal angles as a function of polar angles.

First we studied the tilted vortex lattice in β-Bi_2Pd as a function of the polar angle θ. Figure 4.3 shows an sketch of the experiment, where we represent how the projected vortex lattice in an isotropic superconductor evolves when the magnetic field is tilted at fixed azimuthal when changing θ.

Figure 4.4 shows images of the tilted vortex lattice at 0.3 T as a function of θ for an azimuthal orientation along a nearest neighbor direction in the vortex lattice frame (white arrow). The experimental results are compared with simulations obtained from the geometrical projection of an hexagonal vortex lattice (lower panels in Fig. 4.4). It easy to observe that the vortex lattice distortion on the surface follows the direction of the magnetic field. As I mention before, at large tilting angles ($\theta = 80^\circ$) the nearest neighbors at the surface do not coincide with the projection of the primitive unit cell at the vortex frame.

The good agreement between the experimental results and the simulations confirms that the bulk vortex lattice remains hexagonal at all angles, following the expectations for tilted lattices in isotropic superconductors.

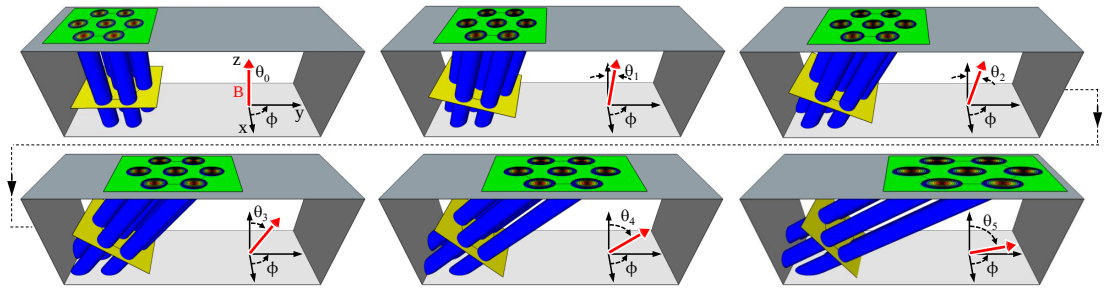

Figure 4.3 Schematic representation of the tilted vortex lattice in an isotropic superconductor at fixed azimuthal angle as a function of polar angle θ. The azimuthal angle coincides with a nearest neighbor direction in the vortex frame. The vortex lattice on the surface frame (green) represents the geometrical projection of the hexagon on the vortex frame (yellow).

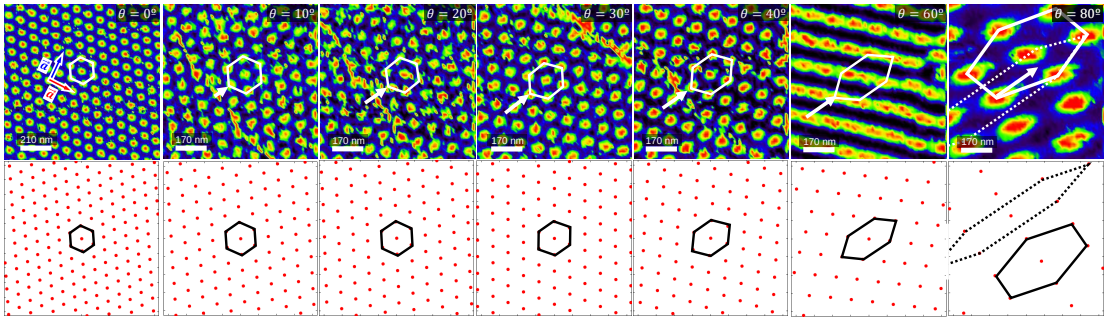

Figure 4.4 (*Upper panel*) Normalized zero bias conductance maps at 150 mK and 0.3 T in β-Bi_2Pd, at fixed azimuthal angle (white arrow) as a function of polar angle θ. The azimuthal angle at $\theta = 0^\circ$ coincides with a nearest neighbor direction in the vortex lattice frame. (*Lower panel*) Calculated patterns of the tilted vortex lattice on the surface frame at the same conditions. White and black hexagons represent the arrangement of nearest neighbors at the surface. Dotted hexagons at $\theta = 80^\circ$ are the surface projection of the primitive unit cell at the vortex frame. Orientation of the atomic lattice is shown in the leftmost upper panel as blue and red arrows. The map color scale represents the lower(higher) conductance by blue (red).

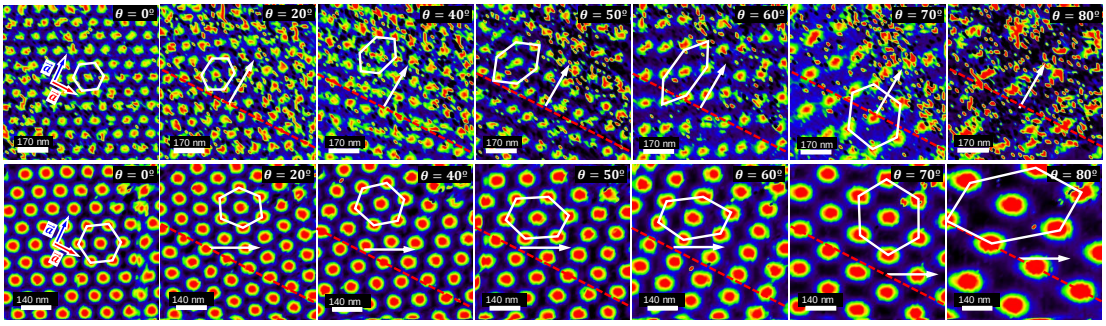

Figure 4.5 Normalized zero bias conductance maps at 0.3 T when changing the polar angle θ for two azimuthal orientations, along one crystalline axis *(upper panel)* and in between crystalline axis *(lower panel)*. In the first panels we represent the atomic lattice orientation by red and blue arrows. In the other panels, red dashed line is parallel to red atomic direction. The white arrows show the in-plane direction of the magnetic field. The white hexagons show the unit cell of the vortex lattice on the surface frame. The color scale represent the lower(higher) conductance by blue (red).

In Figure 4.5, we show other experiments where we measure the tilted vortex lattice also at 0.3T as a function of the polar angle for two different azimuthal angles; one parallel to the blue crystalline axis (upper panel) and in between crystalline axis (lower panel). In both experiments, the magnetic field is tilted along a nearest neighbor direction in the vortex lattice frame.

The distortion of the surface vortex lattice is gradual with tilting the magnetic field. The vortex lattice is highly distorted, forming rhombic structures when tilting away from the perpendicular field. Sometimes we find rotations in the vortex lattice. In the left panels of Fig.4.5 ($\theta = 0°$), the vortex lattices are of type A. At the upper panel, for $\theta = 50°$, we observe that the vortex lattice has turned to A' (the lattice has an axis parallel to the red dashed line). Then, it goes back to A for higher polar angles. Same situation is observed at the lower panel, for $\theta = 20°$.

For fixed angular and polar angles, we find different orientations when looking on another scanning window, as in perpendicular magnetic fields (see Figs.3.11 and 3.12). We also find changes between A and A' when changing the magnitude of the magnetic field or the temperature. The choice between A and A' is thus random for polar angles that are not too large, although we can identify a tendency, as discussed in the following.

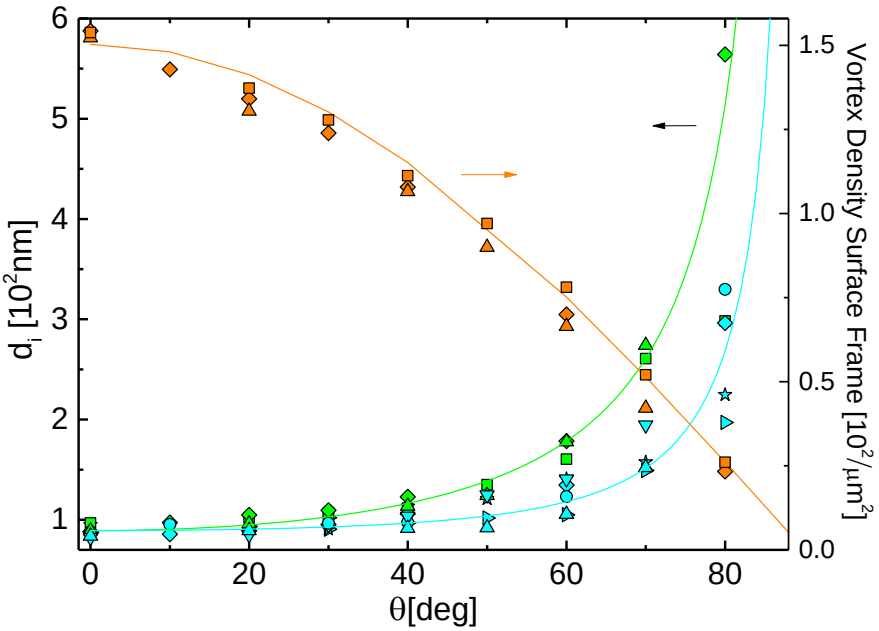

Figure 4.6 Magnitude of the basis vectors of the projected vortex lattice at the surface frame (left) and vortex density (right) as a function of the polar angle (See Fig. 4.1). Different symbols represent different experiments with $\vec{d}_1$ (green), $\vec{d}_2$(cyan) and vortex lattice density (orange). Lines with the same code color, provide the calculated $\vec{d}_1$ and $\vec{d}_2$ and vortex lattice density on the surface frame for a tilted perfect hexagonal lattice.

The vortex density at the surface frame decreases when tilting the magnetic field. In figure 4.6 we show the evolution of the projection of the primitive cell vectors in the vortex frame to the surface ($\vec{d}_1$ and $\vec{d}_2$ in Fig. 4.1) and of the surface vortex density for different experiments. Lines provide calculations following the geometrical projection of a hexagon on a tilted surface described by the expressions 4.1 and 4.2. The vortex density at the surface frame depends on the polar angle as $4\cos\theta/\pi d_0$. We find a very good agreement between our data and the geometrical projection of a perfect hexagonal lattice. This is the result expected for a isotropic superconductor where the tilted vortex lattice remains hexagonal (unlike the distorted lattice that appears in anisotropic superconductors).

4.3.2 Vortex core shape in tilting magnetic fields

We address now how the vortex shape at the surface changes with the tilt of the magnetic field by comparing the vortices at perpendicular fields and at highly tilted fields (Fig.4.7). In the previous chapter, we shown that vortices in β-Bi_2Pd, at perpendicular magnetic fields, have a circular

shape with core size $\mathscr{C} \approx 24$ nm at 0.3 T [97, 168]. In left panel of Fig.4.7 we we mark $\mathscr{C}$ by a white circle in an image taken at perpendicular fields.

If we assume that the vortex arrives to the surface straight in highly tilted fields, without any bending, the expected shape at the surface is an ellipse with minor and mayor axis of $r_- = 2\mathscr{C}$ and $r_+ = 2\mathscr{C}/\cos(\theta)$ (white ellipse in the right panel of Fig.4.7). If however the vortex bends to exit perpendicular to the surface we expect to observe the same vortex shape as for perpendicular fields. As we show by the circle in right panel of Fig.4.7, the vortex bends and exits perpendicular to the surface.

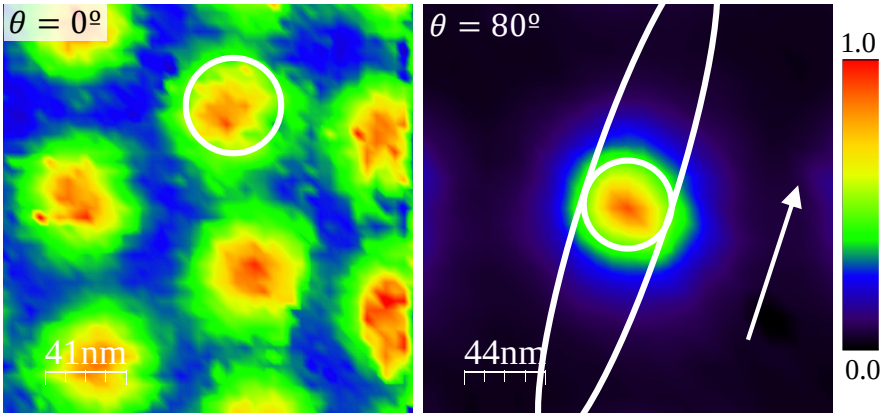

Figure 4.7 Zero bias conductance maps for 0.3T at $\theta = 0°$ (left) and $\theta = 80°$, $\varphi = 72°$ (right). The vortices in both situations have circular shape. White circles have radius of $\mathscr{C} \sim 24$ nm. The white ellipse has mayor axis of $r_+ = 2\mathscr{C}/\cos(\theta) = 269.5$ nm. Color bar represents the normalized tunneling conductance for both images.

Figure 4.8 we show schematically a 3D picture of the situation discussed above where vortices bend to exit perpendicular to the surface. The figure displays the two lattices A and A' and how these are projected to the surface, taking into account vortex bending. Vortex curvature is expected to occur over a length $r = min(d_0, \lambda)$[182]. Using $\lambda \approx 105$ nm obtained from Hall probe magnetometry measurements in our samples [152], we find that at 0.3 T the length over which the vortex is curved beneath the surface is of $r \approx d_0(0.3T) = 89.2$ nm. Therefore, it is not expected that the electronic density of states at the surface is influenced by the vortex bending. This is in agreement with our data under large tilting field which give the actual core radius $\mathscr{C}$.

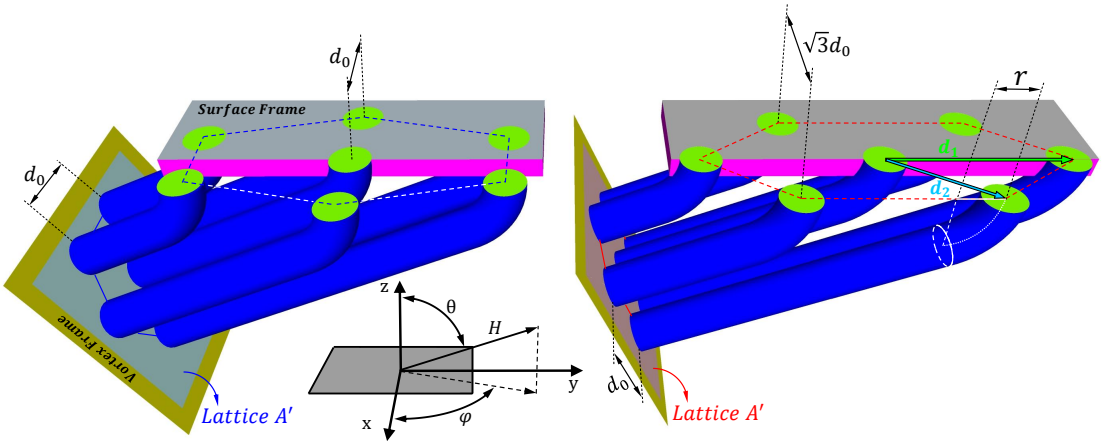

Figure 4.8 Schematic representation of the two possible vortex lattice orientations, A and A' in the vortex frame (yellow) and their projections in the surface frame (gray). d_0 is the intervortex distance in the vortex lattice frame. Vortex bending with a bending radius of r occurs near the surface.

4.3.3 Tilted vortex lattice at fixed polar angles as a function of azimuthal angle

In the last section of this chapter, I will present our results in the study of the behavior of the whole vortex lattice when changing the azimuthal orientation of the magnetic field with fixed θ. Figure 4.9 shows an sketch of this experiment where we represent how the projected vortex lattice in an isotropic superconductor evolves when rotating the in-plane direction of the magnetic field, φ, by keeping the polar angle θ fixed.

We have found different results for low and large values of the polar angle θ as discussed in the following.

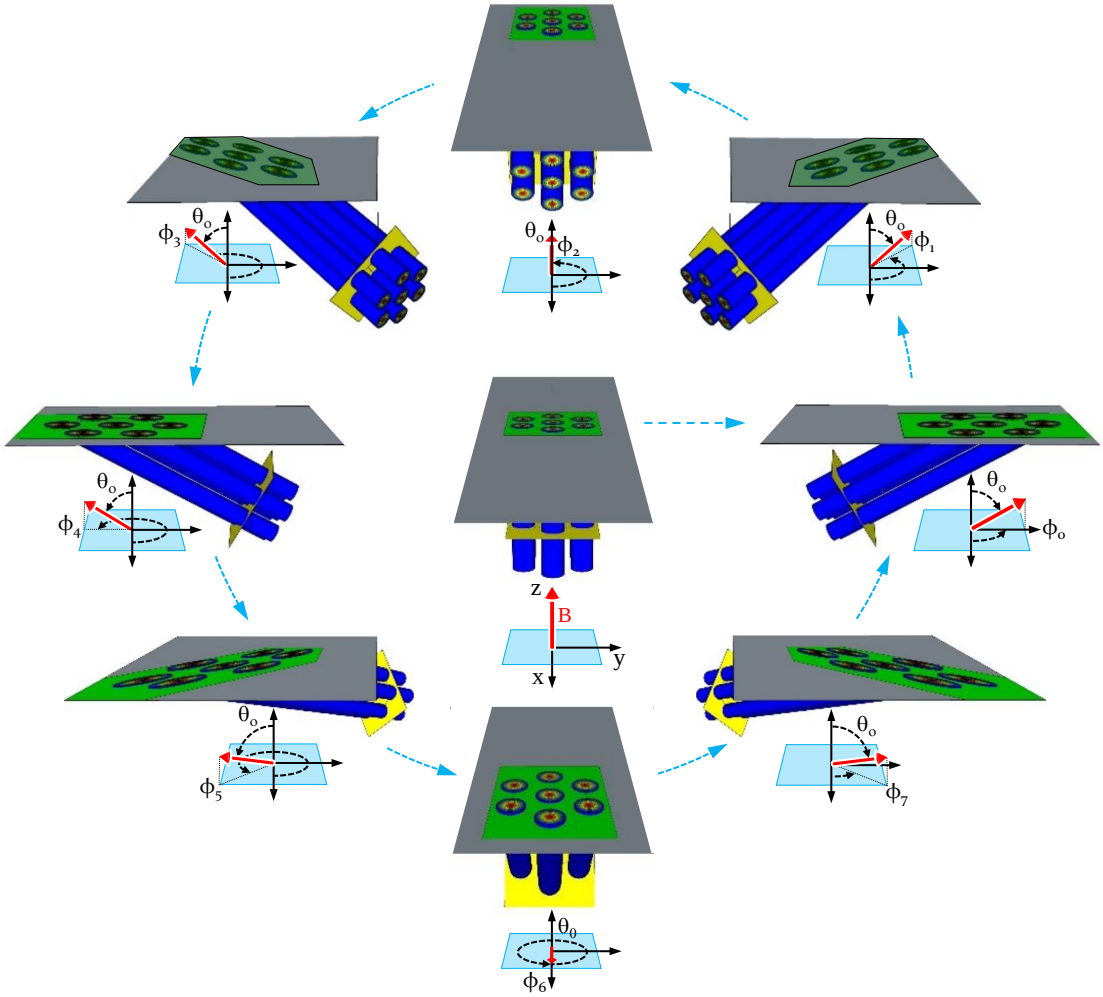

Figure 4.9 Schematic representation of the tilted vortex lattice in an isotropic superconductor at fixed polar angle as a function of azimuthal angle. The vortex lattice on the surface frame (green) represents the geometrical projection of the hexagon on the vortex frame (yellow). Note that, due to the perspective used in the figure, vortex bending close to the surface cannot be appreciated in the images.

Tilted vortex lattice as a function of azimuthal angle at small polar angles

Figure 4.10 shows some of the spectroscopy maps taken in a region of 0.7 $\times$0.7 μm^2, at 0.3 T, a fixed small polar angle $\theta = 20^\circ$ varying the azimuthal angle. We represent the surface projection of the primitive unit cell on each image by white circles.

To analyze the behavior of the tilted lattice, we determined the positions (x,y) of the six vortices that belong to the surface projection of the primitive unit cell (white circles) expressed in a new basis given by the high symmetry direction of the crystal lattice. Here the horizonal x-axis corresponds to the crystalline axis represented by the red line. Left panel of Fig.4.11 (a)

shows the experimental result for all the azimuthal angles studied. The crystalline axis have been rotated for clarity.

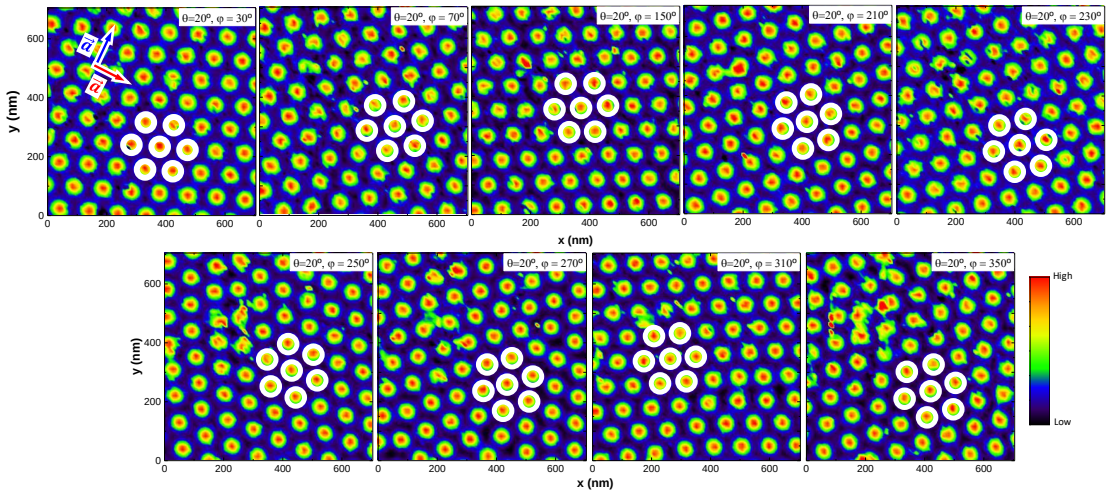

Figure 4.10 Normalized zero bias conductance maps in β-Bi_2Pd, on a region of 0.7 $\times$0.7 μm^2, at 0.3 T for a small polar angle $\theta = 20^\circ$ as a function of the azimuthal angle φ. In the first panel, the atomic lattice orientation is represented by red and blue arrows. The white circles represent the arrangement of nearest neighbors of the surface vortex lattice. Color scale represents qualitatively the conductance values.

In the right panels of Fig.4.11(a), we show the expected result for the A and A' vortex lattices. The polar angle is very small and the distortion of the surface hexagonal lattice is minor. The maximum distortion of the intervortex distance and the maximum angular deviation with respect to the A or A' lattices obtained when changing the azimuthal angle are $\vec{d}_{1max}(\theta = 20^\circ) = 1.06 d_0$ and $|\Delta\alpha_{max}| = 2^\circ$, respectively. Therefore, as mentioned before, the vortex lattice at the surface for small polar angles is practically the same as in the vortex lattice frame.

There are just slight deviations of the situation encountered for magnetic fields along the c-axis. These consist of small rotations of the vortex positions around the hexagonal positions adopted in perpendicular fields. We can plot the average among all six nearest neighbor of the angular deviation between the surface vortex lattice and expectations for A and A' lattices (Fig.4.10b). To this end, we average over the six high symmetry directions $\bar{\varphi} = \sum_{i=1}^{6} \left| \frac{1}{6}(\varphi_i - \varphi_{close-by,A}) \right|$, where φ_i are the nearest neighbor vortex positions observed in the experiment and $\varphi_{close-by,A}$ the closest vortex position for the A orientation. In Fig.4.11(b) we plot the difference between the experimental vortex positions (left panel of Fig.4.11(a)) and the positions found in the lattice A (middle panel of Fig.4.11(a)). We find that points accumulate close to zero deviation mostly when the magnetic field is tilted on a crystalline direction. When the magnetic field is tilted on intermediate directions, we find lattices oriented in between the expected A and A' situations. Thus, the vortex lattice is mostly in between A and A', but has a clear tendency to lock to A or A' when the field is tilted along a crystal axis.

Tilted vortex lattice as a function of azimuthal angle at large polar angles

In figure 4.12 we show images of the surface vortex lattice obtained at $|B| = 0.3$T and 150 mK as a function of the azimuthal angle φ with a fixed polar angle of $\theta = 80^\circ$.

We analyse the data following the procedure described before for the data at $\theta = 20^\circ$. In figure 4.13 we compare the experimental positions of the first neighbors in the surface vortex lattice taken over many experiments (left panel) with the result expected for for lattices A and A' (middle and right panels).

As it was described previously, the surface vortex lattice forms highly distorted hexagons

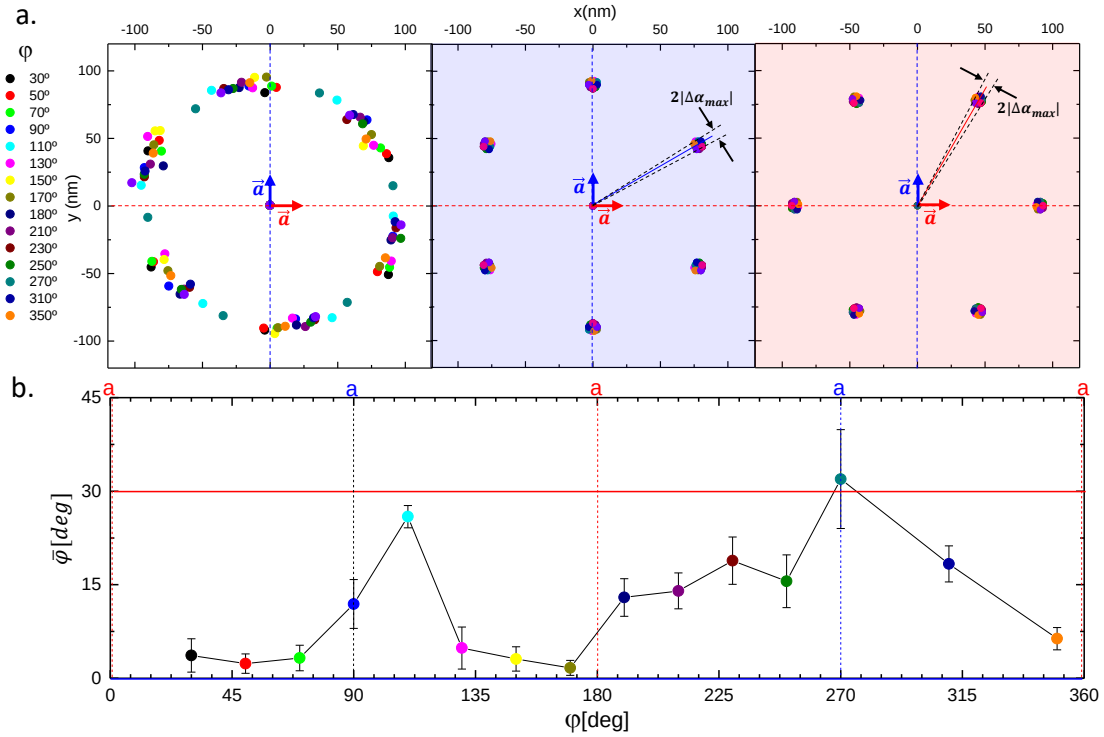

Figure 4.11 (a) (*Left panel*) Coordinates of the nearest neighbors' position in the surface vortex lattice (points) with respect to the crystalline directions for a polar angle of $\theta = 20^\circ$ and different azimuthal angles φ ($|\vec{B}| = 0.3$ T). (*Middle and right panels*) Expected result for the A and A' vortex lattice at the same experimental conditions. $\Delta\alpha_{max}$ is the maximum angular deviation of the experimental data with respect to the A or A' lattices. **(b)** Averaged deviation $\bar{\varphi}$ between the experimental vortex positions at the surface and the surface projection of A lattice. Points maintain the same color code as in the left panel of **(a)**. Horizontal blue and red lines represent the A and A' lattices, respectively. Vertical red and blue dashed lines represent the crystalline axis. $\varphi = 0^\circ$ gives the horizontal axis.

with large polar angles(see Fig. 4.2). Clearly, the lattice at the surface frame can be very different depending on the orientations A and A', in particular for certain azimuthal angles. For example, in the situations shown in the right panels of Fig.4.2, the minimal intervortex distance depends strongly on the orientation of the vortex lattice in the vortex frame. For $\theta = 80^\circ$ and $\varphi = 0^\circ$ in Fig.4.2, the minimum intervortex distance is shorter for A than for A', and the opposite occurs $\theta = 80^\circ$ and $\varphi = 90^\circ$.

In the experiment (left panel in Fig. 4.13), none of the most distorted hexagons is observed. There are no points at the square area defined by dashed squares of Fig.4.2 to distinguish between the most distorted and less distorted vortex lattices at the surface. In the middle and right panels of Fig.4.13, all possible surface vortex lattices for each orientation is given by colored points. Points that fall outside the dashed squares are empty and represent the less distorted lattices, whereas points inside are filled and correspond to the most distorted vortex lattices. None of the configurations having points outside (empty symbols) is observed in the experiment. Instead, we observe a square arrangement with nearest neighbors clustering around a distance that is of approximately ∼200 nm, always along one of the main crystalline directions. Without the central vortex, all the experimental data can be enclosed by an area limited by squares of sides $2d_0 \simeq 182$ nm and $d_0/\cos\theta \simeq 524$ nm, being $d_0 \simeq 91$ nm, the intervortex distance on the vortex frame.

To gain further insight into the behavior of the tilted vortex lattice, we analyzed individually several particular orientations. Fig. 4.14 (a) and (b), show images of the surface vortex lattice and positions of the corresponding positions of the first neighbors for $\varphi = -8^\circ$ and $\varphi = -43^\circ$.

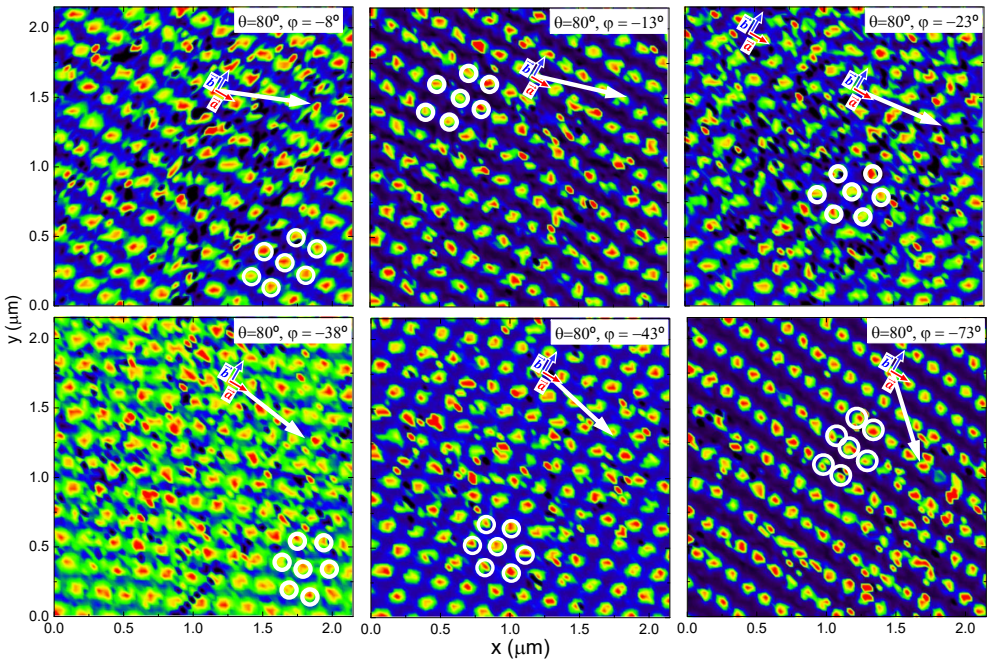

Figure 4.12 Normalized zero bias conductance maps in β-Bi_2Pd, on a region of $2.17\times2.17\mu m^2$, at 0.3 T for a large polar angle of $\theta = 80^\circ$ as a function of the azimuthal angle φ (white arrows indicate the in-plane orientation of the magnetic field). The atomic lattice orientation is represented by red and blue arrows. The white circles represent the arrangement of first neighbors in the surface vortex lattice.

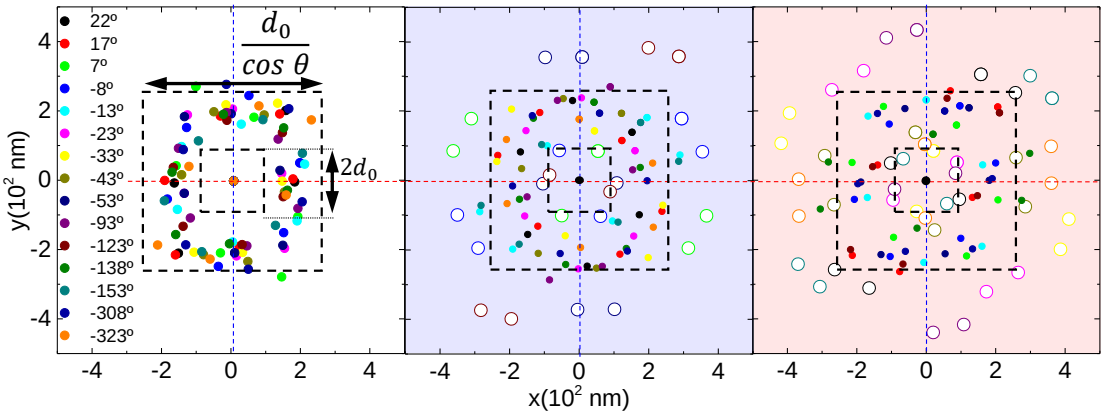

Figure 4.13 (*Left panel*) Vortex positions for the first neighbors on the surface (points) for a polar angle of $\theta = 80^\circ$ and different azimuthal angles φ at $|\vec{B}| = 0.3$ T and 150 mK. (*Middle and right panels*) Vortex positions expected for the A and A' lattice orientations at the same experimental conditions. The most distorted lattices are represented by empty circles. Dashed squares have sides of 524 nm and 182 nm (see Fig. 4.2). Red and blue vertical dashed lines represent the crystalline axis. $\varphi = 0^\circ$ gives the horizontal axis. We use the same code color for all values of φ.

The result expected for the A or A' lattices at the same conditions is shown in Fig. 4.14 (c) and (d). We observe that at each azimuthal angle, there is a lattice at the surface frame that lies within the dashed squares if we switch the orientation of the vortex lattice between A and A' or viceversa. It turns out that for all azimuthal angles, the vortex lattice chooses the orientation with respect to the crystal lattice that provides largest intervortex distances on the surface frame. Our experiment shows that the vortex lattice in the bulk rotates in such a way to maximize the smallest intervortex distance at the surface so that all the nearest neighbors are located within the distances defined by $2d_0$ and $d_0/\cos\theta$.

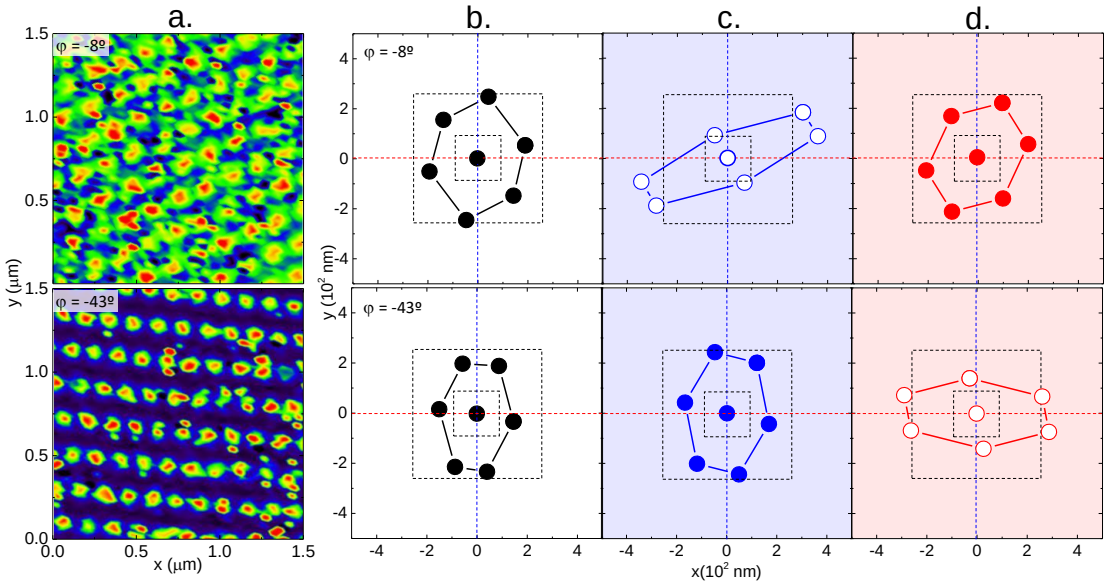

Figure 4.14 (a) Normalized zero bias conductance maps in β-Bi_2Pd, on a region of $1.5\times1.5\mu m^2$, at 0.3 T, for a large polar angle of $\theta = 80^\circ$ at $\varphi = -8^\circ$ and $\varphi = -43^\circ$. White circles represent the vortex positions of the first neighbors at the surface. **(b)** Vortex positions of nearest neighbors obtained in the experiment (black points) and atomic lattice directions (red and blue dashed lines). Black arrow represents the in-plane direction of the magnetic field. **(c)** and **(d)** Surface vortex positions expected for lattices A and A' respectively. We highlight the simulated vortex positions for lattices A and A' that are more similar to the experimental data. In the experiment, we do not observed any of the most distorted hexagons located outside the region limited by the dashed squares (defined by $2d_0$ and $d_0/\cos\theta$).

4.3.4 Discussion

The overall behavior of the tilted vortex lattice in β-Bi_2Pd is as might be expected in an isotropic superconductor. The tilted vortex lattice at fixed azimuthal angles as a function of the polar angle (Figs. 4.4, 4.5, 4.6) shows equilibrium patterns, where the repulsion between vortices leads to hexagonal vortex lattices, which are independent of the tilt angle. These bulk vortex lattices remain hexagonal at all tilts, and can be described by a tilted Abrikosov lattices in isotropic superconductors.

The result found for low polar tilt angles ($\theta = 20^\circ$) shows that the tilted vortex lattice has a tendency to align along the crystalline directions (Figs. 4.10 and 4.11). As discussed in the previous chapter, non local contribution to the intervortex interaction can strongly influenced the orientation of the vortex lattice in crystalline superconductors. The elastic contributions to the interaction between vortices has been calculated by several authors and it has been shown that, in tetragonal systems, it might be strong enough to favor orientations of the vortex lattice along the crystalline directions [183, 184, 185, 186].

The result for very large tilt angles is however unexpected. In particular, as shown in Figs. 4.13, 4.14, the smallest intervortex distance increases from d_0 to $\sqrt{3}d_0$ (see Fig. 4.2) by changing the bulk vortex lattice from A to A' and viceversa at 80° for given azimuthal angles. But, how can the intervortex distance at the surface impose the vortex lattice in the whole crystal to choose between A and A'?

To address this question, let us estimate the relevant energy scales. We can assume that the degeneracy in the orientation of the hexagonal vortex lattice with respect to the square crystalline lattice is lifted in a given area by pinning. We can then compare the pinning energy with the difference in intervortex repulsion energy among the two lattices observed at the surface. We can

estimate the pinning energy per unit length of a vortex core using [24, 187]

$$U_{core} = \frac{B_c^2 \pi \xi^2}{\mu_0} \tag{4.3}$$

with B_c the thermodynamic critical field and ξ the superconducting coherence length. We find $1.43 \times 10^{-11} Jm^{-1}$. Then, we can estimate the repulsive interaction energy of two vortices using

$$E(r_{12}) = \frac{\phi_0}{4\pi\mu_0\lambda^2} K\left(\frac{r_{12}}{\lambda}\right) \tag{4.4}$$

with λ the penetration depth, ϕ_0 the flux quantum and r_{12} the intervortex distance [24, 187]. We find $E(d_0) = 1.422 \times 10^{-11} Jm^{-1}$ and $E(\sqrt{3}d_0) = 1.581 \times 10^{-11} Jm^{-1}$ (see Fig.4.2), which gives $E(d_0) - E(\sqrt{3}d_0) = 1.6 \times 10^{-12} Jm^{-1}$.

To estimate the length over which these energies act on the vortex behavior, let us note again that the bending radius is of order of the smallest value between the intervortex distance d_0 and the penetration depth λ[182, 188]. The length scale over which a pinning center acts on a vortex is smaller, of order of the superconducting coherence length ξ. At 0.3 T, the intervortex distance is of order of 89.2 nm. With $\xi \approx 25$ nm, we find that the repulsive interaction at the surface is nearly of the same order as the pinning energy. More generally, for every magnetic field, the bending radius is larger than ξ. If pinning is weak, with a small fraction of vortices pinned over the length of the sample, the intervortex repulsive interaction at the surface will dominate pinning and will determine the orientation of the vortex lattice.

Degenerate vortex lattices appear in other topical superconductors with the field parallel to one crystalline axis. For instance, heavy fermions such as CeCoIn5 [190], borocarbide superconductors [191] or MgB2 [192, 193], have also shown two hexagonal domains with the field applied along the crystalline c-axis. In these materials non-local contributions to the spatial dependence of the intervortex interaction is provided by anisotropy in either the electronic, magnetic or superconducing properties. However, the effect of tilting magnetic fields has not been yet addressed in these systems. It will be interesting to know how the intervortex repulsion at the surface might be relevant to anisotropic superconductors as well, provided that the distortions induced by the anisotropy are taken into account.

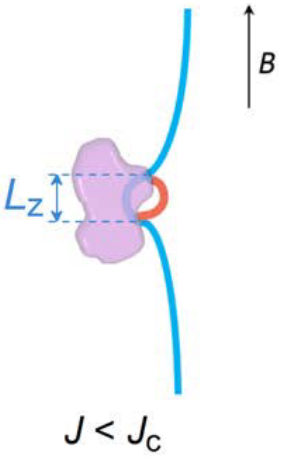

Figure 4.15 Illustration of a vortex crossing a irregular shape pining center. Observe the detail when the vortex goes in and goes out of the pining center. The bend angle is ~90° [189].

Bent vortex lattice appear often in real materials [194, 195]. If we consider extended pinning centers that are aligned parallel to the vortex lattice, which provides generally the largest critical currents, vortices bend out of the pinning center when applying a current. Vortices start moving far from the pinning center, but remain pinned along it and bend close to the pinning center to remain perpendicular to the normal-superconductor interface (Fig. 4.15). When the elastic energy overcomes pinning energy, the vortex de-pins[24, 187, 194, 195]. Vortices are thus bent close to large size pinning centers in any practical situation. It will be interesting to see how the configurations of nearest neighbors at the normal-superconductor interface influences this result. In the case of highly anisotropic superconductors, the vortex lattice far from the interface is distorted, so the distribution of intervortex distances along the bent paths are more complex than discussed here. In principle, from the results obtained here, we expect that bent vortex lattices will be favorable for pinning, because the vortex lattice will be able to sense for more favorable situations to maximize the intervortex distance along the bending radius.

As was shown in Ref.[97], surfaces found in our crystals show atomically resolved surfaces with no evidence for isolated surface states. Furthermore vortex cores are round and do not show any zero bias peak, but instead a flat tunneling conductance. This indicates that the Fermi surface anisotropy and other surface related issues preferentially show up in very thin films and that the bulk samples show simple and neat s-wave BCS behavior at the surface. In turn, it would be interesting to do experiments in tilted fields in the epitaxial thin films of Ref.[196] and see how the observed behavior, very different in some aspects from what we find here, is modified is modified by a tilted field and how it compares to the case of 2H-$NbSe_2$[181].

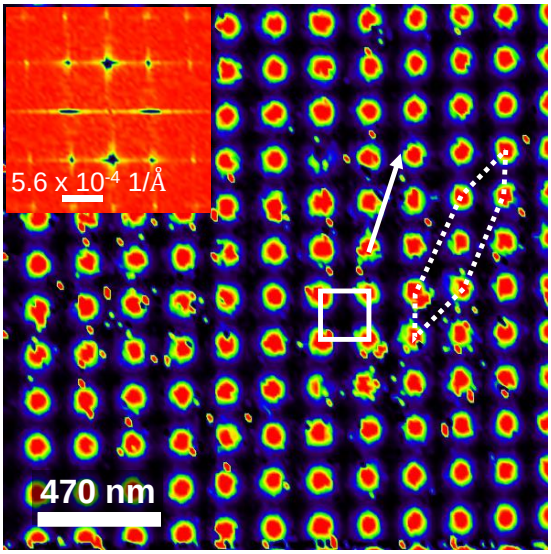

Figure 4.16 Zero bias conductance map on a scan window of 2.35×2.35 μm^2 for $\theta = 80^\circ$ and $\phi = 72^\circ$. White arrow provides the tilt of the magnetic field and the dashed hexagon the projection of the primitive cell of the bulk vortex lattice. The symmetry of the surface vortex lattice is square. The Fourier transform of the image is shown as an inset. This is also the result expected by projecting such a tilted vortex lattice onto the surface.

It is also interesting to note that one can construct nearly any kind of surface vortex arrangement by modifying the tilt angle (Fig. 4.16) as long as the polar angle is less than 80°. This result is applicable to any isotropic superconductor. In particular, it can be used to modify vortex matching configurations in nanostructured thin films[197, 198, 199, 200].

4.4 Concluding Remarks

We have studied in detail the tilted vortex lattice in the superconductor β-Bi_2Pd. We find that the vortex lattice at the surface distorts following expectations for an isotropic superconductor. Patterns and vortex shapes at the surface correspond to a hexagonal lattice in the bulk projected on the surface plane.

We first show experimentally that vortices exit the sample perpendicular to the surface and are thus bent beneath the surface.

For magnetic fields close to the perpendicular direction (low polar angles), we observe the same dichotomy between two orientations of the vortex lattice previously noticed in perpendicular magnetic fields.

We analyze the orientation of the vortex lattice for magnetic fields nearly parallel to the surface (polar angle of the tilt > 80°) as a function of the azimuthal angle and find that the intervortex repulsion along the bent vortex path is large enough to induce a rotation in the bulk vortex lattice so that the intervortex distance in the surface hexagon can be maximized. Estimations of the bulk pinning energy and the intervortex repulsion along bent paths confirm that this effect is a relevant to the overall energy landscape. This contribution to the intervortex interaction appears to have been largely overlooked till now and can be important to explain the behavior of bent vortex lattices.

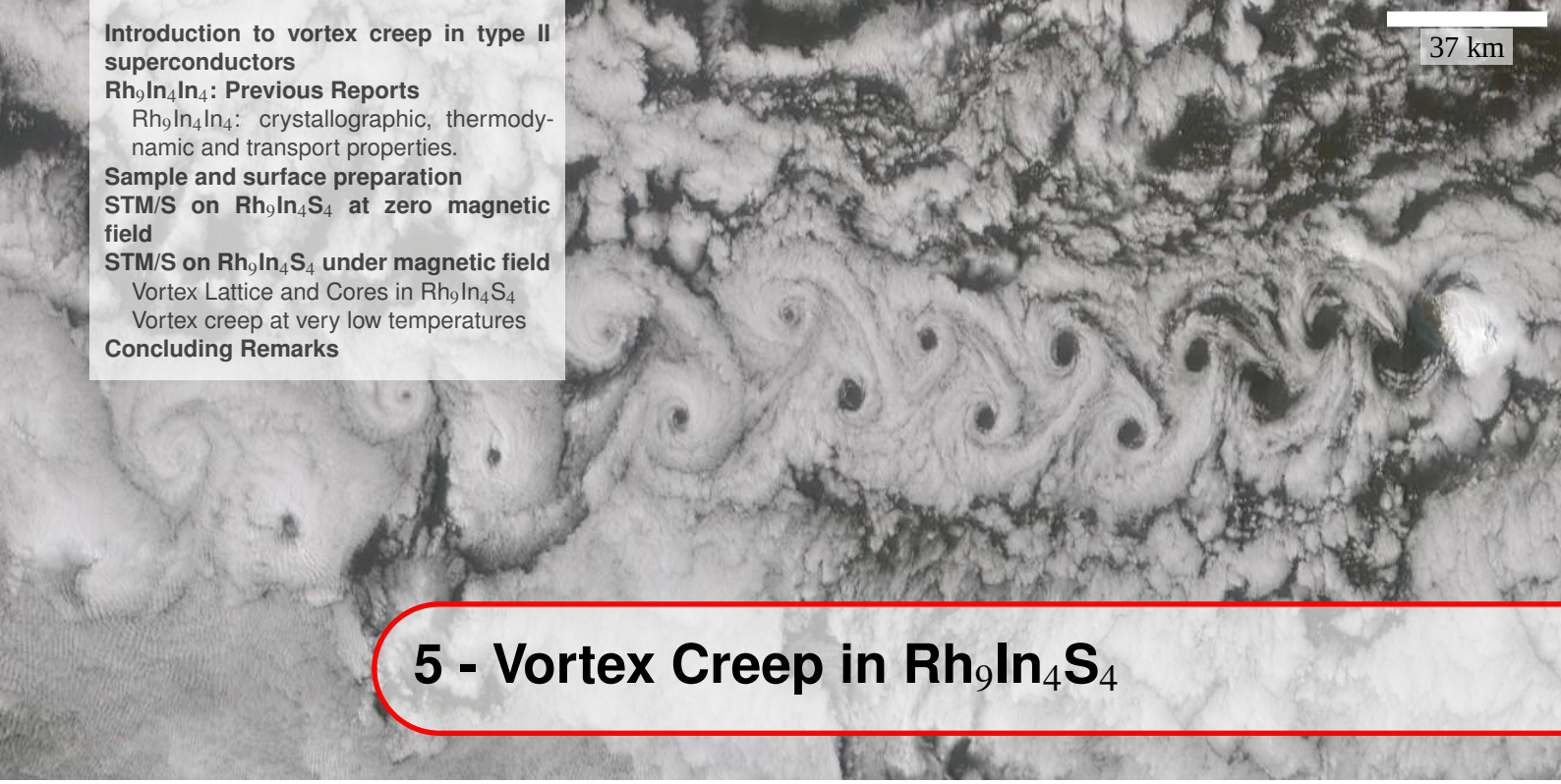

5 - Vortex Creep in $Rh_9In_4S_4$

Top Image:
Von Kármán, Vortex Street
on the Jan Mayen island (Norway).
When the flow of marine stratocumulus clouds is interrupted by an obstacle such as an island, a series of organized eddies (vortices) can appear within the cloud layer downwind of the obstacle.
NASA - MISR Team [201]

While vortex-vortex repulsion gives rise to an ordered vortex lattice, vortex pinning and thermal fluctuations induce the formation of non equilibrium vortex states. These appear when changing the relative contribution of the competing energies. Under the action of a current, vortices move and this motion produces non-zero resistance. Hence, understanding vortices in presence of pinning at finite temperatures remains a challenging problem and a key issue to any practical application of superconductors.

In this chapter we have studied the extreme type II superconductor $Rh_9In_4S_4$. Superconductivity in this compound was discovered in 2015. As I will discuss, this material appears as a model system to study unusual residual vortex creep dynamics at very low temperatures.

I will start by introducing the problem of vortex creep in type II superconductors. Then, in section II, I will review the main electronic and superconducting properties of $Rh_9In_4S_4$ reported by previous macroscopic measurement. Before presenting our results I will discuss, in Section III, the experimental procedures that we used in our measurements. In section IV and V, I will present the data we have obtained in the microscopic study of this material. Section IV is focused on the results at zero magnetic field where we have characterized the topography and provided first data of the superconducting gap and its temperature dependence. In section V, I will present images of the hexagonal vortex lattice and show that it moves at temperatures as low as 150 mK due to vortex creep. Finally, I will discuss the origin of vortex creep in $Rh_9In_4S_4$ and draw some conclusions.

5.1 Introduction to vortex creep in type II superconductors

Among the most relevant topics in the physics of type II superconductors is the knowledge and control over flux line arrangements. Applications of these materials always require fixing vortices by an adequate distribution of pinning centers. The characteristics and behavior of both, vortices and pinning centers, are critically dependent on the structural and superconducting properties of each sample. However, there are some important aspects which have general character.

When changing the magnetic field below the superconducting critical temperature T_c in a type-II superconductor, vortices enter from the edges and fill the interior of the sample. They are driven towards the interior by the Lorentz force due to the Meissner shielding currents.

As first proposed by Bean [202], in real superconductors, with defects acting as pinning centers, motion towards the sample center is hindered by the pinning centers, which tend to pin any vortex that passes by. In this process, some vortices jump over pinning barriers and experience the pinning force $\mathbf{F_p}$ that retards its motion and others are trapped by pinning centers that obstruct the motion of nearby vortices[24, 187, 203, 204]. A nonequilibrium state, the critical state, is created with spatially varying vortex density, usually largest in the regions where magnetic flux enters the sample. This inhomogeneous vortex distribution is however only metastable, and a very small drive is enough to move vortices owards regions of the sample with lower vortex density.

The small current drive is present in any real situation in a type II superconductor, particularly fluctuations are strong. It is often observed when changing the magnetic field below T_c after an initial fast relaxation of the magnetization to its near-equilibrium situation. But also when the magnetic field is decreased from above T_c. In that case, the sample has crossed the region close to T_c where the vortex lattice is liquid, leaving a spatially anisotropic pinning landscape at low temperatures. The resulting residual vortex motion is called vortex creep and can create a resistance. Therefore, vortex creep is a limiting factor in the use of superconductors for practical applications.

The current j that drives vortex creep can be far below the critical current j_c[205], that is the current that produces a finite voltage drop across the sample. Vortex creep can last for very long times. At finite temperature, vortices can jump over the pinning barriers. This so-called thermal creep might be expected to exponentially decrease when the thermal energy (k_BT) drops well below the pinning energy (U_p)[206]. This could result in a ground state that has always some infinitesimally small dissipation. However, it was shown that, due to the intrinsic disorder present in a vortex lattice, the height of the pinning barriers depends on j and diverges as $U \propto j^{-\alpha}$ when $j \to 0$[205]. So, for low currents, the barrier for vortex motion grows eliminating residual creep and providing a dissipationless ground state.

Vortex creep is particularly easy to observe in superconductors that are prone to thermal fluctuations. A useful parameter to understand the relevance of thermal fluctuations is the Levanyuk-Ginzburg number, G_L[24, 187, 205, 206, 25, 207, 208, 209, **?**, **?**]. It describes the effect of fluctuations by comparing the condensation energy in a correlated volume with the critical temperature,

$$G_L = \frac{1}{2}\left(\frac{\mu_o k_B T_c}{4\pi H_c^2 \xi_{GL}^3}\right)^2 \tag{5.1}$$

G_L is small in classical low T_c superconductors ($\sim 10^{-11} - 10^{-14}$), making vortex creep effects only relevant at temperatures close to T_c. The situation is different in high T_c superconductors where G_L usually takes high values ($\sim 10^{-1} - 10^{-3}$), and thermal creep can be important at very low temperatures. Moreover, G_L can also increase significantly in superconductors with a reduced mean free path even if they present low T_c [210].

Vortices can also pass through the pinning barriers even at vanishing temperature through quantum tunneling. This quantum creep is similar to the quantum tunneling of a single particle through any energy barrier but now concerns a vortex line spreading all the way through the sample.

Much experimental and theoretical work has focused on the understanding of vortex creep. It has been studied in a variety of materials using macroscopic measurements, such as magnetization (see e.g. Ref.[209]). Until now, only few imaging experiments address vortex creep, and these are mostly made at temperatures or magnetic fields close to the critical values, where the expected currents j are also high[211, 212, 213, **?**, 214]. However, there is still no direct information, at the level of single vortices at very low temperatures, on how vortices move under creep. Probably, this is mainly because the vortex lattice of high T_c superconductors, which have been considered so far the best candidates to show vortex creep at low temperatures, remains quite difficult to observe using STM.

In this thesis, we have directly observed vortex creep at millikelvin temperatures in crystals of the newly found superconducting material $Rh_9In_4S_4$ (T_c=2.25 K) [98]. The coherence length is of $\xi \approx 9$ nm. The mean free path from resistivity measurements is very low and provides large $\xi/\ell \approx 200$. The penetration depth is very large too, of nearly 600 nm. The Ginzburg-Landau parameter is of $\kappa \approx 61$. The Ginzburg Levanyuk parameter is of $G_L \approx 1.78 \times 10^{-5}$, which is in between the the value found in high T_c and low T_c superconductors. We found that the superconducting tunneling conductance is spatially homogeneous at zero magnetic field and that the vortex lattice can be nicely observed down to mK temperatures. Thus, this material appears to have conditions that are particularly appropriate to observe and characterize residual vortex creep at very low temperatures.

5.2 $Rh_9In_4In_4$: Previous Reports

Single crystals of $Rh_9In_4S_4$ were synthesized by the group of P. C. Canfield for the first time in 2015[98]. Their motivation rises from the discovery of superconductivity in $Bi_2Rh_{3.5}S_2$ also during the same year [215]. They aimed at extending the synthesis of new superconducting materials to the Rh-In-S system where only the compound $Rh_3In_2S_2$ had been previously studied [216].

Canfield's group reported first macroscopic measurements of resistivity, magnetization, and specific heat that all clearly indicated bulk superconductivity with $T_c \approx 2.25$ K[98]. As I will briefly present in the following, they established the relevant superconducting and normal-state parameters that makes this material so interesting to visualize vortex creep at low temperatures. In this thesis we have performed the first microscopic study of the superconducting properties in this material.

5.2.1 $Rh_9In_4In_4$: crystallographic, thermodynamic and transport properties.

Synthesis and Crystal Structure

$Rh_9In_4S_4$ crystallizes in a tetragonal structure (spacial group I4/mmm), with three layers of Rh/S joined by In/Rh layers, along the z as shown in Figure 5.A (a). The unit cell parameters are $a = 7.79\mathring{A}$ and $c = 8.85\mathring{A}$ [98]. All the Rh atoms are six-coordinated, i.e., they are in the center of octahedras. According to the Rh surrounding atoms and bond distances, Rh has three different configurations in the unit cell whereas the In and S have two and one respectively (numbers in Fig. 5A (a)). The different positions and atomic configurations are extended in equivalent sites along the ab-plane and the c-axis. In particular, Rh(1) and S atoms form zigzag chains along the c-axis [98].

Figure 5A(b) shows the powder x-ray diffraction pattern of a ground phase pure, single crystal of $Rh_9In_4S_4$. Lattice parameters obtained from fits on the powder pattern coincide with the values of the tetragonal structure [98].

Single crystals of $Rh_9In_4S_4$ were grown using the solution growth technique [99, 100] described in Section 2.7 (Fig. 2.24). Details of the synthesis are explained in Ref. [98]. The thermodynamics and transport properties of the samples used in this work are shown in the following sections.

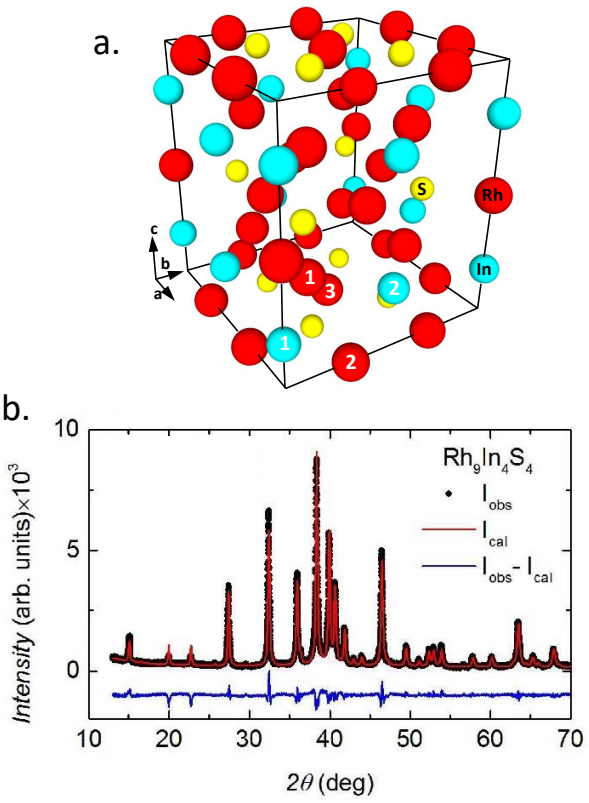

Figure 5.A (a) Crystal structure of $Rh_9In_4S_4$. Numbers represent different types of bounding on Rh and In [98]. **(b)** Powder diffraction pattern of $Rh_9In_4S_4$. Red line represents the calculated diffraction pattern. Blue line represents the difference between the experimental and calculated intensities [98].

Resistivity, Specific Heat and Upper Critical Field

Figure 5.1(a) shows the resistivity as a function of temperature of $Rh_9In_4S_4$ for current flowing along the a-axis. The resistivity decreases monotonically with a superconducting transition at $T_c = 2.25$ K. The samples have a residual resistivity ratio (RRR) ($\rho_{300K}/\rho_{5.5K}$) of 1.2.

The low temperature specific heat is shown in Figure 5.1(b). Fits for specific heat at normal state reveals a Sommerfeld coefficient of $\gamma = 34$ mJ mol^{-1} K^{-4}, a Debye temperature of $\Theta_D = 217$ K, and a specific heat jump of $\Delta C = 125$ mJ mol^{-1} K^{-1}. Thus $\Delta C/\gamma T_c = 1.66$ [98]. This value is bigger than the BCS weak-coupling limit of 1.43 [8, 29]. This difference and the value of the electron-phonon coupling constant[217], $\lambda_{e-ph} = 0.56$, indicate that the sample is an intermediate coupled superconductor [98].

Figures 5.1(c) and 5.1(d) show the resistivity as a function of the temperature and magnetic field for several measuring currents with H$\|$[011] in $Rh_9In_4S_4$. In both situations we observe two kinds of resistivity anomalies. At fixed magnetic fields, from 0.2 T to 1.2 T, the resistivity data show a kink in between the onset and the offset of the transition. At 1.8 T, this kink evolves with the temperature to a dip before increasing and then gradually going to zero. For higher currents these anomalies in resistivity become more prominent. A similar behavior is observed when the temperature is fixed and the magnetic field changes below 0.5 K (Fig. 5.1(d)). This

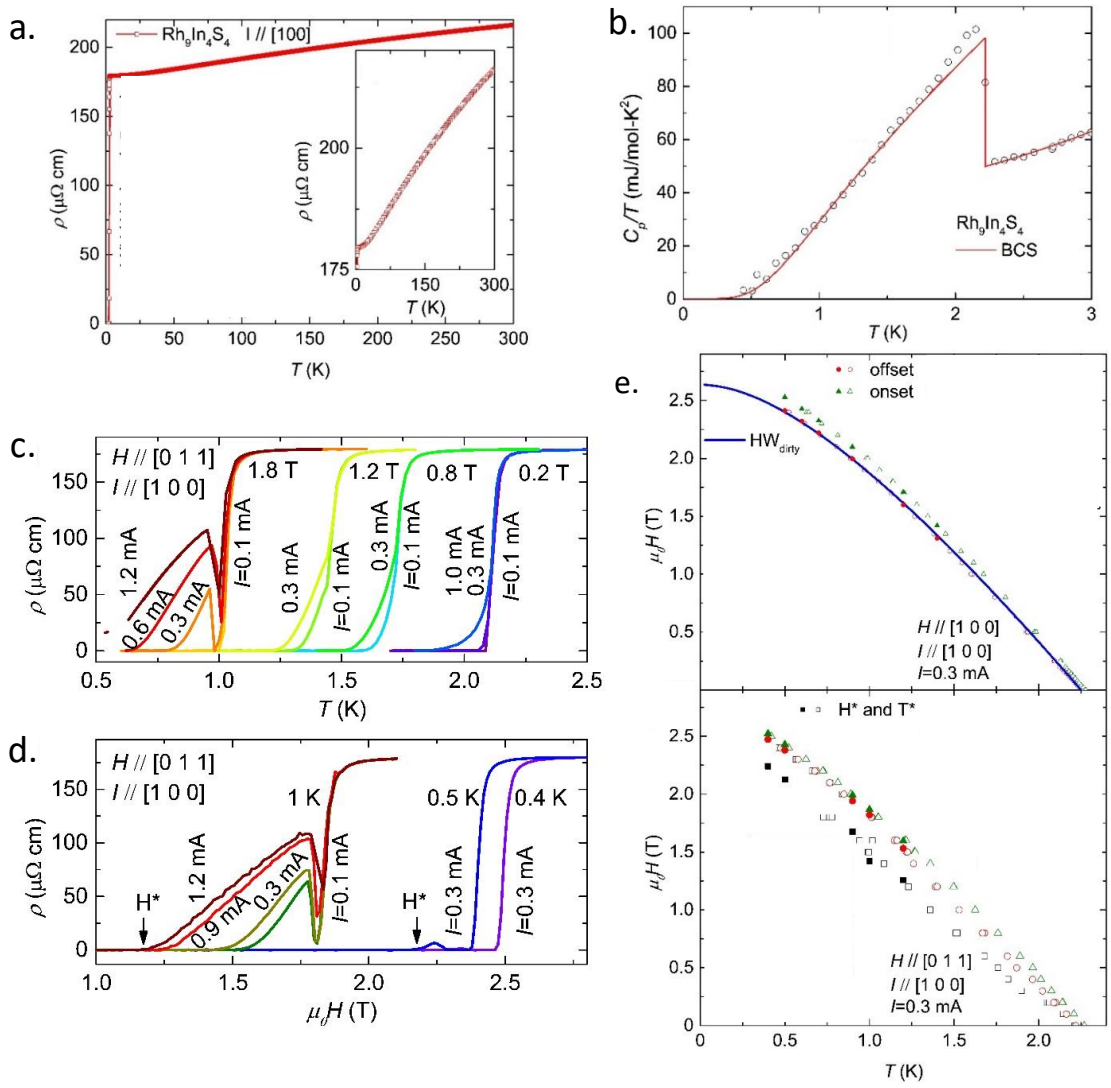

Figure 5.1 **(a)** Temperature-dependent resistivity of $Rh_9In_4S_4$ along [100]. The inset shows the normal state resistivity in expanded scale and weak negative curvature visible at high temperatures. **(b)** Low-temperature C_p/T vs. T of $Rh_9In_4S_4$. Red solid line represents the fit to BCS theory. **(c)** and **(d)** Low-temperature resistivity as a function of temperature and field respectively for several applied currents within H||[011] configuration where the current flows along the [1 0 0] direction. **(e)** Shows the upper critical field H_{c2} vs. T of $Rh_9In_4S_4$ for H||I *(upper panel)* and H⊥I *(lower panel)* with current along the *a*-axis. Solid and open symbols represent the data obtained by field scans and temperature scans, respectively. The blue solid line in **(c)** indicates the HW calculations for the dirty limit [98].

effect is called "peak effect" (or fishtail effect [218]) and has been observed in other type-II superconductors including Nb, $CeRu_2$, $NbSe_2$, V_3Si and MgB_2 [219, 220, 221, 222, 223, 224]. It appears as a sharp peak in the critical current as a function of temperature or magnetic field below $H_{c2}(T)$ [218, 225, 226]. For the explanation of the peak effect, several mechanisms have been proposed such as elementary pinning by weakly superconducting regions [227, 228], the synchronization of the flux line lattice [229, 230] and the reduction in elastic moduli of the flux line [203]. However, the underlying physics is not yet fully understood so far. The observation of peak effect in Rh_9In_4S indicates that pinning is important in our crystals.

Figure 5.1(e) shows the H vs. T phase diagrams for H||[100] (upper panel) and H||[011] (lower panel) configurations. The diagrams were obtained from R vs. T and R vs. H measure-

ments for $I = 0.3$ mA. Closed and open symbols represent data obtained from field scans and temperature scans, respectively. The peak effect is only noticeable in the H||[011] configuration [98]. Comparison between the phase diagrams indicates isotropic H_{c2} behavior. The experiment for H||[100] was compared with the Helfand-Wertharmer (HW) model for a one-band, type-II superconductor [34]. The experiment shows a good agreement with the calculated HW curve for the dirty limit (blue solid line in upper panel of Fig. 5.1(e). This is in agreement with the large value for the residual resistivity and the low RRR measured in this compound. The absence of multiband effects in the temperature dependence of H_{c2} shows that possible effects induced by anisotropic features in the Fermi surface are smeared out by disorder in this material.

In Table 5.1, we summarizes some of the measured and derived superconducting state parameters for $Rh_9In_4S_4$ presented by Kaluarachchi et. al. [98].

Relevant Parameters for $Rh_9In_4S_4$

Property	Value
T_c (K)	2.25
γ (mJ mol^{-1} K^{-2})	34
Θ_D (K)	217
ΔC (mJ mol^{-1} K^{-1})	1.66
$\Delta C/\gamma T_c$	1.66
ρ_0 ($\mu\Omega$ cm)	180
H_{c2}(T = 0) (T) (clean/dirty limit)	2.78/2.62
H_c(T = 0) (mT)	25
ξ_{GL} (Å)	94
λ_{GL} (Å)	5750
$\kappa = \lambda_{GL}/\xi_{GL}$	61

Table 5.1 Relevant superconducting and normal-state parameters for $Rh_9In_4S_4$. Data from Ref. [98]

5.3 Sample and surface preparation

We used crystals with lateral sizes between 1-3 mm and transversal areas less than 1 mm^2 for the STM experiments at low temperatures. Figure 5.2(a) shows pictures of the samples. To prepare the surface, we tried to cleave the samples in both ambient and cryogenic conditions using the pulling system described in Section 2.5 (Figs. 2.21 and 2.22). We combined this with either a ceramic blade or a piece of brass glued on top of the crystals so as to break the crystals by pushing on the slab at low temperatures. Most often crystals did not break and the few ones that broke revealed irregular surfaces which were not shiny and where we did not achieve stable tunneling conditions as we find usually in metals with a cleaving plane. We finally obtained good results by using the pristine as-grown samples.

This method provides good results in many materials, such as 2H-$NbSe_2$, MgB_2 or β-Bi_2Pd, but one cannot totally eliminate surface contamination. Nevertheless, we have been able to find excellent scanning conditions at low temperatures, with reproducible imaging, being independent of the tunneling conductance. The in-situ positioning system described in Section 2.5 (Fig. 2.20) was very useful to change the scanning window and find positions that were clean and showed good tunneling conditions.

Vortex lattice STS images were taken at fixed magnetic field applied parallel to the c-axis. We normalized the tunneling conductance to one at bias voltages above 0.8 mV. Vortex lattice images are obtained by making maps of the normalized zero bias conductance as is described in Section 2.4.2. We applied the magnetic field along the c-axis. No filtering nor treatment has been

made to the images we present here. We mostly measured in field cooled conditions although zero field cooled experiments lead to quite similar results. We did not vary systematically the temperature and magnetic field history. The results I will present in relation to vortex creep are representative for situation in which we observed moving lattices at the lowest temperatures.

5.4 STM/S on $Rh_9In_4S_4$ at zero magnetic field

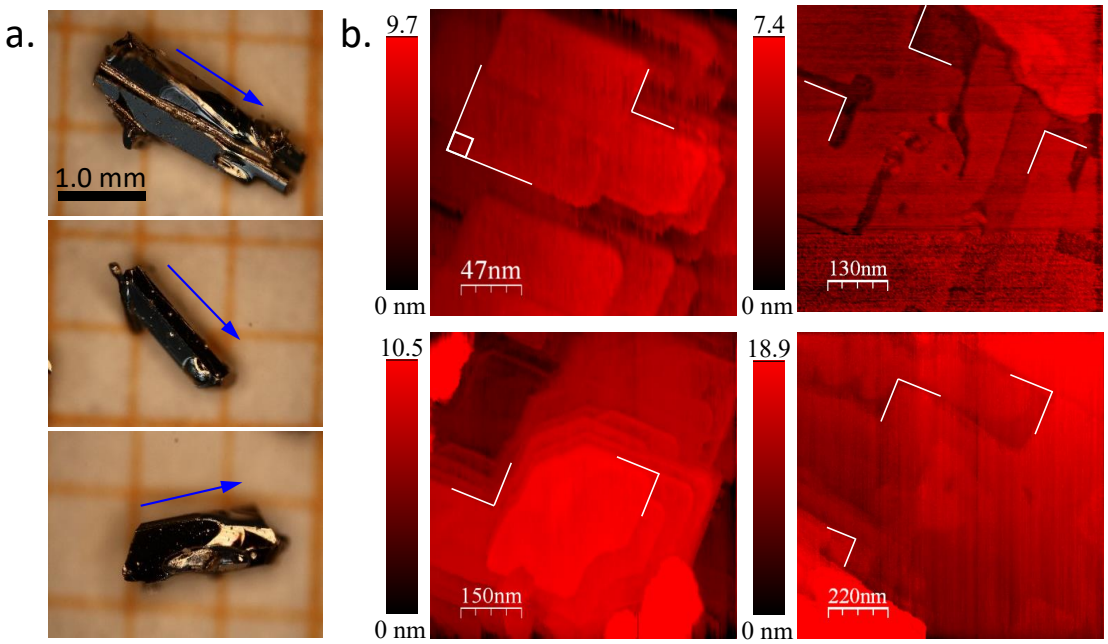

Figure 5.2 (a) Photographs of a few single crystals of $Rh_9In_4S_4$, with t arrows pointing to the [100] direction. **(b)** Topography images at 150 mK on different samples of $Rh_9In_4S_4$. We observe big flat areas in between steps. The white dashed lines represent the right angle at the corners of the steps, suggesting that steps are aligned with the crystalline directions. Images were taken at bias voltage of 2 mV and conductance 0.1 mS.

Surface Characterization

Figures 5.2 (b) and 5.3 show typical topographic STM images that present big flat areas with square symmetry. We did not obtain atomic resolution, although we always observe steps that are integers of the c-axis unit cell. We observed flat areas of $\approx$ 50-200 nm^2 in between steps that most often appear aligned along two particular perpendicular directions (highlighted by white lines in Fig. 5.2(b)). This feature can be related with the square symmetry on *ab*-plane.

Density of States and Superconducting Gap in $Rh_9In_4S_4$

Figure 5.4(a) shows the tunneling conductance as a function of temperature (left panel). At the lowest temperatures we observe a smeared tunneling conductance that deviates strongly from the high quasiparticle peaks and zero bias conductance expected in a simple s-wave superconductor (see e.g. [97]). The tunneling conductance remains mostly unaltered as a function of the position over the surface, both in the value of the zero bias conductance and the shape of the quasiparticle peaks.

In order to find the superconducting gap, we de-convolute the density of states from the tunneling conductance (using the derivative of the Fermi function at each temperature, see Fig. 2.12 and Refs. [112, 231]). The temperature dependence of the density of states is shown in right

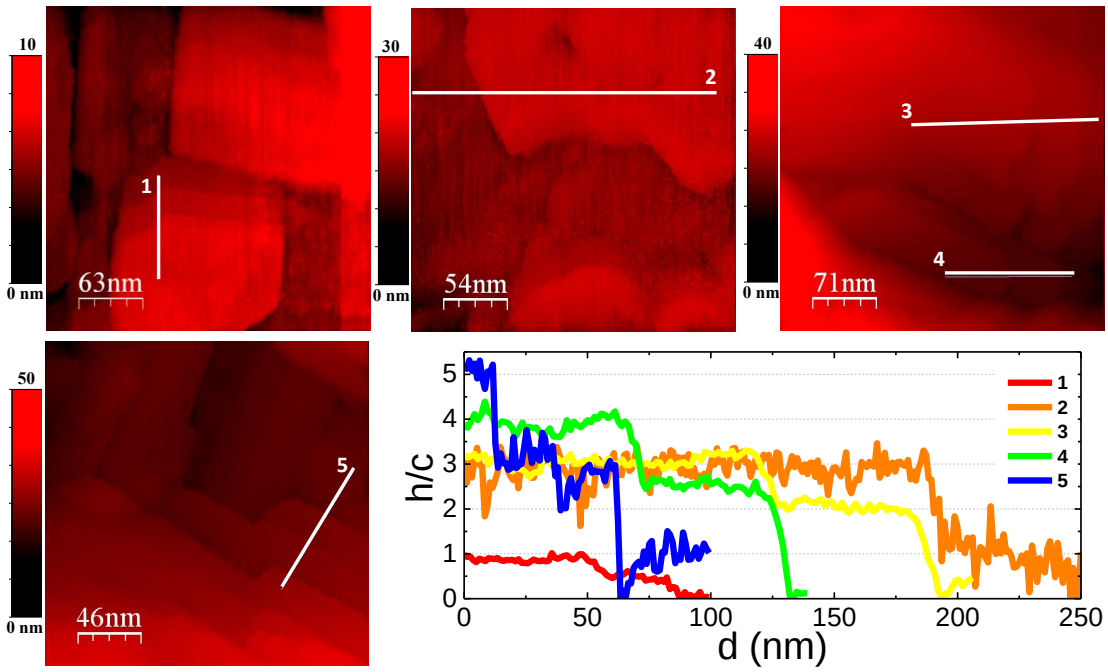

Figure 5.3 Topography images at 100 mK on single crystals of $Rh_9In_4S_4$. In the lower right panel we show different height profiles along the white lines shown in the images. We normalize the vertical displacement to the c-axis parameter. The distance between consecutive surfaces corresponds to integers of the c-axis unit cell.

panel of Fig.5.4(a). We observe that the density of states becomes featuresless at a temperature of 2.3 K, which coincides with the transition temperature from resistivity measurements found in Ref.[98]. The quasiparticle peaks in the density of states are located at an energy of 0.33 meV, which is the value expected for the superconducting gap within simple s-wave BCS theory ($1.76k_BT_c$). The temperature dependence of the position of the quasiparticle peaks also follows expectations from single gap s-wave BCS theory (Fig.5.4(b)).

The size of the superconducting gap found with our measurements coincides well within expectations from macroscopic measurements and simple gap s-wave BCS theory. The appearance of a finite density of states at the Fermi level remains however unexplained. Whereas other intermetallic compounds such as MgB_2 or β-Bi_2Pd, prepared under similar conditions (although with a much larger mean free path), show zero tunneling conductance withing the gap [104, 97, 231]. However, this is not the case in $Rh_9In_4S_4$.

Measurements in strongly disordered superconducting thin films with very short mean free path often show superconducting tunneling conductance curves with a high zero bias conductance withing the gap [232, 233]. It is thus tempting to associate this feature to the short mean free path also found in $Rh_9In_4S_4$. However, we cannot exclude some sort of surface contamination which could eventually lead to a normal contribution to the tunneling conductance by, for instance, a normal surface layer.

Furthermore, the bulk density of states is clearly zero within the gap, as shown by specific heat measurements (Fig. (b)), [98]. This being said, we observe the bulk T_c and H_{c2}, as well as the value of Δ expected within s-wave BCS theory, so that the tunneling conductance reflects indeed bulk features.

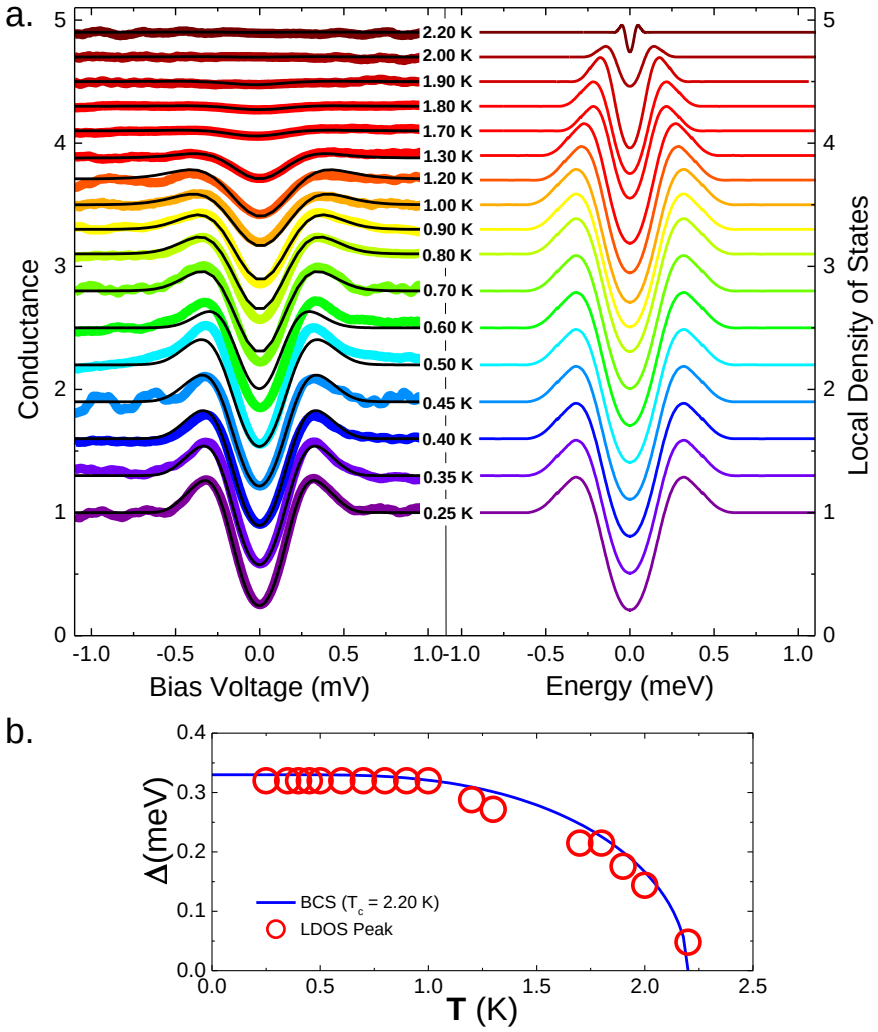

Figure 5.4 **(a)** Tunneling conductance curves are shown at different temperatures in the left panel. Black lines are the fits obtained from convoluting the density of states shown in the right panel with the derivative of the Fermi function at each temperature (See. eq. ECUACIÓN DEL SEGUNDO CAP). **(b)** Temperature dependence of the position in energy of the quasiparticle peaks of the density of states (right panel in (a)). The blue line is the expression from BCS theory, using $\Delta = 1.76 k_B T_c = 0.33$ meV obtained with $T_c = 2.20$ K.

5.5 STM/S on $Rh_9In_4S_4$ under magnetic field

5.5.1 Vortex Lattice and Cores in $Rh_9In_4S_4$

Fig. 5.5 shows images of the vortex lattice with the magnetic fields along the c-axis from 0.2 T up to 2.0 T, which is close to $H_{c2} \sim 2.5$ T. The intervortex distance decreases as expected for the hexagonal vortex lattice, $d = 1.075\sqrt{\phi_0}/B$ (with ϕ_0 being the flux quantum). We do not observe signatures of Caroli-de Gennes-Matricon Andreev core states [41, 112, 40]. Instead, the normalized tunneling conductance at the vortex center reaches one. This is not much surprising, taking into account that $Rh_9In_4S_4$ is strongly in the dirty limit, as discussed in the previous section, and that the discrete core states are expected to turn into a continuum in the dirty limit [146].

We discuss the vortex lattice orientation in Fig. 5.5(b). There we show the position of the six lowest Bragg peaks from the Fourier transform of the vortex lattice images obtained at different

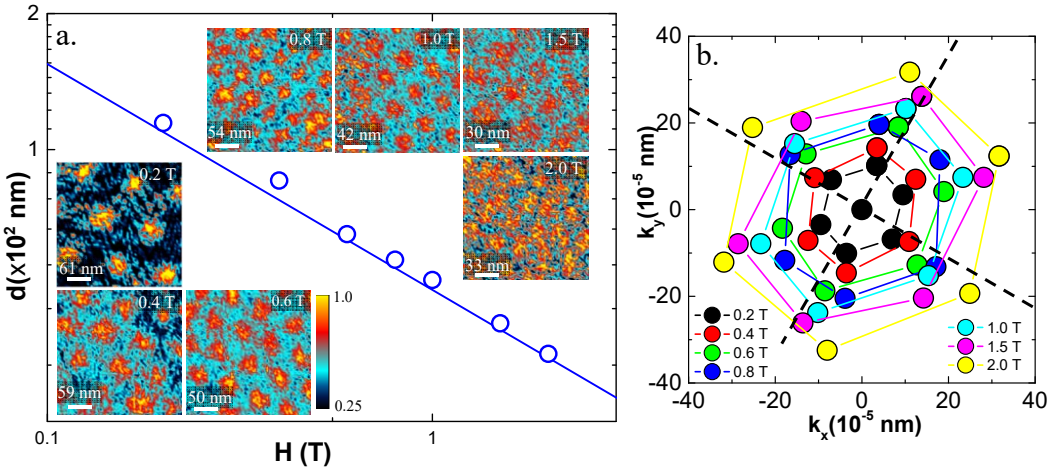

Figure 5.5 (a) Vortex lattice evolution as a function of the magnetic field at 150 mK. The insets show zero bias conductance images at different magnetic fields (and at different scanning windows). Contrast in the zero-bias conductance maps is shown by the vertical color scale bar. We plot the obtained intervortex distance vs. the magnetic field as open circles. The blue line is the prediction for a hexagonal Abrikosov lattice. **(b)** Main six Bragg peaks of the vortex lattices shown in **(a)**. Black lines have the same orientation of the steps (white lines) of figure 5.2(b).

magnetic fields. As we do not find atomic resolution, we cannot obtain the actual orientation of the vortex lattice with respect to the crystalline axis by comparing atomic and vortex lattice images, as we made previously in the tetragonal material β-Bi_2Pd (Figs. 3.11 and **??**) [97]. However, we find that the Bragg peaks of the vortex lattice images are mostly oriented along the directions defined by the steps observed at the surface (marked as white lines in Fig. 5.2(b)). The average deviation around this position is approximately $\sim$7-10°. This shows that the vortex lattice orients along one of the two crystalline directions of the square atomic lattice at the basal plane, similarly as in the compound $\beta-Bi_2Pd$ (See Chapter 3) [97].

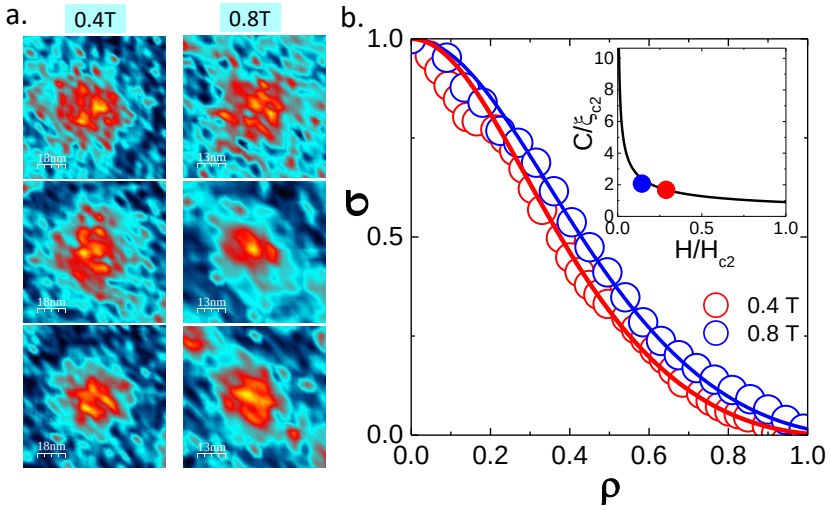

Figure 5.6 (a) Vortices at 0.4 T and 0.8 T analyzed to obtain the vortex core radius following the method described in Ref. [168] for a single gap superconductor. **(b)** Normalized tunneling conductance σ vs. normalized distance ρ obtained from vortices shown in **(a)** (points represent the experimental data and continuous lines are the fits obtained using the model (see text for normalization procedures). Inset shows the core size $\mathscr{C}$ vs. the magnetic field. Dots are the values of $\mathscr{C}$ obtained from the fits given in the main panel. Continuous black line is proportional to $1/\sqrt{H}$.

All these data show that the properties of the superconducting vortex lattice follow expectations for a simple type-II superconductor.

We have furthermore applied same method used in Chapter 3 for $\beta-Bi_2Pd$ [Ref. [168]] to find the vortex core radius in $Rh_9In_4S_4$. We make a radial average of the tunneling conductance σ (normalized in such a way as to provide one at the vortex center and zero in between vortices) around the center of a vortex. We then fit the result to the radial dependence of the density of states. We use only images made at low fields (Fig. 5.6(a)), where we obtain sufficient contrast to perform the analysis. The experimental result is shown as points and the fits as lines in Fig. 5.6(b). From the fits, we obtain the vortex core radius $\mathscr{C}$ (inset of Fig. 5.6(b)). We find values around two times the superconducting coherence length ξ_{c2} obtained from H_{c2}. They are in rough agreement with the expected dependence as $\mathscr{C} \propto 1/\sqrt{H}$ [168]. Extrapolating these values to H_{c2}, gives ξ_{c2} obtained from H_{c2}, as expected within the theory of Ref. [168].

We have also analyzed the magnetic field dependence of the intervortex density of states by taking tunneling conductance curves exactly in between three vortices at 150 mK. The result is shown in Figure 5.7. We find that the intervortex density of states at the Fermi level increases linearly with the magnetic field, extrapolating to one at H_{c2}. This is again in agreement with the result expected for a simple s-wave BCS superconductor.

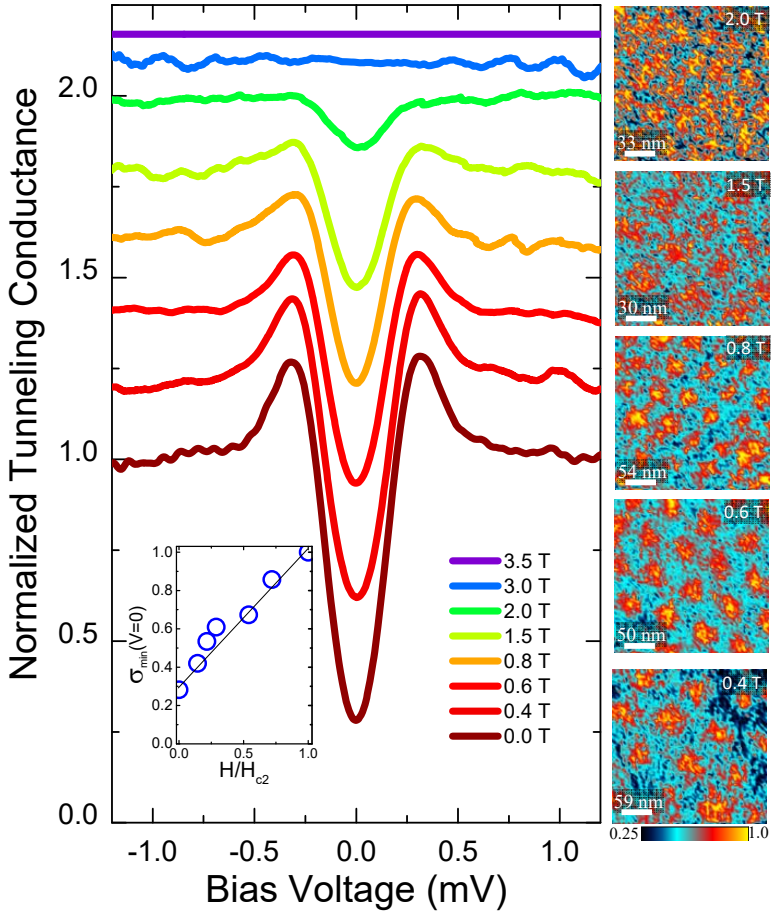

Figure 5.7 Magnetic field dependence of the full normalized tunneling conductance σ_{mid} obtained at the center point between vortex cores. Curves are shifted vertically for clarity. Some images are shown at the right panel. Inset shows the magnetic field dependence of the σ_{mid}(V = 0 mV) (blue points). Line is a guide to the eye.

5.5.2 Vortex creep at very low temperatures

Very often we find that that vortices are moving in our vortex lattice images. This occurs at temperatures as low as 150 mK and after remaining more than one day at the same magnetic field. The mobility of the vortex lattice depends strongly on the position. In Fig.5.8 we show experiments in some of these moving lattices at three different magnetic fields (0.4 T, 0.6 T and 0.8 T). To be able to observe vortices under these conditions, we have decreased the imaging time to just a few minutes and acquired consecutively images over the same area during a period of several hours. For instance, we took 51, 17 and 40 consecutive images at respectively 0.4 T, 0.6 T and 0.8 T. Fig.5.8 shows some of the vortex images taken at each magnetic field. When comparing different images within the same series, we can clearly see that vortex positions change with time.

In Fig.5B we show the average over each series of consecutive images shown in Fig. 5.8 (left panels of Fig.5B) and the vortex trajectories during the whole experiment (right panels of Fig.5B) at, respectively, 0.4 T *(upper panel)*, 0.6 T *(middle panel)* and 0.8 T *((lower panel))*. The vortex velocity is completely different in each image. We observe net vortex motion in the two upper panels, whereas in the lower panel, vortices appear to fluctuate around their positions, rather than moving along a certain direction. Vortex velocity is, on average, of 100 nm/h in the upper panel and of 40 nm/h in the middle panel. In the upper panel, we find that vortices move along a main axis of the vortex lattice and that vortex motion is smooth, without any signature of jumps or steps. To show the correlated nature of motion, we have acquired an image (Fig.5.9) during 16 hours at the same position where we did the experiment shown in the upper panel of Fig.5B. Scanning was very slow, so that vortices were moving below the tip. The image gives a highly compressed vortex lattice along one direction. By stretching the image with the intervortex distance at this magnetic field (0.4 T), we reproduce a highly ordered hexagonal vortex lattice over the whole time window (Fig.5.9d). The scanning direction is important to understand this effect (Fig.5.9c). The fast scanning axis is along a direction nearly perpendicular to vortex motion. Therefore, vortices appear compressed along the slow scanning direction. For this to work, there must be a relation between vortex and tip motion. Vortices have to move with a constant velocity over the time frame given by the time a vortex remains below the tip, which is of approximately two hours. In this experiment, the vortex lattice moves in the opposite direction to the slow scanning motion. The tip velocity along this direction is of $v_{tip} = 18nm/h$. Using this velocity and the ratio between the intervortex distance expected for this field, d, and the value found in the compressed vortex lattice, d', we obtain for the vortex velocity $v = (d/d' - 1)v_{tip} = 100nm/h$. This value

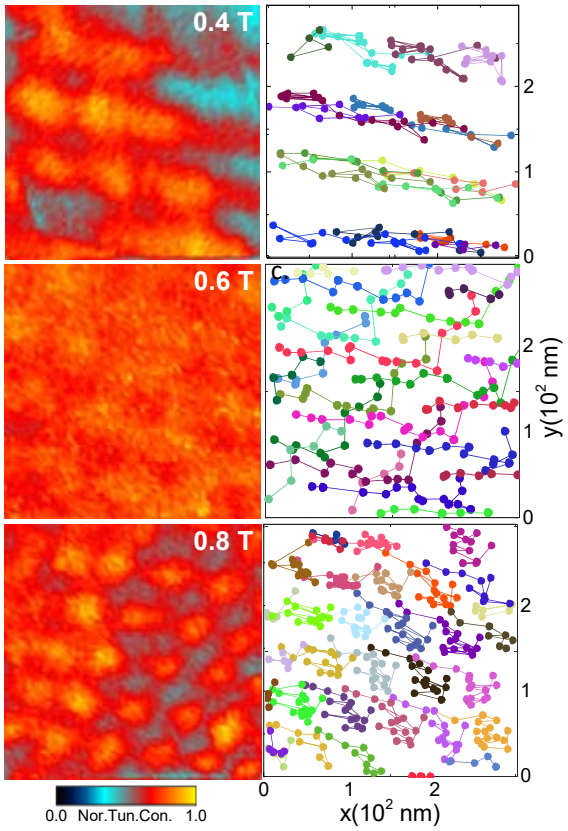

Figure 5B. *(Left)* Average images over all spectroscopy maps provided partially in Fig. 5.8 which show the moving vortex lattice at 0.15 K and 0.4 T, 0.6 T and 0.8 T. Color scale is given by the horizontal bottom bar. *(Right)* Trajectories of vortices (points). Lines joining the points provide the sequence of motion between consecutive images.

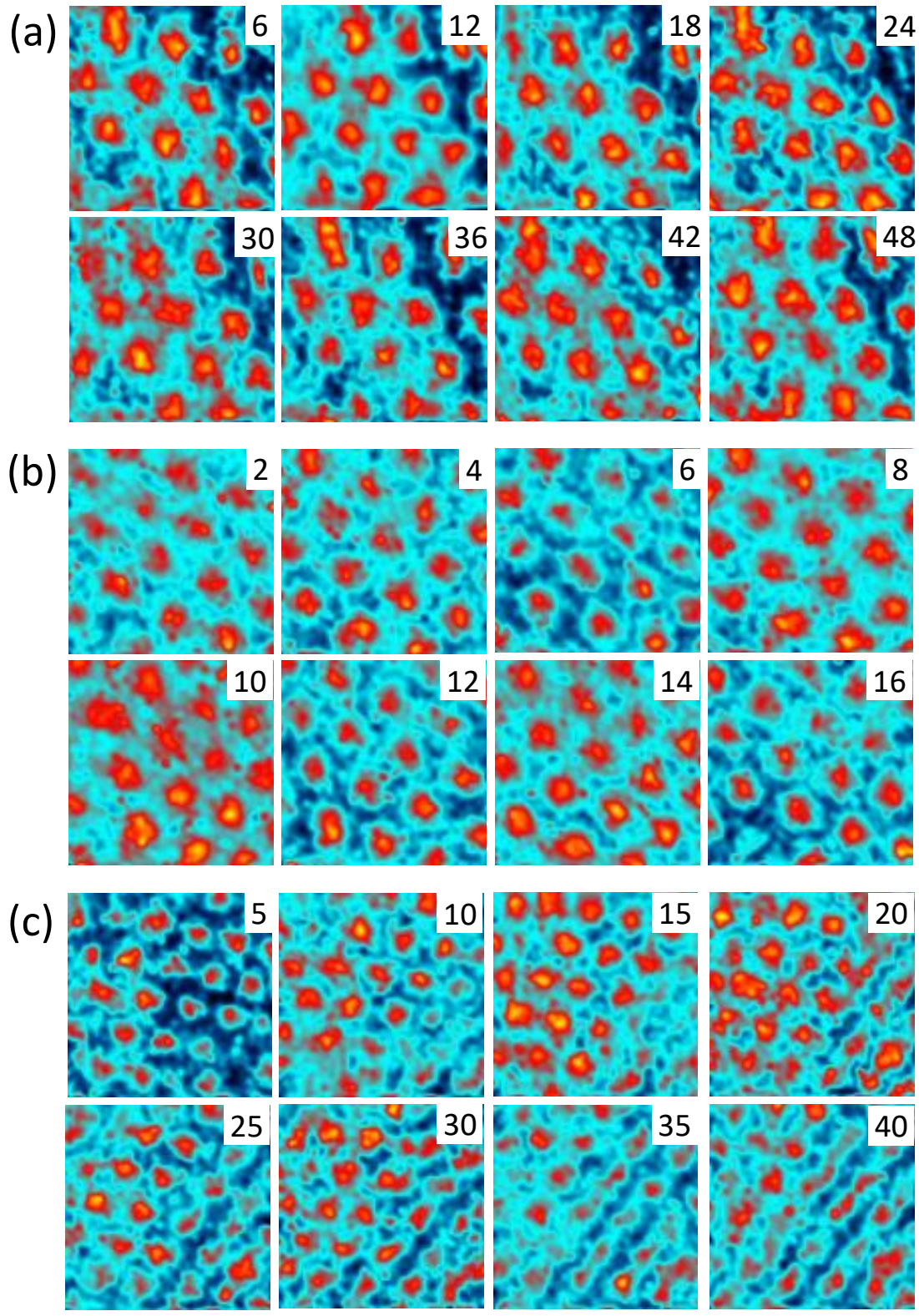

Figure 5.8 (a) Some of the tunneling conductance maps of the moving vortex lattice in $Rh_9In_4S_4$ at 0.4 T (a), 0.6 T (b) and 0.8 T (c) and 0.15 K (∼18 min/map). Numbers indicate the frame at each magnetic field. Same color scale as in Fig. **??**.

coincides with the value measured by making fast consecutive images discussed above in the same field of view (upper panels of Fig.5B).

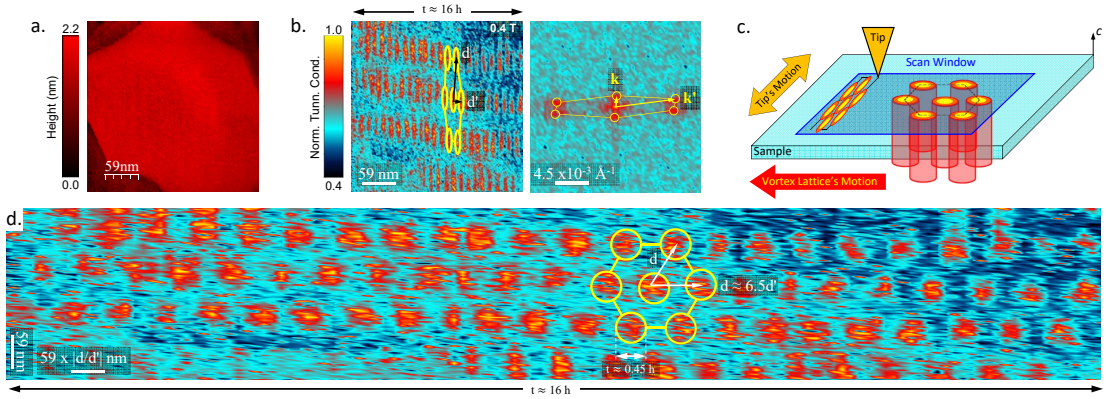

Figure 5.9 (a) Topography image of the spectroscopy map at 0.4 T and 150 mK shown in left panel of **(b)**. Color scale is given by the vertical bar. In**(b)** we show a (left) single image of a moving vortex lattice, taken during 16 hours at the same conditions as in image shown in **(a)**. Due to vortex motion, the vortex lattice appears squeezed in one direction. We mark one hexagon with yellow circles and the observed lattice constants d and d' with black arrows. From its Fourier transform (right panel) we find that the the intervortex distance along the y-axis of the image corresponds to the value expected at 0.4 T, $d \sim 75$ nm. Along the axis where the vortices move, we find $d' \sim 11.5$ nm. In **(c)** we provide a cartoon of the situation found in **(b)**. The vortex lattice (cylinders in a hexagonal configuration) moves along the direction given by the red arrow. The direction of the scan is given by the orange arrow. The scanning window is schematically marked by a blue square. **(d)** We show the same image shown in **(b)**left, but stretched along the x-axis by d/d'. We show again the hexagon with yellow circles and the lattice constant d with white arrows.

Moving vortex lattices have been imaged in real space at very low magnetic fields using magnetic decoration and at high magnetic fields using STM [211, 212, 213, 234, 214]. Flowing vortex lattices with different structure factors changing from hexagonal to smectic-like have been discussed [235]. Smectic structures forming channels where vortex positions are uncorrelated along the flow direction but correlated perpendicular to it appear more often at low magnetic field where intervortex interaction is weak [236]. In contrast, crystalline-like hexagonal moving lattices are predicted for stiff dense lattices under high driving currents suggesting that motion can induce order in the vortex lattice. The latter, known as moving Bragg glass, are free from topological defects and show long range positional and orientational correlations [237, 238]. For instance, the smectic driven phase has been observed in 2H-$NbSe_2$ at extremely low fields and high driving currents, with crystalline order appearing at higher fields [211]. In our experiment, we measure at high fields in the dense lattice regime and at very low temperatures where the stiffness is maximum. We find that the lattice flows maintaining a crystalline structure but, contrary to previous cases, the flow velocity is low and, importantly, the resulting creep rate strongly changes as a function of the position. This indicates that creep is likely induced by diverging vortex barriers produced by an inhomogeneous distribution of pinning centers for low currents.

As mentioned in the introduction of this chapter, creep can be thermal and quantum activated. The relevant scales are given, respectively, by the collective pinning energy [24]

$$U_c = H_c^2 \xi^3 \left(\frac{j_c}{j_0} \right)^{1/2} \tag{5.2}$$

and the Euclidian action

$$S_E = \frac{\hbar}{Q_u}\left(\frac{j_0}{j_c}\right)^{1/2} \tag{5.3}$$

with H_c the thermodynamic critical field, ξ the coherence length, j_c and j_0 the critical and the depairing current densities (current value at which the kinetic energy of the superconducting electrons exceeds the binding energy of the Cooper pairs) and Q_u the quantum resistance defined as

$$Q_u = \frac{e^2}{\hbar}\frac{\rho_n}{\xi} \tag{5.4}$$

The crossover temperature

$$T_0 = \frac{\hbar U_c}{S_E} \tag{5.5}$$

determines the temperature below which quantum effects dominate.

In $Rh_9In_4S_4$, we find $U_c = 7K$ using $j_c = 3\times10^8 A/m^2$ [239], $j_0 = 3\times10^10 A/m^2$ and the superconducting parameter for this material presented in Table 3.1. On the other hand, superconductors with a large normal state resistivity and small coherence lengths, i.e., quantum resistance Q_u of the order of a kΩ are candidates for quantum creep [25]. In $Rh_9In_4S_4$, Q_u if of 4×10^{-2} in between the values reported for conventional superconductors ($Q_u \sim 10^{-3}$) where quantum effects are negligible and high T_c superconductors ($Q_u \sim 10^{-1}$) where the quantum fluctuations are large [24]. When comparing thermal and quantum contributions, we find that the crossover temperature T_0 is of about 30 mK, indicating that, even at 150 mK, motion is thermally activated.

Generally, vortex motion is related to the inertial mass of the vortex. The vortex mass has been estimated using different approaches. In dirty superconductors, the vortex mass is given by the amount of normal electrons in the vortex core, $\mu \propto m_e\xi^2 n_0$ with m_e the effective electronic mass, ξ the superconducting coherence length and n_0 the electron density, and gives typically a few thousand electron masses[240, 241]. The value of n_0 in $Rh_9In_4S_4$ found in Hall effect measurements made in Ames in similar samples is close to the values reported in normal metals. Thus, the vortex dynamics in $Rh_9In_4S_4$ is expected to be conventional and dominated by the pinning landscape.

Vortex motion is expected to be overdamped due to the small value of the vortex mass, except in the clean limit where the vortex core states play a relevant role, meaning that, in general, no resonances or characteristic quantum effects might appear in the quantum limit for vortex creep[242, 243, 244, 245, 246]. Materials with a higher residual resistivity could show a larger range of quantum activated vortex motion than $Rh_9In_4S_4$.

Thus, our data show that thermally activated vortex creep is compatible with diverging vortex barriers for low currents, which result in spread values for vortex velocities, depending on the actual position and probably also on the magnetic field and temperature history. Creep leads to correlated motion in a hexagonal lattice over large amounts of time. It seems quite clear that the length over which the lattice keeps the hexagonal order, known as the Larkin length, is in this superconductor well above the image size (comprising here one or two hexagons), so that the overall behavior of the vortex lattice reflects glassy properties within hexagonal order[203]. In any event, here we show that, for small sized vortex bundles and small driving currents, pinning of isolated vortices plays a minor role in the motion, which rather reflects collective thermally activated motion over the pinning landscape.

5.6 Concluding Remarks

The $Rh_9In_4S_4$ is a superconductor with extreme type-II behavior that leads to interesting dynamic vortex behavior at very low temperatures. The origin for the high normal state resistance in this system remains puzzling. The resistivity is nearly temperature independent, with a residual resistance ratio of 1.2. The tetragonal crystalline structure shows a modulation whose properties remain to be understood[98]. Present results suggest that the observed high resistance is a consequence of strong disorder and also leads to unusual residual vortex dynamics at very low temperatures.

We have determined the superconducting gap of $Rh_9In_4S_4$, showing that it follows expectations from simple s-wave BCS theory. We have observed that the superconducting vortex lattice has hexagonal symmetry and locks to the square crystalline lattice. The vortex core size provides values of the coherence length comparable to those obtained using macroscopic upper critical field measurements.

We have obtained first direct observations of vortex creep at mK temperatures ($T/T_c < 0.1$) using STM, making this material adequate to study vortex creep using macroscopic experiments. From our direct observation, we conclude that the creep velocity strongly depends on each experiment, and show that the local distribution of pinning centers influences vortex creep, so that the hexagonal vortex lattice has glassy dynamic properties.

6 - Signatures of the SC gap in URu_2Si_2

Marty McFly: *Whoa. This is heavy.*
Dr. Emmett Brown: *There's that word again. "Heavy."*
Why are things so heavy in the future?
Is there a problem with the Earth's gravitational pull?
Back to the Future (1985)

Steven Spielberg

Among the heavy fermion compounds there exists a very special problem, the so called hidden-order transition (HO) in URu_2Si_2. This transition is considered by many as the condensed matter equivalent to the dark matter problem in high energy physics [247]. The microscopic excitations leading to this phase have been a mystery since its discovery 30 years ago [248, 249]. Much effort has been devoted to understand this ground state and its elementary excitations, without a definitive outcome yet [56, 57]. Superconductivity (SC) emerges in URu_2Si_2 at $T_c = 1.5$ K. This new phase has been characterized by thermodynamic and transport measurements [248, 250, 251, 252, 253], however, no atomic scale study of the density of states in the superconducting phase has been made yet.

This chapter presents measurements that solve some of the outstanding issues in the low energy behavior of the electronic excitations in URu_2Si_2 and how the superconducting phase emerges inside the anomalous normal phase properties of this material. The first part provides a general review of those properties of the URu_2Si_2 compound that I believe are useful to understand the rest of the work. The second part exposes some details about the crystal's quality and experimental procedures. The third part discuses the topographic characterization in the URu_2Si_2 after a cryogenic cleavage. The spectroscopy study of the SC phase within the HO phase is presented in the fourth part. Section five exposes the experimental results derived of quasiparticle interference imaging (QPI). In the sixth section of the chapter, we analyze some unidirectional electronic modulations observed in the topography maps at 150 mK. Finally, some concluding remarks are presented.

6.1 Spin, electronic and structural changes caused by Hidden Order

Among the U-Heavy fermion superconductors family, the URu_2Si_2 system is one of the most perplexing, and, in spite of having understood much of the properties of its elementary excitations, it remains a puzzle how to classify these within present knowledge.

URu_2Si_2 crystallizes in a body-centered tetragonal structure (spacial group I4/mmm) with constants $a = 4.12\AA$ and $c = 9.58\AA$ (Fig. 6A). According to Mydosh et. al., [248], the first published references on the superconducting and "antiferromagnetic" phase transitions at 17.5 K on URu_2Si_2 appeared in 1985 [254] and 1986 [255, 256]. While the bulk superconductivity was confirmed at $T_c \approx 1.5$ K, differences on the interpretation of the magnetic transition at 17.5 K started the controversial road to reveal the elementary excitations in this phase. From that moment, the origin of the transition is unknown and the term hidden order (HO) was linked for the mysterious phase appearing at $T_{HO} = 17.5$ K. Figure 6.1 illustrates the first reports on the two phase transitions in the specific heat and the resistivity at low temperatures [254, 257]. The superconducting transition temperature T_c varies significantly (between 0.8 and 1.5 K) according to the crystal growth method [248]. Transport and thermodynamic measurements indicated a considerable Fermi-surface reconstruction occurring at the HO transition [258, 248]. The jump in resistivity and the measured electronic specific heat in the HO state at the T_{HO} (see Fig. 6.1) are consistent with the opening of a energy gap (Δ_{HO}) over substantial part of the Fermi surface.

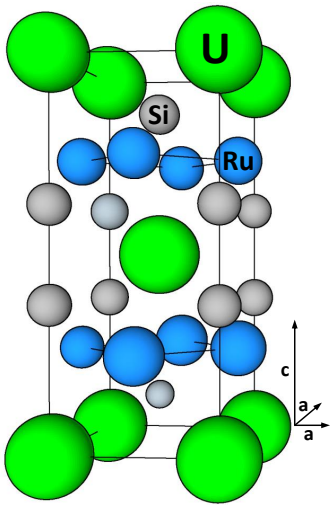

Fig. 6A Crystal structure of body centered tetragonal URu_2Si_2.

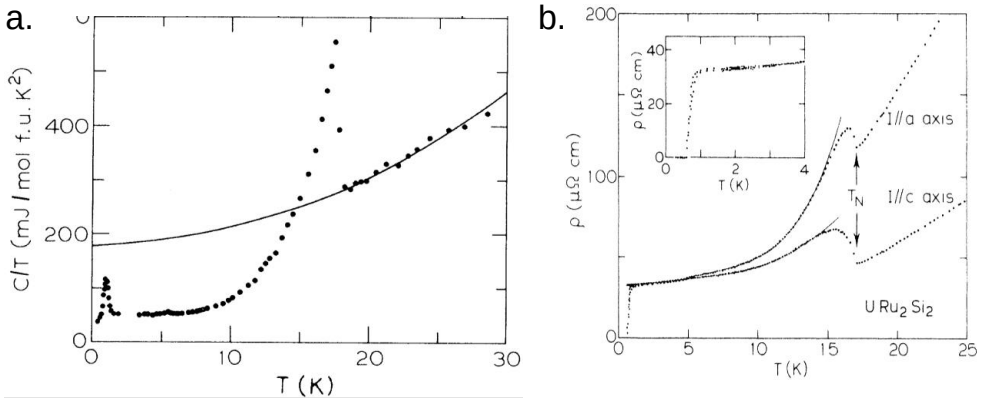

Figure 6.1 (a) Normalized Specific heat, C/T as a function of the temperature showing the hidden order (T_{HO}) and superconducting (T_c) phase transitions.**(b)** Low-Temperature resistivity along the a and c axis showing T_{HO} and T_c. Plots from Refs. [254] and [257].

Initially, the superconducting phase received some attention [248, 259]. However, most of the experimental and theoretical work deals with trying to explain the HO transition [260, 261, 262, 56, 57, 249, 263, 264, 265, 250].

6.1.1 Hidden Order and Spin gap.

One of the first approaches to elucidate the magnetic response of the URu_2Si_2 was done by neutron and x-ray magnetic scattering [266, 267].

Detailed neutron experiments to detect the magnetic excitations at low temperatures were performed by Broholm et. al. [266]. They observed a continuous magnetic excitation spectrum, with two distinct gapped modes appearing at the commensurate wave vector $\mathbf{Q_0} = (1,0,0)$ and

at $\mathbf{Q_1} = (1 \pm 0.4, 0, 0)$. These modes are commensurate and incommensurate, respectively with the lattice. They sharply form at $T \leq T_{HO}$ with gaps of about 2 to 4.5 meV and were designed as ordinary magnon modes [248, 266].

The group of Grenoble, has studied the magnetic response in URu_2Si_2 with special focus at $\mathbf{Q_0}$ [268]. They have analyzed the dynamical spin susceptibility $\chi(Q, \omega, T)$, which is related to the spin-spin correlation function, above and below T_{HO}. They observed correlations at $\mathbf{Q_0}$ as a function of the temperature, with a spin-gap energy Δ_{spin} and a BCS-like T behavior of the integrated imaginary susceptibility (see Fig. 6.2). The temperature dependence of the sharp low energy excitation at the wave vector $\mathbf{Q_0}$ shows that this resonance is a signature of the hidden order state.

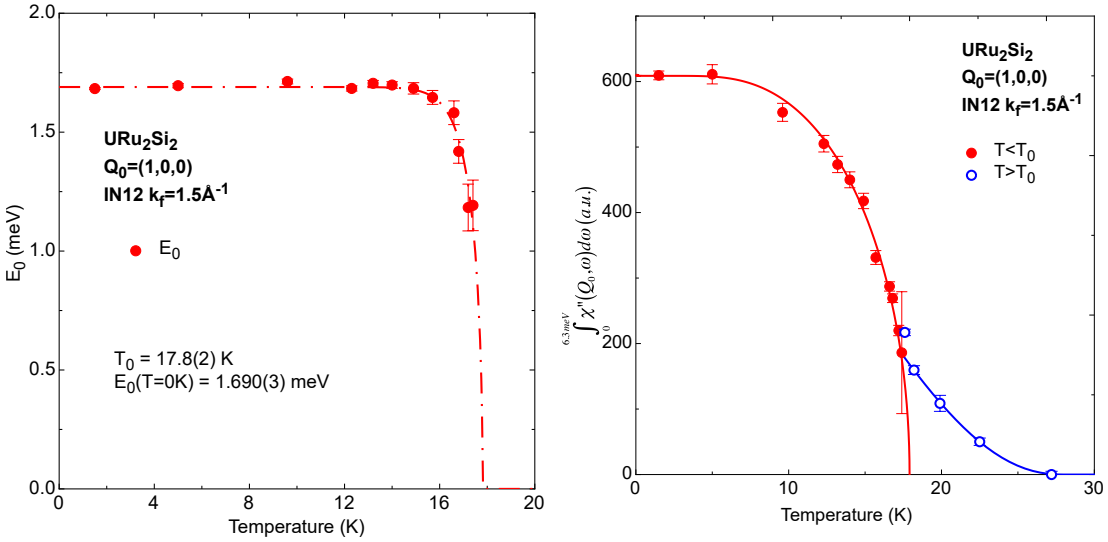

Figure 6.2 (Left) Temperature dependence of the spin resonance gap Δ_{Spin} (E_0 in refs. [248, 268]). Note the sudden onset upon entering the HO state. (Center) The integrated dynamical spin susceptibility of the antiferromagnetic spin resonance as a function of the temperature. The integrated intensity displays order parameter behaviour and thus tracks the Order Parameter of the HO. It is much faster than the temperature evolution of the BCS-type gap [248, 268, 269]

6.1.2 Hidden Order and Charge gap.

Two groups at Princeton (Ref. [56]) and Cornell (Ref. [57]) have been the pioneers in detecting the atomically resolved properties of the URu_2Si_2 and shown by spectroscopy measurements the presence of the HO gap (Δ_{HO}). Figure 6.3 shows their results on topography and spectroscopy. Both groups have characterized surfaces which are atomically ordered with a lattice spacing corresponding to either U or the Si. However, they did not agree on which surface was actually there. This is an important issue that was left insolved.

Therefore, the presence of multiple surfaces for cleaved URu_2Si_2 samples, (U [56, 270], Si [57] or Ru [56, 66, 270]) indicates that obtaining local surface structure information is critical to identifying which spectroscopic properties are more related to the bulk properties [56].

The Δ_{HO} have characterized using STM by Aynajian et. al. [56]. They are fitting the spectra to a thermally convoluted DOS with a BCS form, from which the magnitude and temperature dependence of the Δ_{HO} is extracted. Figure 6.4 shows some of the results from which the authors identified the bias asymmetric Δ_{HO} behavior with respect to the Fermi energy for $T < T_{HO} = 17.5$ K, and most importantly, how its temperature dependence mimics a BCS mean field gap opening. At the lowest temperatures, between 4 K and 2.5 K, they saw some additional features in the tunneling density of states that remained unaddressed in their work (Fig. 6.4 (b)).

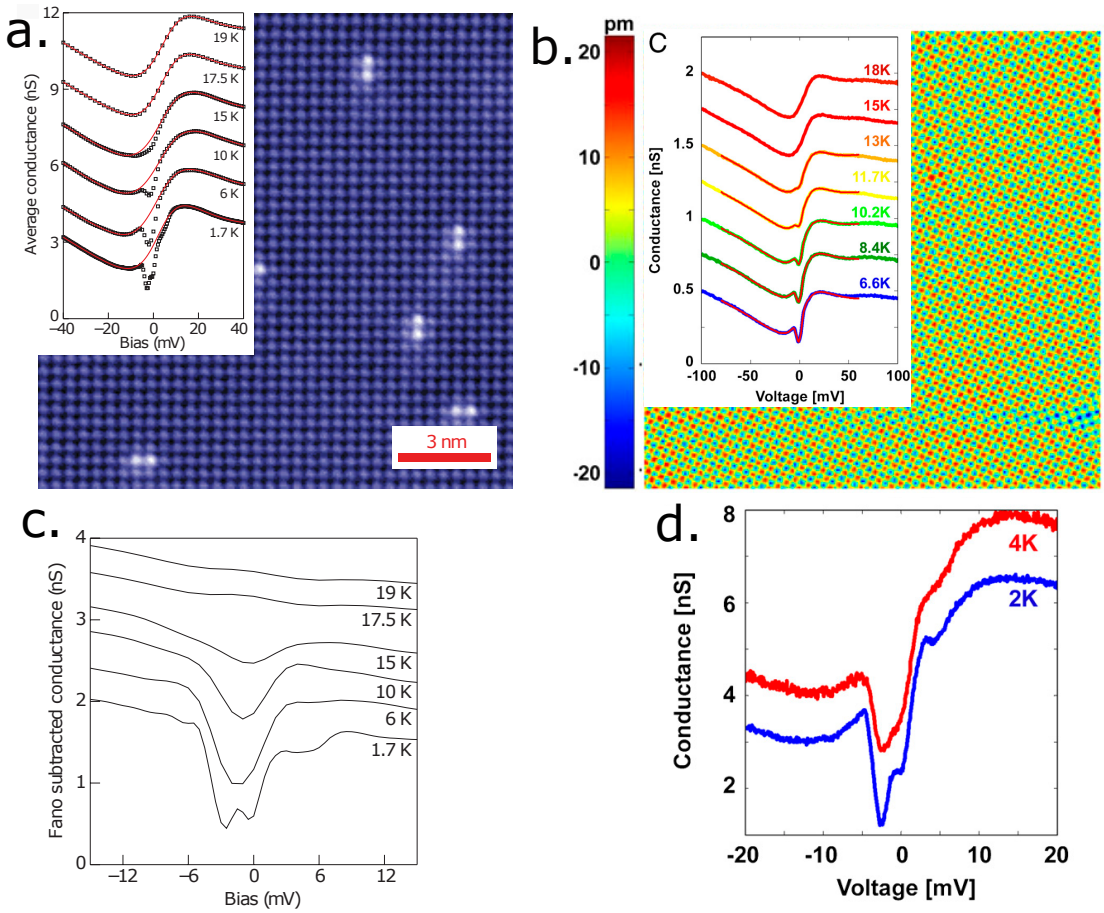

Figure 6.3 Si- or U-terminated surface? and Δ_{HO} oppening. STM and STS on URu_2Si_2. **(a)** Si-terminated surface [57] and **(b)** U-terminated surface [56]. Insets shown the temperature dependence of the tunneling conductance on each surface. The continuous red lines on the experimental data are the fits to a parametrization of a Fano function in **(a)** [57] whereas in **(b)** [56], the fit is a function which includes a Fano multiplied by a BCS-like gap [56]. Note in both the Δ_{HO} appearance withing the Fano spectrum bellow T_{HO} at energies below $|10|$ mV. In **(c)** is shown the same espectrum of the inset in **(a)** but subtracting the fit to a Fano function, thus is more clear the modifications due to the appearance of the Δ_{HO} at the Si-surface. As a complement of the inset in **(b)**, **(d)** shows two low temperatures curves displaying additional features withing the Δ_{HO}, below |5| mV. The point of surface termination remains unresolved [248]. Figures adapted from [56, 57].

Results of the tunneling spectroscopy (insets in Fig. 6.3 and Figs. 6.3(c) and (d)) coincide to identify the evolution of electronic structure of URu_2Si_2 for temperatures $T > T_c$. Avobe T_{HO} the Fano electronic structure predicted for Kondo screening of a magnetic lattice is revealed. Bellow T_{HO} a bias-asymmetric energy gap is reported and it is associated with the HO phase emerging from the Fano lattice (see insets in Figs. 6.3 (a-b)) [57, 56].

In a theoretical work, it was shown that advanced band structure calculations reproduce the main features of the formation of the heavy bandstructure when cooling [271, 57, 56]. They have calculated the one electron spectral function and their results give the observed Fano resonances.

In a previous work in our laboratory, Maldonado et. al. did STM measurements of the superconducting gap using a tip of Aluminum [249]. After cleaving the URu_2Si_2 sample at room temperature, the authors reported irregular surfaces without atomic resolution at 150 mK. They found tunneling conductance curves with a finite value at the Fermi level. The temperature dependence of the tunneling curves reveals structures, with values of the order of the weak-coupling BCS gap (1.73 $k_B T_c$). The absence of additional structures at low energies is associated

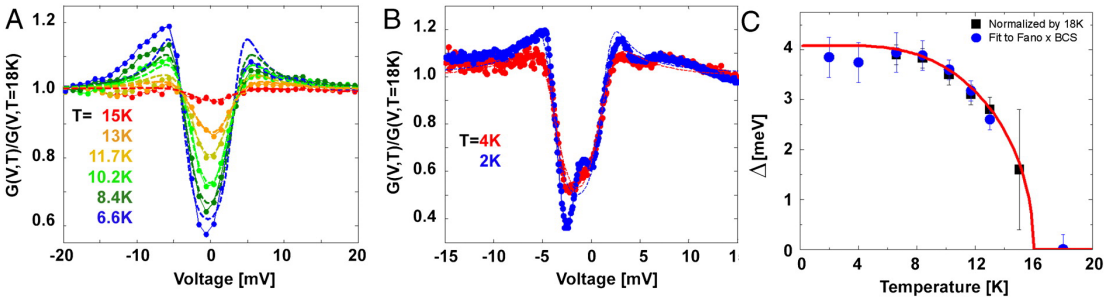

Figure 6.4 Experimental data to identify the Δ_{HO} reported by Aynajian et. al. [56]. **(a-b)** Evolution of an asymmetric BSC-like DOS, below T_{HO} after divide the spectra shown in Fig. 6.3 (inset in (b) and (d)) by the 18 K data. **(c)** Temperature dependence of the Δ_{HO} extracted. The gap displays a BCS-like temperature dependence. Note the new structures inside the HO gap for $T < 4$ K.

to the unavoidable contamination of the surface of the sample, due to the room temperature cleaving procedure.

6.1.3 Hidden Order and Structural transition.

Recent work has reported the appearance of electronic nematicity and structural changes in the crystal symmetry that break the rotational fourfold symmetry in the HO phase [272, 273, 274]. Nematicity has been also observed in the fluctuating order at temperatures above T_{HO} [275]. Different experiments in high magnetic field, such as magnetic torque [273] and nuclear magnetic resonance resonance [274] measurements, have suggested the existence of an electronic nematic order with in-plane anisotropy elongated along the [110] direction of the tetragonal crystalline structure below T_{HO}. More recently, high-resolution synchrotron X-ray diffraction measurements at zero magnetic field have reported the observation of lattice symmetry breaking from the fourfold tetragonal structure to twofold orthorhombic structure[272]. These have confirmed the existence of rotational symmetry breaking in HO phase, ruling out the possibility that the observed nematicity is induced by the applied magnetic field. The conduction electrons and the ions of the lattice are coupled through electromagnetic interactions and therefore, it is expected that when the electrons in a metal undergo the transition to a state that breaks one of the space symmetries of the crystal, the same symmetry breaking of the underlying lattice can occur.

X-ray diffraction measurements show that a small orthorhombic symmetry-breaking distortion sets in at T_{HO} only in ultrapure samples. Fig.6.5 (b) and (c) present the two possible orthorhombic distortions allowed for the body-centred tetragonal crystal structure of URu_2Si_2 that belongs to the $I4/mmm$ symmetry group (Fig. 6.5a. Synchrotron X-ray data are consistent with $Fmmm$-type orthorhombicity (Fig. 6.5b) which is compatible with the nematic in-plane anisotropy found along the [110] directions. Note that the ab plane primitive vector directions in the tetragonal $I4/mmm$ structure and in orthorhombic $Fmmm$ structure are rotated 45° with respect to each other.

The magnitude of orthorhombicity is of the order of 10^{-5}, which is two orders of magnitude smaller than that of similar structural transitions from the tetragonal $I4/mmm$ to orthorhombic $Fmmm$ phase in isomorphic iron based superconductors [276]. The lattice distortion is very weak implying that the HO transition is not a conventional structural transition but it is driven by an electronic ordering so that a small but finite electron-lattice coupling gives rise to the lattice distortion.

Note that previous STM measurements in the HO phase of URu_2Si_2 have not reported any signature of symmetry breaking electronic properties[56, 57].

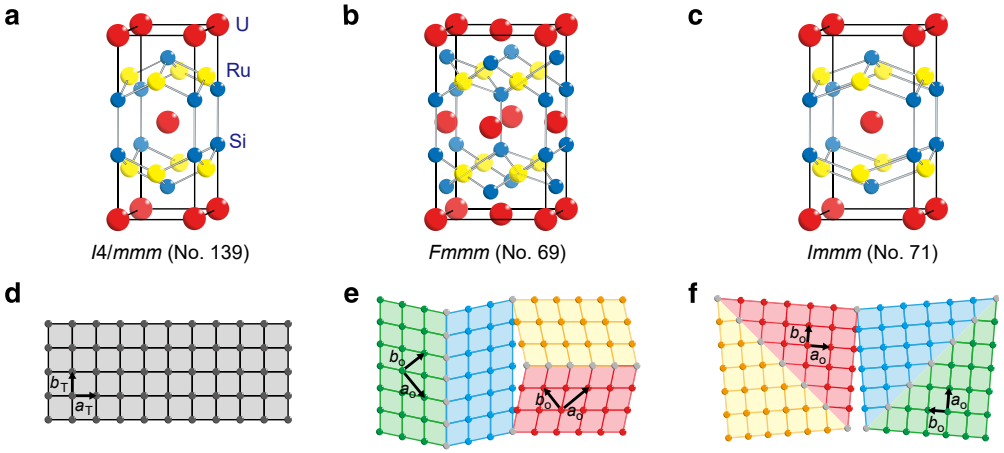

Figure 6.5 (a) Body-centred tetragonal $I4/mmm$ structure for $T > T_{HO}$. **(b)** Orthorhombic $Fmmm$ structure revealed by high-resolution synchrotron X-ray diffraction measurements at zero field at $T > T_{HO}$. **(c)** Another orthorhombic $Immm$ structure with broken fourfold symmetry, which belongs to a subgroup of $I4/mmm$, is shown for a comparison. Thin solid line indicates the unit cell. **(d-f)**, Schematic U atom arrangements in the basal plane for each structure, and formation of four degenerate domains sketched by different colors. In-plane primitive vectors are indicated by arrows. Figure adapted from ref. [272].

6.1.4 Hidden order and Fermi surface reconstruction

The electronic band structure and the Fermi Surface (FS) of URu_2Si_2 have been examined with excellent agreement between theoretical and experimental results [277, 278, 279, 280, 281, 282]. Fig.6.6a shows a 3D picture of the FS in the tetragonal phase above T_{HO}. It is characterized by four electron pockets around the Γ point and two hole pockets around the Z point (see Fig.6.6a).

Recent quantum oscillations [283] and angle-resolved photoemission spectroscopy [284] studies have revealed that the FS in the HO phase is reconstructed in a similar manner than in the antiferromagnetic phase under pressure. This implies that in the HO phase the Brillouin zone (BZ) is folded with the antiferromagnetic wave vector $Q = (001)$ and the nested parts of Fermi surface are gapped as in the antiferromagnetic phase.

The FS reconstruction in the HO phase is shown in Fig.6.6b in a 3D representation in the folded BZ (Left panel in Fig.6.6a is in the unfolded BZ). The HO introduces a void in the formerly closed FS body at the Z points and slices the FS parallel to k_z at the crossing points of the nested sheets. In the corresponding k_x-k_y-plane cut (middle panel in Fig. 6.6b), the formerly closed and rounded square-like sheets (Fig.6.6a) therefore break up into four smaller and four larger petal-like shapes. The smaller ones vanish when the HO parameter is increased at low temperatures.

6.2 Samples and Surface Preparation

It is important to stress that the recent boom of activity in this compound, as testified by the papers appeared in arXiv during last five to ten years, is due to the availability of extremely high quality single crystals in several groups. We have been working with the group of Dai Aoki, who has grown large size crystals and carefully cut out those pieces of the large crystal that are particularly prone to show excellent superconducting features. He prepared the crystals in a shape that we could use for cleaving at low temperatures and characterized them carefully in advance to make sure that their purity, measured by the residual resistivity and the superconducting critical temperature, corresponds to the highest quality to date standards in this field.

We use high-quality single crystals URu_2Si_2, grown by Czochralski method (see Section 2.7) [101]. Typical crystals size were 1 mm^2 within the crystallographic ab-plane and 2-4 mm along

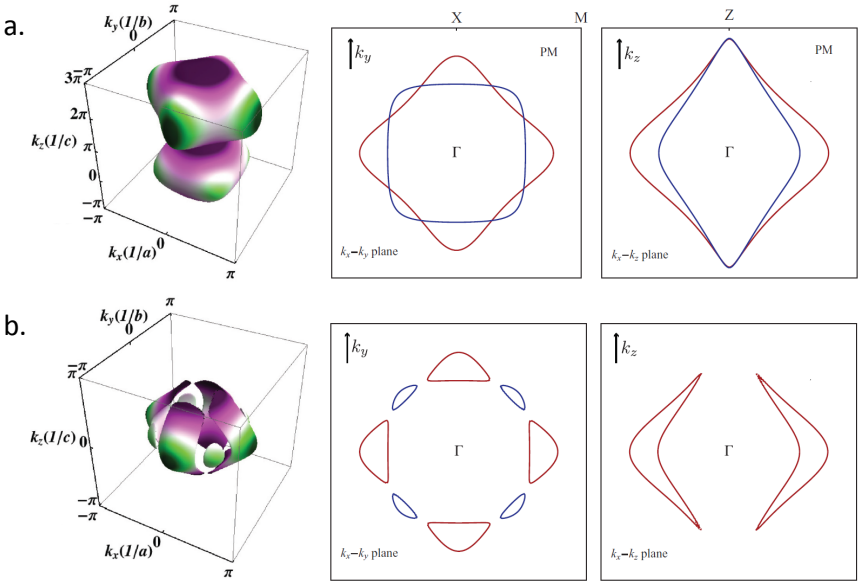

Figure 6.6 (Figure adapted from [285])**(a)** The URu_2Si_2 Fermi surface (FS) for $T > T_{HO}$ (paramagnetic phase). Left panel shows a 3D picture of the FS sheets in the extended simple tetragonal BZ with electron sheets around γ(0,0,0) and hole sheet around Z(0,0,2π/c). Here c=1. Electron and hole sheets are nested by Q=(0,0,1). Middle and right panels show FS cuts with k_z=0 and k_y=0, respectively in the reduced BZ (Z-point folded onto γ). Red and blue lines correspond to electron and hole sheets. **(b)** FS of URu_2Si_2 in the HO phase in the reduced BZ (folded by Q). The FS is reconstructed in the k-space regions connected by the nesting vector Q=(0,0,1) and breaks into small petal-like shapes FS sheets. Middle and right panels in **(b)** show FS cuts with k_z=0 and k_y=0, respectively.

the c direction. Figure 6.7 (a) shows a photography of two of the URu_2Si_2 crystals measured in this work. The crystals exhibit residual resistivities of $\rho_0 \approx 1\mu\Omega$cm, with residual-resistivity ratios of ~ 121 on ab-plane and RRR ~ 122 on c-axis and critical temperatures of 1.7 K (Fig. 6.7 (b)).

At least 10 crystals were cleaved *in situ* at 4.2 K along the ab-plane using the method described in Figure 2.21, resulting in flat surfaces (see Figs. 6.8, 6.9, 6.11, 6.12).

Best images were obtained at constant current mode (some nA), with a bias voltage from 100 mV to 5 mV and a tunneling resistance of 10 MΩ. The *in-situ* positioning system described in Section 2.5 (Fig. 2.20) was very useful to change the scanning window and find positions that were clean and showed good tunneling conditions.

6.3 Topography in URu_2Si_2: A- and B-Surfaces

Figure 6.8 shows topographies on URu_2Si_2 obtained at 150 mK at different regions on the sample cleaved at 4.2 K. Height versus distance profiles on consecutive terraces (Fig. 6.8 lower panel) show values which often correspond to one or half c-axis constant ($c = 9.58\mathring{A}$).

Figure 6.9 shows a topography image where we can differentiate two types of surfaces, one with the expected square arrangement of the atoms, which spacing corresponds to either an Si- or U-terminated surface (4.2 $\mathring{A}$) termed A-surface (see Fig. 6.10), and other where we do not observe atomic order, termed B-surface (see Figs. 6.9(d) and 6.11). A profile, in between consecutive steps of A- and B-surfaces (Fig.6.9(b)), shows that the distance corresponds to U-Ru atoms unite cell separation. Thus, B-surface is made of Ruthenium atoms. A detailed topography map on B-surfaces (Fig.6.9(d)) shows interference patterns with circular shape around the defects with a radius of $\approx$1 nm.

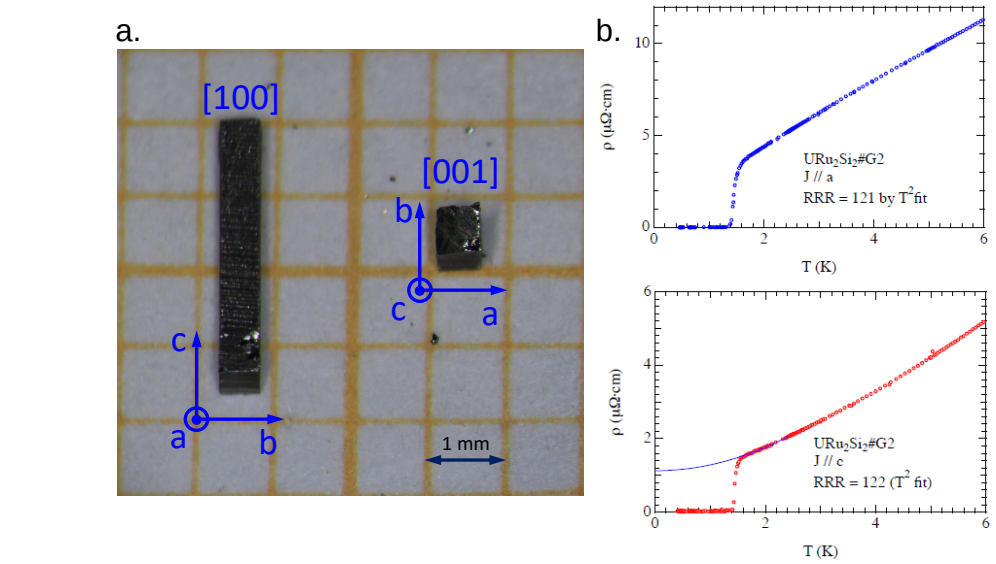

Figure 6.7 (a) Photograph of two crystals of URu_2Si_2 showing the size of the samples and its orientation according to the crystalline direction. **(a)** Temperature dependence of the resistivity of two URu_2Si_2 crystals used in this work. Both samples with $T_c \approx 1.4K$ and RRR of 121 and 122 respectively and $\rho_0 \approx 1\ \mu\Omega$cm. The samples were growth by Pr. D. Aoki at Grenoble (FR) using the Czochralski method (See Chapter 2) [101].

Therefore, after the cleaving process, the crystal has cleaved perpendicular to the crystallographic c-axis.

That we don't observe atomic ordering of Ru atoms (whose interatomic space is less than U and it is rotated 45°) on Type-B is probably because the conduction electrons in the s and d orbitals of the Ruthenium atoms are delocalized. The perturbations with circular shape ((Fig.6.9(d)) can be described as Friedel oscillations [286, 287], where the scattered electrons around the defects form a rippling structure circling the impurity.

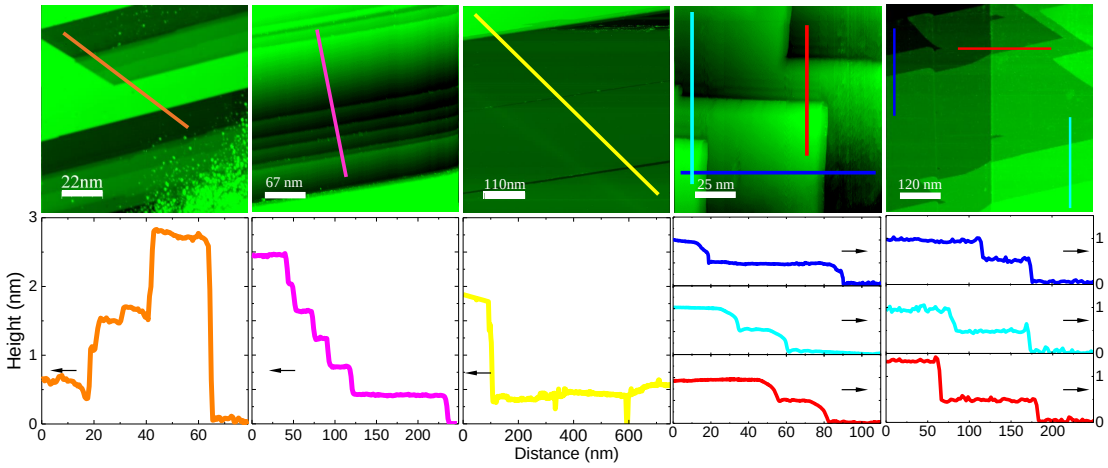

Figure 6.8 (Upper panel) Topography maps on URu_2Si_2 at 150 mK after the cleavage process at 4.2 K. The color lines represent the height vs. distance profiles plotted in the lower panel. Distance between steps are closed to $c \approx 9.6\ \AA$ and $c/2 \approx 4.8\ \AA$.

The presence of different types of surfaces after the cleavage process is not only a particular feature of URu_2Si_2, this result has been observe in other heavy fermion compounds such as $CeCoIn_5$ [60, 66] and the $YbRh_2Si_2$ [59].

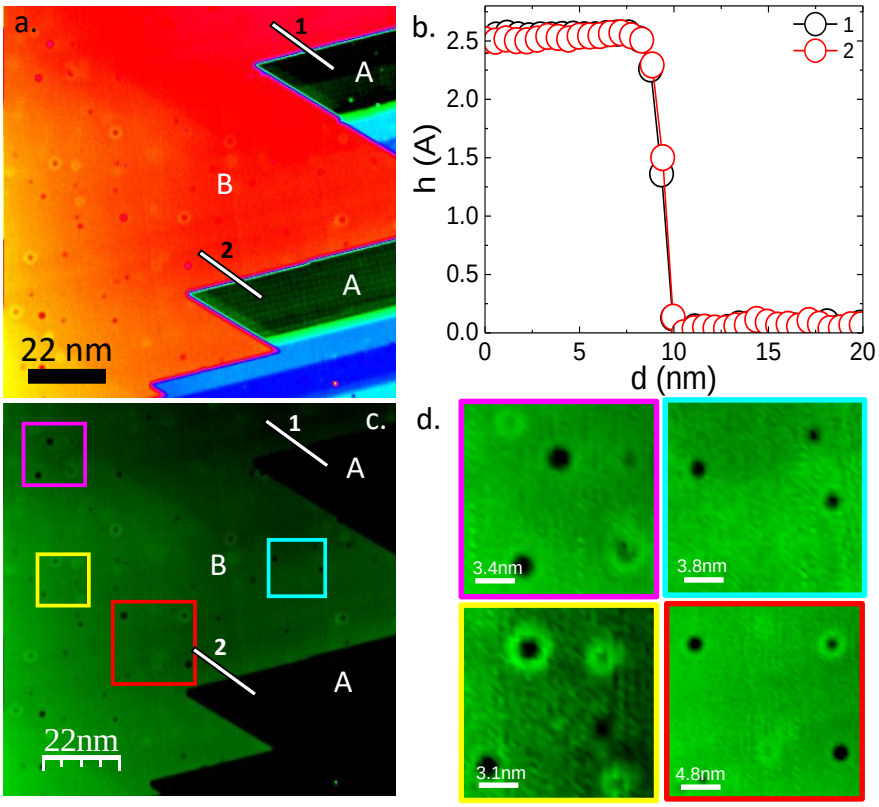

Figure 6.9 (a) Topography in URu_2Si_2 showing the two types of surfaces after the cleaving process at 4.2 K. An atomic ordered termed A-surface and the B-surface with circular shape defects. **(b)** The relative heights between surfaces *A* and *B* (white lines 1 and 2 in (**a**)) are approximately 2.5 Å, which roughly corresponds to 26 %×*c*-axis. Thus, the circular shape defects on B-surface, could be originated by breaking of bonds Si-Ru. **c**. Same topography of (**a**) with a different color scale to highlight the circular shape defects on B-surface. **d**. Insets of (**c**) showing details in the defects on B-surfaces.

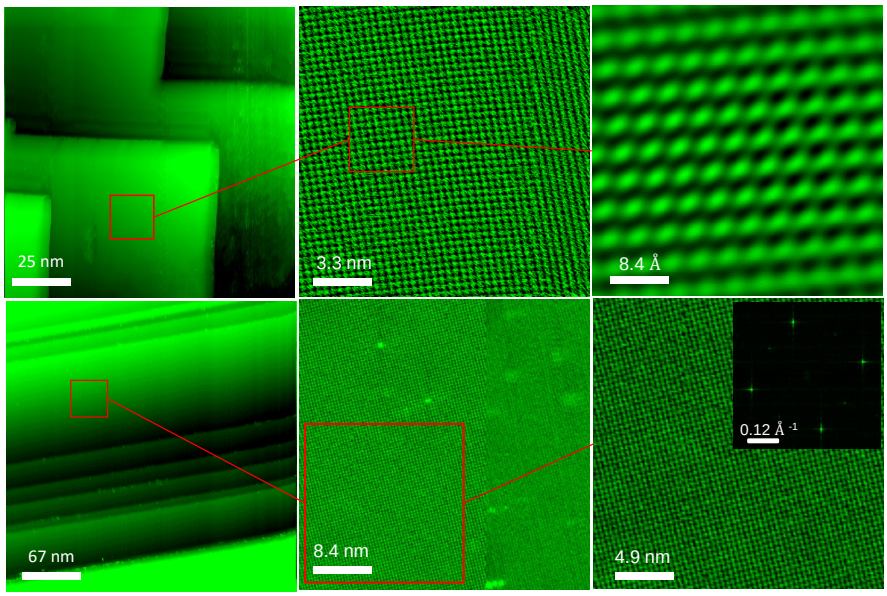

Figure 6.10 Type-A surfaces in URu_2Si_2 Different size scan windows on Type-A surfaces with areas showing atomically ordered surfaces. The Bragg peaks in the Fourier transform (inset) shown the square symmetry of the *ab*-plane of URu_2Si_2.

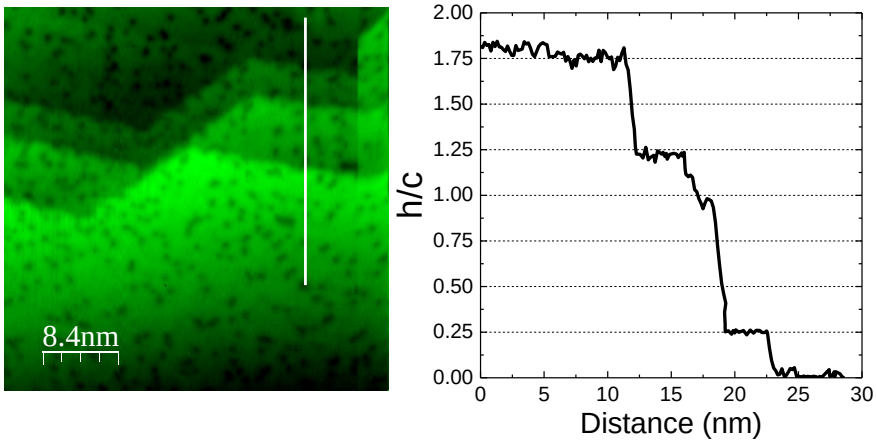

Figure 6.11 Type-B surfaces in URu_2Si_2. Flat surfaces with irregular shape defects (Type-B Surfaces in Fig. 6.9). We plot the relative heights between surfaces (white line on topography) normalized to the c-axis constant as a function of the distance. They are approximately 25% and 75 % of the *c*-axis distance; this value can be associated with the distance between consecutive U-Ru layers. Thus, the irregular and circular shape defects on B-surface, could be originated by breaking of bonds Si-Ru.

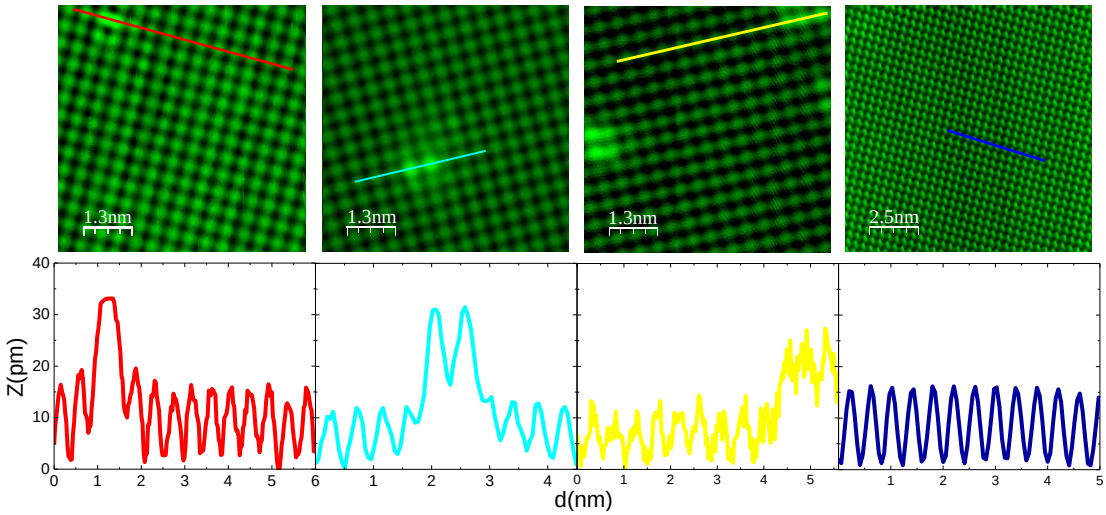

Figure 6.12 *(Upper panel)* Topographies of a cleaved URu_2Si_2 single crystal at 150 mK after the cleavage process at 4.2 K, showing some defects and the perfect square symmetry in the *ab*-plane $a = 4.2$ *Å*. *(Lower panel)* Profiles along the lines indicated in the upper panel. The quality of the measurements (low noise in the profiles) indicate excellent stability of the experimental setup.

The A-surfaces shown excellent atomic order with a lattice spacing corresponding to either the U or the Si layer. In addition, on A-surfaces we frequently find different kind of defects. Some of them produce changes on surface's height of ∼20 pm (Fig. 6.12); others (Fig. 6.13) show fourfold symmetry order.

Topographies in Fig. 6.12 and the leftmost panels in Fig. 6.13, reveal two type of defects: single or double humps and dents. Same type of defects have been reported in $YbRh_2Si_2$ [59]. The authors, by simple comparison between the atomic radius of Rh and Si have classified these surfaces as Si-terminated [59]. We follow the procedure described in Ref. [59], to identify the surface termination in our case.

The involved height scale (∼20 pm) for the defects, indicates a replacement of a surface atom by an impurity rather than an adatom or a missing one [59]. The extremely low residual resistance in the URu_2Si_2 crystals that we have used (see Fig. 6.7(b)), is in agreement with the

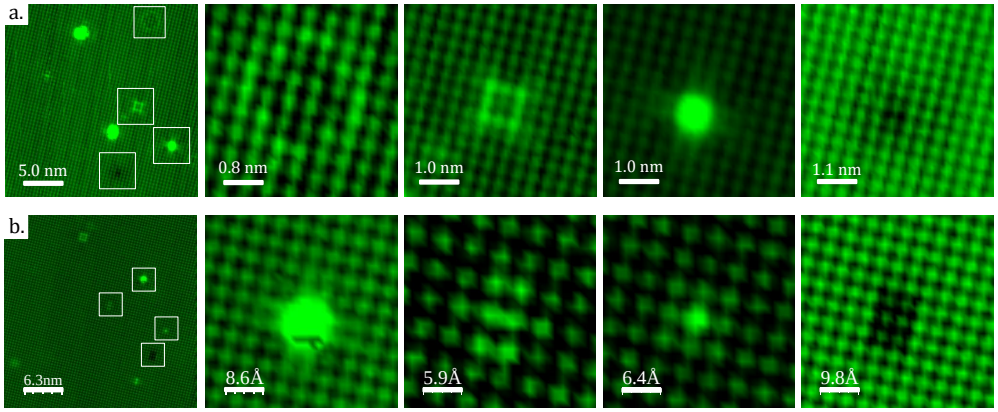

Figure 6.13 Topography images of 25×25 nm^2 (**a**) and 31.5×31.5 nm^2 (**b**) on atomically ordered surfaces type-A at 150 mK in URu_2Si_2. The right panels shown zoom in the white squares in (**a**) and (**b**) respectively. Defects shown fourfold symmetry.

low defects density. Likely, the observed defects are site exchanges between Ru and Si atoms, *i. e.* a Ru atom may reside on a Si site and Si on a Ru site. Consequently, the surfaces shown in Figs. 6.12 and 6.13 are Si-terminated: an exchange of Si by the larger Ru then accounts for the humps in surface topography. On the other hand, replacing a Ru ion by a smaller Si would correspondingly take place in the second-to-topmost atomic layer (see Fig. 6A). Given the crystallographic structure of URu_2Si_2 the two adjacent Si ions in the topmost atomic layer could then move deeper into the surface and the resulting dents. Again, we emphasize the excellent agreement of interatomic distances in topography with the lattice constants and the atom's square arrangement [59] .

6.4 Spectroscopic study of the SC phase within HO

The overlapping between the tunneling electrons and the heavy fermion excitations can be influenced not only by the coupling of the tip to the *spd*- or *f*-like components of such states, but also by the interference between these tunneling process [44].

In order to clarify the density of states behavior in the superconducting phase of URu_2Si_2, we focus on the study of the tunneling conductance curves on Si-terminated surfaces. Figure 6.14 shows the normalized tunneling conductance as a function of the temperature from 18.2 K to 250 mK. The agreement with previous results on the HO phase, reported by Ref. [56], is clear.

Below the HO temperature (T_{HO}=17.5K), we observe the evolution of a local minima between -5 meV to 0 meV which corresponds to the HO state, its amplitude increases when the temperature decreases. At the lowest temperatures we observe new features at very low energies, around 0.4 meV and -1.5 meV.

The presence of a gap asociated with the HO phase Δ_{HO} has been indicated by previous reports [254, 255, 256, 288, 289, 258] including the recent work of spectroscopic measurements by Aynajian et. al., [56] which reports an asymmetric Δ_{HO} with $\Delta_{HO}(0K) \approx 4.1$ meV.

In addition, the structures near to -4.0 meV support the observed gapping of the inconmensurate spin excitations by inelastic neutron scattering experiments ($\mathbf{Q_1}$, see Fig. 6.2) [248, 268, 253].

As we discuss below, in our work we have observed an additional feature due to the ($\mathbf{Q_0}$ spin excitations at -1.5 meV.

To establish with more detail how the gap emerges on the superconducting phase, we have perform a study of the density of states on the normal state as a function of the temperature. To reach the normal phase below $T_c = 1.5$ K, we have applied a magnetic field of 4 T parallel to the

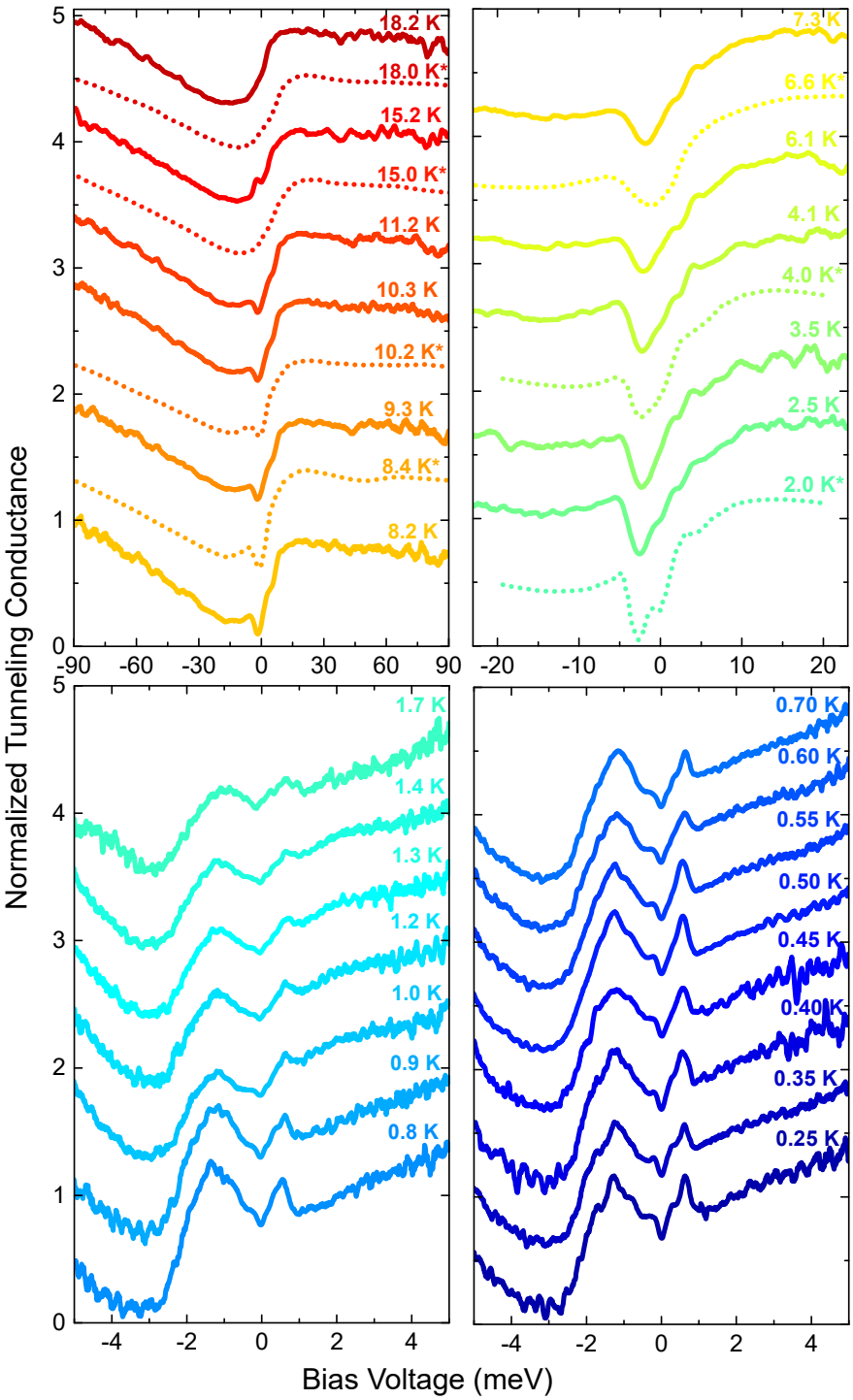

Figure 6.14 Normalized tunneling conductance below the HO temperature (T_{HO}=17.5K) with a vertical offset for clarify. For $18.2K < T < 2K$, we observe the evolution of a local minima between -5 meV to 0 meV which corresponds to the HO state. The previous results by Aynajian et. al., [56] (dashed lines) are in agreement with our measurements. Bellow $T_c = 1.7$ K, we observe new structures inside HO state which are evidence of the superconducting gap evolution.

c-axis ($H_{c2} = 2.8$ T) [290]. Figure 6.15 shows the normalized tunneling conductance curves as a function of the temperature for $H = 0$ T and $H = 4$ T.

The main structures of the HO for energies above of +1.0 meV and bellow of -2.0 meV

for the temperature ranges studied, remain unaltered with the magnetic field. The structures centered near -1.5 meV and -4.0 meV, associated with the gap of the spin excitations at $\mathbf{Q_0}$ and $\mathbf{Q_1}$ respectively (see Fig. 6.2) [291, 268] (see Fig. 6.2) also remain unchanged as a function of the magnetic field (see Fig. 6.2) [291].

We compare the conductance curves in the normal phase (H = 4 T) with conductance curves in the superconducting phase (H = 0 T) at same temperatures (Fig. 6.16 (a)). Lowering the temperature, below T_c, we find that some structures, (a positive structure near to +0.9 meV and a negative structure near to the Fermi level) are modified by the onset of the superconducting gap feature at smaller energy scale. Further cooling shows the onset of an asymmetric superconducting gap bellow T_c inside the HO gap.

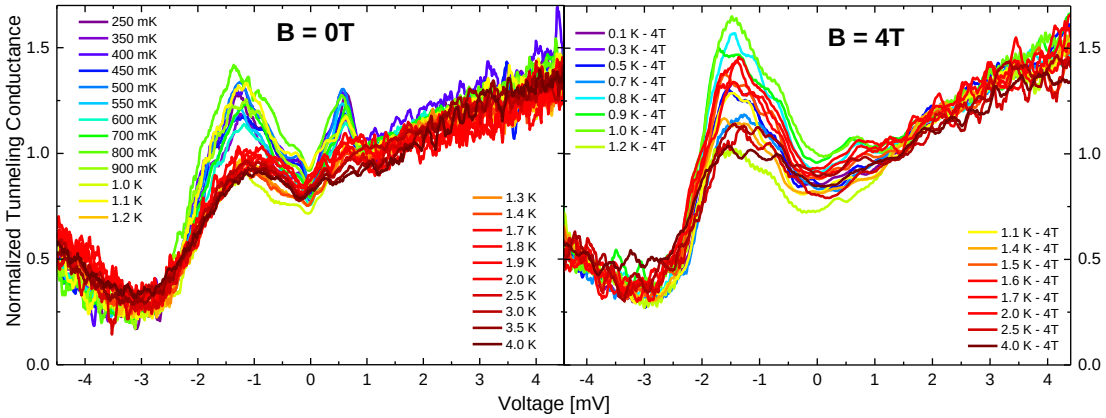

Figure 6.15 Temperature dependence of the normalized tunneling conductance at two different magnetic fields, 0T (left) and 4T (right) in URu_2Si_2 (H_{c2}=2.8T). It is evident in both cases the reduction of the structure between -0.5 mV and 1.0 mV and the amplification of the signal at values near to -1.5 mV as a result of the magnetic field.

A way to characterize the superconducting gap is normalize the conductance curves in the superconducting phase respect to the curves at the normal phase for the same temperature. Results are shown in Figure 6.16 (b). The normalized spectra reveals the onset of a low asymmetric energy gap centered nearly at the Fermi level energy with an energy scale lower that $\sim \pm 300 \mu V$.

Finding the Superconducting signal: fitting the $\sigma(E)$ curves on Si-terminated surfaces to a phenomenological model

In order to understand the curves, we are using a model provided by Alfredo Levy Yeyati (see Fig. 6.17) that mimics tunneling between a normal tip and a superconducting sample through a series of resonant systems. These kind of models are widely used to study transport through quantum dots and include all needed features to account for detailed quantum mechanical processes in the tunneling phenomenon [292]. The fits to the tunneling conductance curves that I took have been made by Victor Barrena. This is work in progress.

Therefore, here I will provide only a brief description of the model and show that it can be used to obtain parameters relevant to URu_2Si_2. I should also remark that the model provides the first microscopic approach giving understanding to the ubiquitous result of an anomalous and highly smeared density of states observed in atomic scale measurements of the superconducting phase of heavy fermions [44, 293].

The model is schematically described in figure 6.17. First, the model brings all high energy features discussed in previous work [56, 57] into a broad resonance. Second, the model assumes that tunneling is not direct between the bulk superconductor and the normal tip. There is an intermediate level which is convoluted with the BCS superconducting density of states. We assume that this level corresponds to the heavy quasiparticle band obtained after hybridization

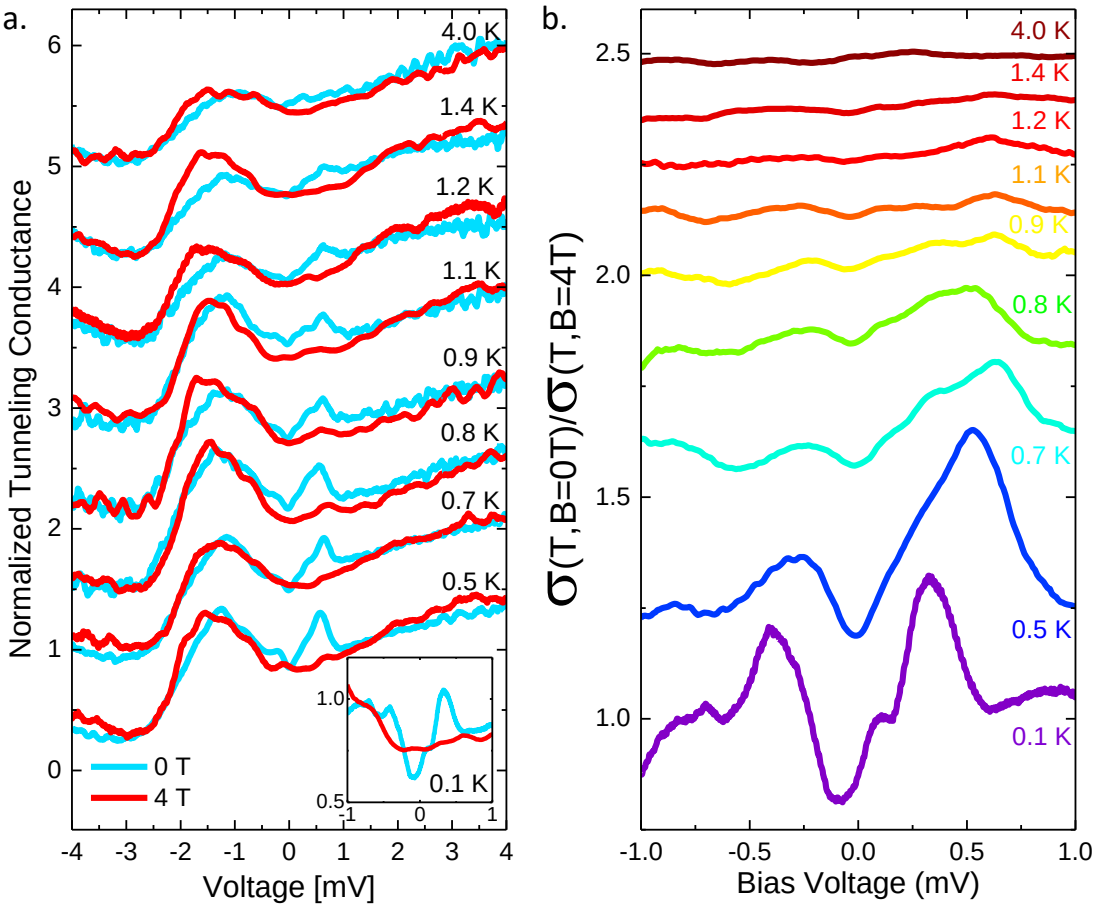

Figure 6.16 (a) Temperature dependence of the normalized tunneling conductance at two different magnetic fields, 0T (blue) and 4T (red) as a funtion of the temperature in URu_2Si_2 (H_{c2}^c=2.8T). **(b)** We divide the spectra obtained without magnetic field with the spectrum measured at 4.0 T at the same temperature. From BCS theory the superconducting gap for a $T_c = 1.7$K is Δ_{BCS}=0.23 meV. Is evident in both cases the changes of the structure between -1.0 meV and +1 meV.

below T_0 at about 100 K. Physically, this could mean that there is a heavy band that is, for this particular orientation of the surface, gapless. This is very likely–there are numerous experiments reporting zero gap along a line node in the basal plane of this material. Third, we put two additional resonances, each one broadened. One for positive bias voltages (ε_2) and one for negative bias voltages (ε_3). Using this model, we can then add thermal smearing and extract the temperature dependence of three relevant parameters, the superconducting gap and the temperature induced broadening of both resonances.

The superconducting gap is of 0.2 meV, approximately $1.55 k_B T_c$ and its temperature dependence follows BCS theory. There seems to be a small feature above the bulk T_c in the tunneling conductance curves which we do not understand well. Probably, there are large amounts of fluctuations, as also suggested in other measurements [273].

The resonance at ε_3 has a temperature dependence that can be understood by a modified Fermi liquid description, in a similar way as previous resonances found in $YbRh_2Si_2$ that were due to features in the bandstructure [59]. The resonance shows the consequence of the gap in the spin excitation spectrum into the electronic bandstructure of this compound. It would be the first available evidence for the long sought connection between the spin excitation and the electronic structure of this compound.

The resonance at ε_2 disappears together with the superconducting features. Its origin is

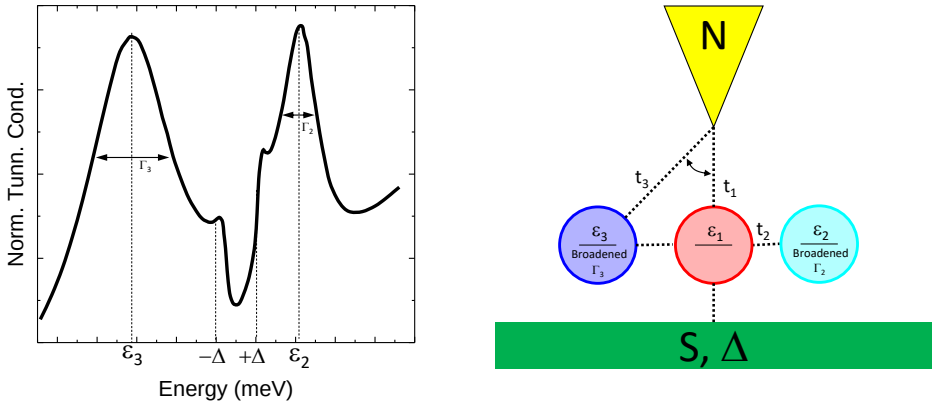

Figure 6.17 (left) It shows the normalized tunneling conductance obtained within a model sketched in the right panel. We highlight the different energy levels ε and the broadening of each one Γ. Δ is the supeconducting gap. The additional level ε_1 is not shown in the left panel. It leads to the increased normalized conductance at zero bias and the smearing of the superconducting features. (Right) It represents schematically the tip (yellow, N), the sample (green, S, with the superconducting gap Δ) and the series of intermediate steps for tunneling. These consist of a single level ε_1 that smears the superconducting density of states and is coupled to two resonances at ε_3 and ε_2. Each one is broadened. The broadening is made by artificially coupling each level to a fictitious normal lead. We allow for interference between direct and indirect tunneling with ε_3.

yet totally unknown. It could hint to electron-hole asymmetric superconducting density of states. This would probably need, however, chiral superconductivity and an additional magnetic field. There are several evidences for chiral superconductivity in this compound, such as the observation of time reversal symmetry breaking in the superconducting phase [294]. However, breaking electron hole symmetry to obtain a resonance at roughly two times the superconducting side would probably need a high spontaneous magnetic field. We are working to elucidate this issue.

6.5 Quasiparticle interference scattering in surface A

We have used quasiparticle interference imaging (QPI) to get information about the electronic properties of URu_2Si_2. This technique has been developed over the last fifteen years as a powerful tool to determine the full (empty-occupied) electronic band structure in metals [295]. It has been particularly useful in superconductors where it provides a measurement of the reciprocal space structure of the superconducting gap [295, 296].

In metals and superconductors, sources of disorder such as topographic defects or impurities produce elastic scattering that mixes electronic states located on the same surface with constant energy E in the reciprocal space. When scattering mixes states k_1 and k_2, an electronic interference pattern with wave vector $q = k_2 - k_1$ appears in the local density of states at energy E. These electronic waves can be observed by STM as modulations of the tunneling conductance. They are referred as Friedel oscillations although this not precise because QPI wave vectors do not always correspond to Fermi wave vectors but a to combination of them. Therefore, STM studies of the QPI wave vectors and their energy dependence can provide the electronic band structure close to the Fermi level.

We have measured QPI in type-A surfaces where we find atomic resolution. Our samples are very pure (RRR well in excess of 100) and therefore QPI signal is expected to be very weak. Previous QPI studies in the normal state of URu_2Si_2 where made in Th-doped samples[57]. These impurities provided for the needed scattering centers to increase the QPI signal although they are also expected to modify the electronic properties of pure URu_2Si_2.

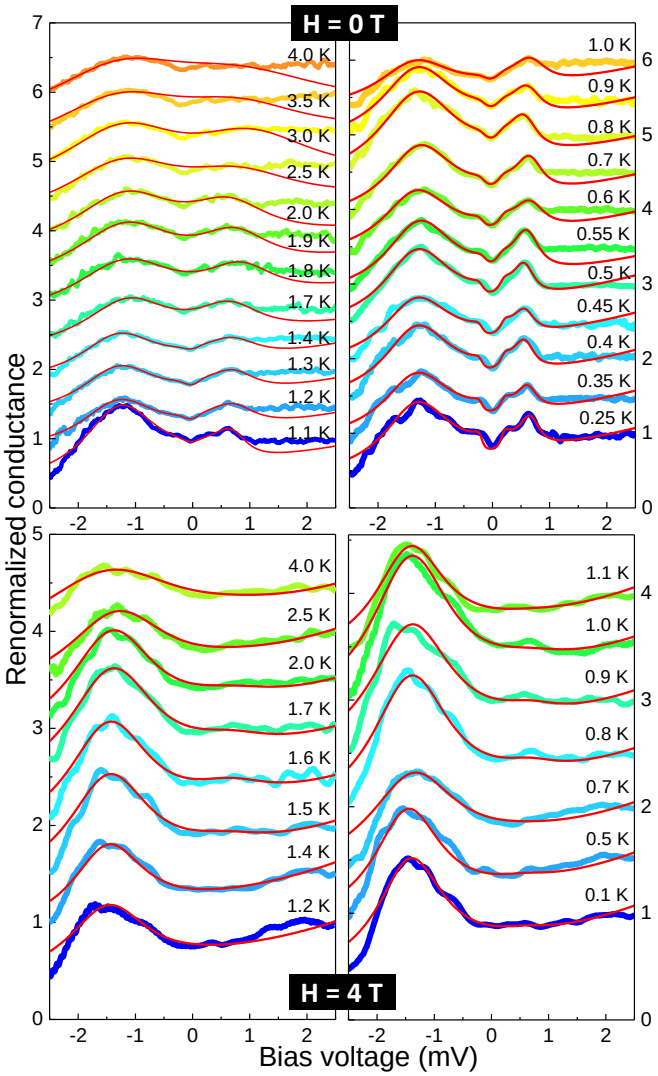

Figure 6.18 Renormalized tunneling conductance (from data in Fig. 6.16) as a function of the temperature at $H = 0$ T and $H = 4$ T. The continuous red lines on the experimental data are the fits to the model described in the text and schematically represented in Fig. 6.17. Note at $H = 0$ T the modifications due to the appearance of the Δ_{SC}.

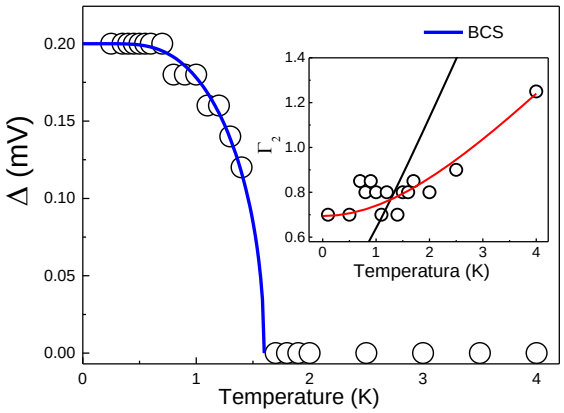

Figure 6.19 Temperature dependence of the superconducting gap. Values extracted from the fits in Fig. 6.18. We use $T_c = 1.6$ K. The inset shows the temperature dependence of the resonance Γ_2.

We, instead, have used intrinsic defects to increase the amplitude of QPI electronic modulations. More often we do not observe QPI patterns in large atomically flat areas on type-A surfaces. But, sometimes, we find small regions showing several consecutive steps between type-A surfaces (Fig.6.20). Atomically flat areas with a lateral size of a few tens of nanometers are confined between steps as can be seen in Fig.6.20. These show the QPI patterns discussed in the following.

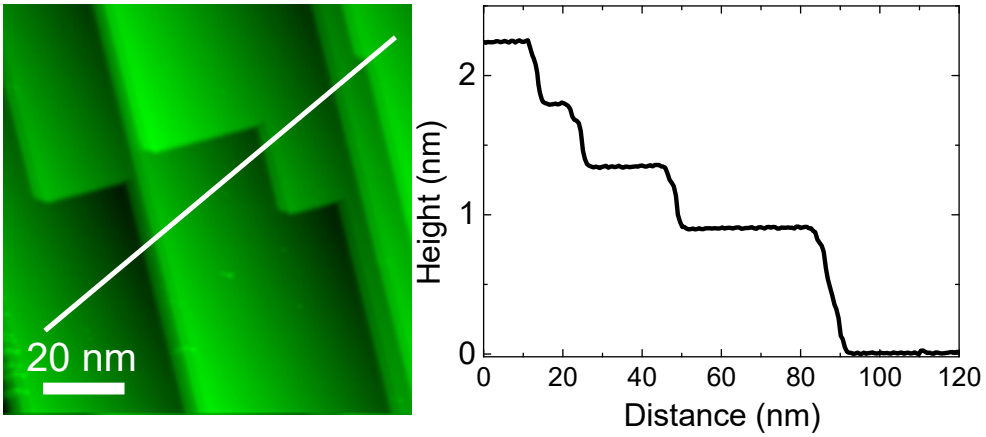

Figure 6.20 a Left panel shows the topography of a region with multiple steps made at 150 mK and 0.7 T. All atomically flat surfaces between steps are type A. Right panel shows the height profile along the white line in panel left. Steps have a size of the order of the c-axis lattice constant and leave flat areas with lateral size of a few tens of nm in between them.

Fig.6.21 shows a series of spectroscopic maps made in the region shown in Fig.6.20 as a function of the bias voltage. We observe the presence of one dimensional surface electronic modulations parallel to the steps. Unlike what happens for point-like scattering centers, which produce isotropic dispersion patterns, here the steps produce anisotropic dispersive electronic waves that occur only in the direction parallel to the steps. The period of the surface electronic waves strongly changes with bias voltage going from 3 to 5 modulations within 20 nm when changing the bias voltage between 1.6 mV to 0.2 mV (see black/white grids in Fig.6.21). We find that the period of the modulations is the same for all the atomically flat regions in between steps independently of their lateral size, indicating that they are directly linked to the intrinsic electronic properties. The QPI patterns are not seen at all energies. Modulations are nicely observed at positive bias voltages above 0.2 mV and they disappear below this value.

Fourier transforms of spectroscopic maps show peaks associated to the modulation along the [100] and [010] directions with wave vectors q one order of magnitude smaller than the Si-lattice wave vectors. These peaks are more intense along the [100] direction because most steps of the region shown in Fig. 6.20 are aligned perpendicular to this direction. Left panel of Fig. 6.22 represents using a color map the Fourier amplitude as a function of the energy and the reciprocal space position along the direction [100]. Each horizontal line of the map at energy E is obtained by doing a height profile in the Fourier transform of the conductance map made at the same energy along the [100] direction. The Fourier amplitude at each energy has a local maximum at q that can be followed as as function of the energy. The energy dependence of q is highlighted by the black line in the left panel of Fig. 6.22. We find that q increases with energy. It is consistent with the decrease in the period of the electronic modulations in the real space seen in Fig. 6.21. Also, as mentioned above, we observed that the local maxima in the Fourier amplitude associated to q disappears at voltages below 0.2 mV. This energy corresponds to the value of the superconducting gap Δ (black dotted lines in Fig.6.22). As it is expected QPI patterns are not observed at energies between $\pm\Delta$.

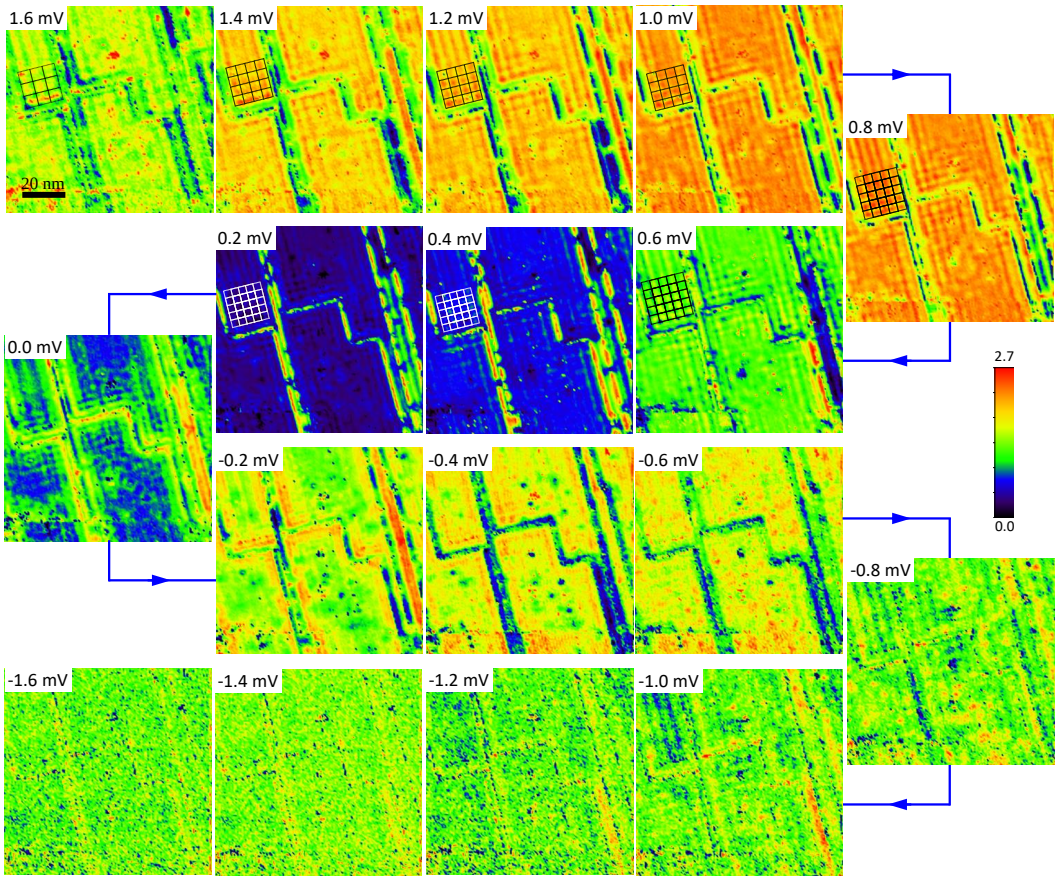

Figure 6.21 Spectrocopic maps made in URu_2Si_2 at 0.7 T and 150 mK as a function of the energy between $\pm$ 1.6 mV in the region shown in Fig.6.20). The value of the bias voltage for each conductance maps is indicated in the left top corner. In the small areas in between steps we observe quasiparticle interference patterns consisting on one dimensional electronic waves parallel to the steps. The wavelenght of the electronic modulations is highlighted by the black/white grids. It changes from s changes from 4.73 nm at 1.6 mV to 3.47 nm at 2 mV. Electronic modulations are not longer observed at bias voltages below 2 meV. Vertical color bar indicates the normalized conductance value.

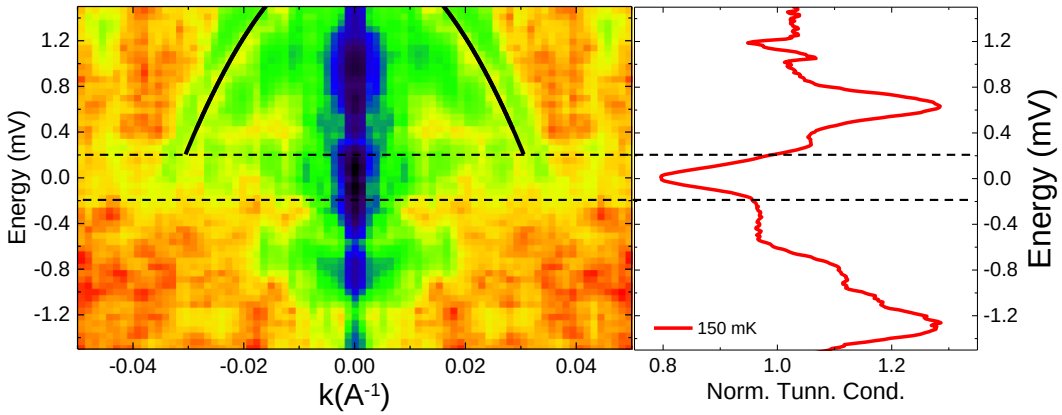

Figure 6.22 Fourier amplitude of the q vector observed in QPI experiments as a function of the bias voltage and the reciprocal space position along the [100] direction (left panel). Color code represents the Fourier amplitude from low values to high values (red-green-yellow and blue, respectively). Black line is the position the q vector (local maxima in the Fourier amplitude) as a function of energy). Right panel shows a typical conductance curve taken in type-A surface within the superconducting state. Horizontal black dotted lines mark the energy position of the superconducting gap $\pm Delta$.

The QPI data provides an independent measurement of the superconducting gap in those parts of the Fermi surface involved in the scattering process associated to q. The size of the superconducting gap obtained from QPI measurements is the same that the observed in tunneling data (right panel in Fig.6.22).

The QPI data data in Fig.6.22 reveal a light hole-like band with an effective mass $m* \sim 5m_e$, being m_e the electron mass. This is of the same order than the effective mass observed in previous QPI experiments in Rh-doped URu_2Si_2 at higher temperatures in the normal phase[57], and much smaller than the very large effective mass values ($m* \sim 50m_e$) deduced by specific heat measurements. The size of the q vector measured in our QPI experiments is however a factor of three smaller than in the Rh-doped samples. Both measurements are made within the HO phase where the FS is already reconstructed (Section 6.1.4). However, while QPI in Rh-doped samples are made at 5 K our data are taken at much lower temperatures in the HO ground state and well below the superconducting critical temperature.

Figure 6.22 A shows the calculated intrasheet and intersheet scattering wave vectors of the HO reconstructed FS [285]. Our data are either consistent with the small intrasheet scattering vectors oriented along the [100] and [001] directions (q_1^a and q_1^b in Fig. 6.22 A). They have a similar size and orientation that the q vector observed in our data. Although, more detailed comparison between the tunneling data and calculated band structure is needed to associate the q vector obtained by QPI to particular features in the FS and to explain its energy dependence and effective mass, our data provide a direct evidence for the presence of the HO reconstructed FS within the superconducting phase and the opening of the superconducting gap.

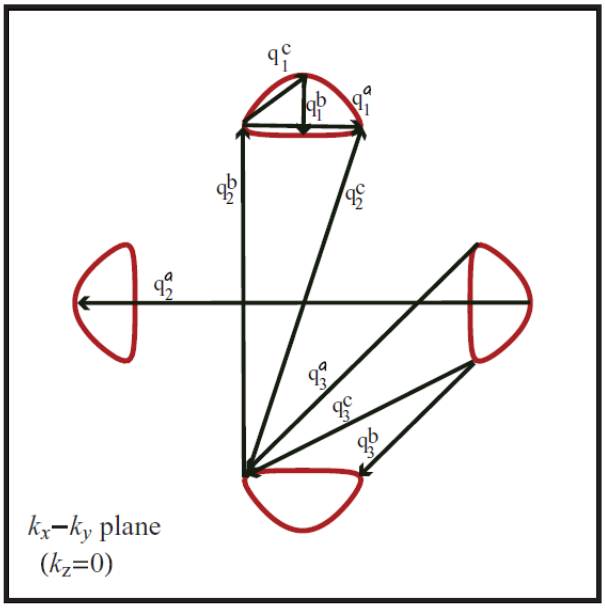

Figure 6.22 A Characteristic scattering vector expected in the QPI patterns for the reconstructed Fermi surface in the HO phase. Figure adapted from Ref. [285].

6.6 Symmetry breaking electronic modulations

Very often we observe a unidirectional electronic modulation in the topographic images taken on type-A surface that appears superposed to the corrugation due to the Si atomic lattice. This symmetry breaking modulation is only observed in large atomically ordered regions far from steps between different atomic planes.

Fig.6.23 show a series of topographic images taken at 150 mK and zero magnetic field for different values of the bias voltage. The signal produces by the symmetry breaking electronic modulation is weak compared to the atomic corrugation but can be clearly identified in all the images. We have marked by yellow dotted lines the position of where the electronic modulation shows minima. This shows that the period of the one-dimensional modulation is more than 10 times larger than the lattice parameter.

The period and the direction of the symmetry breaking modulation is better defined in the Fourier transforms of the topographic images (Fig.6.23). The wave vector associated to the modulation q_0 and its harmonics are highlighted by yellow dashed lines. Right bottom panel in Fig.6.23 shows profiles for several bias voltages corresponding to the Fourier transform intensity along the reciprocal space direction where the one dimensional modulation appears. We find a

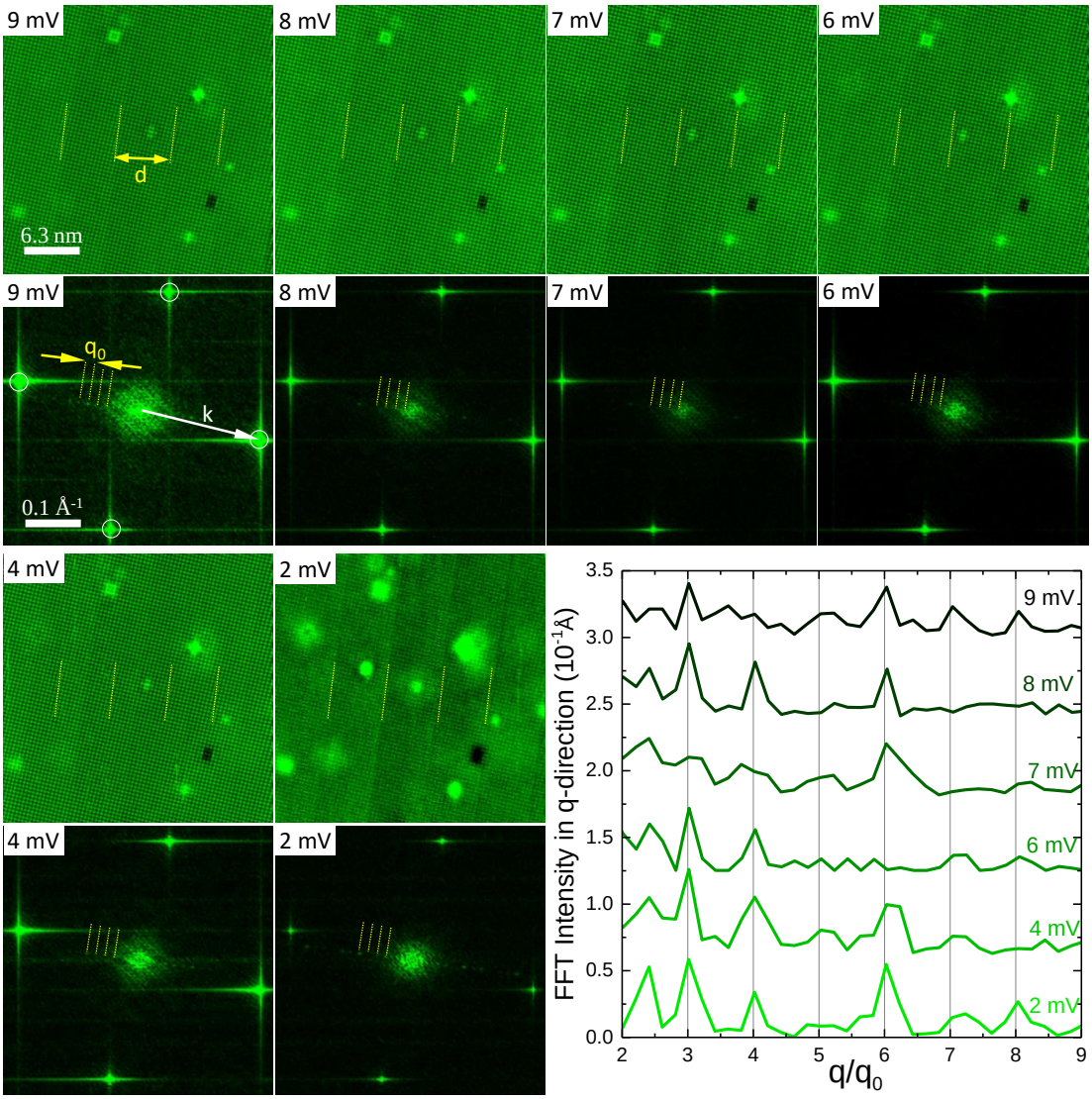

Figure 6.23 Topography images taken in a region of 31.5 nm × 31.5 nm and their FFT as a function of the bias voltage in URu_2Si_2 at 150 mK and zero magnetic field. The white arrow indicates the Bragg peaks associated to the Si lattice with $k = 1/a$, (a being the constant lattice on ab-plane). Yellow dashed lines are a guide to represent the period of the symmetry breaking modulation with spacing d in the real space and wave vector q_0 in the reciprocal space. The height vs. distance profiles in the FFT are shown in the lower right panel (distance is normalized to q_0).

periodic increase in the Fourier transform intensity that correspond to the position of the Bragg peaks associated to the symmetry breaking modulation. We determine q_0 from the reciprocal space distance between consecutive peaks and obtain that $q_0 = 0.016$ 1/Å. This corresponds to an electronic modulation of period $d = 1/q_0 = 6.5 \pm 0.5$ nm.

We have also determined the relative orientation between the symmetry breaking modulation and the Si atomic lattice. Real space and Fourier transform maps show that the symmetry breaking electronic modulation is nearly parallel to one crystalline direction with an angular deviation of a few degrees. This angular deviation can be obtained by measuring the angle between the Bragg peaks associated to each modulation in the Fourier transforms. We find that the symmetry breaking electronic modulation is rotated by 9 degrees from the crystal lattice.

It is important to note that neither the orientation nor the amplitude of q_0 change with the bias voltage as shown in Fig. 6.23. This is different from what we found for the surface electronic

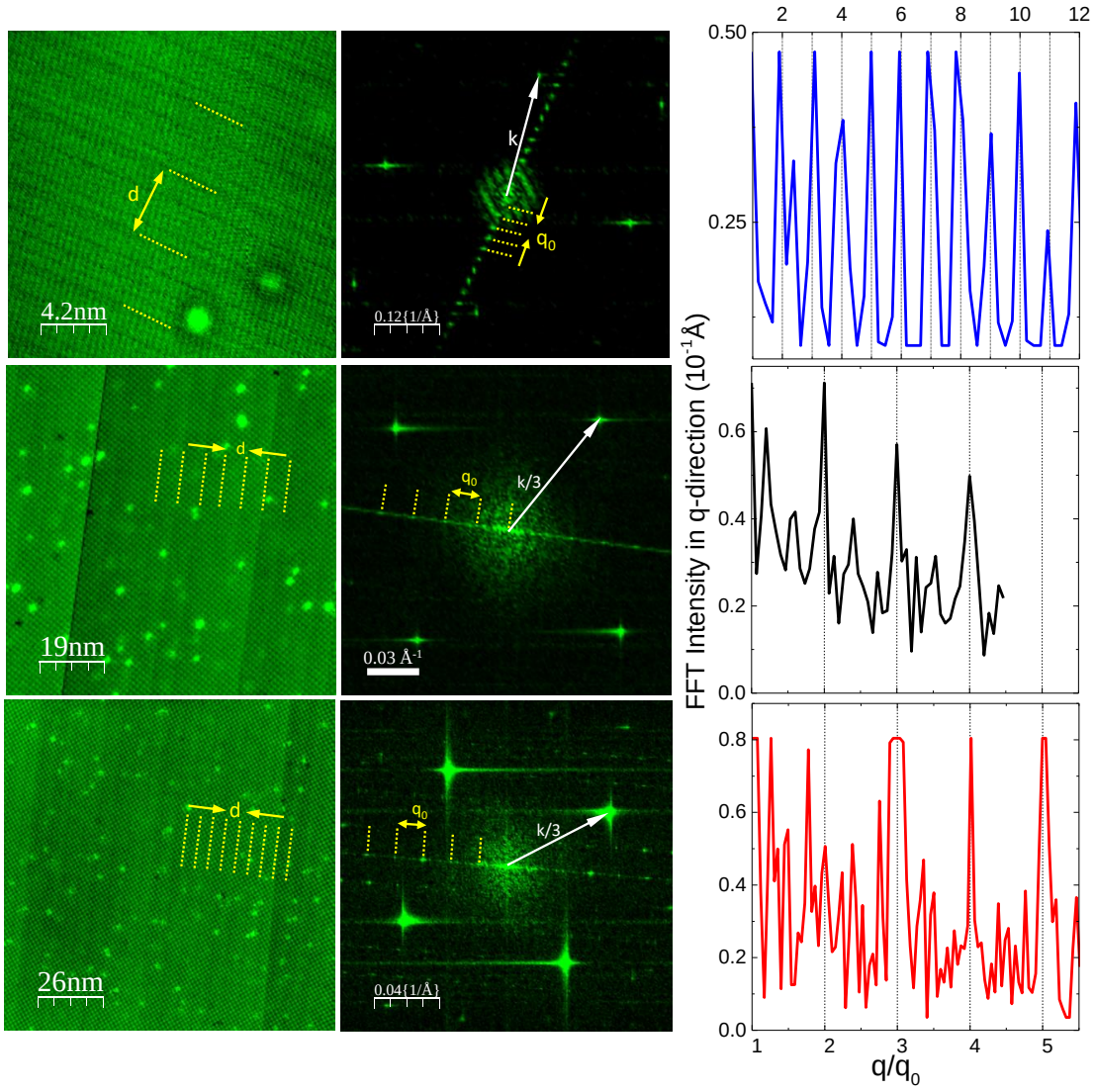

Figure 6.24 (Left column) Topographic images on different cleaved single crystals of URu_2Si_2 at 150 mK and zero magnetic field (left panels) and their Fourier transforms (middle panels). Yellow dashed lines highlight are the same than in Fig.6.23. White arrows in FFT maps represent the positions of the atomic lattice Bragg peaks k (upper image) and different harmonics of k (middle and lower panel) corresponding to frequencies that appear in the MoirÃ© patterns formed in real space because the distance between consecutive points in the images is higher that a (with $k = 1/a$, a being the constant lattice on ab-plane). (Right column) We show the profiles in the FFT along the direction of the modulation, normalized to the q_0 vector.

modulations observed in Si-surfaces due to scattering by steps (Section 6.5). This implies that the reported symmetry breaking electronic modulations are not due to dispersive electronic scattering but an intrinsic property of URu_2Si_2. Moreover this result is fully reproducible. Fig.6.24 shows larger scale atomic resolved topographic images showing the presence of the symmetry breaking electronic modulation. These have been taken in different samples and areas within the same sample. The modulation due to symmetry breaking field is better defined in both real and reciprocal space due to the larger size of the images. A similar analysis to the one described above leads to the same value for the wave vector associated to the modulation, $q_0 = 0.016\ 1/\mathring{A}$. We also find that the symmetry breaking electronic modulation is oriented nearly parallel to one crystalline axis.

The symmetry breaking modulation observed in our experiments is consistent with the nematic in-plane anisotropy reported by microscopic measurements under magnetic field [273, 274] and the orthorhombic structural distortion found at zero field[272]. We find that the orientation of the symmetry breaking electronic modulation is nearly parallel to the crystalline [100] direction while other macroscopic measurements have pointed to electronic nemacity with in-plane anisotropy elongated along the [110] direction [273, 274]. However, theoretical calculations of this order without impurity scattering have shown that the direction of in-plane anisotropy is preferred to be along [110] than [100], but the energy difference between these two is very small [277]. Then it is feasible than impurities can induce disorder in the nematic direction within the ab plane. Indeed, recent analysis of the in-plane field angle dependence NMR results shows that there exists noticeable distribution of the twofold anisotropic local fields [274].

Moreover, we have found that this nematic ordering has an intrinsic wavevector q_0 that corresponds to an electronic modulation of period 6.5±0.5. This has been experimentally observed for the first time in our work. Future work needs to be done in order to associated this vector with any feature in the reconstructed Fermi surface that allows to shed light into the origin of the order parameter behind the HO phase.

As I mentioned above, previous STM measurements made in the HO phase of URu_2Si_2 have not reported any evidence for the existence of symmetry breaking electronic modulations. This can be due to the difference in either the energy resolution or the sample quality between different experiments. Our measurements are made at temperatures one order of magnitude lower than previous experiments. We also measure very high quality samples with residual resistivity ratio (RRR) of 122 (RRR values for the crystals measured in previous STM work are not reported). Synchrotron X-ray experiments found that the orthorhombic distortion is very sensitive to disorder. This is difficult to be observed for crystals with RRR less than 50[272]. Regarding electronic nematicity, clear twofold anisotropic fields were reported in NMR measurements for samples with RRR$\sim$70 [274].

6.7 Concluding Remarks

We have identifed two types of atomically flat surfaces in high quality single crystals of URu_2Si_2 cleaved in-situ at very low temperatures: type-A and type-B surface. An analysis of the topographic features compared to the atomic radios of the different elements allow us to determine the chemical nature of the two surface. Type-A surface shows the atomic lattice of Si while type-B surface correspond to Ru planes although it does not show atomic resolution.

We have directly observed in the tunneling conductance curves measured down to 150 mK the gap opening of the spin resonance in the density of states at -1.5 meV, associated to the antiferromagnetic wave vector $\mathbf{Q_0}$.

We have directly measured the superconducting gap of URu_2Si_2 and used a phenomenological model to fit its temperature dependence. We find $\Delta_{SC} \approx 0.21$ meV with a critical temperature of $T_c = 1.5$ K.

We have reported the first observation of symmetry breaking electronic modulations associated to the structural transition from tetragonal to orthorhombic structure below T_{HO}. The symmetry breaking modulation are oriented along the [110] direction of the tetragonal structure in agreement with previous macroscopic measurements. We have determined a wave vector associated to the electronic nematicity of $q_0 = 0.016$ 1/Å.

QPI measurements on type-A surfaces have shown evidence for the FS reconstruction below T_HO. Our data shows QPI vector associated to a small sheet of the FS with reduced effective mass $m* \sim 5m_e$.

7 - General Conclusions

In this PhD thesis we have used tunneling microscopy at very low temperatures to characterize the electronic properties of three superconducting materials. Some of them under tilted magnetic fields.

The main conclusions of this thesis are:

- We have successfully implemented and tested a a system to cleave single crystalline samples in-situ and at very low temperatures. The mechanical noise level has been reduced by improving the isolation and decoupling from the build. In parallel, the running time of the cryostat was increased from 3.5 days to 5 days approximately.

- We have reported the first measurements of the supercondcuting gap and the vortex lattice in β-Bi_2Pd. We found that β-Bi_2Pd has multiband features with only one superconducting gap. This result was not observed before because multiband superconductivity has been always though to be linked to multigap behaviour. . The vortex lattice with magnetic fields parallel to the c-axis in β-Bi_2Pd shows hexagonal symmetry and its orientation is determined by the tetragonal crystal lattice. We observe enhancement of the intervortex density of states; this effect is explained by the multiband structure of the Fermi surface in β-Bi_2Pd.

- We have studied with detail the tilted vortex lattice in β-Bi_2Pd. We demonstrate by comparison between the size of the cores at perpendicularand tilted fields that the vortices bend close to the surface to exit perpendicular to it. At large tilted angles, the repulsive interaction between bent vortices at the surface induces rotations of the bulk vortex lattice to maximize the intervortex distance on the surface.

- We have measured the superconducting gap and the vortex lattice by the first time in $Rh_9In_4S_4$. We observe that, in spite of being an extreme type-II superconductor, the superconducting gap follows a BCS behavior. In this material, we have obtained the first direct observation of vortex creep at very low temperatures using STM, making this material adequate to study vortex creep through macroscopic experiments. We found that the creep velocity strongly depends on each experiment, and show that the local distribution of

pinning centers influences vortex creep, so that the hexagonal vortex lattice has glassy dynamic properties.

- We have identified and characterize the electronic properties two types of surfaces on in-situ cleaved single crystals of URu_2Si_2: one corresponding to Si atoms and another to Ru atoms. We have measured the tunneling conductance at 150 mK and its dependence with temperature and magnetic field, identifying for the first time structures, in the electron density of states, associated to the spin resonance at -1.5 meV for the commensurate vector Q_0 and the superconducting gap at 0.2 meV. We have used a phenomenological model to fit our experimental data and obtained the temperature dependence of the superconducting gap. Atomic scale images on ordered Si surfaces shown the presence of an electronic order that breaks the tetragonal symmetry, being this result the first microscopic evidence for the existence of a nematic order and a structural transition reported previously by macroscopic measurements at $T < T_{HO}$. QPI experiments on Si surface with many consecutive steps have allowed us to obtain an intraband dispersion vector and its energy dependence. Our results are consistent with the reconstruction of the Fermi surface observed in macroscopic measurements within the HO phase.

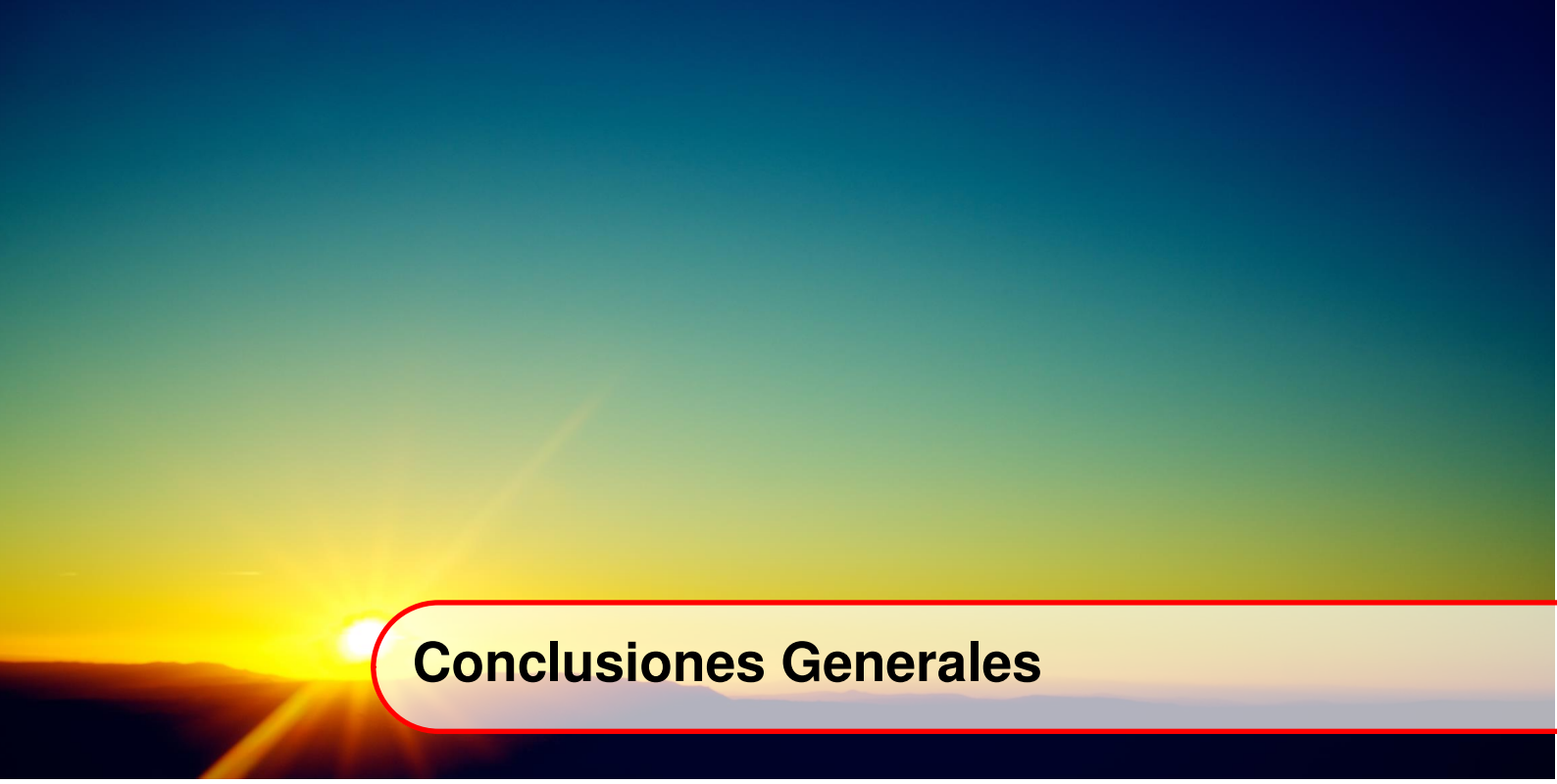

Conclusiones Generales

En esta Tesis doctoral hemos utilizado microscopía de efecto túnel a muy bajas temperaturas para estudiar propiedades electrónicas de tres materiales superconductores. Algunas de ellas aplicando campos magnéticos inclinados.

A continuación se exponen las conclusiones generales de la tesis.

- En cuanto al sistema experimental, se ha implementado y puesto en funcionamiento exitosamente un sistema de rotura de muestras en frío. Hemos reducido el nivel de ruido mecánico realizando mejoras en en el sistema de anclaje al edificio. En paralelo, se incrementó el tiempo hábil de operación del criostato de 3.5 días a aproximadamente 5 días.

- Hemos obtenido las primeras medidas del gap superconductor y de la red de vórtices en el compuesto β-Bi_2Pd. Encontramos que este material es un superconductor multibanda con un único gap superconductor, en contra de la creencia general de que la superconductividad multibanda esta asociada de manera unívoca a la superconductividad multigap. Los resultados de la red de vórtices con campo paralelo al eje-c en β-Bi_2Pd, muestran la formación de una red de Abrikosov hexagonal cuya orientación está determinada por la estructura tetragonal de la red cristalina. Observamos un aumento de la densidad de estados superconductora entre vórtices con respecto a lo esperado dentro de la teoría BCS. Encontramos que dicho efecto esta determinado por la estructura multibanda de la superficie de Fermi del material.

- Hemos hecho un estudio muy detallado del comportamiento de la red de vórtices en β-Bi_2Pd bajo campos magnéticos inclinados. Hemos demostrado a partir de las medidas del tamaño de núcleo de los vórtices que estos se doblan cerca a la superficie para salir perpendicularmente a ella. Encontramos que, para ángulos de inclinación grandes, la interacción repulsiva entre vórtices a lo largo de la trayectoria en la que se doblan cerca de la superficie, induce rotaciones en la red de vórtices dentro del volumen que maximizan la distancia entre vórtices en la superficie.

- Hemos obtenido las primeras medidas del gap superconductor y de la red de vórtices, con

campo paralelo al eje-*c* en el compuesto $Rh_9In_4S_4$. Observamos que, a pesar de ser un material tipo-II extremo, el gap superconductor sigue un comportamiento BCS. En este material, hemos obtenido las primeras observaciones directas de dinámica de vórtices a muy bajas temperaturas usando microscopía de efecto túnel, lo que hace de este compuesto un candidato adecuado para estudiar la dinámica de vórtices usando experimentos macroscópicos. Encontramos que la velocidad de movimiento de los vórtices depende de las condiciones iniciales de cada experimento. Demostramos que la distribución local de los centros de anclaje tiene una influencia notable en el movimiento residual de la red de vórtices.

- A partir de imágenes de topografía sobre muestras de URu_2Si_2 clivadas *in situ* a 4.2 K hemos identificado dos tipos de superficies y caracterizado sus propiedades electrónicas: una correspondiente a átomos de Ru y la otra a átomos de Si. Hemos realizado medidas de la conductancia túnel a 150 mK y su dependencia en temperatura y campo magnético, identificando por primera vez estructuras en la densidad electrónica asociadas a la resonancia de espín a -1.5 meV para el vector conmensurado Q_0 y del gap superconductor a 0.2 meV. Hemos obtenido la dependencia en temperatura del gap superconductor usando un modelo fenomenológico que permite ajustar nuestras curvas de conductancia. Imágenes a escala atómica sobre superficies de Si ordenadas muestran la presencia de un orden electrónico que rompe la simetría tetragonal, siendo este resultado la primera evidencia microscópica de la existencia de un orden nemático y de una transición estructural anteriormente mostrados en medidas macroscópicas para $T < T_{HO}$. Un estudio de los patrones superficiales de interferencia electrónica producidos por dispersión en escalones sobre superficies de Si, nos ha permitido obtener un vector de dispersión intrabanda y su dependencia en energía, consistente con la reconstrucción de la superficie de Fermi observada en medidas macroscópicas dentro de la fase de HO.

Publications

- *E. Herrera*, I. Guillamón, J. A. Galvis, A. Correa, A. Fente, R. F. Luccas, F. J. Mompean, M. García-Hernandez, S. Vieira, J. P. Brison and H. Suderow.*Magnetic field dependence of the density of states in the multiband superconductor β-Bi2Pd*. Physical Review B. **92**, 054507 (2015)
- A. Fente, *E. Herrera*, I. Guillamón, H. Suderow, S. Mañas-Valero, M. Galbiati, E. Coronado and V. G. Kogan. *Field dependence of the vortex core size probed by STM*. Physical Review B. **94**, 014517 (2016)
- J. A. Galvis, *E. Herrera*, I. Guillamón, S. Vieira and H. Suderow. *Vortex cores and vortex motion in superconductors with anisotropic Fermi surfaces*. Physica C. **-** , Acepted Nov. (2016)
- J. Kačmarčík, Z. Pribulová, T. Samuely, P. Szabó, V. Cambel, J. Šoltýs, *E. Herrera*, H. Suderow, A. Correa-Orellana, D. Prabhakaran, P. Samuely.*Single gap superconductivity in β-Bi2Pd*. Physical Review B. **93**, 144502 (2016)
- J. A. Galvis, *E. Herrera*, I. Guillamón, J. Azpeitia, R. F. Luccas, C. Munuera, M. Cuenca, J. A. Higuera, N. Díaz, M. Pazos, M. García-Hernandez, A. Buendía, S. Vieira, and H. Suderow. *Three axis vector magnet set-up for cryogenic scanning probe microscopy*. Review of Scientific Instruments. **86**, 013706 (2015)
- Luccas, R. F. Fente, A. Hanko, J. Correa-Orellana, A. *E. Herrera*. Climent-Pascual, E. Azpeitia, J. Pérez-Castañeda, T. Osorio, M. R. Salas-Colera, E. Nemes, N. M. Mompean, F. J. García-Hernández, M. Rodrigo, J. G. Ramos, M. A. Guillamón, I. Vieira, S. Suderow, H. *Charge density wave in layered $La_{1-x}Ce_xSb_2$*. Physical Review B, **92**, 235153 (2015)
- *E. Herrera*, I. Guillamón, J. A. Galvis, A. Correa, A. Fente, R. F. Luccas, S. Vieira and H. Suderow. *Vortex bending and the orientation of the superconducting vortex lattice*. In preparation.
- *E. Herrera*, J. Benito-Llorens, U. Kaluarachi, S. Bud'ko, P. C. Canfield, I. Guillamón and H. Suderow. *Direct observation of vortex creep at millikelvin temperatures in single crystals of the extreme type-II superconductor $Rh_9In_4S_4$*. In preparation.
- J. A. Galvis, *E. Herrera*, Ch. Berthod, S. Vieira, I. Guillamón and H. Suderow. *Tilted vortex cores in the layered anisotropic superconductor 2H-$NbSe_2$*. In Preparation.

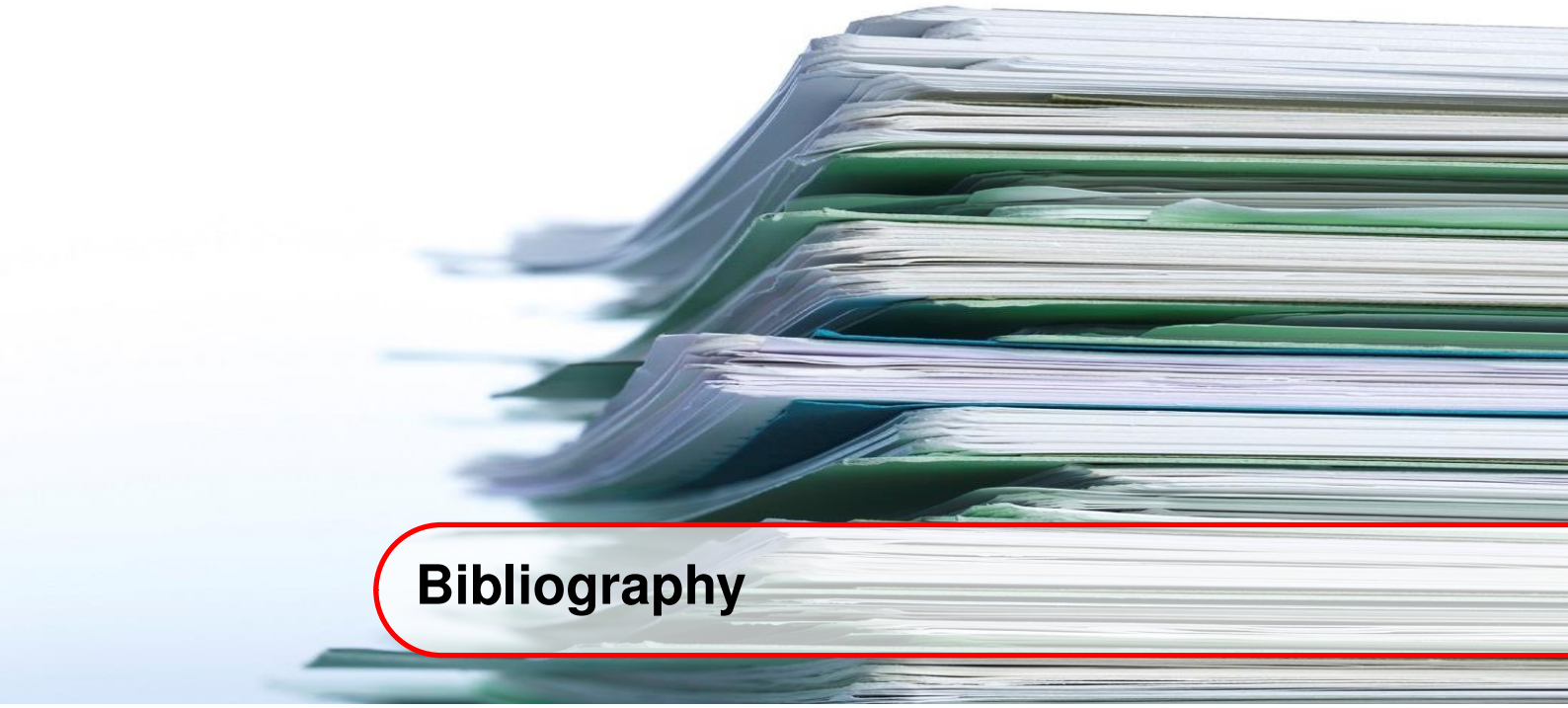

Bibliography

[1] Juan Gossaín. Un amigo vale más que un nobel. *Revista SEMANA*, Enviado especial a México, compartió con García Márquez las primeras emociones del Premio Nobel, 1982.

[2] H. K. Onnes. Further experiments with liquid helium. d. on the change of electrical resistance of pure metals at very low temperatures, etc. v. the disappearance of the resistance of mercury. *Comm. Phys. Lab. Univ. Leiden*, Supp. 29, 1911.

[3] Dirk van Delft and Peter Kes. The discovery of superconductivity. *Physics Today*, 63(9):38, September 2010.

[4] Horacio A . Farach Charles Poole, Jr. and Richard J. Creswick. *Superconductivity*, volume I. Academic Press Limited, 1995.

[5] Nobelprize.org. The nobel prize in physics 1913. http://www.nobelprize.org/nobel_prizes/physics/laureates/1913/onnes-facts.html, May 2014.

[6] K. Onnes. Further experiments with liquid helium. c. on the change of electric resistance of pure metals at very low temperatures etc. iv. the resistance of pure mercury at helium temperatures, 1911.

[7] W. Meissner and R. Ochsenfeld. Ein neuer effekt bei eintritt der supraleitfähigkeit. *Naturwissenschaften*, 21:787–788, November 1933.

[8] Michael Tinkham. *Introduction to Superconductivity*, volume I of *International series in pure and applied physics.* Robert E. Krieger Publishing Company, INC., reprint 1980 edition, 1975.

[9] F. London and H. London. The electromagnetic equations of the supraconductor. *Proceedings of the Royal Society of London. Series A - Mathematical and Physical Sciences*, 149(866):71–88, 1935.

[10] Nobelprize.org. The nobel prize in physics 2003. http://www.nobelprize.org/nobel_prizes/physics/laureates/2003/abrikosov-facts.html, May 2014.

[11] Nobelprize.org. The nobel prize in physics 1962. "Lev Landau - Facts". Nobelprize.org. Nobel Media AB 2013. Web. 19 May 2014. <http://www.nobelprize.org/nobel_prizes/physics/laureates/1962/landau-facts.html, May 2014.

[12] L.D. Landau V.L. Ginzburg. On the theory of superconductivity. *Zh. Eksp. Teor. Fiz.*, 20:1064–1082, 1950.

[13] L.D. Landau. On the theory of phase transitions. *Zh. Eksp. Teor. Fiz*, 7:19–32, 1969.

[14] Shepelev Yu.D. Ryabinin Yu.N. Shubnikov L.V., Khotkevich V.I. Magnetic properties of supercondcuting metals and alloys. *Zh. Eksper. Teor. Fiz*, 7:221–237, 1937.

[15] A. A. Abrikosov. On the magnetic properties of superconductors of the second group. *Soviet Physics JETP*, 5(1174):71–88, 1957.

[16] Hitoshi Nishimori, Kazuharu Uchiyama, Shin ichi Kaneko, Akio Tokura, Hiroyuki Takeya, Kazuto Hirata, and Nobuhiko Nishida. First observation of the fourfold-symmetric and quantum regime vortex core in yni2b2c by scanning tunneling microscopy and spectroscopy. *Journal of the Physical Society of Japan*, 73(12):3247–3250, 2004.

[17] M. Yethiraj, D. McK. Paul, C. V. Tomy, and E. M. Forgan. Neutron scattering study of the flux lattice in yni_2b_2c. *Phys. Rev. Lett.*, 78:4849–4852, Jun 1997.

[18] U. Essmann and H. Trauble. The direct observation of individual flux lines in type ii superconductors. *Physics Letters A*, 24(10):526 – 527, 1967.

[19] H. F. Hess, R. B. Robinson, R. C. Dynes, J. M. Valles, and J. V. Waszczak. Scanning-tunneling-microscope observation of the abrikosov flux lattice and the density of states near and inside a fluxoid. *Phys. Rev. Lett.*, 62:214–216, Jan 1989.

[20] K. Harada, T. Matsuda, J. Bonevich, M. Igarashi, S. Kondo, G. Pozzi, U. Kawabe, and A. Tonomura. Real-time observation of vortex lattices in a superconductor by electron microscopy. *Nature*, 360(6399):51–53, Nov 1992.

[21] A Oral, S J Bending, R G Humphreys, and M Henini. Microscopic measurement of penetration depth in $yba_2cu_3o_{7-\Delta}$ thin films by scanning hall probe microscopy. *Superconductor Science and Technology*, 10(1):17, 1997.

[22] A. Volodin, K. Temst, C. Van Haesendonck, Y. Bruynseraede, M. I. Montero, and I. K. Schuller. Magnetic-force microscopy of vortices in thin niobium films: Correlation between the vortex distribution and the thickness-dependent film morphology. *EPL (Europhysics Letters)*, 58(4):582, 2002.

[23] R. Straub, S. Keil, R. Kleiner, and D. Koelle. Low-frequency flux noise and visualization of vortices in a yba2cu3o7 dc superconducting quantum interference device washer with an integrated input coil. *Applied Physics Letters*, 78(23):3645–3647, 2001.

[24] G. Blatter, M. V. Feigel'man, V. B. Geshkenbein, A. I. Larkin, and V. M. Vinokur. Vortices in high-temperature superconductors. *Rev. Mod. Phys.*, 66:1125–1388, Oct 1994.

[25] Gianni Blatter and Vadim Geshkenbein. Quantum collective creep: Effects of anisotropy, layering, and finite temperature. *Phys. Rev. B*, 47:2725–2741, Feb 1993.

[26] G.P. Mikitik. Upper critical field and melting line of the flux-line lattice in clean high-tc superconductors near tc. *Physica C: Superconductivity*, 245(3):287 – 294, 1995.

[27] Nobelprize.org. The nobel prize in physics 1972. http://www.nobelprize.org/nobel_prizes/physics/laureates/1972, May 2014.

[28] J. Bardeen, L. N. Cooper, and J. R. Schrieffer. Microscopic theory of superconductivity. *Phys. Rev.*, 106:162–164, Apr 1957.

[29] J. Bardeen, L. N. Cooper, and J. R. Schrieffer. Theory of superconductivity. *Phys. Rev.*, 108:1175–1204, Dec 1957.

[30] Leon N. Cooper. Bound electron pairs in a degenerate fermi gas. *Phys. Rev.*, 104:1189–1190, Nov 1956.

[31] F. Steglich, J. Aarts, C. D. Bredl, W. Lieke, D. Meschede, W. Franz, and H. Schäfer. Superconductivity in the presence of strong pauli paramagnetism: $Cecu_2si_2$. *Phys. Rev. Lett.*, 43:1892–1896, Dec 1979.

[32] J. G. Bednorz and K. A Muller. "possible high tc superconductivity in the ba-la-cu-o system. *Zeitschrift fur Physik B*, 64:189–193, 1983.

[33] H. Suhl, B. T. Matthias, and L. R. Walker. Bardeen-cooper-schrieffer theory of superconductivity in the case of overlapping bands. *Phys. Rev. Lett.*, 3:552–554, Dec 1959.

[34] N. R. Werthamer, E. Helfand, and P. C. Hohenberg. Temperature and purity dependence of the superconducting critical field, H_{c2}. iii. electron spin and spin-orbit effects. *Phys. Rev.*, 147:295–302, Jul 1966.

[35] M. Mansor and J. P. Carbotte. Upper critical field in two-band superconductivity. *Phys. Rev. B*, 72:024538, Jul 2005.

[36] H. Suderow, V. G. Tissen, J. P. Brison, J. L. Martínez, S. Vieira, P. Lejay, S. Lee, and S. Tajima. Pressure dependence of the upper critical field of Mgb_2 and of Yni_2b_2C. *Phys. Rev. B*, 70:134518, Oct 2004.

[37] H. Suderow, V. G. Tissen, J. P. Brison, J. L. Martínez, and S. Vieira. Pressure induced effects on the fermi surface of superconducting 2H-$nbse_2$. *Phys. Rev. Lett.*, 95:117006, Sep 2005.

[38] Ivar Giaever. Electron tunneling between two superconductors. *Phys. Rev. Lett.*, 5:464–466, Nov 1960.

[39] G. Binnig, A. Baratoff, H. E. Hoenig, and J. G. Bednorz. Two-band superconductivity in nb-doped $srtio_3$. *Phys. Rev. Lett.*, 45:1352–1355, Oct 1980.

[40] H. F. Hess, R. B. Robinson, and J. V. Waszczak. Vortex-core structure observed with a scanning tunneling microscope. *Phys. Rev. Lett.*, 64:2711–2714, May 1990.

[41] C. Caroli, P.G. De Gennes, and J. Matricon. Bound fermion states on a vortex line in a type ii superconductor. *Physics Letters*, 9(4):307 – 309, 1964.

[42] I. Guillamon, H. Suderow, F. Guinea, and S. Vieira. Intrinsic atomic-scale modulations of the superconducting gap of 2*h*-$nbse_2$. *Phys. Rev. B*, 77:134505, Apr 2008.

[43] Can-Li Song, Yi-Lin Wang, Peng Cheng, Ye-Ping Jiang, Wei Li, Tong Zhang, Zhi Li, Ke He, Lili Wang, Jin-Feng Jia, Hsiang-Hsuan Hung, Congjun Wu, Xucun Ma, Xi Chen, and Qi-Kun Xue. Direct observation of nodes and twofold symmetry in fese superconductor. *Science*, 332(6036):1410–1413, 2011.

[44] Brian B. Zhou, Shashank Misra, Eduardo H. da Silva Neto, Pegor Aynajian, Ryan E. Baumbach, J. D. Thompson, Eric D. Bauer, and Ali Yazdani. Visualizing nodal heavy fermion superconductivity in cecoin5. *Nat Phys*, 9(8):474–479, Aug 2013. Letter.

[45] Shin ichi Kaneko, Ken Matsuba, Muhammad Hafiz, Keigo Yamasaki, Erika Kakizaki, Nobuhiko Nishida, Hiroyuki Takeya, Kazuto Hirata, Takuto Kawakami, Takeshi Mizushima, and Kazushige Machida. Quantum limiting behaviors of a vortex core in an anisotropic gap superconductor. *Journal of the Physical Society of Japan*, 81(6):063701, 2012.

[46] P. Martinez-Samper, J.G. Rodrigo, G. Rubio-Bollinger, H. Suderow, S. Vieira, S. Lee, and S. Tajima. Scanning tunneling spectroscopy in mgb2. *Physica C: Superconductivity*, 385(12):233 – 243, 2003.

[47] J. P. Franck, F. D. Manchester, and Douglas L. Martin. The specific heat of pure copper and of some dilute copper+iron alloys showing a minimum in the electrical resistance at low temperatures. *Proceedings of the Royal Society of London A: Mathematical, Physical and Engineering Sciences*, 263(1315):494–507, 1961.

[48] Markus Ternes, Andreas J Heinrich, and Wolf-Dieter Schneider. Spectroscopic manifestations of the kondo effect on single adatoms. *Journal of Physics: Condensed Matter*, 21(5):053001, 2009.

[49] W.J. de Haas, J. de Boer, and G.J. van den Berg. The electrical resistance of gold, copper and lead at low temperatures. *Physica*, 1(7):1115 – 1124, 1934.

[50] W. Meissner and B. Voigt. Messungen mit hilfe von flüssigem helium xi widerstand der reinen metalle in tiefen temperaturen. *Annalen der Physik*, 399(7):761–797, 1930.

[51] Jun Kondo. Resistance minimum in dilute magnetic alloys. *Progress of Theoretical Physics*, 32(1):37–49, 1964.

[52] J. Kondo. Effect of ordinary scattering on exchange scattering from magnetic impurity in metals. *Phys. Rev.*, 169:437–440, May 1968.

[53] Jiutao Li, Wolf-Dieter Schneider, Richard Berndt, and Bernard Delley. Kondo scattering observed at a single magnetic impurity. *Phys. Rev. Lett.*, 80:2893–2896, Mar 1998.

[54] V. Madhavan, W. Chen, T. Jamneala, M. F. Crommie, and N. S. Wingreen. Tunneling into a single magnetic atom: Spectroscopic evidence of the kondo resonance. *Science*, 280(5363):567–569, 1998.

[55] H. C. Manoharan, C. P. Lutz, and D. M. Eigler. Quantum mirages formed by coherent projection of electronic structure. *Nature*, 403(6769):512–515, Feb 2000.

[56] Pegor Aynajian, Eduardo H. da Silva Neto, Colin V. Parker, Yingkai Huang, Abhay Pasupathy, John Mydosh, and Ali Yazdani. Visualizing the formation of the kondo lattice and the hidden order in uru2si2. *Proceedings of the National Academy of Sciences*, 107(23):10383–10388, 2010.

[57] A. R. Schmidt, M. H. Hamidian, P. Wahl, F. Meier, A. V. Balatsky, J. D. Garrett, T. J. Williams, G. M. Luke, and J. C. Davis. Imaging the fano lattice to hidden order transition in uru2si2. *Nature*, 465(7298):570–576, Jun 2010.

[58] Mohammad H. Hamidian, Andrew R. Schmidt, Inês A. Firmo, Milan P. Allan, Phelim Bradley, Jim D. Garrett, Travis J. Williams, Graeme M. Luke, Yonatan Dubi, Alexander V. Balatsky, and J. C. Davis. How kondo-holes create intense nanoscale heavy-fermion hybridization disorder. *Proceedings of the National Academy of Sciences*, 108(45):18233–18237, 2011.

[59] S. Ernst, S. Kirchner, C. Krellner, C. Geibel, G. Zwicknagl, F. Steglich, and S. Wirth. Emerging local kondo screening and spatial coherence in the heavy-fermion metal ybrh2si2. *Nature*, 474(7351):362–366, Jun 2011.

[60] Pegor Aynajian, Eduardo H. da Silva Neto, Andras Gyenis, Ryan E. Baumbach, J. D. Thompson, Zachary Fisk, Eric D. Bauer, and Ali Yazdani. Visualizing heavy fermions emerging in a quantum critical kondo lattice. *Nature*, 486(7402):201–206, Jun 2012.

[61] U. Fano. Effects of configuration interaction on intensities and phase shifts. *Phys. Rev.*, 124:1866–1878, Dec 1961.

[62] K. Nagaoka, T. Jamneala, M. Grobis, and M. F. Crommie. Temperature dependence of a single kondo impurity. *Phys. Rev. Lett.*, 88:077205, Feb 2002.

[63] S. Doniach. The kondo lattice and weak antiferromagnetism. *Physica B+C*, 91:231 – 234, 1977.

[64] Alexander Cyril Hewson. *The Kondo problem to heavy fermions*, volume 2. Cambridge university press, 1997.

[65] P. W. Anderson. Localized magnetic states in metals. *Phys. Rev.*, 124:41–53, Oct 1961.

[66] Pegor Aynajian, Eduardo H. da Silva Neto, Brian B. Zhou, Shashank Misra, Ryan E. Baumbach, Zachary Fisk, John Mydosh, Joe D. Thompson, Eric D. Bauer, and Ali Yazdani. Visualizing heavy fermion formation and their unconventional superconductivity in f-electron materials. *Journal of the Physical Society of Japan*, 83(6):061008, 2014.

[67] B.D. White, J.D. Thompson, and M.B. Maple. Unconventional superconductivity in heavy-fermion compounds. *Physica C: Superconductivity and its Applications*, 514:246 – 278, 2015. Superconducting Materials: Conventional, Unconventional and Undetermined.

[68] E. Bucher, J. P. Maita, G. W. Hull, R. C. Fulton, and A. S. Cooper. Electronic properties of beryllides of the rare earth and some actinides. *Phys. Rev. B*, 11:440–449, Jan 1975.

[69] Christian Pfleiderer. Superconducting phases of f-electron compounds. *Rev. Mod. Phys.*, 81:1551–1624, Nov 2009.

[70] J. A. Galvis. *Superconductividad y dimensionalidad: microscopía túnel bajo campos magnéticos Inclinados.* PhD thesis, Universidad Autónoma de Madrid, Noviembre 2013.

[71] Frank Pobell. *Matter and Methods at Low Temperatures*. 2007.

[72] O. V. Lounasmaa. *Experimental Principles and Methods Below 1K*. Academic Press INC. New York., 1974.

[73] G Frossati. Experimental techniques: Methods for cooling bellow 300 mk. *Journal of Low Temperature Physics*, 87(3/4):595–633, 1992.

[74] John C. Wheatley. Dilute solutions of 3he in 4he at low temperatures. *American Journal of Physics*, 36(3):181–210, 1968.

[75] G. K. White and P. Meeson. *Experimental Techniques in Low-Temperature Physics*. Oxford University Press, 1979.

[76] Oxford Instruments. www.oxford-instruments.com/products/cryogenic-environments/dilution-refrigerator/wet-dilution-refrigerators, 2016.

[77] Merlett Tecnoplastic S.p.A. www.merlett.com/products-list/armorvin-hna, 2014.

[78] Lake Shore Cryotronics Inc. www.lakeshore.com, 2016.

[79] Scientific Instruments. www.scientificinstruments.com/product-detail/model-ro-105100k-ruthenium-oxide-rtd/.

[80] J. A. Galvis, E. Herrera, I. Guillamón, J. Azpeitia, R. F. Luccas, C. Munuera, M. Cuenca, J. A. Higuera, N. Díaz, M. Pazos, M. Garcá-Hernandez, A. Buendá, S. Vieira, and H. Suderow. Three axis vector magnet set-up for cryogenic scanning probe microscopy. *Review of Scientific Instruments*, 86(1):–, 2015.

[81] Nobelprize.org. The nobel prize in physics 1986. $http$: $//www.nobelprize.org/nobel_prizes/physics/laureates/1986/$, September 2013.

[82] Gerber Ch. Binnig G., Rohrer H. and Weibel E. Tunneling through a controllable vacuum gap. *Applied Physics Letters*, 40:178, 1982.

[83] L. Esaki and P. J. Stiles. New type of negative resistance in barrier tunneling. *Phys. Rev. Lett.*, 16:1108–1111, Jun 1966.

[84] B.D. Josephson. Possible new effects in superconductive tunnelling. *Physics Letters*, 1(7):251 – 253, 1962.

[85] J. Bardeen. Tunnelling from a many-particle point of view. *Phys. Rev. Lett.*, 6:57–59, Jan 1961.

[86] J. Tersoff and D. R. Hamann. Theory and application for the scanning tunneling microscope. *Phys. Rev. Lett.*, 50:1998–2001, Jun 1983.

[87] Øystein Fischer, Martin Kugler, Ivan Maggio-Aprile, Christophe Berthod, and Christoph Renner. Scanning tunneling spectroscopy of high-temperature superconductors. *Rev. Mod. Phys.*, 79:353–419, Mar 2007.

[88] Claude Cohen Tannoudji. *Quantum Mechanics*, volume 1,2. Willey-VHC, Berlin, 1977.

[89] Julian Chen. *Introduction to Scanning Tunneling Microscopy*. Oxford University Press, 1993.

[90] Isabel Guillamón. *Orden y Desorden en Superconductividad*. PhD thesis, Universidad Autónoma de Madrid, 2009.

[91] Jennifer Eve Hoffman. *A Search for Alternative Electronic Order in the High Temperature Superconductor $Bi_2Sr_2CaCu_2O_{8+\delta}$ by Scanning Tunneling Microscopy*. PhD thesis, University of California, Berkeley, 2003.

[92] R. Merservey and P.M. Tedrow. Spin-polarized electron tunneling. *Physics Reports*, 238(4):173–243, 1994.

[93] EBL Products Inc. Piezoceramic tubes, for ultra-precise positioning applications. www.eblproducts.com/piezotube.html, May 2016.

[94] H. Suderow, I. Guillamon, and S. Vieira. Compact very low temperature scanning tunneling microscope with mechanically driven horizontal linear positioning stage. *Review of Scientific Instruments*, 82(3), 2011.

[95] R. F. Luccas, A. Fente, J. Hanko, A. Correa-Orellana, E. Herrera, E. Climent-Pascual, J. Azpeitia, T. Pérez-Castañeda, M. R. Osorio, E. Salas-Colera, N. M. Nemes, F. J. Mompean, M. García-Hernández, J. G. Rodrigo, M. A. Ramos, I. Guillamón, S. Vieira, and H. Suderow. Charge density wave in layered $la_{1-x}ce_xsb_2$. *Phys. Rev. B*, 92:235153, Dec 2015.

[96] Paulstra Industry. Elastomer mounts. www.paulstra-industry.com/traxiflex-p16-es.html, Sept. 2016.

[97] E. Herrera, I. Guillamón, J. A. Galvis, A. Correa, A. Fente, R. F. Luccas, F. J. Mompean, M. García-Hernández, S. Vieira, J. P. Brison, and H. Suderow. Magnetic field dependence of the density of states in the multiband superconductor $\beta - bi_2Pd$. *Phys. Rev. B*, 92:054507, Aug 2015.

[98] Udhara S. Kaluarachchi, Qisheng Lin, Weiwei Xie, Valentin Taufour, Sergey L. Bud'ko, Gordon J. Miller, and Paul C. Canfield. Superconducting properties of $rh_9in_4s_4$ single crystals. *Phys. Rev. B*, 93:094524, Mar 2016.

[99] P. C. Canfield and Z. Fisk. Growth of single crystals from metallic fluxes. *Phil. Mag. B*, 65:1117, 1992.

[100] Paul C. Canfield. *Solution growth of intermetallic single crystals: a beginner's guide.*, chapter 2, pages 93–111. World Scientific Books, 2009.

[101] D Aoki, F Bourdarot, E Hassinger, G Knebel, A Miyake, S Raymond, V Taufour, and J Flouquet. Field re-entrant hidden-order phase under pressure in uru 2 si 2. *Journal of Physics: Condensed Matter*, 22(16):164205, 2010.

[102] V. Prasad M. Dudley G. Dhanaraj, K. Byrappa. *Springer Handbook of Crystal Growth*. Springer, 2010.

[103] T. Muranaka Y. Zenitani J. Nagamatsu, N. Nakagawa and J. Akimitsu. Superconductivity at 39?k in magnesium diboride. *Nature*, 410:63–64, March 2001.

[104] G. Rubio-Bollinger, H. Suderow, and S. Vieira. Tunneling spectroscopy in small grains of superconducting mgb_2. *Phys. Rev. Lett.*, 86:5582–5584, Jun 2001.

[105] E. Bascones and F. Guinea. Surface effects in two-band superconductors: Application to mgb_2. *Phys. Rev. B*, 64:214508, Nov 2001.

[106] J. Kortus, I. I. Mazin, K. D. Belashchenko, V. P. Antropov, and L. L. Boyer. Superconductivity of metallic boron in mgb_2. *Phys. Rev. Lett.*, 86:4656–4659, May 2001.

[107] Amy Y. Liu, I. I. Mazin, and Jens Kortus. Beyond eliashberg superconductivity in mgb_2: Anharmonicity, two-phonon scattering, and multiple gaps. *Phys. Rev. Lett.*, 87:087005, Aug 2001.

[108] Eva Pavarini and I. I. Mazin. Nmr relaxation rates and knight shifts in mgb_2. *Phys. Rev. B*, 64:140504, Sep 2001.

[109] A A Golubov, J Kortus, O V Dolgov, O Jepsen, Y Kong, O K Andersen, B J Gibson, K Ahn, and R K Kremer. Specific heat of mgb 2 in a one- and a two-band model from first-principles calculations. *Journal of Physics: Condensed Matter*, 14(6):1353, 2002.

[110] C. Panagopoulos, B. D. Rainford, T. Xiang, C. A. Scott, M. Kambara, and I. H. Inoue. Penetration depth measurements in mgb_2 : evidence for unconventional superconductivity. *Phys. Rev. B*, 64:094514, Aug 2001.

[111] H Suderow, I Guillamón, J G Rodrigo, and S Vieira. Imaging superconducting vortex cores and lattices with a scanning tunneling microscope. *Superconductor Science and Technology*, 27(6):063001, 2014.

[112] I. Guillamón, H. Suderow, S. Vieira, L. Cario, P. Diener, and P. Rodière. Superconducting density of states and vortex cores of 2h-nbs_2. *Phys. Rev. Lett.*, 101:166407, Oct 2008.

[113] Lei Shan, Yong-Lei Wang, Jing Gong, Bing Shen, Yan Huang, Huan Yang, Cong Ren, and Hai-Hu Wen. Evidence of multiple nodeless energy gaps in superconducting $ba_{0.6}k_{0.4}fe_2as_2$ single crystals from scanning tunneling spectroscopy. *Phys. Rev. B*, 83:060510, Feb 2011.

[114] H. Ding, P. Richard, K. Nakayama, K. Sugawara, T. Arakane, Y. Sekiba, A. Takayama, S. Souma, T. Sato, T. Takahashi, Z. Wang, X. Dai, Z. Fang, G. F. Chen, J. L. Luo, and N. L. Wang. Observation of fermi-surface dependent nodeless superconducting gaps in ba 0.6 k 0.4 fe 2 as 2. *EPL (Europhysics Letters)*, 83(4):47001, 2008.

[115] S. Teknowijoyo M. A. Tanatar T. Kong W. Meier U. Kaluarachchi I. Guillamón H. Suderow S. L. Bud'ko P. C. Canfield R. Prozorov Kyuil Cho, A. Fente. Nodeless multiband superconductivity in stoichiometric single crystalline $cakfe_4as_4$. *arXiv:1606.06245v1*, June 2016.

[116] T. Kong V.G. Kogan S.L. Bud'ko P.C. Canfield I. Guillamon H. Suderow A. Fente, W.R. Meier. Vortices in two-effective-band, stoichiometric high t_c $cakfe_4as_4$ superconductor. *arXiv:1608.00605v1*, page 12, August 2016.

[117] Hyoung Joon Choi, David Roundy, Hong Sun, Marvin L. Cohen, and Steven G. Louie. The origin of the anomalous superconducting properties of mgb2. *Nature*, 418(6899):758–760, 8 2002.

[118] Y. Nakajima, T. Nakagawa, T. Tamegai, and H. Harima. Specific-heat evidence for two-gap superconductivity in the ternary-iron silicide $lu_2fe_3si_5$. *Phys. Rev. Lett.*, 100:157001, Apr 2008.

[119] Manfred Sigrist and Michael E. Zhitomirsky. Pairing symmetry of the superconductor sr 2ruo 4. *Journal of the Physical Society of Japan*, 65(11):3452–3455, 1996.

[120] D. F. Agterberg, T. M. Rice, and M. Sigrist. Orbital dependent superconductivity in sr_2ruo_4. *Phys. Rev. Lett.*, 78:3374–3377, Apr 1997.

[121] S. V. Shulga, S.-L. Drechsler, G. Fuchs, K.-H. Müller, K. Winzer, M. Heinecke, and K. Krug. Upper critical field peculiarities of superconducting yni_2B_2c and $luni_2B_2c$. *Phys. Rev. Lett.*, 80:1730–1733, Feb 1998.

[122] T. Dahm and N. Schopohl. Fermi surface topology and the upper critical field in two-band superconductors: Application to mgb_2. *Phys. Rev. Lett.*, 91:017001, Jul 2003.

[123] A. Gurevich. Enhancement of the upper critical field by nonmagnetic impurities in dirty two-gap superconductors. *Phys. Rev. B*, 67:184515, May 2003.

[124] V. G. Tissen, M. R. Osorio, J. P. Brison, N. M. Nemes, M. García-Hernández, L. Cario, P. Rodière, S. Vieira, and H. Suderow. Pressure dependence of superconducting critical temperature and upper critical field of $2h$-nbs_2. *Phys. Rev. B*, 87:134502, Apr 2013.

[125] P J Hirschfeld, M M Korshunov, and I I Mazin. Gap symmetry and structure of fe-based superconductors. *Reports on Progress in Physics*, 74(12):124508, 2011.

[126] E Bauer, Ch Paul, St Berger, S Majumdar, H Michor, M Giovannini, A Saccone, and A Bianconi. Thermal conductivity of superconducting mgb 2. *Journal of Physics: Condensed Matter*, 13(22):L487, 2001.

[127] G. M. Schmiedeshoff, J. A. Detwiler, W. P. Beyermann, A. H. Lacerda, P. C. Canfield, and J. L. Smith. Critical fields and specific heat of $luni_2b_2C$. *Phys. Rev. B*, 63:134519, Mar 2001.

[128] D. Lipp, M. Schneider, A. Gladun, S.-L. Drechsler, J. Freudenberger, G. Fuchs, K. Nenkov, K.-H. M$\tilde{A}\frac{1}{4}$ller, T. Cichorek, and P. Gegenwart. Specific heat and disorder in the mixed state of non-magnetic borocarbides. *EPL (Europhysics Letters)*, 59(4):633, 2002.

[129] G. Seyfarth, J. P. Brison, M.-A. Méasson, D. Braithwaite, G. Lapertot, and J. Flouquet. Superconducting $pros_4sb_{12}$: A thermal conductivity study. *Phys. Rev. Lett.*, 97:236403, Dec 2006.

[130] H. Okamoto. The bi-pd (bismuth- palladium) system. *Journal of Phase Equilibria*, 15(2):191–194, April 1994.

[131] N.N. Zhuravlev and G.S. Zhdanov. Structures of superconductors. iv. x-ray and metallographic investigations on the system bismuth-palladium. *Journal of Experimental and Theoretical Physics*, 25:485–490, 1953.

[132] N.N. Zhuravlev. Structure of superconductors. x. thermal microscopic and x-ray investigation of the bismuth-palladium system. *Journal of Experimental and Theoretical Physics*, 32(6):1305–1312, 1957.

[133] J. Brasier and W. Hume-Rothery. The equilibrium diagram of the system bismuth-palladium. *Journal of the Less Common Metals*, 7(2):157–164, 1959.

[134] N. Sarah and K. Schubert. Crystal structure of pd5bi2. *Journal of the Less Common Metals*, 63(2):75–82, 1959.

[135] Mintu Mondal, Bhanu Joshi, Sanjeev Kumar, Anand Kamlapure, Somesh Chandra Ganguli, Arumugam Thamizhavel, Sudhansu S. Mandal, Srinivasan Ramakrishnan, and Pratap Raychaudhuri. Andreev bound state and multiple energy gaps in the noncentrosymmetric superconductor bipd. *Phys. Rev. B*, 86:094520, Sep 2012.

[136] Yasuyuki Nakajima, Rongwei Hu, Kevin Kirshenbaum, Alex Hughes, Paul Syers, Xiangfeng Wang, Kefeng Wang, Renxiong Wang, Shanta R. Saha, Daniel Pratt, Jeffrey W. Lynn, and Johnpierre Paglione. Topological rpdbi half-heusler semimetals: A new family of noncentrosymmetric magnetic superconductors. *Science Advances*, 1(5), 2015.

[137] Darren C. Peets, Ana Maldonado, Mostafa Enayat, Zhixiang Sun, Peter Wahl, and Andreas P. Schnyder. Upper critical field of the noncentrosymmetric superconductor bipd. *Phys. Rev. B*, 93:174504, May 2016.

[138] B. T. Matthias, T. H. Geballe, and V. B. Compton. Superconductivity. *Rev. Mod. Phys.*, 35:1–22, Jan 1963.

[139] Yoshinori Imai, Fuyuki Nabeshima, Taiki Yoshinaka, Kosuke Miyatani, Ryusuke Kondo, Seiki Komiya, Ichiro Tsukada, and Atsutaka Maeda. Superconductivity at 5.4 k in βbi$_2$pd. *Journal of the Physical Society of Japan*, 81(11):113708, 2012.

[140] I. R. Shein and A. L. Ivanovskii. Electronic band structure and fermi surface of tetragonal low-temperature superconductor bi2pd as predicted from first principles. *Journal of Superconductivity and Novel Magnetism*, 26(1):1–4, 2013.

[141] Zhixiang Sun, Mostafa Enayat, Ana Maldonado, Calum Lithgow, Ed Yelland, Darren C. Peets, Alexander Yaresko, Andreas P. Schnyder, and Peter Wahl. Dirac surface states and nature of superconductivity in noncentrosymmetric bipd. *Nature Communications*, 6:6633, 3 2015.

[142] M. Kanou H. Sanjo T. Okuda T. Sasagawaand K Ishizaka M. Sakano, K. Okawa. Topologically protected surface states in a centrosymmetric superconductor βbi$_2$pd. *Nature*, 6(8595), October 2015.

[143] Yan-Feng Lv, Wen-Lin Wang, Yi-Min Zhang, Hao Ding, Wei Li, Lili Wang, Ke He, Can-Li Song, Xu-Cun Ma, and Qi-Kun Xue. Experimental observation of topological superconductivity and majorana zero modes on beta-bi2pd thin films. *arXiv preprint arXiv:1607.07551*, 2016.

[144] Juan Rodríguez-Carvajal. Recent advances in magnetic structure determination by neutron powder diffraction. *Physica B: Condensed Matter*, 192(1):55 – 69, 1993.

[145] Z. Hiroi, S. Yonezawa, Y. Nagao, and J. Yamaura. Extremely strong-coupling superconductivity and anomalous lattice properties in the β-pyrochlore oxide Kos$_2$o$_6$. *Phys. Rev. B*, 76:014523, Jul 2007.

[146] Ch. Renner, A. D. Kent, Ph. Niedermann, Ø. Fischer, and F. Lévy. Scanning tunneling spectroscopy of a vortex core from the clean to the dirty limit. *Phys. Rev. Lett.*, 67:1650–1652, Sep 1991.

[147] A. Gurevich. Limits of the upper critical field in dirty two-gap superconductors. *Physica C: Superconductivity*, 456(1-2):160 – 169, 2007. Recent Advances in MgB2 Research.

[148] A Gurevich, S Patnaik, V Braccini, K H Kim, C Mielke, X Song, L D Cooley, S D Bu, D M Kim, J H Choi, L J Belenky, J Giencke, M K Lee, W Tian, X Q Pan, A Siri, E E Hellstrom, C B Eom, and D C Larbalestier. Very high upper critical fields in mgb 2 produced by selective tuning of impurity scattering. *Superconductor Science and Technology*, 17(2):278, 2004.

[149] Sergey L. Bud'ko and Paul C. Canfield. Temperature-dependent H_{c2} anisotropy in mgb$_2$ as inferred from measurements on polycrystals. *Phys. Rev. B*, 65:212501, May 2002.

[150] M. Angst, S. L. Bud'ko, R. H. T. Wilke, and P. C. Canfield. Difference between al and c doping in anisotropic upper critical field development in Mgb$_2$. *Phys. Rev. B*, 71:144512, Apr 2005.

[151] M. Putti, V. Braccini, C. Ferdeghini, I. Pallecchi, A. S. Siri, F. Gatti, P. Manfrinetti, and A. Palenzona. Critical field of mgb_2: Crossover from clean to dirty regimes. *Phys. Rev. B*, 70:052509, Aug 2004.

[152] J. Kačmarčík, Z. Pribulová, T. Samuely, P. Szabó, V. Cambel, J. Šoltýs, E. Herrera, H. Suderow, A. Correa-Orellana, D. Prabhakaran, and P. Samuely. Single-gap superconductivity in β-Bi_2Pd. *Phys. Rev. B*, 93:144502, Apr 2016.

[153] Paul F. Sullivan and G. Seidel. Steady-state, ac-temperature calorimetry. *Phys. Rev.*, 173:679–685, Sep 1968.

[154] J. Kačmarčík, Z. Pribulová, V. Pal'uchová, P. Szabó, P. Husaníková, G. Karapetrov, and P. Samuely. Heat capacity of single-crystal cu_xtise_2 superconductors. *Phys. Rev. B*, 88:020507, Jul 2013.

[155] H. Padamsee, J. E. Neighbor, and C. A. Shiffman. Quasiparticle phenomenology for thermodynamics of strong-coupling superconductors. *Journal of Low Temperature Physics*, 12(3):387–411, 1973.

[156] J.G. Rodrigo and S. Vieira. Stm study of multiband superconductivity in $nbse_2$ using a superconducting tip. *Physica C*, 404:306, 2004.

[157] M. R. Eskildsen, N. Jenkins, G. Levy, M. Kugler, Ø. Fischer, J. Jun, S. M. Kazakov, and J. Karpinski. Vortex imaging in magnesium diboride with $h \perp c$. *Phys. Rev. B*, 68:100508, Sep 2003.

[158] M. R. Eskildsen, A. B. Abrahamsen, D. López, P. L. Gammel, D. J. Bishop, N. H. Andersen, K. Mortensen, and P. C. Canfield. Flux line lattice reorientation in the borocarbide superconductors with $H \parallel a$. *Phys. Rev. Lett.*, 86:320–323, Jan 2001.

[159] M. R. Eskildsen, A. B. Abrahamsen, V. G. Kogan, P. L. Gammel, K. Mortensen, N. H. Andersen, and P. C. Canfield. Temperature dependence of the flux line lattice transition into square symmetry in superconducting $luni_2B_2c$. *Phys. Rev. Lett.*, 86:5148–5151, May 2001.

[160] L. DeBeer-Schmitt, M. R. Eskildsen, M. Ichioka, K. Machida, N. Jenkins, C. D. Dewhurst, A. B. Abrahamsen, S. L. Bud'ko, and P. C. Canfield. Pauli paramagnetic effects on vortices in superconducting $tmni_2b_2C$. *Phys. Rev. Lett.*, 99:167001, Oct 2007.

[161] V. G. Kogan, M. Bullock, B. Harmon, P. Miranovic-acute, Lj. Dobrosavljevic-acute Grujic-acute, P. L. Gammel, and D. J. Bishop. Vortex lattice transitions in borocarbides. *Phys. Rev. B*, 55:R8693–R8696, Apr 1997.

[162] C. E. Sosolik, Joseph A. Stroscio, M. D. Stiles, E. W. Hudson, S. R. Blankenship, A. P. Fein, and R. J. Celotta. Real-space imaging of structural transitions in the vortex lattice of v_3Si. *Phys. Rev. B*, 68:140503, Oct 2003.

[163] I. Guillamón, M. Crespo, H. Suderow, S. Vieira, J.P. Brison, S.L. Budko, and P.C. Canfield. Atomic resolution and vortex lattice studies of magnetic superconductors: A first approach in the nickel borocarbide tmni2b2c. *Physica C: Superconductivity*, 470(19):771 – 775, 2010. Vortex Matter in Nanostructured Superconductors.

[164] M. R. Eskildsen, M. Kugler, S. Tanaka, J. Jun, S. M. Kazakov, J. Karpinski, and Ø. Fischer. Vortex imaging in the π band of magnesium diboride. *Phys. Rev. Lett.*, 89:187003, Oct 2002.

[165] M. D. Johannes, I. I. Mazin, and C. A. Howells. *Phys. Rev. B*, 73:205102, 2006.

[166] D. J. Rahn, S. Hellmann, M. Kalläne, C. Sohrt, T. K. Kim, L. Kipp, and K. Rossnagel. Gaps and kinks in the electronic structure of the superconductor $2h$-nbse$_2$ from angle-resolved photoemission at 1 k. *Phys. Rev. B*, 85:224532, Jun 2012.

[167] V. G. Kogan and N. V. Zhelezina. Field dependence of the vortex core size. *Phys. Rev. B*, 71:134505, Apr 2005.

[168] A. Fente, E. Herrera, I. Guillamón, H. Suderow, S. Mañas Valero, M. Galbiati, E. Coronado, and V. G. Kogan. Field dependence of the vortex core size probed by scanning tunneling microscopy. *Phys. Rev. B*, 94:014517, Jul 2016.

[169] Jeff E Sonier. Investigations of the core structure of magnetic vortices in type-ii superconductors using muon spin rotation. *Journal of Physics: Condensed Matter*, 16(40):S4499, 2004.

[170] R. Descartes. *The World and Other Writings*, volume 1 of *Cambridge Text in the History of Philosophy*. Cambridge University Press, 2004.

[171] T. Tamegai S. Ooi A. Grigorenko, S. Bending and M. Henini. A one-dimensional chain state of vortex matter. *Nature*, 414:728–731, December 2001.

[172] A. Buzdin and I. Baladié. Attraction between pancake vortices in the crossing lattices of layered superconductors. *Phys. Rev. Lett.*, 88:147002, Mar 2002.

[173] A. E. Koshelev. Tilted and crossing vortex chains in layered superconductors. *Journal of Low Temperature Physics*, 139(1):111–125, 2005.

[174] H. F. Hess, C. A. Murray, and J. V. Waszczak. Scanning-tunneling-microscopy study of distortion and instability of inclined flux-line-lattice structures in the anisotropic superconductor 2 H -nbse$_2$. *Phys. Rev. Lett.*, 69:2138–2141, Oct 1992.

[175] H. F. Hess, C. A. Murray, and J. V. Waszczak. Flux lattice and vortex structure in 2 H -nbse$_2$ in inclined fields. *Phys. Rev. B*, 50:16528–16540, Dec 1994.

[176] I. V. Grigorieva, J. W. Steeds, G. Balakrishnan, and D. M. Paul. Vortex-chain state in bi$_2$sr$_2$cacu$_2$o$_{8+\delta}$: Experimental evidence for coexistence of two vortex orientations. *Phys. Rev. B*, 51:3765–3771, Feb 1995.

[177] P. L. Gammel, D. A. Huse, R. N. Kleiman, B. Batlogg, C. S. Oglesby, E. Bucher, D. J. Bishop, T. E. Mason, and K. Mortensen. Small angle neutron scattering study of the magnetic flux-line lattice in single crystal 2 H -nbse$_2$. *Phys. Rev. Lett.*, 72:278–281, Jan 1994.

[178] S. Bending. Local magnetic pprobe of superconductors. *Advances in Physics*, 48(4):449–535, 1999.

[179] L. J. Campbell, M. M. Doria, and V. G. Kogan. Vortex lattice structures in uniaxial superconductors. *Phys. Rev. B*, 38:2439–2443, Aug 1988.

[180] S. Mühlbauer, C. Pfleiderer, P. Böni, M. Laver, E. M. Forgan, D. Fort, U. Keiderling, and G. Behr. Morphology of the superconducting vortex lattice in ultrapure niobium. *Phys. Rev. Lett.*, 102:136408, Apr 2009.

[181] J.A. Galvis. *In preparation*, (2016).

[182] Ernst Helmut Brandt. Tilted and curved vortices in anisotropic superconducting films. *Phys. Rev. B*, 48:6699–6702, Sep 1993.

[183] V. G. Kogan, L. N. Bulaevskii, P. Miranović, and L. Dobrosavljević-Grujić. Vortex-induced strain and flux lattices in anisotropic superconductors. *Phys. Rev. B*, 51:15344–15350, Jun 1995.

[184] V. G. Kogan. Elastic contribution to interaction of vortices in uniaxial superconductors. *Phys. Rev. B*, 88:144514, Oct 2013.

[185] A. Cano, A. P. Levanyuk, and S. A. Minyukov. Elasticity-driven interaction between vortices in type-ii superconductors. *Phys. Rev. B*, 68:144515, Oct 2003.

[186] A. Cano, A.P. Levanyuk, and S.A. Minyukov. Elasticity-driven interaction between vortices in high-tc superconductors: leading role of a non-core contribution. *Physica C: Superconductivity*, 404(1-4):226 – 229, 2004. Proceedings of the Third European Conference on Vortex Matter in Superconductors at Extreme Scales and Conditions.

[187] E H Brandt. The flux-line lattice in superconductors. *Reports on Progress in Physics*, 58(11):1465, 1995.

[188] A. Yu. Martinovich. Magnetic vortices in layered superconducting slabes. *Zh. Eksp. Teor. Fiz (JETP)*, 105(4):912–927, April 1994.

[189] Boris Maiorov Leonardo Civale Serena Eley, Masashi Miura. Universal lower limit on vortex creep in superconductors. *arXiv:1608.08092v2*, August 2016.

[190] Morten Ring Eskildsen, Charles D. Dewhurst, Bart W. Hoogenboom, Cedomir Petrovic, and Paul C. Canfield. Hexagonal and square flux line lattices in $cecoin_5$. *Phys. Rev. Lett.*, 90:187001, May 2003.

[191] M. R. Eskildsen, K. Harada, P. L. Gammel, A. B. Abrahamsen, N. H. Andersen, G. Ernst, A. P. Ramirez, D. J. Bishop, K. Mortensen, D. G. Naugle, K. D. D. Rathnayaka, and P. C. Canfield. Intertwined symmetry of the magnetic modulation and the flux-line lattice in the superconducting state of tmni2b2c. *Nature*, 393(6682):242–245, May 1998.

[192] P. Das, C. Rastovski, T. R. O'Brien, K. J. Schlesinger, C. D. Dewhurst, L. DeBeer-Schmitt, N. D. Zhigadlo, J. Karpinski, and M. R. Eskildsen. Observation of well-ordered metastable vortex lattice phases in superconducting mgb_2 using small-angle neutron scattering. *Phys. Rev. Lett.*, 108:167001, Apr 2012.

[193] Tomoya Hirano, Kenta Takamori, Masanori Ichioka, and Kazushige Machida. Rotation of triangular vortex lattice in the two-band superconductor mgb2. *Journal of the Physical Society of Japan*, 82(6):063708, 2013.

[194] Wai-Kwong Kwok, Ulrich Welp, Andreas Glatz, Alexei E Koshelev, Karen J Kihlstrom, and George W Crabtree. Vortices in high-performance high-temperature superconductors. *Reports on Progress in Physics*, 79(11):116501, 2016.

[195] A. Glatz, V. K. Vlasko-Vlasov, W. K. Kwok, and G. W. Crabtree. Vortex cutting in superconductors. *Phys. Rev. B*, 94:064505, Aug 2016.

[196] Yi-Min Zhang Hao Ding Wei Li Lili Wang Ke He Can-Li Song Xu-Cun Ma Qi-Kun Xue Yan-Feng Lv, Wen-Lin Wang. Experimental observation of topological superconductivity and majorana zero modes on beta-bi2pd thin films. *arXiv*, arXiv:1607.07551v1:1–25, Jul 2016.

[197] K. Harada, O. Kamimura, H. Kasai, T. Matsuda, A. Tonomura, and V. V. Moshchalkov. Direct observation of vortex dynamics in superconducting films with regular arrays of defects. *Science*, 274(5290):1167–1170, 1996.

[198] J. E. Villegas, Sergey Savel'ev, Franco Nori, E. M. Gonzalez, J. V. Anguita, R. García, and J. L. Vicent. A superconducting reversible rectifier that controls the motion of magnetic flux quanta. *Science*, 302(5648):1188–1191, 2003.

[199] J. Van de Vondel A. V. Silhanek and V. V. Moshchalkov. *Nanoscience and Engineering in superconductivity*, volume 1- Ch.1. Springer, 2010.

[200] J. Sesé J. M. De Teresa M. R. Ibarra S. Vieira I. Guillamón, R. Córdoba and H. Suderow. Enhancement of long-range correlations in a 2d vortex lattice by an incommensurate 1d disorder potential. *Nature Physics*, 10:851–856, October 2014.

[201] MISR Team. NASA/GSFC/LaRC/JPL. A vortex street in the arctic. photojournal.jpl.nasa.gov/catalog/PIA03448, March 2002.

[202] CHARLES P. BEAN. Magnetization of high-field superconductors. *Rev. Mod. Phys.*, 36:31–39, Jan 1964.

[203] A. I. Larkin and Yu. N. Ovchinnikov. Pinning in type ii superconductors. *Journal of Low Temperature Physics*, 34(3):409–428, 1979.

[204] E. Altshuler and T. H. Johansen. *Colloquium* : Experiments in vortex avalanches. *Rev. Mod. Phys.*, 76:471–487, Apr 2004.

[205] M. V. Feigel'man, V. B. Geshkenbein, A. I. Larkin, and V. M. Vinokur. Theory of collective flux creep. *Phys. Rev. Lett.*, 63:2303–2306, Nov 1989.

[206] P H Kes, J Aarts, J van den Berg, C J van der Beek, and J A Mydosh. Thermally assisted flux flow at small driving forces. *Superconductor Science and Technology*, 1(5):242, 1989.

[207] J. Kierfeld, H. Nordborg, and V. M. Vinokur. Theory of plastic vortex creep. *Phys. Rev. Lett.*, 85:4948–4951, Dec 2000.

[208] M. Konczykowski, C. J. van der Beek, M. A. Tanatar, Huiqian Luo, Zhaosheng Wang, Bing Shen, Hai Hu Wen, and R. Prozorov. Vortex creep and critical current densities in superconducting (ba,k)fe_2as_2 single crystals. *Phys. Rev. B*, 86:024515, Jul 2012.

[209] S. Eley, M. Leroux, M. W. Rupich, D. J. Miller, H. Sheng, P. M. Niraula, A. Kayani, U. Welp, W.-K. Kwok, and L. Civale. Decoupling and tuning competing effects of different types of defects on flux creep in irradiated $YBa_2Cu_3O_{7-\delta}$ coated conductors. *arXiv:1602.04344*, February 2016.

[210] A. Fernández-Pacheco J. Sesé R. Córdoba J. M. De Teresa M. R. Ibarra I. Guillamón, H. Suderow and S. Vieira. Direct observation of melting in a two-dimensional superconducting vortex lattice. *Nature Physics*, 5(5):651 – 655, 2009.

[211] F. Pardo, F. de la Cruz, P.L. Gammel, E. Bucher, and D.J. Bishop. Observation of smectic and moving Bragg glass phases in flowing vortex lattices. *Nature*, 396:348, 1998.

[212] A. M. Troyanovski, J. Aarts, and P. H. Kes. Collective and plastic vortex motion in superconductors at high flux densities. *Nature*, 399:665, 1999.

[213] A.M. Troyanovski, M.van Hecke, J. Aarts, and P.H. Kes. Stm imaging of flux line arrangements in the peak effect regime. *Phys. Rev. Lett.*, 89:147006, 2002.

[214] Jonghee Lee, Hui Wang, Michael Dreyer, Helmuth Berger, and Barry I. Barker. Nonuniform and coherent motion of superconducting vortices in the picometer-per-second regime. *Phys. Rev. B*, 84:060515(R), 2011.

[215] Udhara S. Kaluarachchi, Weiwei Xie, Qisheng Lin, Valentin Taufour, Sergey L. Bud'ko, Gordon J. Miller, and Paul C. Canfield. Superconductivity versus structural phase transition in the closely related $bi_2rh_{3.5}s_2$ and $bi_2rh_3s_2$. *Phys. Rev. B*, 91:174513, May 2015.

[216] S. Natarajan, G.V.Subba Rao, R. Baskaran, and T.S. Radhakrishnan. Synthesis and electrical properties of shandite-parkerite phases, a2m3ch2. *Journal of the Less Common Metals*, 138(2):215 – 224, 1988.

[217] W. L. McMillan. Transition temperature of strong-coupled superconductors. *Phys. Rev.*, 167:331–344, Mar 1968.

[218] Grigorii P. Mikitik and Ernst Helmut Brandt. Peak effect, vortex-lattice melting line, and order-disorder transition in conventional and high-T_c superconductors. *Phys. Rev. B*, 64:184514, Oct 2001.

[219] S. H. Autler, E. S. Rosenblum, and K. H. Gooen. High-field superconductivity in niobium. *Phys. Rev. Lett.*, 9:489–493, Dec 1962.

[220] Masato Hedo, Yoshihiko Kobayashi, Yoshihiko Inada, Etsuji Yamamoto, Yoshinori Haga, Junichi Suzuki, Naoto Metoki, Yoshichika Anuki, Hitoshi Sugawara, Hideyuki Sato, Kenichi Tenya, Takashi Tayama, Hiroshi Amitsuka, and Toshiro Sakakibara. Peak effect in ceru 2: Role of crystalline defects. *Journal of the Physical Society of Japan*, 67(10):3561–3569, 1998.

[221] Mark J. Higgins and S. Bhattacharya. Varieties of dynamics in a disordered flux-line lattice. *Physica C: Superconductivity and its Applications*, 257(3):232 – 254, 1996.

[222] S. Chaudhary, A.K. Rajarajan, K.J. Singh, S.B. Roy, and P. Chaddah. Peak effect in the vortex state of v3si: a study of history dependence. *Physica C: Superconductivity*, 353(1-2):29 – 37, 2001.

[223] L. Lyard, P. Samuely, P. Szabo, T. Klein, C. Marcenat, L. Paulius, K. H. P. Kim, C. U. Jung, H.-S. Lee, B. Kang, S. Choi, S.-I. Lee, J. Marcus, S. Blanchard, A. G. M. Jansen, U. Welp, G. Karapetrov, and W. K. Kwok. Anisotropy of the upper critical field and critical current in single crystal mgb_2. *Phys. Rev. B*, 66:180502, Nov 2002.

[224] U. Welp, A. Rydh, G. Karapetrov, W. K. Kwok, G. W. Crabtree, Ch. Marcenat, L. Paulius, T. Klein, J. Marcus, K. H. P. Kim, C. U. Jung, H.-S. Lee, B. Kang, and S.-I. Lee. Superconducting transition and phase diagram of single-crystal mgb_2. *Phys. Rev. B*, 67:012505, Jan 2003.

[225] Ted G. Berlincourt. Hall effect, resistivity, and magnetoresistivity of th, u, zr, ti, and nb. *Phys. Rev.*, 114:969–977, May 1959.

[226] W. DeSORBO. The peak effect in substitutional and interstitial solid solutions of high-field superconductors. *Rev. Mod. Phys.*, 36:90–94, Jan 1964.

[227] A.M. Campbell and J.E. Evetts. Flux vortices and transport currents in type ii superconductors. *Advances in Physics*, 21(90):199–428, 1972.

[228] J. D. Livingston. Flux pinning by superconducting precipitates. *Applied Physics Letters*, 8(12):319–320, 1966.

[229] A. B. Pippard. A possible mechanism for the peak effect in type ii superconductors. *Philosophical Magazine*, 19(158):217–220, 1969.

[230] Edward J. Kramer. Scaling laws for flux pinning in hard superconductors. *Journal of Applied Physics*, 44(3):1360–1370, 1973.

[231] M. Crespo, H. Suderow, S. Vieira, S. Bud'ko, and P. C. Canfield. Local superconducting density of states of $erni_2b_2C$. *Phys. Rev. Lett.*, 96:027003, Jan 2006.

[232] P. Szabó, T. Samuely, V. Hašková, J. Kačmarčík, M. Žemlička, M. Grajcar, J. G. Rodrigo, and P. Samuely. Fermionic scenario for the destruction of superconductivity in ultrathin moc films evidenced by stm measurements. *Phys. Rev. B*, 93:014505, Jan 2016.

[233] Y. Noat, V. Cherkez, C. Brun, T. Cren, C. Carbillet, F. Debontridder, K. Ilin, M. Siegel, A. Semenov, H.-W. Hübers, and D. Roditchev. Unconventional superconductivity in ultrathin superconducting nbn films studied by scanning tunneling spectroscopy. *Phys. Rev. B*, 88:014503, Jul 2013.

[234] I. Guillamón, H. Suderow, S. Vieira, J. Sesé, R. Córdoba, J. M. De Teresa, and M. R. Ibarra. Direct observation of stress accumulation and relaxation in small bundles of superconducting vortices in tungsten thin films. *Phys. Rev. Lett.*, 106:077001, Feb 2011.

[235] C. J. Olson, C. Reichhardt, and Franco Nori. Nonequilibrium dynamic phase diagram for vortex lattices. *Phys. Rev. Lett.*, 81:3757–3760, Oct 1998.

[236] Kyungsun Moon, Richard T. Scalettar, and Gergely T. Zimányi. Dynamical phases of driven vortex systems. *Phys. Rev. Lett.*, 77:2778–2781, Sep 1996.

[237] Thierry Giamarchi and Pierre Le Doussal. Elastic theory of pinned flux lattices. *Phys. Rev. Lett.*, 72:1530–1533, Mar 1994.

[238] Thierry Giamarchi and Pierre Le Doussal. Elastic theory of flux lattices in the presence of weak disorder. *Phys. Rev. B*, 52:1242–1270, Jul 1995.

[239] D. Dew-Hughes. The critical current of superconductors: an historical review. *Low Temperature Physics*, 27(9):713–722, 2001.

[240] H. Suhl. Inertial mass of a moving fluxoid. *Phys. Rev. Lett.*, 14:226–229, Feb 1965.

[241] M.Yu. Kupriyanov and K. K. Likharev. Microwave impedance of superconductors in the mixed state. *Zh. Eksp. Teor. Fiz.*, 68:1506, 1975.

[242] E. M. Chudnovsky and A. B. Kuklov. Inertial mass of the abrikosov vortex. *Phys. Rev. Lett.*, 91:067004, Aug 2003.

[243] Mark W. Coffey and John R. Clem. Vortex inertial mass for a discrete type-ii superconductor. *Phys. Rev. B*, 44:6903–6908, Oct 1991.

[244] Ji-Min Duan and Anthony J. Leggett. Inertial mass of a moving singularity in a fermi superfluid. *Phys. Rev. Lett.*, 68:1216–1219, Feb 1992.

[245] N. B. Kopnin and V. M. Vinokur. Dynamic vortex mass in clean fermi superfluids and superconductors. *Phys. Rev. Lett.*, 81:3952–3955, Nov 1998.

[246] Jung Hoon Han, June Seo Kim, Min Jae Kim, and Ping Ao. Effective vortex mass from microscopic theory. *Phys. Rev. B*, 71:125108, Mar 2005.

[247] Piers Coleman. *Heavy Fermions: Electrons at the Edge of Magnetism*. John Wiley & Sons, Ltd, 2007.

[248] J. A. Mydosh and P. M. Oppeneer. *Colloquium* : Hidden order, superconductivity, and magnetism: The unsolved case of uru_2si_2. *Rev. Mod. Phys.*, 83:1301–1322, Nov 2011.

[249] A. Maldonado, I. Guillamon, J. G. Rodrigo, H. Suderow, S. Vieira, D. Aoki, and J. Flouquet. Tunneling spectroscopy of the superconducting state of uru_2si_2. *Phys. Rev. B*, 85:214512, Jun 2012.

[250] W. Knafo, F. Duc, F. Bourdarot, K. Kuwahara, H. Nojiri, D. Aoki, J. Billette, P. Frings, X. Tonon, E. LeliÃ¨vre-Berna, J. Flouquet, and L.-P. Regnault. Field-induced spin-density wave beyond hidden order in uru2si2. *Nature Communications*, 7:13075, 10 2016.

[251] M. Jaime, K. H. Kim, G. Jorge, S. McCall, and J. A. Mydosh. High magnetic field studies of the hidden order transition in uru_2si_2. *Phys. Rev. Lett.*, 89:287201, Dec 2002.

[252] E. Hassinger, G. Knebel, K. Izawa, P. Lejay, B. Salce, and J. Flouquet. Temperature-pressure phase diagram of Uru_2si_2 from resistivity measurements and ac calorimetry: Hidden order and fermi-surface nesting. *Phys. Rev. B*, 77:115117, Mar 2008.

[253] A. Villaume, F. Bourdarot, E. Hassinger, S. Raymond, V. Taufour, D. Aoki, and J. Flouquet. Signature of hidden order in heavy fermion superconductor uru_2si_2: Resonance at the wave vector $q_0 = (1,0,0)$. *Phys. Rev. B*, 78:012504, Jul 2008.

[254] T. T. M. Palstra, A. A. Menovsky, J. van den Berg, A. J. Dirkmaat, P. H. Kes, G. J. Nieuwenhuys, and J. A. Mydosh. Superconducting and magnetic transitions in the heavy-fermion system uru_2si_2. *Phys. Rev. Lett.*, 55:2727–2730, Dec 1985.

[255] W. Schlabitz, J. Baumann, B. Pollit, U. Rauchschwalbe, H. M. Mayer, U. Ahlheim, and C. D. Bredl. Superconductivity and magnetic order in a strongly interacting fermi-system: Uru2si2. *Zeitschrift für Physik B Condensed Matter*, 62(2):171–177, 1986.

[256] M. B. Maple, J. W. Chen, Y. Dalichaouch, T. Kohara, C. Rossel, M. S. Torikachvili, M. W. McElfresh, and J. D. Thompson. Partially gapped fermi surface in the heavy-electron superconductor uru_2si_2. *Phys. Rev. Lett.*, 56:185–188, Jan 1986.

[257] T. T. M. Palstra, A. A. Menovsky, and J. A. Mydosh. Anisotropic electrical resistivity of the magnetic heavy-fermion superconductor uru_2si_2. *Phys. Rev. B*, 33:6527–6530, May 1986.

[258] J. G. Rodrigo, F. Guinea, S. Vieira, and F. G. Aliev. Point-contact spectroscopy on uru_2si_2. *Phys. Rev. B*, 55:14318–14322, Jun 1997.

[259] J.A. Mydosh and P.M. Oppeneer. Hidden order behaviour in uru2si2 (a critical review of the status of hidden order in 2014). *Philosophical Magazine*, 94(32-33):3642–3662, 2014.

[260] Shigeru Takagi, Shu Ishihara, Satoru Saitoh, Hiko ichiro Sasaki, Hiroshi Tanida, Makoto Yokoyama, and Hiroshi Amitsuka. No evidence for small-moment antiferromagnetism under ambient pressure in uru2si2: Single-crystal 29si nmr study. *Journal of the Physical Society of Japan*, 76(3):033708, 2007.

[261] S. Elgazzar, J. Rusz, M. Amft, P. M. Oppeneer, and J. A. Mydosh. Hidden order in uru2si2 originates from fermi surface gapping induced by dynamic symmetry breaking. *Nat Mater*, 8(4):337–341, Apr 2009.

[262] R Okazaki, Y Kasahara, H Shishido, M Konczykowski, K Behnia, Y Haga, T D Matsuda, Y Onuki, T Shibauchi, and Y Matsuda. Vortex lattice melting in the ultraclean heavy-fermion superconductor uru 2 si 2. *Journal of Physics: Conference Series*, 150(5):052198, 2009.

[263] J. Buhot, M.-A. Méasson, Y. Gallais, M. Cazayous, A. Sacuto, G. Lapertot, and D. Aoki. Symmetry of the excitations in the hidden order state of uru_2si_2. *Phys. Rev. Lett.*, 113:266405, Dec 2014.

[264] H.-H. Kung, R. E. Baumbach, E. D. Bauer, V. K. Thorsmølle, W.-L. Zhang, K. Haule, J. A. Mydosh, and G. Blumberg. Chirality density wave of the "hidden order" phase in uru2si2. *Science*, 2015.

[265] R. P. S. M. Lobo, J. Buhot, M. A. Méasson, D. Aoki, G. Lapertot, P. Lejay, and C. C. Homes. Optical conductivity of uru_2si_2 in the kondo liquid and hidden-order phases. *Phys. Rev. B*, 92:045129, Jul 2015.

[266] C. Broholm, H. Lin, P. T. Matthews, T. E. Mason, W. J. L. Buyers, M. F. Collins, A. A. Menovsky, J. A. Mydosh, and J. K. Kjems. Magnetic excitations in the heavy-fermion superconductor uru_2si_2. *Phys. Rev. B*, 43:12809–12822, Jun 1991.

[267] E. D. Isaacs, D. B. McWhan, R. N. Kleiman, D. J. Bishop, G. E. Ice, P. Zschack, B. D. Gaulin, T. E. Mason, J. D. Garrett, and W. J. L. Buyers. X-ray magnetic scattering in antiferromagnetic uru_2si_2. *Phys. Rev. Lett.*, 65:3185–3188, Dec 1990.

[268] Frederic Bourdarot, Elena Hassinger, Stephane Raymond, Dai Aoki, Valentin Taufour, Louis-Pierre Regnault, and Jacques Flouquet. Precise study of the resonance at q0=(1,0,0) in uru2si2. *Journal of the Physical Society of Japan*, 79(6):064719, 2010.

[269] P. Santini, G. Amoretti, R. Caciuffo, F. Bourdarot, and B. Fåk. Field-dependent energy scales in uru_2si_2. *Phys. Rev. Lett.*, 85:654–657, Jul 2000.

[270] H. Suderow et. al. E. Herrera. I. Guillamón. Supercondcuting gap on u-terminated surfaces of uru_2si_2. *In preparation*, (2016).

[271] Kristjan Haule and Gabriel Kotliar. Arrested kondo effect and hidden order in uru2si2. *Nat Phys*, 5(11):796–799, Nov 2009.

[272] S. Tonegawa, S. Kasahara, T. Fukuda, K. Sugimoto, N. Yasuda, Y. Tsuruhara, D. Watanabe, Y. Mizukami, Y. Haga, T. D. Matsuda, E. Yamamoto, Y. Onuki, H. Ikeda, Y. Matsuda, and T. Shibauchi. Direct observation of lattice symmetry breaking at the hidden-order transition in uru2si2. *Nature Communications*, 5, 6 2014.

[273] R. Okazaki, T. Shibauchi, H. J. Shi, Y. Haga, T. D. Matsuda, E. Yamamoto, Y. Onuki, H. Ikeda, and Y. Matsuda. Rotational symmetry breaking in the hidden-order phase of uru2si2. *Science*, 331(6016):439–442, 2011.

[274] S. Kambe, Y. Tokunaga, H. Sakai, T. D. Matsuda, Y. Haga, Z. Fisk, and R. E. Walstedt. Nmr study of in-plane twofold ordering in uru_2si_2. *Phys. Rev. Lett.*, 110:246406, Jun 2013.

[275] Scott C. Riggs, M.C. Shapiro, Akash V Maharaj, S. Raghu, E.D. Bauer, R.E. Baumbach, P. Giraldo-Gallo, Mark Wartenbe, and I.R. Fisher. Evidence for a nematic component to the hidden-order parameter in uru2si2 from differential elastoresistance measurements. *Nature Communications*, 6:6425, 3 2015.

[276] S. Kasahara, H. J. Shi, K. Hashimoto, S. Tonegawa, Y. Mizukami, T. Shibauchi, K. Sugimoto, T. Fukuda, T. Terashima, Andriy H. Nevidomskyy, and Y. Matsuda. Electronic nematicity above the structural and superconducting transition in bafe2(as1-xpx)2. *Nature*, 486(7403):382–385, Jun 2012.

[277] Hiroaki Ikeda, Michi-To Suzuki, Ryotaro Arita, Tetsuya Takimoto, Takasada Shibauchi, and Yuji Matsuda. Emergent rank-5 nematic order in uru2si2. *Nat Phys*, 8(7):528–533, Jul 2012.

[278] J.D Denlinger, G.-H Gweon, J.W Allen, C.G Olson, M.B Maple, J.L Sarrao, P.E Armstrong, Z Fisk, and H Yamagami. Comparative study of the electronic structure of xru2si2: probing the anderson lattice. *Journal of Electron Spectroscopy and Related Phenomena*, 117-118:347 – 369, 2001. Strongly correlated systems.

[279] C. Bareille, F. L. Boariu, H. Schwab, P. Lejay, F. Reinert, and A. F. Santander-Syro. Momentum-resolved hidden-order gap reveals symmetry breaking and origin of entropy loss in uru2si2. *Nature Communications*, 5, 7 2014.

[280] H. Shishido, K. Hashimoto, T. Shibauchi, T. Sasaki, H. Oizumi, N. Kobayashi, T. Takamasu, K. Takehana, Y. Imanaka, T. D. Matsuda, Y. Haga, Y. Onuki, and Y. Matsuda. Possible phase transition deep inside the hidden order phase of ultraclean uru_2si_2. *Phys. Rev. Lett.*, 102:156403, Apr 2009.

[281] P. M. Oppeneer, S. Elgazzar, J. Rusz, Q. Feng, T. Durakiewicz, and J. A. Mydosh. Spin and orbital hybridization at specifically nested fermi surfaces in uru_2si_2. *Phys. Rev. B*, 84:241102, Dec 2011.

[282] J.A. Janik and The Florida State University. *Understanding Hidden Order in Uranium Ruthenium Silicide*. Florida State University, 2008.

[283] E. Hassinger, G. Knebel, T. D. Matsuda, D. Aoki, V. Taufour, and J. Flouquet. Similarity of the fermi surface in the hidden order state and in the antiferromagnetic state of uru_2si_2. *Phys. Rev. Lett.*, 105:216409, Nov 2010.

[284] Jian-Qiao Meng, Peter M. Oppeneer, John A. Mydosh, Peter S. Riseborough, Krzysztof Gofryk, John J. Joyce, Eric D. Bauer, Yinwan Li, and Tomasz Durakiewicz. Imaging the three-dimensional fermi-surface pairing near the hidden-order transition in uru_2si_2 using angle-resolved photoemission spectroscopy. *Phys. Rev. Lett.*, 111:127002, Sep 2013.

[285] Alireza Akbari and Peter Thalmeier. Hidden-order symmetry and superconductivity in uru_2si_2 investigated by quasiparticle interference. *Phys. Rev. B*, 90:224511, Dec 2014.

[286] E. Landemark, R.I.G. Uhrberg, P. Kroger, and J. Pollmann. Surface electronic structure of ge(001)2-1: experiment and theory. *Surface Science*, 236(3):L359 – L364, 1990.

[287] M. Wenderoth, M. A. Rosentreter, K. J. Engel, A. J. Heinrich, M. A. Schneider, and R. G. Ulbrich. Low-temperature scanning tunneling spectroscopy as a probe for a confined electron gas. *EPL (Europhysics Letters)*, 45(5):579, 1999.

[288] D. A. Bonn, J. D. Garrett, and T. Timusk. Far-infrared properties of uru_2si_2. *Phys. Rev. Lett.*, 61:1305–1308, Sep 1988.

[289] St Thieme, P. Steiner, L. Degiorgi, P. Wachter, Y. Dalichaouch, and M. B. Maple. Itinerant antiferro- and ferro-magnetic instability in re-doped uru 2 si 2 : Optical and point-contact spectroscopy results. *EPL (Europhysics Letters)*, 32(9):783, 1995.

[290] Y Kasahara, H Shishido, T Shibauchi, Y Haga, T D Matsuda, Y Onuki, and Y Matsuda. Superconducting gap structure of heavy-fermion compound uru 2 si 2 determined by angle-resolved thermal conductivity. *New Journal of Physics*, 11(5):055061, 2009.

[291] F. Bourdarot, B. Fåk, K. Habicht, and K. Prokeš. Inflection point in the magnetic field dependence of the ordered moment of uru_2si_2 observed by neutron scattering in fields up to 17 t. *Phys. Rev. Lett.*, 90:067203, Feb 2003.

[292] Bernd Braunecker, Pablo Burset, and Alfredo Levy Yeyati. Entanglement detection from conductance measurements in carbon nanotube cooper pair splitters. *Phys. Rev. Lett.*, 111:136806, Sep 2013.

[293] M. P. Allan, F. Massee, D. K. Morr, J. Van Dyke, A. W. Rost, A. P. Mackenzie, C. Petrovic, and J. C. Davis. Imaging cooper pairing of heavy fermions in cecoin5. *Nat Phys*, 9(8):468–473, Aug 2013. Letter.

[294] E. R. Schemm, R. E. Baumbach, P. H. Tobash, F. Ronning, E. D. Bauer, and A. Kapitulnik. Evidence for broken time-reversal symmetry in the superconducting phase of uru_2si_2. *Phys. Rev. B*, 91:140506, Apr 2015.

[295] J. E. Hoffman, K. McElroy, D.-H. Lee, K. M Lang, H. Eisaki, S. Uchida, and J. C. Davis. Imaging quasiparticle interference in bi2sr2cacu2o8+Î´. *Science*, 297(5584):1148–1151, 2002.

[296] M. P. Allan, A. W. Rost, A. P. Mackenzie, Yang Xie, J. C. Davis, K. Kihou, C. H. Lee, A. Iyo, H. Eisaki, and T.-M. Chuang. Anisotropic energy gaps of iron-based superconductivity from intraband quasiparticle interference in lifeas. *Science*, 336(6081):563–567, 2012.